Exploring Drug Bioaccumulation and Stabilization with Respect to Endolysosomal Ion Homeostasis Using a Systems-Based Mathematical Modeling Approach

by

Tehetina B. Woldemichael

A dissertation submitted in partial fulfillment
of the requirement for the degree of
Doctor of Philosophy
(Biophysics)
in the University of Michigan
2018

Doctoral Committee:

Professor Gustavo Rosania, Co-Chair
Professor Qiong Yang, Co-Chair
Professor Ayyalusamy Ramamoorthy
Professor Nair Rodriguez-Hornedo

Tehetina B. Woldemichael

wolte@umich.edu

ORCID iD: 0000-0002-7749-8084

Acknowledgments

My deepest gratitude goes to the most High and His infinite expressions. I would also like to thank my advisor, Professor Gus Rosania, for creating the space, which made this PhD dissertation possible. His guidance and mentorship throughout the years have been crucial to my advancement as a graduate student and as an individual. I would additionally like to thank my dissertation committee members, Professors Ayyalusamy Ramamoorthy, Nair Rodriguez-Hornedo, and Qiong Yang, for their insights, questions, and feedbacks, which have all been instrumental to the fruition of my PhD research experience. Furthermore, I would like to thank past and current Rosania lab members for being the support system I have needed during my time in the lab. I would also like to thank the Biophysics Student Services Administrator, Sara Grosky, for making my PhD experience as smooth as possible. And last, but not least, I would like to thank my family and friends for serving as beautiful mirrors, so I wouldn't lose sight of the core essence of the whole journey.

Table of Contents

List of Tables

List of Figures

List of Appendices

Abstract

Even though most of the FDA approved drugs currently out in the market and in the process of development are weakly basic drugs, the bioaccumulation and stabilization of these drugs are not well understood. For this purpose, we use a model drug, clofazimine (CFZ), which is an FDA-approved, weakly basic, and poorly soluble drug that has been used worldwide to treat patients with leprosy and tuberculosis diseases, curing over 16 million people in the last twenty years, to investigate its bioaccumulation and stabilization properties. During prolonged oral administration, CFZ accumulates in macrophages of humans and mice as Crystal Like Drug Inclusions (CLDIs), which have been chemically characterized to be composed of hydrochloride salts of CFZ ($CFZ\text{-}H^{+}Cl^{-}$) crystals. However, the mechanism by which the formation and stabilization of these insoluble complexes occur in cells is not known. Thus, to address this gap, we test the following hypothesis in this dissertation: due to the sufficient proton and chloride levels in endolysosomes, we hypothesize that the phase-transition-dependent drug accumulation and stabilization processes are occurring inside intracellular compartments of likely endolysosomal origin, in macrophages of humans as well as mice.

To test our hypothesis, we adapt a systems-based mathematical lysosomal ion regulation model, which consists of lysosomal membrane proteins, such as the proton-pump known as Vacuolar ATPase (V-ATPase), Cl^{-}/H^{+} antiporter known as CLC7, and membrane proton leak, in order to investigate the key lysosomal parameters that play essential role in the physiological, dose-dependent $CFZ\text{-}H^{+}Cl^{-}$ crystal bioaccumulation. Furthermore, we examine the stabilization

of the free base (CFZ) versus salt form (CFZ-H^+Cl^-) of the drug by mathematically fitting an *in vitro* pH-dependent solubility data of CFZ-H^+Cl^- crystal obtained at pH ranging between extracellular, cellular, and subcellular pH values, and determining the drug's solubility properties, which include the apparent pK_a, intrinsic free base and salt solubility, pH_{max}, and K_{sp} values. Moreover, we model the cellular and subcellular drug transportation and calculate i) the non-membrane and membrane drug accumulation by accounting for the cell-type dependent heterogeneous and asymmetric lipid bilayer of the biological membranes ii) the degree of supersaturation, which is a measure of thermodynamic propensity of precipitation, of both free base CFZ and CFZ-H^+Cl^- salt using the aforementioned solubility properties.

Collectively, our computational results as well as the CFZ-H^+Cl^- physicochemical properties in relation to the ion contents and pH of the microenvironment suggest that the physiological and preferential phase-transition-dependent accumulation and stabilization mechanisms of CFZ-H^+Cl^- crystals in macrophages, more specifically in macrophage lysosomes, are primarily determined by the lysosomal V-ATPase. Moreover, we have shown that the alteration of lysosomal physiology due to lysosomal morphological changes induced upon the accumulation of intrinsic and extrinsic materials, such as cholesterol and biocrystal drugs, respectively can be reversed upon V-ATPase upregulation or inhibition of membrane proton permeability. In addition, in terms of characterizing the stabilization of free base CFZ and CFZ-H^+Cl^- salt, we have found the degree of supersaturation of CFZ-H^+Cl^- salt to be at least 1000-fold greater than that of free base CFZ in all of the cellular compartments, including the biological membranes; emphasizing the propensity of the formation and stabilization of massive CFZ-H^+Cl^- salt precipitate in the lysosomal environment even when introducing low (picomolar) total extracellular drug concentration.

Chapter 1: Introduction

1.1. Introduction

Nearly 40% of drug failure is attributed to the lack of full understanding of a drug's pharmacokinetic (PK) property, comprised of administration, distribution, metabolism, excretion, and toxicity (ADMET)[1]. This jeopardizes the high-risk investment associated with drug development from conception to putting the drug out on the market, which therefore demands researchers to address drugs' PK properties from early-on. Moreover, understanding a drug's biodistribution and bioabsorption is essential to minimize potential off-target side effects. Even in cases where repositioning of FDA-approved drugs has been favored due to cost and time-effective ways of disease treatment, determining and characterizing the PK properties of such drugs is very important[2,3].

Most drugs that are currently in drug discovery and development pipelines are weakly basic molecules and therefore, it is essential to understand ways of improving their solubility[4]. Counterion-mediated drug salt formation has been the primary mechanism by which the solubility of ionizable drugs that are rather weakly soluble in an aqueous environment is enhanced[5]. The most prevalent counterion in salt formation of such drugs is chloride[6]. Solubility improvement favors drug bioavailability, which can in turn increase the probability of the drug reaching its site of action quickly and effectively. However, there are reported cases where such favorable effects are not observed[7]. Although these are generally associated with the poor

understanding of the drug's PK properties prior and/or post administration in relation to the physicochemical interactions of the drug with the host environment, post administration phase transition of drugs manifesting as drug precipitation remains among the most major factors affecting drug bioavailability[8-10].

Drugs with poor solubility precipitate out of solution, thereby generally deteriorating their chances of reaching their sites of action, which in turn would lead to unwanted off-target reactions that could potentially result in toxicity. Attesting to this, structures of toxic insoluble drug complexes have been implicated in favoring inflammation by resulting in the destabilization of lysosome[11], which is a subcellular organelle containing various pH-dependent lysosomal enzymes involved in digesting unwanted materials delivered from the cytoplasm and extracellular environment to the lysosome. To the contrary, there are insoluble drug complexes that are not toxic if their bioavailability is physiological, indicating that toxicity can be due to dose-response and lack of conducive cellular environment that can withstand the biophysical and thermodynamic properties of the drug[12]. Thus, we need to have a better understanding of the phase-transition-dependent drug bioaccumulation not only as a separate phenomenon, but in conjunction with the cellular environment. This will allow us to distinguish the effective dose-regimen and cellular conditions that favor insoluble versus soluble drug species in the hope of predicting and delineating effective from toxic profile of any given drug.

Indeed, there have been many efforts in the study of drug accumulation and precipitation *in vivo* as well as *in vitro*[8-10]. Most studies have been focused on improving drug bioavailability by introducing excipients, such as cosolvents and surfactants, that could improve the drug's solubility while minimizing its potential of precipitation[13]. In addition, various formulation advancements, such as particle size reduction, solid dispersions, lipid-based formulations, salts

and cocrystals are generally used to improve drug solubility and bioavailability[13]. However, the complexity of a cellular environment, characterized by ion homeostasis, pH, and lipid content – to name few – can change the intended outcome of the formulations. Indeed, consistent with this, challenges reported in various *in vitro* and *in vivo* correlation studies[13,14] highlight the gap that remains in the field of phase-transition-dependent PK studies in concert with cellular environment.

Among the aforementioned important cellular features, the effect of pH on phase transition properties of drugs can be determined using the well-established solubility-pH relationship developed by Kramer and Flynn[15]. This is especially important when studying the effect of different cellular pH on the accumulation and stabilization of drug species. It is well established that when weak base drug molecules enter acidic cellular environment, such as the lysosome, they undergo a phenomenon known as lysosomotropism[16], which is the ionization of the drug molecule and its consequent sequestration within the organelle due to its low permeability. However, the stability of the drug upon entry into the lysosomes must be well understood to avoid unwanted side effects. In fact, while some weak base drug accumulation within lysosomes have been associated with favorable effects[17], some are rather associated with the destabilization of the lysosomal physiology which leads to toxicity[18,19]. Thus, elucidating the relationship between maintaining the acidic endolysosomal functionality and stabilizing the phase-transition-dependent drug accumulation is necessary.

For this purpose, utilizing a mathematical model[20,21] that incorporates the biophysics of the endolysosomal proton pumping protein and chloride channel, and the electrophysiological roles of the chloride ion and membrane potential can greatly benefit the understanding of the dynamic subcellular physiology, including its molecular genetics that can accommodate drug

accumulation, salt formation, and stability, which is rather challenging—if not impossible—to study by solely relying on wet lab experiments. Predictions that arise from hypothesis and exploratory-driven mathematical models could potentially bridge the gap between *in vitro* and *in vivo* drug pharmacokinetic disparities. Furthermore, they can help shed light on the potential of repositioning many insoluble complex-forming drugs that have rather been neglected.

1.2. Introduction to model drug: Clofazimine

Clofazimine (CFZ) is an FDA-approved antibiotic used to treat leprosy[22], curing over 16 million people worldwide[23]. Even though the exact mechanism of the drug's action is multifaceted, it is likely that bacterial growth hindrance, membrane disruption, and increment of antimicrobial reactive oxidant species play important roles[24-26]. Regardless of the mechanism, clofazimine's antibiotic and anti-inflammatory properties have made researchers to-date interested in using this drug for various treatments including cancer, respiratory disease, skin-targeted autoimmune diseases, multi-drug resistant tuberculosis (MDRTB), and TB-HIV co-infections[27-30]. Along with its definitive antimycobacterial activity *in vitro*, CFZ has had a success rate of 87.9% when administered along with other drugs such as, ethambutol, isoniazid, and pyrazinamide to treat MDRTB[31]. MDRTB arises due to the pathogen's capability of perturbing phagosomal maturation process by disrupting endolysosomal acidification in macrophages[32]. Thus, possible mechanism through which CFZ reverses the resistance of the growing mycobacteria to previously used drugs could be by maintaining endolysosomal pH necessary for phagosomal maturation, which facilitates the removal of the mycobacteria from the host.

Moreover, it has been shown that clofazimine inhibits cathepsins B, H, and L, which are lysosomal enzymes involved in the progression of various deadly diseases including cancer, arthritis, and Alzheimer's disease[33-39].Tumoricidal properties of clofazimine have also been useful in treating cancer patients by possibly increasing lysophospholipids in membranes[40]. These findings indicate that although the drug has had tremendous success in treating bacterial and non-bacterial diseases, its full potential has not been exploited and demands more studies that can capitalize on its efficacy while diminishing its clinically-reported, dose-related reversible side effects, such as skin discoloration[41]. Among the interesting features of CFZ is that it forms Crystal Like Drug Inclusions (CLDIs) in both humans as well as mice[42-44]. After three to four weeks of feeding the drug to mice, our lab has shown that the crystals accumulate in liver, spleen, and lung macrophages[45]. Our wet lab studies have indicated that these crystals give rise to the drug's anti-inflammatory property[12,46]. However, the mechanism of crystal formation is unknown. In addition, for the drug accumulation to be sustained and induce effects, the drug containing macrophages must go through accommodative process to remain viable and active. Thus, it is important to understand the conditions required by macrophages for accumulating CFZ crystals as it would lay the groundwork for understanding the mechanisms of bioaccumulation, crystallization, and stabilization of CFZ.

To explain the relatively complex *in vivo* phenomenon, we initially have to have better understanding of *in vitro* studies that can correspond to *in vivo* CLDI formation. In support of this, previous work in our lab has indicated that the *in vitro* accumulation and crystallization of CFZ is within order of magnitude consistent with that of the *in vivo*[47]. Moreover, we have shown that CLDIs are comprised of CFZ-H^+Cl^- crystals, and that both show similar fluorescence, 1D nuclear magnetic resonance (NMR), and powder X-ray diffraction (pXRD) profiles[48]. Thus, we

hypothesize that, due to pH decrement and chloride increment along the endocytic pathway, the accumulation, protonation, and subsequent crystallization of clofazimine is coupled with the endocytic pathway, more specifically with the endolysosomal organelles based on ion-trapping mechanism and chloride sequestration. Ion-trapping mechanism has been implicated in studies of subcellular accumulation of other weakly basic amines, with similar solubility and hydrophobicity profile to CFZ[49]. Because most weakly basic molecules have ionizable groups with high pK_a greater than 5, they become mainly protonated upon entering an acidic environment, such as the endolysosomes. Once protonated, the molecule will have less permeability and therefore, gets trapped in the organelle, consequently inducing change in organellar size[50,51]. Such phenomenon could arise due to the phase-transition-dependent accumulation and stabilization of insoluble drug complexes upon chloride sequestration by the protonated drug, also known as a common-ion effect[5,6].

Alternatively, in the event of phagocytosed CFZ crystals, there could be an accommodative process in macrophages where the regulation of certain endolysosomal genes may contribute for the phase-transition-dependent drug accumulation and crystallization processes to not induce toxicity by perturbing phagosomal maturation. It has been shown that the transcription factor EB (TFEB) regulates lysosomal biogenesis upon the introduction of a foreign material to the lysosome[52]. Thus, we suggest that the expression level of TFEB-regulated lysosomal genes will be essential to our understanding of the maintenance of accumulation and crystallization of CFZ in the endolysosomes while keeping the integrity of the host cells intact. Moreover, the heterogeneous expression of endolysosomal genes will aid our understanding of the relationship between different expression levels of genes that are essential for regulating proton and chloride ions, and the overall heterogeneous distribution of CLDIs in macrophages.

1.3. The role of endolysosomal biogenesis in the cell-type specific phase-transition-dependent drug bioaccumulation and salt precipitation

Macrophages are categorized into two based on their induced polarization states in response to environmental stimuli. These states are known as M1 and M2 types of macrophages. M1 macrophage is characterized by pro-inflammatory responses, such as interferon-gamma-receptor after induction by lipopolysaccharides (LPS) antagonist; whereas M2 macrophage is characterized by anti-inflammatory cytokines, such as, IL-10 and TGM2, after stimulation with IL-4 and IL-3 agonists. In addition, macrophages are heterogeneously distributed *in vivo*[53]. This is in agreement with our lab's observation of the heterogeneously distributed CLDIs in peritoneal and alveolar macrophages[42]. Thus, understanding the necessary conditions for various types of macrophages to accommodate various amounts of CLDIs require a modeling prediction that incorporates analysis of the literature, which elucidate different expression levels of the electrogenic, multi-subunit proton pumping protein known as vacuolar-type ATPase (V-ATPase), and chloride channels and transporters in macrophages, and more specifically in endolysosomes. Chloride channels/transporters that dominate the endolysosomes are classified as CLC family, where CLCs 3-5 are primarily found in the early stages, and CLCs 6 and 7 are localized in the later stages of the endocytic pathway[54].

It is suggested that the expression levels of V-ATPase subunits must be regulated by a transcriptional and post-transcriptional universal mechanisms. Stat6 is among the transcription factors that highly regulates lysosomal genes. In the presence of IL-4 stimulant in Stat6+/+ mouse macrophages, some of the V-ATPase subunits are upregulated, indicating that M2 macrophages have higher V-ATPase expression[55]. Beyond Stat6, transcription factor EB (TFEB) is a lysosomal transcription factor that has been shown to play significant role in regulating

lysosomal biogenesis, including V-ATPase expression[56-58]. Although TFEB has not been associated with CLC7 expression, Microphthalmia transcription factor (MITF), which is in the same family as TFEB has been shown to regulate CLC7 expression[59,60].

In osteoclasts, where the prevalence of CLC7 is necessary for bone resorption, CLC7 and V-ATPase (more specifically, the a3 subunit) expression levels must change with the size of the cell[61-64]. This can be due to an increase in TFEB expression, as that has been shown to expand lysosomal compartment as well as increase the number of lysosomes per cell in HeLa cells[50]. Similarly, we expect the TFEB expression to increase with the size of the lysosome as well, because the translocation of TFEB from the cytoplasm to the nucleus has been associated with an increase in lysosomal volume upon accumulation of a weakly basic molecule[51]. Not only is CLC7 expression level important, but also its Ostm1 subunit[64], which is required for the role of CLC7 in dissipating membrane potential for the V-ATPase to regulate physiological pH. Moreover, among the V-ATPase subunits, the ratio of a1 to a3 expression level has been shown to vary with different cell types including macrophages and osteoclasts, and have a direct relationship with the change in phagolysosomal pH[65-67]. In the case of non-physiological change in pH, less localization of V-ATPase a3 subunit in osteoclasts occurs, hence affecting bone resorption[66,68].

In addition to cell-type specific heterogeneous lysosomal gene expression, lysosomes are known to have different morphologies[69]. Although most lysosomes are known to be spherical in shape, there have been reports showing lysosomes with tubular and disc-shaped geometries[69,70]. While tubular lysosomes are primarily prevalent before the initiation of material uptake by the endolysosomes[70,71], the disc-shaped lysosomes are reported in the case of prolonged material accumulation within the lysosomes, such as those in various lysosomal storage disorders

(LSDs)[72-74]. Indeed, the non-degradable materials range from intrinsic cellular materials, such as cholesterol and lipids, to extrinsic materials, such as weak base drugs[69,75-77].

The disc-shaped lysosomes have non-physiological pH[74,78], which arrests the proper functioning of the pH-dependent lysosomal enzymes that induce the timely degradation of the accumulating materials. Given physiological lysosomes are important for the degradation of cellular materials, recycling of membrane materials, such as membrane proteins, cholesterol, and lipids, such perturbation of lysosomal physiology is detrimental to the overall cellular function[58]. Therefore, thorough understanding of lysosomal ion homeostasis with respect to drug-induced change in lysosomal morphology is important to avoid the negative side effects of prolonged material accumulation in lysosomes. Indeed, this is very essential to our understanding of physiological cellular drug accumulation, especially in cases where drugs are administered for longer periods of time.

Although there have been studies showing the role of TFEB nuclear translocation to remedy lysosomal malfunction observed in LSDs[52,79,80], the mechanism by which this occurs is not well recognized[81]. This could be attributed to the dynamic, interdependent processes of lysosomal biogenesis, ion homeostasis, membrane trafficking, and membrane protein expression and turnover, all of which are extremely difficult to monitor and investigate in wet lab experiments where appropriate experimental techniques lack. Therefore, utilizing a mathematical model[20] that allows us to investigate the interdependence of lysosomal morphology, gene expression, and ion homeostasis, is deemed necessary. This will especially be important in our understanding of the cell's mechanistic role in the phase-dependent prolonged accumulation and stabilization of CFZ as biocrystalline CFZ-H^+Cl^- salts in macrophages, *in vivo*[42,47].

1.4. Modeling phase-transition-dependent cellular drug accumulation and stabilization

Weak base drugs can undergo phase transition depending on their physicochemical properties, such as their pK_a, intrinsic free base and salt solubility, pH_{max} (pH at which the free base and salt forms of the drug coexist), and salt solubility product (K_{sp}), as well as the pH and ion content of their cellular microenvironments[6,15], which can affect their distribution profile, thereby affecting their overall PK properties. While the precipitation of CFZ into insoluble complexes known as CLDIs has not been associated with any major side effects[12,46], reports have shown phase transition of other drugs, such as ciprofloxacin, are linked with adverse drug side-effects, such as kidney injury known as crystal nephropathy[82,83]. Although alkaline urine is suggested to contribute to such side effect, the exact mechanism by which this occurs is not well defined[84].

Furthermore, there are various weak base drugs which permeabilize the lysosomal membrane, thereby inducing cellular toxicity upon the release of lysosomal enzymes from the lysosome to the cytosol[19]. However, the relationship between drug accumulation within the various cellular compartments, including cell and organelle membranes, such as lysosomal membrane and the degree of membrane permeabilization is not well characterized. Moreover, whether the amount and type of lipids in the biological membranes contribute to this effect is not known. Indeed, the presence of surfactants is known to affect the solubility of most drugs[85] including weak base drugs[86]. Thus, whether biological membrane lipids could induce similar effects, thereby affecting the overall cellular drug disposition and stabilization remains to be investigated.

However, regarding the knowledge of subcellular drug disposition, it is well known that weak base compounds accumulate to a greater extent in the lysosomes as ionized forms[16,51,87].

However, not much is known regarding the stability of those entrapped, ionized drugs in the lysosome. Moreover, although experimental determination of subcellular drug concentrations of non-fluorescent compounds has been possible[88], the subcellular concentration of the phase-transition-dependent drug species is not accounted for, and remains to be challenging to investigate.

Indeed, in order to address the gap in wet lab experimental techniques, there have been multiple mathematical models built to study drug accumulation, which generally follow Fick's first law of diffusion and Nernst-Planck equation[42,89], and in some more elaborate cases incorporate the effect of drug transporters[90,91]. Although these models are very useful in predicting drug accumulation in different cellular compartments, they neither elucidate the stability of these drugs nor the propensity of these drugs to precipitate out of solution inside the organelles and the membranes. This suggests that building a mathematical model that investigates the phase transition of drugs in different cellular environments while accounting for the effect of biological membrane lipids is important to not only better predict and understand the PK properties of a given drug, but also to minimize unwanted, drug-induced adverse side effects.

1.5. Dissertation objectives

Cellular drug disposition, accumulation, and stabilization, collectively remain to be topics that are not well characterized in the drug discovery and development fields, which in turn leads to drug failure following high-risk time and financial investments, and unwanted adverse drug side effects associated with various health complications. Thus, in this dissertation, I first investigate the relationship between endolysosomal membrane proteins and endoylsosomal ion

homeostasis, and their roles in physiologically accommodating and stabilizing biocrystal drug accumulation (Chapter 2). In concert with this, I study the physicochemical properties of a given biocrystal drug, which are important in elucidating the stability of the drug in endolysosomes. Second, I investigate the key lysosomal parameters that can explain drug accumulation observed in macrophages with respect to changes in lysosomal morphology (Chapter 3), which is important for our understanding of the cell-type specific drug accumulation and stabilization phenomenon. Third, I investigate how phagosome maturation influences biocrystal biocompatibility by studying the phase-transition-dependent accumulation and stability of the biocrystal drug in relation to different cellular compartments (Chapter 4). Lastly, I perform computational pharmacokinetic analysis of *in vivo* clofazimine accumulation and efflux experiments, which have allowed us to determine the steady-state clofazimine accumulation in different macrophage populations (Chapter 5).

1.6. References

1 van de Waterbeemd, H. & Gifford, E. ADMET in silico modelling: towards prediction paradise? *Nat Rev Drug Discov* **2**, 192-204, doi:10.1038/nrd1032 (2003).

2 Arrowsmith, J. & Harrison, R. in *Drug Repositioning* 7-32 (John Wiley & Sons, Inc., 2012).

3 Ashburn, T. T. & Thor, K. B. Drug repositioning: identifying and developing new uses for existing drugs. *Nat Rev Drug Discov* **3**, 673-683, doi:10.1038/nrd1468 (2004).

4 Charifson, P. S. & Walters, W. P. Acidic and basic drugs in medicinal chemistry: a perspective. *J Med Chem* **57**, 9701-9717, doi:10.1021/jm501000a (2014).

5 David, S. E., Timmins, P. & Conway, B. R. Impact of the counterion on the solubility and physicochemical properties of salts of carboxylic acid drugs. *Drug Dev Ind Pharm* **38**, 93-103, doi:10.3109/03639045.2011.592530 (2012).

6 Serajuddin, A. T. Salt formation to improve drug solubility. *Adv Drug Deliv Rev* **59**, 603-616, doi:10.1016/j.addr.2007.05.010 (2007).

7 Elder, D. P., Holm, R. & Diego, H. L. Use of pharmaceutical salts and cocrystals to address the issue of poor solubility. *Int J Pharm* **453**, 88-100, doi:10.1016/j.ijpharm.2012.11.028 (2013).

8 Augustijns, P. & Brewster, M. E. Supersaturating drug delivery systems: fast is not necessarily good enough. *J Pharm Sci* **101**, 7-9, doi:10.1002/jps.22750 (2012).

9 Miller, D. A., DiNunzio, J. C., Yang, W., McGinity, J. W. & Williams, R. O., 3rd. Enhanced in vivo absorption of itraconazole via stabilization of supersaturation following acidic-to-neutral pH transition. *Drug Dev Ind Pharm* **34**, 890-902, doi:10.1080/03639040801929273 (2008).

10 Yalkowsky, S. H., Valvani, S. C. & Johnson, B. W. In vitro method for detecting precipitation of parenteral formulations after injection. *J Pharm Sci* **72**, 1014-1017 (1983).

11 Shi, Y., Mucsi, A. D. & Ng, G. Monosodium urate crystals in inflammation and immunity. *Immunol Rev* **233**, 203-217, doi:10.1111/j.0105-2896.2009.00851.x (2010).

12 Yoon, G. S. *et al.* Phagocytosed Clofazimine Biocrystals Can Modulate Innate Immune Signaling by Inhibiting TNFalpha and Boosting IL-1RA Secretion. *Mol Pharm* **12**, 2517-2527, doi:10.1021/acs.molpharmaceut.5b00035 (2015).

13 Williams, H. D. *et al.* Strategies to address low drug solubility in discovery and development. *Pharmacol Rev* **65**, 315-499 (2013).

14 Bevernage, J., Brouwers, J., Brewster, M. E. & Augustijns, P. Evaluation of gastrointestinal drug supersaturation and precipitation: strategies and issues. *Int J Pharm* **453**, 25-35, doi:10.1016/j.ijpharm.2012.11.026 (2013).

15 Kramer, S. F. & Flynn, G. L. Solubility of organic hydrochlorides. *J Pharm Sci* **61**, 1896-1904 (1972).

16 de Duve, C. *et al.* Commentary. Lysosomotropic agents. *Biochem Pharmacol* **23**, 2495-2531 (1974).

17 Logan, R., Funk, R. S., Axcell, E. & Krise, J. P. Drug-drug interactions involving lysosomes: mechanisms and potential clinical implications. *Expert Opin Drug Metab Toxicol* **8**, 943-958, doi:10.1517/17425255.2012.691165 (2012).

18 Zhao, H., Cai, Y., Santi, S., Lafrenie, R. & Lee, H. Chloroquine-mediated radiosensitization is due to the destabilization of the lysosomal membrane and subsequent induction of cell death by necrosis. *Radiat Res* **164**, 250-257 (2005).

19 Boya, P. & Kroemer, G. Lysosomal membrane permeabilization in cell death. *Oncogene* **27**, 6434-6451, doi:10.1038/onc.2008.310 (2008).

20 Ishida, Y., Nayak, S., Mindell, J. A. & Grabe, M. A model of lysosomal pH regulation. *J Gen Physiol* **141**, 705-720, doi:10.1085/jgp.201210930 (2013).

21 Grabe, M. & Oster, G. Regulation of organelle acidity. *J Gen Physiol* **117**, 329-344 (2001).

22 Yawalkar, S. J. & Vischer, W. Lamprene (clofazimine) in leprosy. Basic information. *Lepr Rev* **50**, 135-144 (1979).

23 Organization, W. H. <Http://www.who.int/mediacentre/factsheets/fs101/en/> (2017).

24 Morrison, N. E. & Marley, G. M. Clofazimine binding studies with deoxyribonucleic acid. *Int J Lepr Other Mycobact Dis* **44**, 475-481 (1976).

25 Yano, T. *et al.* Reduction of clofazimine by mycobacterial type 2 NADH:quinone oxidoreductase: a pathway for the generation of bactericidal levels of reactive oxygen species. *J Biol Chem* **286**, 10276-10287, doi:10.1074/jbc.M110.200501 (2011).

26 Oliva, B., O'Neill, A. J., Miller, K., Stubbings, W. & Chopra, I. Anti-staphylococcal activity and mode of action of clofazimine. *J Antimicrob Chemother* **53**, 435-440, doi:10.1093/jac/dkh114 (2004).

27 Padayatchi, N. *et al.* Clofazimine in the treatment of extensively drug-resistant tuberculosis with HIV coinfection in South Africa: a retrospective cohort study. *J Antimicrob Chemother* **69**, 3103-3107, doi:10.1093/jac/dku235 (2014).

28 Arbiser, J. L. & Moschella, S. L. Clofazimine: a review of its medical uses and mechanisms of action. *J Am Acad Dermatol* **32**, 241-247 (1995).

29 Koot, D. & Cromarty, D. Anticancer efficacy and toxicokinetics of a novel paclitaxel-clofazimine nanoparticulate co-formulation. *Drug Deliv Transl Res* **5**, 257-267, doi:10.1007/s13346-015-0222-6 (2015).

30 Bezerra, E. L., Vilar, M. J., da Trindade Neto, P. B. & Sato, E. I. Double-blind, randomized, controlled clinical trial of clofazimine compared with chloroquine in patients with systemic lupus erythematosus. *Arthritis Rheum* **52**, 3073-3078, doi:10.1002/art.21358 (2005).

31 Van Deun, A. *et al.* Short, highly effective, and inexpensive standardized treatment of multidrug-resistant tuberculosis. *Am J Respir Crit Care Med* **182**, 684-692, doi:10.1164/rccm.201001-0077OC (2010).

32 Huynh, K. K. & Grinstein, S. Regulation of vacuolar pH and its modulation by some microbial species. *Microbiol Mol Biol Rev* **71**, 452-462, doi:10.1128/MMBR.00003-07 (2007).

33 Kamboj, R. C. *et al.* Effects of some antituberculous and anti-leprotic drugs on cathepsins B, H and L. *Indian J Clin Biochem* **18**, 39-47, doi:10.1007/BF02867366 (2003).

34 Sarracent, J. & Finlay, C. M. The action of Clofazimine on the level of lysosomal enzymes of cultured macrophages. *Clin Exp Immunol* **48**, 261-267 (1982).

35 Gondi, C. S. & Rao, J. S. Cathepsin B as a cancer target. *Expert Opin Ther Targets* **17**, 281-291, doi:10.1517/14728222.2013.740461 (2013).

36 Lankelma, J. M. *et al.* Cathepsin L, target in cancer treatment? *Life Sci* **86**, 225-233, doi:10.1016/j.lfs.2009.11.016 (2010).

37 Mohamed, M. M. & Sloane, B. F. Cysteine cathepsins: multifunctional enzymes in cancer. *Nat Rev Cancer* **6**, 764-775, doi:10.1038/nrc1949 (2006).

38 Kindy, M. S. *et al.* Deletion of the cathepsin B gene improves memory deficits in a transgenic ALZHeimer's disease mouse model expressing AbetaPP containing the wild-type beta-secretase site sequence. *J Alzheimers Dis* **29**, 827-840, doi:10.3233/JAD-2012-111604 (2012).

39 Yasuda, Y., Kaleta, J. & Bromme, D. The role of cathepsins in osteoporosis and arthritis: rationale for the design of new therapeutics. *Adv Drug Deliv Rev* **57**, 973-993, doi:10.1016/j.addr.2004.12.013 (2005).

40 Van Rensburg, C. E., Van Staden, A. M. & Anderson, R. The riminophenazine agents clofazimine and B669 inhibit the proliferation of cancer cell lines in vitro by phospholipase A2-mediated oxidative and nonoxidative mechanisms. *Cancer Res* **53**, 318-323 (1993).

41 Xu, H. B., Jiang, R. H. & Xiao, H. P. Clofazimine in the treatment of multidrug-resistant tuberculosis. *Clin Microbiol Infect* **18**, 1104-1110, doi:10.1111/j.1469-0691.2011.03716.x (2012).

42 Baik, J., Stringer, K. A., Mane, G. & Rosania, G. R. Multiscale distribution and bioaccumulation analysis of clofazimine reveals a massive immune system-mediated xenobiotic sequestration response. *Antimicrob Agents Chemother* **57**, 1218-1230, doi:10.1128/AAC.01731-12 (2013).

43 Desikan, K. V., Ramanujam, K., Ramu, G. & Balakrishnan, S. Autopsy findings in a case of lepromatous leprosy treated with clofazimine. *Lepr Rev* **46**, 181-189 (1975).

44 Lewis, J. T., Candelora, J. N., Hogan, R. B., Briggs, F. R. & Abraham, S. C. Crystal-storing histiocytosis due to massive accumulation of charcot-leyden crystals: a unique association producing colonic polyposis in a 78-year-old woman with eosinophilic colitis. *Am J Surg Pathol* **31**, 481-485, doi:10.1097/01.pas.0000213420.46127.9c (2007).

45 Baik, J. & Rosania, G. R. Modeling and Simulation of Intracellular Drug Transport and Disposition Pathways with Virtual Cell. *J Pharm Pharmacol (Los Angel)* **1**, doi:10.13188/2327-204X.1000004 (2013).

46 Yoon, G. S. *et al.* Clofazimine Biocrystal Accumulation in Macrophages Upregulates Interleukin 1 Receptor Antagonist Production To Induce a Systemic Anti-Inflammatory State. *Antimicrob Agents Chemother* **60**, 3470-3479, doi:10.1128/AAC.00265-16 (2016).

47 Baik, J. & Rosania, G. R. Molecular imaging of intracellular drug-membrane aggregate formation. *Mol Pharm* **8**, 1742-1749, doi:10.1021/mp200101b (2011).

48 Keswani, R. K. *et al.* Chemical Analysis of Drug Biocrystals: A Role for Counterion Transport Pathways in Intracellular Drug Disposition. *Mol Pharm* **12**, 2528-2536, doi:10.1021/acs.molpharmaceut.5b00032 (2015).

49 Kaufmann, A. M. & Krise, J. P. Lysosomal sequestration of amine-containing drugs: analysis and therapeutic implications. *J Pharm Sci* **96**, 729-746, doi:10.1002/jps.20792 (2007).

50 Funk, R. S. & Krise, J. P. Cationic amphiphilic drugs cause a marked expansion of apparent lysosomal volume: implications for an intracellular distribution-based drug interaction. *Mol Pharm* **9**, 1384-1395, doi:10.1021/mp200641e (2012).

51 Logan, R., Kong, A. C. & Krise, J. P. Time-dependent effects of hydrophobic amine-containing drugs on lysosome structure and biogenesis in cultured human fibroblasts. *J Pharm Sci* **103**, 3287-3296, doi:10.1002/jps.24087 (2014).

52 Sardiello, M. *et al.* A gene network regulating lysosomal biogenesis and function. *Science* **325**, 473-477, doi:10.1126/science.1174447 (2009).

53 Tedesco, S. *et al.* Phenotypic activation and pharmacological outcomes of spontaneously differentiated human monocyte-derived macrophages. *Immunobiology* **220**, 545-554, doi:10.1016/j.imbio.2014.12.008 (2015).

54 Stauber, T. & Jentsch, T. J. Chloride in vesicular trafficking and function. *Annu Rev Physiol* **75**, 453-477, doi:10.1146/annurev-physiol-030212-183702 (2013).

55 Brignull, L. M. *et al.* Reprogramming of lysosomal gene expression by interleukin-4 and Stat6. *BMC Genomics* **14**, 853, doi:10.1186/1471-2164-14-853 (2013).

56 McMains, E., Krishnan, V., Prasad, S. & Gleason, E. Expression and localization of CLC chloride transport proteins in the avian retina. *PLoS One* **6**, e17647, doi:10.1371/journal.pone.0017647 (2011).

57 Wang, W. *et al.* Up-regulation of lysosomal TRPML1 channels is essential for lysosomal adaptation to nutrient starvation. *Proc Natl Acad Sci U S A* **112**, E1373-1381, doi:10.1073/pnas.1419669112 (2015).

58 Samie, M. A. & Xu, H. Lysosomal exocytosis and lipid storage disorders. *J Lipid Res* **55**, 995-1009, doi:10.1194/jlr.R046896 (2014).

59 Meadows, N. A. *et al.* The expression of Clcn7 and Ostm1 in osteoclasts is coregulated by microphthalmia transcription factor. *J Biol Chem* **282**, 1891-1904, doi:10.1074/jbc.M608572200 (2007).

60 Esumi, N., Kachi, S., Campochiaro, P. A. & Zack, D. J. VMD2 promoter requires two proximal E-box sites for its activity in vivo and is regulated by the MITF-TFE family. *J Biol Chem* **282**, 1838-1850, doi:10.1074/jbc.M609517200 (2007).

61 Bar-Shavit, Z. The osteoclast: a multinucleated, hematopoietic-origin, bone-resorbing osteoimmune cell. *J Cell Biochem* **102**, 1130-1139, doi:10.1002/jcb.21553 (2007).

62 Trebec, D. P. *et al.* Increased expression of activating factors in large osteoclasts could explain their excessive activity in osteolytic diseases. *J Cell Biochem* **101**, 205-220, doi:10.1002/jcb.21171 (2007).

63 Manolson, M. F. *et al.* The a3 isoform of the 100-kDa V-ATPase subunit is highly but differentially expressed in large (>or=10 nuclei) and small (<or= nuclei) osteoclasts. *J Biol Chem* **278**, 49271-49278, doi:10.1074/jbc.M309914200 (2003).

64 Weinert, S. *et al.* Transport activity and presence of ClC-7/Ostm1 complex account for different cellular functions. *EMBO Rep* **15**, 784-791, doi:10.15252/embr.201438553 (2014).

65 Wang, S. P., Krits, I., Bai, S. & Lee, B. S. Regulation of enhanced vacuolar H+-ATPase expression in macrophages. *J Biol Chem* **277**, 8827-8834, doi:10.1074/jbc.M111959200 (2002).

66 Voronov, I. *et al.* The R740S mutation in the V-ATPase a3 subunit increases lysosomal pH, impairs NFATc1 translocation, and decreases in vitro osteoclastogenesis. *J Bone Miner Res* **28**, 108-118, doi:10.1002/jbmr.1727 (2013).

67 Guo, M. *et al.* High-resolution quantitative proteome analysis reveals substantial differences between phagosomes of RAW 264.7 and bone marrow derived macrophages. *Proteomics* **15**, 3169-3174, doi:10.1002/pmic.201400431 (2015).

68 Nyman, J. K. & Vaananen, H. K. A rationale for osteoclast selectivity of inhibiting the lysosomal V-ATPase a3 isoform. *Calcif Tissue Int* **87**, 273-283, doi:10.1007/s00223-010-9395-7 (2010).

69 Lüllmann-Rauch, R. in *Lysosomes* 1-16 (Springer US, 2005).

70 Knapp, P. E. & Swanson, J. A. Plasticity of the tubular lysosomal compartment in macrophages. *J Cell Sci* **95 (Pt 3)**, 433-439 (1990).

71 Swanson, J., Burke, E. & Silverstein, S. C. Tubular lysosomes accompany stimulated pinocytosis in macrophages. *J Cell Biol* **104**, 1217-1222 (1987).

72 Schultz, M. L., Tecedor, L., Chang, M. & Davidson, B. L. Clarifying lysosomal storage diseases. *Trends Neurosci* **34**, 401-410, doi:10.1016/j.tins.2011.05.006 (2011).

73 te Vruchte, D. *et al.* Accumulation of glycosphingolipids in Niemann-Pick C disease disrupts endosomal transport. *J Biol Chem* **279**, 26167-26175, doi:10.1074/jbc.M311591200 (2004).

74 Emanuel, R. *et al.* Induction of lysosomal biogenesis in atherosclerotic macrophages can rescue lipid-induced lysosomal dysfunction and downstream sequelae. *Arterioscler Thromb Vasc Biol* **34**, 1942-1952, doi:10.1161/ATVBAHA.114.303342 (2014).

75 Morissette, G., Lodge, R. & Marceau, F. Intense pseudotransport of a cationic drug mediated by vacuolar ATPase: procainamide-induced autophagic cell vacuolization. *Toxicol Appl Pharmacol* **228**, 364-377, doi:10.1016/j.taap.2007.12.031 (2008).

76 Ohkuma, S. & Poole, B. Cytoplasmic vacuolation of mouse peritoneal macrophages and the uptake into lysosomes of weakly basic substances. *J Cell Biol* **90**, 656-664 (1981).

77 Strausbauch, P. & Sehgal, N. Three-dimensional reconstruction of anomalous beige mouse macrophage lysosomes. *J Leukoc Biol* **46**, 441-449 (1989).

78 Raychowdhury, M. K. *et al.* Molecular pathophysiology of mucolipidosis type IV: pH dysregulation of the mucolipin-1 cation channel. *Hum Mol Genet* **13**, 617-627, doi:10.1093/hmg/ddh067 (2004).

79 Settembre, C., Fraldi, A., Medina, D. L. & Ballabio, A. Signals from the lysosome: a control centre for cellular clearance and energy metabolism. *Nat Rev Mol Cell Biol* **14**, 283-296, doi:10.1038/nrm3565 (2013).

80 Sardiello, M. & Ballabio, A. Lysosomal enhancement: a CLEAR answer to cellular degradative needs. *Cell Cycle* **8**, 4021-4022 (2009).

81 Lu, S., Sung, T., Lin, N., Abraham, R. T. & Jessen, B. A. Lysosomal adaptation: How cells respond to lysosomotropic compounds. *PLoS One* **12**, e0173771, doi:10.1371/journal.pone.0173771 (2017).

82 Yarlagadda, S. G. & Perazella, M. A. Drug-induced crystal nephropathy: an update. *Expert Opin Drug Saf* **7**, 147-158, doi:10.1517/14740338.7.2.147 (2008).

83 Izzedine, H., Launay-Vacher, V. & Deray, G. Antiviral drug-induced nephrotoxicity. *Am J Kidney Dis* **45**, 804-817 (2005).

84 Stratta, P., Lazzarich, E., Canavese, C., Bozzola, C. & Monga, G. Ciprofloxacin crystal nephropathy. *Am J Kidney Dis* **50**, 330-335, doi:10.1053/j.ajkd.2007.05.014 (2007).

85 Jain, N., Yang, G., Tabibi, S. E. & Yalkowsky, S. H. Solubilization of NSC-639829. *Int J Pharm* **225**, 41-47 (2001).

86 Kadam, Y., Yerramilli, U. & Bahadur, A. Solubilization of poorly water-soluble drug carbamezapine in pluronic micelles: effect of molecular characteristics, temperature and added salt on the solubilizing capacity. *Colloids Surf B Biointerfaces* **72**, 141-147, doi:10.1016/j.colsurfb.2009.03.027 (2009).

87 Duvvuri, M. & Krise, J. P. A novel assay reveals that weakly basic model compounds concentrate in lysosomes to an extent greater than pH-partitioning theory would predict. *Mol Pharm* **2**, 440-448, doi:10.1021/mp050043s (2005).

88 Fu, D. *et al.* Imaging the intracellular distribution of tyrosine kinase inhibitors in living cells with quantitative hyperspectral stimulated Raman scattering. *Nat Chem* **6**, 614-622, doi:10.1038/nchem.1961 (2014).

89 Ufuk, A. *et al.* In Vitro and in Silico Tools To Assess Extent of Cellular Uptake and Lysosomal Sequestration of Respiratory Drugs in Human Alveolar Macrophages. *Mol Pharm* **14**, 1033-1046, doi:10.1021/acs.molpharmaceut.6b00908 (2017).

90 Nagar, S. *et al.* Compartmental models for apical efflux by P-glycoprotein--part 1: evaluation of model complexity. *Pharm Res* **31**, 347-359, doi:10.1007/s11095-013-1164-7 (2014).

91 Korzekwa, K. R. *et al.* Models to predict unbound intracellular drug concentrations in the presence of transporters. *Drug Metab Dispos* **40**, 865-876, doi:10.1124/dmd.111.044289 (2012).

Chapter 2: Elucidating the Relationship between Endolysosomal Membrane Proteins and Endolysosomal Ion Homeostasis and Their Roles in Accommodating and Stabilizing Biocrystal Drug Accumulation

This chapter was adapted from submitted manuscript:

Woldemichael, T., Keswani, R.K., Rzeczycki, P., Murashov, M.D., LaLone, V., Gregorka, B., Swanson, J.A., Stringer, K.A., and Rosania, G.R. (2017) Reverse Engineering the Intracellular Self-Assembly of a Functional Mechanopharmaceutical Device.

2.1. Relevance to Thesis

This chapter incorporates the interdependence of lysosomal ion homeostasis and biocrystal drug accumulation, and discusses the key lysosomal parameter for the physiological accumulation of biocrystal drug in a cell-type dependent manner by i) investigating the physicochemical properties of free base CFZ and CFZ-H^+Cl^- salt in relation to different cellular and subcellular conditions, such as pH and ion content, ii) modeling the effects of various cell-type dependent lysosomal features, such as membrane proteins and ion content on biocrystal drug accumulation.

Our findings enabled us to further design and characterize the subcellular accumulation of the drug *in vitro*. Moreover, the combination of wet lab and computational results have strengthened our understanding of previously published results from our lab in regards to the unique occurrence of the self-assembled, crystal packing of the clofazimine hydrochloride salt *in*

vivo, in macrophages. In addition, the conclusions we have drawn from our findings will allow us to design and test new hypothesis-driven studies of physiological drug bioaccumulation.

Furthermore, given that most drugs that are already FDA approved or in clinical trials are weak base compounds, our findings are critical for elucidating the mechanism of a weak base drug accumulation and stabilization in cells in a cell-type dependent manner, which is a phenomenon closely associated with the drug's overall pharmacokinetic profile. Thus, our findings will further open doors to the fields of drug delivery and drug repurposing where drug stability and accumulation, in relation to the biochemical, biophysical, and biomechanical features of its natural carriers: cells, play a significant role in the success of a drug development process.

2.2. Personal Contribution

I modeled and analyzed wet lab experimental solubility-pH data to obtain the physicochemical properties of free base CFZ and CFZ-H^+Cl^- salt, which are important in our understanding of the cellular and subcellular drug disposition and stabilization in concert with cellular and subcellular environments.

In addition, I modeled and performed simulations of the effects of various cell-type dependent lysosomal features, such as membrane proteins and ion content on biocrystal drug accumulation, which have allowed us to identify the key lysosomal parameter that is essential and sufficient to explain the preferential physiological bioaccumulation and stabilization of CFZ in macrophages. The findings from the model and simulation results have allowed the design of wet lab experiments which have further strengthened our conclusions regarding the mechanistic role of lysosomal membrane proteins on the accumulation of clofazimine hydrochloride salt.

2.3. Abstract

Weakly basic, poorly soluble chemical agents could be exploited as building blocks for constructing sophisticated molecular devices inside the cells of living organisms. Here, using experimental and computational approaches, we probed the relationship between the biological mechanisms mediating lysosomal ion homeostasis and the self-assembly of a weakly basic small molecule building block into a functional, mechanopharmaceutical device in macrophage lysosomes. Physicochemical considerations indicate that the intralysosomal stabilization of the self-assembled mechanopharmaceutical device depends on the pH_{max} of the weakly basic building block and its affinity for chloride, both of which are consistent with the pH and chloride content of a physiological lysosomal microenvironment. Most importantly, *in vitro* and *in silico* studies revealed that high expression levels of the vacuolar ATPase (V-ATPase), irrespective of the expression levels of chloride channels, are necessary and sufficient to explain the cell-type dependent formation, stabilization, and biocompatibility of the self-assembled mechanopharmaceutical device within macrophages.

2.4. Introduction

Clofazimine (CFZ) is a weakly basic, poorly soluble, FDA-approved small molecule antibiotic that self-assembles[1,2] into insoluble, biocrystalline structures known as Crystal Like Drug Inclusions (CLDIs) in macrophages of both mice and humans[3-5]. In mice, CFZ precipitates and accumulates in tissue macrophages as a biocrystalline hydrochloride salt ($CFZ\text{-}H^+Cl^-$). Remarkably, in Kupffer cells, splenocytes, alveolar macrophages, and peritoneal macrophages, the amount of intracellular $CFZ\text{-}H^+Cl^-$ typically exceeds that of every other cellular component except water[5]. Known factors that contribute to this massive bioaccumulation and self-assembly

phenomenon include the drug's high oral bioavailability, coupled with large daily doses, prolonged treatment regimens, and long elimination half-life[6].

The observed accumulation, self-assembly, and mechanical properties[7] of CFZ-H^+Cl^- in macrophages inspired our thinking about reverse engineering this weakly basic, small molecule chemical agent as a molecular building block for constructing functional mechanopharmaceutical devices. These devices constitute the mechanical properties of cells and the pharmaceutical agent, and capitalize on the biomechanical synergy between cells and the self-assembled biocrystalline salt, inside cells, *in vivo*[3,5,8]. In macrophages, CFZ-H^+Cl^- forms elastic structures, which bend and relax in response to biomechanical forces[7]. Furthermore, the presence of these mechanopharmaceutical devices is associated with augmented anti-inflammatory activity[9,10]: upon phagocytosis, they lead to changes in cellular function, which include alterations in signal transduction pathways that affect the cell's inflammatory response[10]. Unlike the soluble form of CFZ, which tends to be cytotoxic, phagocytosis of the self-assembled mechanopharmaceutical device does not lead to toxicity[8,11].

Thus, given that macrophages express high levels of proton pumping vacuolar ATPase (V-ATPase) and chloride channels on their lysosomal membranes[12-14], and that weak bases are prone to accumulate inside lysosomes[15], we probed whether the expression levels of these lysosomal membrane proteins in macrophages actively drive the accumulation of CFZ-H^+Cl^- and its self-assembly in these cells. Using a well-established and published lysosomal ion regulation model[16], we studied how proton pumping and chloride transport mechanisms influenced cell-type specific stabilization of CFZ-H^+Cl^- inside lysosomes. In addition to verifying model predictions and further refining our understanding of the computational simulation results, we performed experiments using pharmacological inhibitors of V-ATPase[17] and chloride channels[18]

to probe the biological mechanism underpinning the massive accumulation and self-assembly of the building block.

2.5. Materials and Methods

2.5.1. Solubility measurements.

Freeze-dried CFZ-H^+Cl^{-11} samples were weighed and 25 mg was added to each of five scintillation vials. Mili-Q water (15 mL) was added to each vial to ensure that CFZ-H^+Cl^- crystals were in great excess. An aliquot of 0.1 M NaOH was added to each vial to achieve the initial equilibration pH measurements as follows: sample vials 1-5 initially contained 0, 40, 80, 120, and 200 µL of 0.1 M NaOH solution, respectively. After a 24-hour equilibration period, 10 µL of 0.1 M NaOH was added each day for a period of five days resulting in pH range of 4.5 to 8.9. The solid phase at equilibrium was qualitatively predicted based on the color of the precipitate: orange precipitate for the free base versus dark red precipitate for the salt form of the drug. The sample vials were placed on a magnetic stirrer plate in a 25 °C water bath. Each sample was allowed to equilibrate for at least 24 hours, after which 500 µL of sample was removed and filtered through a Spin-X centrifuge tube filter (0.45 µm cellulose acetate, 2 mL polypropylene tubes, non-sterile, Costar®, Cat # 8163) for 4 min @ 10,000 rpm. The pH of the filtered sample was determined (UltraBasic pH meter, Denver Instrument, Bohemia, NY), after which the sample was subjected to HPLC analysis (see Appendix A.1) (Waters Alliance, Separations Module 2695) to determine the total solubility of the drug at the measured pH. For each sample, solubility measurement was performed in triplicate, and the average was used to construct the total drug solubility-pH profile. The standard curve was generated using CFZ-H^+Cl^- crystals that were dissolved in the mobile phase at known concentrations (1-50 µM).

2.5.2. Thermodynamic equilibrium model of CFZ's solubility.

For weak electrolytes such as weakly basic drugs, the protonation state of the drug (B) is dictated by the relationship between the drug's association constant (K_a) and the acidity of its environment (H_3O^+). This is represented by the following equilibrium expression:

$$B + H_3O^+ \rightleftarrows BH^+ + H_2O \quad (1)$$

Where BH^+ is the protonated form of the drug as a result of the interaction of the free base form of the drug with hydronium ion, and H_2O is the byproduct of the reaction and remains constant. Thus, the equilibrium constant (K) is multiplied by H_2O to obtain K_a. Therefore, equation (1) is re-written using K_a.

$$B + H_3O^+ \rightleftarrows BH^+ \quad (2)$$

The mass law equilibrium equation is written as the following, assuming an ideal solution where the activity of a given species equals the concentration of the species (represented by the brackets):

$$K_a = \frac{[BH^+]}{[B][H_3O^+]} \quad (3)$$

By writing the logarithmic form of equation (3), we have the following relationship, which is the Henderson-Hasselbach equation:

$$pH - pK_a = \log\frac{[B]}{[BH^+]} \quad (4)$$

The equation is re-written as the following to express the concentrations of both the neutral and ionized forms of the drug:

$$[B] = [BH^+] \times 10^{pH-pK_a} \quad (5)$$

$$[BH^+] = [B] \times 10^{pK_a-pH} \quad (6)$$

According to thermodynamic laws of mass action, the total amount of drug is comprised of both the neutral and the ionized forms at any given pH of its environment[19]. Thus, the total solubility (S_T) of the drug is written as:

$$S_T = [B] + [BH^+] \quad (7)$$

However, depending on the pH of the solution, the total drug solubility equation must be slightly modified to account for the distinction of the primary species in the solid versus solution phase[19]. For pH < pH_{max}, the ionized form of the drug is the saturated species that is in equilibrium with the salt from of the drug in the solid phase; therefore, its solubility remains constant while the solubility of the neutral form of the drug varies with respect to pH. Therefore, by substituting equation (5) into equation (7), the total drug solubility for pH < pH_{max} is re-written as:

$$S_T = [BH^+]_S \times (1 + 10^{pH-pK_a}) \quad (8)$$

Where the solid phase is denoted by the subscript "s".

To the contrary, for pH > pH_{max}, the neutral form of the drug is in the solid phase; thus, its solubility remains constant whereas the solubility of the ionized form of the drug varies with respect to pH. Therefore, by substituting equation (6) into equation (7), the total solubility for pH < pH_{max} can be re-written as:

$$S_T = [B]_S \times (1 + 10^{pK_a-pH}) \quad (9)$$

Moreover, at pH = pH_{max}, both the ionized and neutral forms of the drug are the saturating species, where both the salt and free base precipitate forms are in the solid phase. Thus, equation (7) can be re-written as:

$$S_T = [B]_S + [BH^+]_S \quad (10)$$

For our purpose, we substituted our model drug CFZ in the above equations (1-10). Rewriting equation (7) results in the following total CFZ-H^+Cl^- solubility equation:

$$S_T = [CFZ]_S + [CFZH^+] \quad (11)$$

Where the solid phase, which in this case is the free form of CFZ, is denoted by the subscript "s", and the ionized form of the drug, $[CFZH^+]$, is in the solution phase, and similar to equation (6), is dictated by pK_a and pH as follows:

$$[CFZH^+] = [CFZ]_S \times 10^{pK_a - pH} \quad (12)$$

Thus, by substituting equation (12) into equation (11), we obtain the following:

$$S_T = [CFZ]_S \times (1 + 10^{pK_a - pH}) \quad (13)$$

Furthermore, by using different combinations of any two solubility-pH data points from the experimental total solubility-pH measurements, the pK_a and the intrinsic free base solubility values were simultaneously solved using equation (13). Then, by substituting these values into equation (13), the total CFZ-H^+Cl^- solubility was calculated for the given range of pH 4.5 to 8.9, and the experimentally obtained total drug solubility-pH curve was fitted. Furthermore, in order to generate the total solubility-pH dataset for pH below pH_{max}, we used the following equation:

$$S_T = [CFZ] + [CFZH^+]_S \quad (14)$$

Similar to equation (8), equation (14) can be further expressed as:

$$S_T = [CFZH^+]_S \times (1 + 10^{pH - pK_a}) \quad (15)$$

However, we first had to determine $[CFZH^+]_S$. Because we only used one form of the drug (CFZ-H^+Cl^- salt) as the starting material in the experimental measurements of total drug solubility as a function of pH, we used a mathematical proof approach to determine $[CFZH^+]_S$ and thereby pH_{max} (see Appendix A.1) without necessarily having to experimentally generate a total drug solubility-pH curve for pH below pH_{max}.

Moreover, the salt solubility product (K_{sp}) of CFZ-H^+Cl^- is given by the following equation:

$$K_{sp} = [CFZH^+]_S \times [Cl^-] \quad (16)$$

However, because of the 1:1 stoichiometric relationship of $CFZH^+$ and Cl^- in CFZ-H^+Cl^-[7], the K_{sp} of CFZ-H^+Cl^- in an aqueous media can be expressed as following:

$$K_{sp} = ([CFZH^+]_S)^2 \quad (17)$$

2.5.3. Animal experiments.

Mice (4 week old, male C57BL/6J) were purchased from the Jackson Laboratory (Bar Harbor, ME) and acclimatized for 1 week in a specific-pathogen-free animal facility. Clofazimine (CFZ) (C8895; Sigma, St. Louis, MO) was dissolved in sesame oil (Shirakiku, Japan) to achieve a concentration of 3 mg/mL, which was mixed with Powdered Lab Diet 5001 (PMI International, Inc., St. Louis, MO) to produce a 0.03% drug to powdered feed mix, which was orally administered *ad libitum* for up to eight weeks. A corresponding amount of sesame oil was mixed with chow for vehicle treatment (control). Mice were euthanized via CO_2

asphyxiation and exsanguination. Animal care was provided by the University of Michigan's Unit for Laboratory Animal Medicine (ULAM), and the experimental protocol was approved by the Committee on Use and Care of Animals (Protocol PRO00005542). All animal experiments were done according to the protocol guidelines.

2.5.4. Alveolar macrophage isolation.

Following euthanasia, the trachea was surgically exposed and cannulated with a 20G needle, and the lungs were lavaged by instilling 1 mL DPBS (Life Technologies) containing 0.5 mM EDTA (Sigma) six times. Approximately 90% of the instilled bronchoalveolar lavage (BAL) was retrieved. BAL was centrifuged (10 min at 400 x g, 4 °C), the supernatant removed, and the cell pellet was resuspended in RPMI 1640 media (Life Technologies) with 5% FBS (Life Technologies) and Penicillin/Streptomycin (Thermofisher). Cells were plated onto 4 or 8 chamber coverglass (#1.5, Lab-Tek II, Nunc, Rochester, NY) in RPMI for imaging studies. The cells were allowed to attach overnight, washed, and imaged in fresh RPMI.

2.5.5. Peritoneal macrophage isolation.

Following euthanasia, a small incision was made in the lower abdomen. The peritoneal cavity was then flushed with 10 mL of ice cold DPBS containing 5% FBS (Sigma) and collected. The peritoneal lavage was centrifuged for 10 min at 400 x g, 4 °C, and then re-suspended in DMEM media (Life Technologies) with 5% FBS and Penicillin /Streptomycin and counted. The cells were plated into Mat-tek dishes overnight in serum-free growth media, and washed five times with phosphate-buffered saline (PBS).

2.5.6. Macrophage depletion.

Mice were fed CFZ or control diet continuously for a four-week period. Following two weeks of feeding, mice were treated with either liposomes containing either 7 mg/mL of clodronate or PBS (FormuMax Scientific Inc., Sunnyvale, CA) for two weeks. Mice were initially treated with 200 µL of liposomes followed by 100 µL injections twice per week (or a matching volume of PBS) to ensure continual macrophage depletion. Liposomes were injected intraperitoneally, as previously described[20]. After completing four weeks of feeding and two weeks of liposome treatment, mice were sacrificed and tissues were collected.

2.5.7. Biochemical analysis of CFZ in tissues.

The concentration of CFZ in the organs of mice was determined spectrophotometrically. After four weeks of CFZ- or vehicle-diet treatment, mice were euthanized via CO_2 asphyxiation, and organs were collected. Tissue (20-30 mg) was homogenized in 500 µL of radioimmunoprecipitation assay buffer (Sigma) with added protease inhibitors (Halt protease and phosphatase inhibitor cocktail and 0.5 M EDTA; Thermo Pierce, Rockford, IL). Drug was extracted from homogenate (350 µL) with three washes with xylenes (1 mL). The drug was then extracted from the xylene with three 1 mL passes of 9 M sulfuric acid. The concentration of CFZ present in the tissue was determined using a 96-well plate reader (Biotek Synergy 2, Winooski, VT) (wavelength 540 nm). To account for extraction yield, untreated liver and spleen samples were spiked with known amounts of CFZ prior to extraction, and were analyzed in the same plate as the CFZ treated samples. The mass of CFZ per organ was determined using the yield-corrected concentration of CFZ in the mass of tissue analyzed, as determined through use of a standard curve with known concentrations of CFZ, and is reported as mg CFZ/g tissue.

2.5.8. Biochemical analysis of CFZ in plasma.

Blood was collected and centrifuged (7,000 × g for 5 minutes). The resulting supernatant serum was extracted with acetonitrile (90% extraction efficiency) for 10 min at 4 °C with vortexing. After centrifugation (15,000 rpm, 4 °C), the supernatant was injected into a Waters Acquity UPLC H-Class (Waters, Milford, MA) equipped with an Acquity UPLC BEH C18 column (1.7 µm, 2.1 mm [inner diameter] by 100 mm; Waters, Milford, MA). Mobile phase A was 5 mM ammonium acetate, adjusted to pH 9.9 with ammonium hydroxide, and mobile phase B was acetonitrile. The flow rate was 0.35 ml/min, with a linear gradient from 50 to 100% phase B over 1.5 min, followed by holding at 100% for 1.5 min, a return to 50% phase B, and then re-equilibration for 2.5 min. Standards were prepared by spiking untreated plasma samples with known amounts of clofazimine, ranging from 0 to 30 µM. Peak area was determined using Empower 3 Software (Waters, Milford, MA).

2.5.9. Sample preparation for microscopy.

In preparation for cryosectioning, portions of each organ were removed, immediately submerged in OCT (Tissue-Tek catalog no. 4583; Sakura), and frozen (-80 °C). Cryosectioning (5 µm) was carried out using a Leica 3050S Cryostat (Leica Biosystems Inc., Buffalo Grove, IL). Immunohistochemistry of F4/80 (Abcam, 1:500 dilution) was performed using Alexa-Fluor 488 (Abcam, 1:500 dilution).

2.5.10. Deep-etch, freeze-fracture electron microscopy.

At the time of euthanasia, the liver was collected and kept cold (4 °C). The organ was frozen against a copper block, cooled with liquid helium, and stored in liquid nitrogen. The

sample was fractured with Balzers 400 nitrogen cooled vacuum evaporator and freeze-etched for two minutes (-100 °C). A rotary replica was generated with 2 nm platinum and backed with 10 nm carbon film support. It was cleaned with chromo-sulfuric cleaning solution (Fisher Scientific, cat# SC88) for twelve hours and rinsed with DI water. The sample was picked up on formvar coated grids and viewed on a JEOL 1400 electron microscope with an AMT camera (JEOL USA, Inc., Peabody, MA).

2.5.11. Spectral confocal microscopy.

For the preparation of slides, CFZ-H^+Cl^- crystals suspended in PBS (20 µl) were placed on a glass slide and a cover-slip was applied onto the sample prior to imaging. Spectral confocal microscopy was performed on a Leica Inverted SP5X confocal microscope system with two-photon FLIM (Leica Microsystems, Buffalo Grove, IL) using excitation wavelengths (470–670 nm). Image analysis and quantification were performed on Leica LAS AF. Several regions of interest of individual crystals were used to obtain fluorescence data, which were imported into MS-Excel for further analysis. All fluorescence yields were normalized to the maximum fluorescence yield measured across the tested spectral range, and background subtracted using data obtained from a blank slide.

2.5.12. Epifluorescence microscopy of cells incubated with CFZ and Lysotracker® Blue.

Macrophage-derived RAW264.7 cells (ATCC, Manassas, VA, ATCC Number: TIB-71™) at a high seeding density of 100,000 cells/well, were grown in 8-chamber multiwell plates (Lab-Tek® II, Nunc, Rochester, NY) in Dulbecco's Modified Eagles Medium (DMEM) + 10% Fetal Bovine Serum (FBS) + 1% Penicillin/Streptomycin (P/S) (500 µl/well growth media); cells

were pre-incubated with CFZ (20 µM) in DMSO for 24-72 hours. For lysosomal confirmation, RAW264.7 cells were seeded at 30,000 cells/well in an 8-chamber multiwell plate (500 µl/well growth media). Twenty-four hours later, the growth media was replaced with media containing varying concentrations (0, 1, 10, 20 µM) of Lysotracker® Blue DND-22 (Thermo Fisher Scientific, Waltham, MA, Catalog No. L7525, excitation/emission maxima ~ 373/422 nm) and CFZ (10 µM). Visualization of all samples (cells or crystals) was done on a Nikon Eclipse T*i* (Nikon Instruments, Melville, NY). Fluorescence filters (excitation/emission) were optimized for 4,6-diamidino-2-phenylindole dihydrochloride (DAPI) (350/405 nm, exposure - 550 ms, *violet*), fluorescein isothiocyanate (FITC) (490/510 nm, exposure - 100–500 ms, *green*), Texas Red (590/610 nm, exposure - < 500 ms, *red*), and Cy5 (640/670 nm, exposure - 500 ms, *far-red*). The Pearson's Co-localization Coefficient (PCC) was computed for each individual cell as ROIs using the scatterplot distribution within the Nikon Elements AR software. Brightfield color photographs were acquired using a Nikon DS-Fi2 camera, whereas fluorescence photographs were acquired using a Photometrics CoolSNAP^{TM} *MYO* (Photometrics, Tucson, AZ) camera.

2.5.13. Quantitative cytometric analysis.

Following macrophage staining, the population of macrophages was determined by taking the ratio of the total F4/80 signal to the total nuclear signal across an image. Because of the unique Cy5-specific fluorescence property of CLDIs[11], the prevalence of CLDIs was determined by taking the ratio of the total Cy5 signal to the total nuclear signal across an image. 5 images per mouse per organ were analyzed.

2.5.14. Drug stability in a lysosomal microenvironment.

CLDIs were isolated from spleen and liver of 8-week CFZ treated mice based on previously published protocols[10,21]. Free base CFZ crystals were pure CFZ crystals (Sigma-Aldrich, C8895). A speck (<< 1mg) of isolated CLDIs, CFZ-H^+Cl^- crystals, and free base CFZ crystals were placed in 2 mL of each of the stability testing medias: 1x PBS (pH 7.4), lysosomal buffer without sodium chloride (LB-, pH 4.5), and lysosomal buffer with sodium chloride (LB+, pH 4.5). Lysosomal buffers were prepared according to a previously published protocol[22]. Samples were stirred in media for 5-7 days; after which the stability of crystals from each sample was monitored using brightfield and fluorescence microscopy using a Nikon Eclipse Ti inverted microscope (Nikon Instruments, Melville, NY). Look-up-tables (LUTs) and exposure times were maintained the same throughout the samples.

2.5.15. Multi-parameter microscopy.

Multi-parameter polarization, brightfield, and fluorescence microscopy was conducted using a Nikon Eclipse Ti inverted microscope (Nikon Instruments, Melville, NY). Polarization microscopy was performed using the LC-PolScope[23], with the illuminating light narrowed to 623 nm by an interference filter (623 ± 23 nm, Semrock Optics, Rochester, NY). Polarization images were captured using an Abrio imaging system (Cambridge Research & Instrumentation, Inc, Woburn, MA). Brightfield images were captured using the Nikon DS-3 camera (Nikon Instruments) and fluorescence images were taken with the Photometrics CoolSnap MYO camera system (Photometrics, Tuscon, AZ) under the control of Nikon NIS-Elements AR software (Nikon Instruments). Illumination for fluorescence imaging was provided by the X-Cite 120Q Widefield Fluorescence Microscope Excitation Light Source (Excelitas Technology, Waltham, MA). Images were acquired and analyzed as previously described[24].

2.5.16. Raman sample preparation and measurements.

Isolated mouse alveolar macrophages were transferred onto pre-sterilized silicon chips (16008; Ted Pella, Inc., Redding, CA) and incubated for 1h (@ 37 ^{o}C and 5% CO_2) to allow adherence to chip. The cell-containing chips were washed by brief submersion into isotonic NaCl (0.9%) solution followed by DI water, then allowed to air-dry. Raman measurements were acquired with the WiTec alpha300R confocal Raman microscope (WITec, Ulm, Germany) equipped with two excitation lasers: a 532 nm solid-state sapphire and a 785 nm wavelength-stabilized diode (0-55 mW and 0-88 mW tunable intensity ranges, respectively). A 100X air objective (Zeiss Epiplan-NEOFLUAR, NA (numerical aperture) = 0.9) coupled to a CCD detector via a multi-mode fiber of 100 μm diameter serving as the confocal pinhole, produced 0.72 μm and 1.06 μm illumination spots (for 532 nm and 785 nm lasers respectively). To minimize fluorescence background from pure CFZ and CFZ-H^+Cl^- reference crystals, samples were excited with 785 nm. The 532 nm laser was utilized for excitation of biological samples due to its elicitation of a stronger Raman signal from the microscopic inclusions/CLDIs of interest. Point spectra were acquired ($n \geq 40$ cells/group) by focusing a laser spot on cytoplasmic inclusions, CLDIs, or pure reference crystals: at each point, the laser was tuned to optimum intensity, and acquired point spectra over an integration time of 25 seconds. Individual raw spectra were baseline-subtracted and normalized using a MATLAB® processing algorithm developed in-house. For single-cell Raman imaging, the 532 nm excitation laser was raster-scanned across a 50×50 micron area with a step-size of 0.5 microns, yielding spectral datasets consisting of 10,000 spectra per cell. Exploiting the dramatic spectral differences arising from fluorescence of different CFZ forms, the un-processed Raman spectra were linearly deconvoluted via WiTec ProjectFOUR software's basis component analysis using representative

un-processed reference spectra obtained from untreated cells, pure free base CFZ crystals, pure CFZ-H^+Cl^- crystals, and the silicon substrate. Dataset acquisition, processing, and image display parameters were performed equivalently for each cell specimen.

2.5.17. CLDI injection and stabilization assay.

To determine how macrophages stabilize CLDIs, mice were treated with either liposomal PBS or liposomal clodronate, as previously described[25]. 48 hours after liposome administration, mice were injected I.P. with 200 μg of CLDIs suspended in 1 mL of PBS (n = 3 mice per group per time point). At time points ranging from 0 to 48 hours, the mice were euthanized, the peritoneal lavage was collected and pelleted, and the drug content within the pellet was analyzed using the previously described spectrophotometric analysis method. Using a simple exponential regression with recovered drug content, the half-life was estimated.

2.5.18. CLDI loading within individual macrophages.

Using the total recovered mass of CLDIs within the liver and spleen, the CLDI loading within individual xenobiotic-sequestering macrophages was estimated using literature reported values for macrophage numbers[26] within the liver and spleen, corrected for the percentage of cells which contained a CLDI. For the clodronate depleted organs, the reduction was accounted for with the quantified reduction in total F4/80 signal.

2.5.19. Cell culture and pharmacological treatment.

For pharmacological inhibition experiments, macrophage-derived RAW264.7 cells (ATCC, Manassas, VA, ATCC Number: TIB-71™), at a very high seeding density of 50,000

cells/well grown in a 96 well tissue culture plate in 280 µl/well of DMEM + 10% FBS + 1% P/S (growth media), were pre-incubated (4h) with varying concentrations of Bafilomycin A1 (BafA1; Sigma-Aldrich, St. Louis, MO, Cat. No. B1793) (0-10 nM) and NPPB (Sigma-Aldrich, St. Louis, MO, Cat. No. N4779) (0-200 µM) after which CFZ (dissolved in DMSO) was added to achieve a final concentration range of 0-10 µM. The effect of the treatment on cell viability was assessed by an XTT assay (Roche, UK).

2.5.20. Drug uptake measurements.

Measurement of CFZ uptake by RAW264.7 cells was performed using a modified absorbance spectroscopy method using 9 M H_2SO_4 (pH << 0.1) to digest the entire cell population and extract CFZ from the cells. At two time points (2 and 4h) after CFZ exposure, growth media was aspirated from the culture dish and the cells were washed twice with PBS before adding 9 M H_2SO_4 (100 µl/well). The plate was incubated at room temperature for 30 min before spectrophotometric quantification of CFZ using a Synergy 2 plate reader (BioTek, Winooski, VT) at 540 nm (Abs_{540}) and 750 nm (Abs_{750}) (for background). Standards were prepared on the same plate by adding 100 µl/well pre-determined standards of CFZ. Total CFZ uptake is reported as total intracellular drug (in picomoles) as measured and calculated using the standard curve. Assuming that the doubling time of 50,000 cells/well is ~ 11h[27], and that no compromise of cell viability occurs because of the optimum dose used for both CFZ and the pharmacological inhibitors, the total number of cells/well at the time of cellular drug uptake measurement is ~ 68,000.

2.5.21. Experimental lysosomal pH measurements.

Lysosomal pH was measured fluorometrically in peritoneal macrophages and macrophage-derived RAW264.7 cells, using methods described previously[28]. In brief, macrophages were incubated for 40h with CFZ crystals. 20h prior to measuring pH, cells were incubated for 15-18h with 150 µg/ml Oregon Green-labeled dextran-10kD (OGDx; Thermo-Fisher Scientific), and transferred to unlabeled culture medium for 3-5h to allow OGDx to traffic fully to lysosomes. Following transfer to Ringer's buffer, cells on Mat-tek dishes were observed in a Nikon TE300 microscope equipped for multichannel fluorescence microscopy with a 60X objective lens (N.A. 1.4). Phase contrast and three fluorescence images (excitation/emission: 440 nm/535 nm; 485 nm/535 nm; and 580 nm/630 nm) were collected from each field. The 580nm/630nm image was used to quantify clofazimine fluorescence. The ratio of the 485nm/525nm to 440nm/525nm images were used to measure lysosomal pH. Calibration of fluorescence ratios was obtained from cells incubated in ionophores and buffers as described in Davis and Swanson[28]. Average lysosomal pH was determined for individual cells.

2.5.22. Modeling lysosomal CFZ-H^+Cl^- accumulation.

A Lysosomal ion regulation model which incorporates lysosomal membrane proteins, such as V-ATPase, CLC7, and membrane proton permeability was utilized[16], and further elaborated and modified (see Appendix A.1) to explore the relationship between lysosomal ion homeostasis and lysosomal CFZ-H^+Cl^- accumulation and stabilization. In order to incorporate the lysosomal accumulation of CFZ-H^+Cl^- into the model as a function of lysosomal proton and chloride ions, the rate of overall drug accumulation obtained from experimental findings[4,29] was used to define the rates of both lysosomal proton ($H_{sequestered}$) and chloride ($Cl_{sequestered}$) sequestrations by CFZ, in units of molecules per second. We assumed these rates to be equal due

to the proposed equal contribution of both proton and chloride ions in the intracellular formation and accumulation of CFZ-H^+Cl^- salt precipitates:

$$CFZH^+Cl^- = H_{sequestered} = Cl_{sequestered} \quad (18)$$

2.5.23. Model parameterization.

The model incorporated 23 parameters: four were adjustable and the remaining 19 were fixed (see Appendix Table A.1). Fixed parameters were given values obtained from the literature[16,30-34], and are associated with physiological lysosomal ion homeostasis. Therefore, these parametric values are interchangeably referred hereon as "baseline input values" or "physiological baseline input values". The adjustable parameters are those values that were varied from their respective baseline input values in order to investigate their individual as well as combined effects on the physiological lysosomal pH, Cl^-, and membrane potential readout values, as discussed in the following subsections. These parameters include the number of active V-ATPase and CLC7 molecules per lysosome, as well as the cytoplasmic chloride concentration. In addition, the rates of proton and chloride sequestrations by CFZ are considered adjustable parameters as they are foreign to the lysosome.

2.5.24. Simulating lysosomal CFZ-H^+Cl^- accumulation.

The previously mentioned rates of proton and chloride sequestrations by CFZ were adjusted to either 0.01 or 0.1 picomoles/cell/day[4,29]. However, in our model simulations, we converted the units of these rates to picomoles/lysosome/day assuming there are ~ 100 lysosomes in a cell. From here onwards, we interchangeably refer to these rates, 0.01 and 0.1

picomoles/cell/day, as 1-fold (1X) and 10-fold (10X) rates of lysosomal CFZ-H^+Cl^- accumulation, respectively.

2.5.25. Simulating changes in lysosomal membrane proteins and cytoplasmic chloride amounts.

In order to study the roles of V-ATPase, CLC7, and cytoplasmic chloride concentration on lysosomal accumulation of CFZ-H^+Cl^-, we varied the total numbers of active V-ATPase and CLC7 molecules per lysosome, and the cytoplasmic chloride concentration, while fixing the values of other lysosomal parameters at their baseline physiological input values in the presence as well as absence of lysosomal CFZ-H^+Cl^- accumulation. More specifically, to simulate the simultaneous inhibition of V-ATPase and CLC7, the total number of CLC7 molecules per lysosome was varied from 0 to 5,000 (resulting in 7-16 data-generating points) while, one parametric simulation at a time, the total number of V-ATPase molecules per lysosome was manually varied from 0 to 300 (resulting in 4-7 data-generating points). Moreover, to simulate the simultaneous inhibition of V-ATPase and cytoplasmic chloride, the cytoplasmic chloride concentration was varied from 0 to 10 mM (resulting in 16 data-generating points) while, one parametric simulation at a time, the total number of V-ATPase molecules per lysosome was manually varied from 0 to 300 (resulting in 4-7 data-generating points).

Using the aforementioned ranges of the adjustable lysosomal parameters, the corresponding lysosomal parameter inhibition range of 0 to 100% was calculated; where 0% represents no change from respective physiological baseline input value, and 100% represents the input value set to ~ zero. The inhibition range was calculated as follows by comparing the

corresponding input value (Adjusted Input Value) from the aforementioned given range with its respective physiological input value (Baseline Input Value):

$$\% \text{ Inhibition} = \frac{\text{Baseline Input Value} - \text{Adjusted Input Value}}{\text{Baseline Input Value}} \times 100\% \quad (19)$$

2.5.26. Calculating the effect of lysosomal CFZ-H^+Cl^- accumulation on lysosomal ion homeostasis.

Final lysosomal pH, chloride, and membrane potential were chosen as readout values because they are direct indicators of lysosomal ion homeostasis and physiology. Thus, parametric simulations of these variables were performed as a function of the aforementioned ranges of V-ATPase, CLC7, and cytoplasmic chloride in the absence and presence of lysosomal CFZ-H^+Cl^- accumulation at the rate of either 1X or 10X. Then, the readout values in the absence of lysosomal CFZ-H^+Cl^- accumulation were subtracted from those in the presence of lysosomal CFZ-H^+Cl^- accumulation in order to determine the effect of lysosomal CFZ-H^+Cl^- accumulation on lysosomal ion homeostasis.

2.5.27. Calculating the effects of V-ATPase, chloride channels, and cytoplasmic chloride on the physiological lysosomal accumulation of CFZ-H^+Cl^-.

Time-plot simulations, where all of the lysosomal parameters were set to their respective baseline values in the absence of lysosomal CFZ-H^+Cl^- accumulation, were performed to obtain physiological final lysosomal pH, chloride accumulation, and membrane potential values, which from hereon we refer to as "physiological baseline readout values". Moreover, model parametric simulations of final lysosomal pH, Cl^-, and membrane potential as a function of simultaneous V-

ATPase-CLC7 and V-ATPase-cytoplasmic chloride inhibitions were performed in the presence of lysosomal CFZ-H^+Cl^- accumulation at the rates of 1X and 10X. These were then subtracted from the physiological baseline readout values in order to calculate the effects of the simultaneous lysosomal parameter inhibitions on the dose-dependent lysosomal CFZ-H^+Cl^- accumulation.

2.5.28. Confirmation of steady-state and mass balance.

For all of the aforementioned simulations, the final readout values were confirmed that they were steady state values by performing the simulations for > 24h. We confirmed that mass balance was maintained in all of the simulations in the presence and absence of lysosomal CFZ-H^+Cl^- accumulation as long as a physiological pH gradient of up to 4.6 pH units was maintained across the lysosomal membrane.

2.6. Results

2.6.1. The weakly basic building block has pH-dependent solubility properties.

CFZ is a weak base with two amines, which can be protonated depending on the pH of the immediate environment (Fig. 2.1a). To study its pH-dependent solubility behavior, we used an established approach[19] (described in Appendix A.1), which allowed an accurate measurement of the total solubility of CFZ-H^+Cl^- as a function of pH. From the experimental measurements, we calculated the solubility properties of CFZ, in an aqueous media at 25 ºC, which include its apparent p$K_{a,2}$ (p$K_{a'}$ = 6.08 ± 2.43x10^{-3}; 95% Confidence Interval = 6.07, 6.09) and intrinsic free base solubility (S_0 = 0.48 ± 4.05x10^{-6} µM; 95% CI = 0.48, 0.48) (Fig. 2.1b). Moreover, to determine the effect of lysosomal Cl^- (Fig. 2.1c) on the stability of the free base versus salt form

of the drug, we performed drug stability experiments (Fig. 2.1d) in the presence and absence of lysosomal buffer (pH 4.5, Cl^- concentration =0-100 mM). We monitored drug stability by relying on the unique fluorescence profile of the different forms of CFZ: free base CFZ exhibits green and red fluorescence; peak excitation: 540–560 nm, peak emission: 560–600 nm, whereas CFZ-H^+Cl^- exhibits red and far red fluorescence; peak excitation: 560–600 nm, peak emission: 650–690 nm[11]. Indeed, the fluorescence of CLDIs resembles the fluorescence of the synthesized CFZ-H^+Cl^- crystals (peak excitation: 560–600 nm, peak emission: 650–690 nm) (see Appendix Fig. A.1).

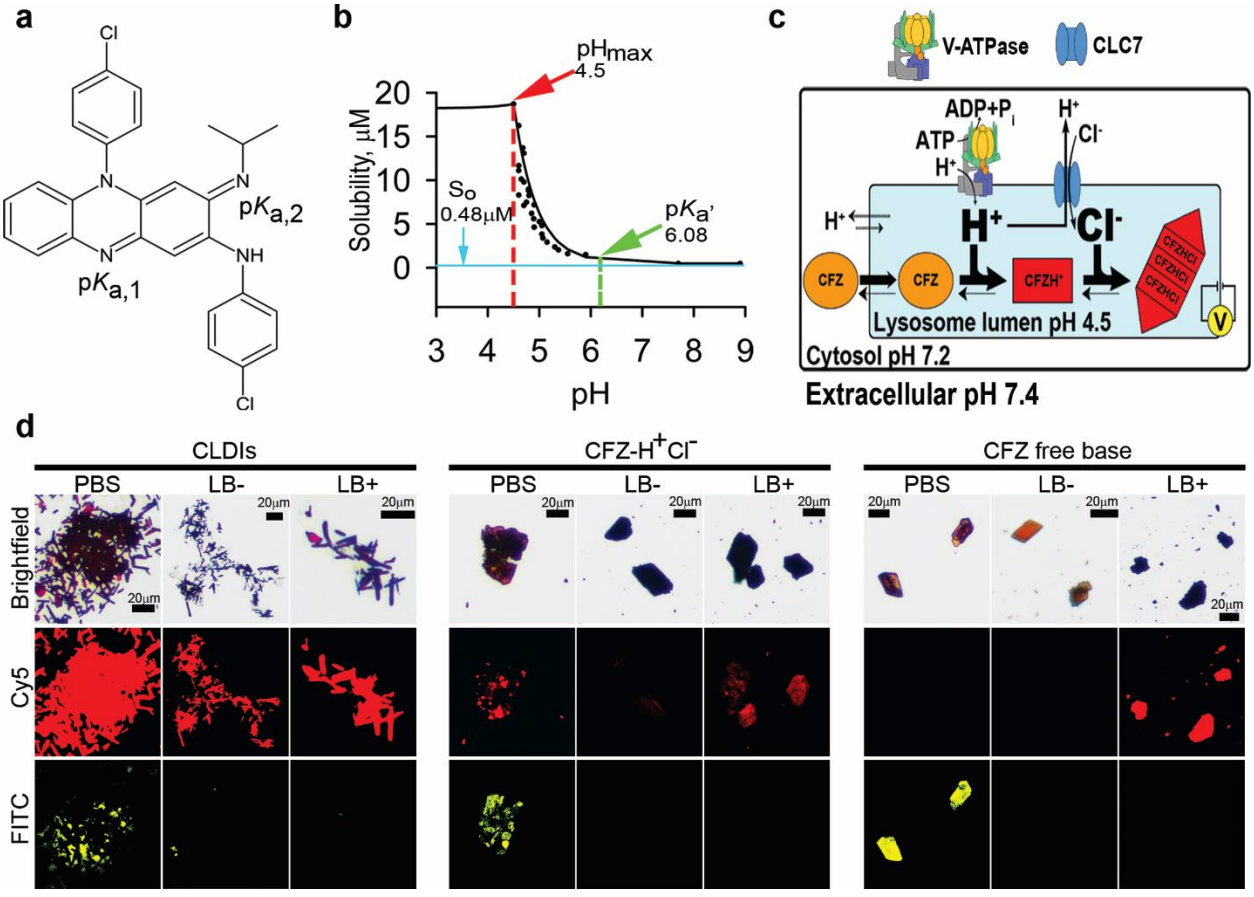

Figure 2.1 Chemical characterization of CFZ.
a, Chemical structure of clofazimine (CFZ) with its two protonation sites and corresponding predicted (chemi-informatic) pK_a values (p$K_{a,1}$ = 2.31 and p$K_{a,2}$ = 9.29). **b**, CFZ-H^+Cl^- solubility-pH study revealed the solution pH dependence of the stabilization of the free base versus salt form of the drug with respect to its solubility parameters; which include the intrinsic free base

solubility (S_o), apparent p$K_{a,2}$ (pK_a'), and pH_{max}. **c**, Illustration showing the cellular and subcellular accumulation of free base CFZ, its subsequent protonation ($CFZH^+$), and ion-ion interaction of $CFZH^+$ and cellular Cl^- to form CFZ-H^+Cl^-. This phenomenon depends on the drug's intrinsic solubility properties as well as the cellular pH and Cl^- levels, which are primarily regulated by membrane proteins: proton-pump known as V-ATPase and Cl^-/H^+ antiporter known as CLC7. **d,** Stability of CLDIs, CFZ-H^+Cl^-, and free base CFZ in PBS (pH 7.4), lysosomal buffer without sodium chloride (LB-, pH 4.5), and lysosomal buffer with 100 mM sodium chloride (LB+, pH 4.5) was monitored via brightfield and fluorescence microscopy.

A low pH environment in the absence of Cl^- (LB-) induced the destabilization of both CFZ-H^+Cl^- and free base CFZ, without affecting the stability of CLDIs. To the contrary, a low pH environment in the presence of a physiological lysosomal Cl^- (LB+) induced the stabilization of CFZ-H^+Cl^- and CLDIs, whereas the free base CFZ precipitated out as CFZ-H^+Cl^- (Fig. 2.1d). Thus, these findings reveal that the precipitation of CFZ as a hydrochloride salt was highly sensitive to small, but physiologically relevant variations in pH and chloride concentrations (pH_{max} = 4.5 ± 7.11x10^{-15}, 95% CI = 4.5, 4.5; and K_{sp} = 332.3 ± 3.71 µM^2, 95% CI = 323.1, 341.5) (Fig. 2.1b, d); where the pH_{max} reveals the pH below which CFZ-H^+Cl^- salt formation occurs, and the K_{sp} elucidates the Cl^- concentration, which is > $(K_{sp})^{1/2}$ µM, that would further stabilize the salt form of the drug through a common-ion effect[35]. Thus, at the pharmacologically-relevant CFZ concentrations that have previously been measured in serum (1 to 20 µM), local variations in pH (~ 7.4 extracellular; ~ 7.2 cytosolic and ~ 4.5 lysosomal) and chloride concentrations (~ 80 mM extracellular; ~ 10-20 mM in cytosol; and ~ 50-200 mM in lysosomes) can lead to a greater propensity of CFZ to precipitate as a hydrochloride salt in the lysosomal microenvironment (Fig. 2.1c, d).

2.6.2. The intracellular organization of the self-assembled mechanopharmaceutical device

Prolonged administration of CFZ results in its accumulation in both human and animals as microscopic, insoluble, and membrane-bound aggregates, known as Crystal Like Drug

Inclusions (CLDIs), which are primarily found within tissue macrophages[3-5]. CLDIs are primarily comprised of a protonated, hydrochloride salt of CFZ (Fig 2.2a)[7], which forms faceted structures possessing three orthogonal cleavage and multiple fracture planes with lamellar spacing of 6 nm to 14 nm[21] (Fig. 2.2b). These orthogonal cleavage and fracture planes correspond to the orthogonal crystallographic planes of the CFZ-H^+Cl^- unit cell (Fig. 2.2c). When examined under polarized light (623 nm wavelength), the orthorhombic crystal structure of the deep red CLDIs[11,29,36] exhibits dichroism (Fig. 2.2d)[24]. Due to the biological origin of the CLDIs[7], the interaction between the cell and crystal often leads to significant variations in its organization, impacting the manner in which it interacts with polarized light (Fig. 2.2d). Furthermore, reference spectra of pure CFZ and CFZ-H^+Cl^- identified characteristic Raman peaks for clear distinction between the two forms (Fig. 2.2e). Spectra obtained from cytoplasmic regions of untreated mouse alveolar macrophages were typical of biological specimens with no apparent contributions from drug. However, spectra obtained from cytoplasmic regions of 4- and 8-week CFZ-fed mouse alveolar macrophages revealed the presence of CFZ-H^+Cl^-, which dominated any Raman signal associated with biological specimens, and exhibited unique peak intensities and peak widths, which attribute to the geometric organization of the supramolecular structures: peaks generally become narrower and more intense with higher degree of order in samples, which suggests that by 8 weeks, the macrophages have organized the accumulated drug into supramolecular crystalline packages of CFZ-H^+Cl^- salt. Moreover, Raman imaging of single-cells revealed cytoplasmic accumulation of both forms of the drug after just 1 week and continuing through 4 weeks; at 8 weeks CLDI formation was apparent and clearly distinguishable from free base CFZ, as evidenced by non-overlapping Raman signals in the biocrystal regions of Raman image (Fig. 2.2f).

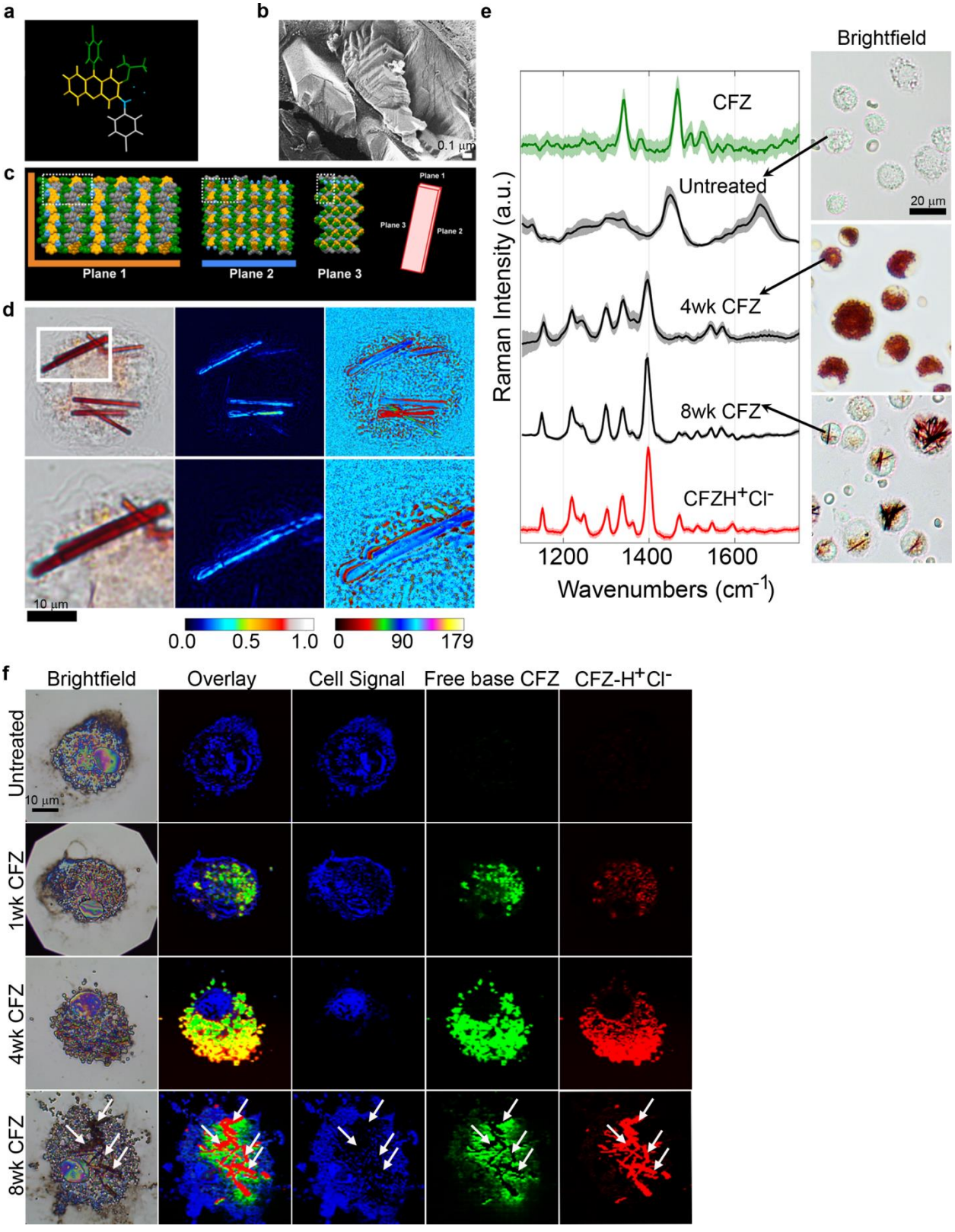

Figure 2.2. Intracellular self-assembled crystal organization of CFZ-H^+Cl^-.

a, CFZ-H^+Cl^- chemical structure with color coding corresponding to the regions of the structure in the crystal arrangement. **b**, Freeze-fracture electron micrograph of CLDIs within a Kupffer cell, showing that the CLDIs are sequestered inside the cell as multiple layered planes with lamellar spacing of 6 nm to 14 nm, by a double membrane of biological origin (~ 20 nm in thickness)[21]. **c**, Crystal packing of CFZ-H^+Cl^- showing the three crystallographic planes of the crystal: a hydrophobic face in orange (plane 1), a hydrophilic face in blue (plane 2), and an amphipathic face (plane 3)[8]. **d**, CLDIs (100-1.5X magnification) zoomed in (zoom factor of 2) in alveolar macrophages show high dichroism and an axis of highest transmittance, with a different profile (represented by the different signal intensity associated with the color bar) observed specifically around the edges of the crystal. **e,** Raman spectra of free base CFZ, CFZ-H^+Cl^-, untreated and treated alveolar macrophages (4 and 8wks CFZ-fed mice) show distinct Raman peaks distinguishing between the different forms of the drug (red in the brightfield images): free base CFZ (1341 and 1465 cm^{-1}), CFZ-H^+Cl^- (1399 cm^{-1}). **f,** Reflected brightfield and Raman images of alveolar macrophages from CFZ-fed mice prepared on silicon chip substrates; basis spectral fitting was used to show the temporal accumulation and cytoplasmic packaging of CFZ into highly ordered CLDIs.

2.6.3. Macrophages are necessary for the self-assembly of the mechanopharmaceutical device

To investigate whether macrophages play an active role in stabilizing CLDIs *in vivo*, macrophages were depleted by injecting mice (n = 3-4 per treatment group) intraperitoneally with clodronate liposomes. This treatment depletes phagocytic cells without affecting non-phagocytic cells[20]. Moreover, the aforementioned CFZ's unique fluorescence characteristics were used to monitor the effect of macrophage depletion on the accumulation of CFZ-H^+Cl^- crystal. Following liposome therapy, the relative number of F4/80 positive macrophages within the liver and spleen of each treatment group was quantified using the total ratio of F4/80 to nuclear signal, revealing a significant reduction in the total macrophage population in the clodronate-CFZ fed group when compared to the PBS-CFZ treated group ($p < 0.05$, ANOVA, Tukey's HSD) (Fig. 2.3a). Consequently, using the ratio between the intrinsic far-red fluorescence of CFZ-H^+Cl^-[37] and total nuclear signal, there was a significant reduction in the accumulation and stabilization of CFZ-H^+Cl^- within the liver and spleen ($p < 0.05$, ANOVA,

Tukey's HSD) compared to the PBS-CFZ treated group (Fig. 2.3b). More specifically, within the PBS-CFZ treated mice, the livers accumulated an average of 0.68 ± 0.27 mg CFZ/g tissue, while the clodronate-CFZ livers accumulated an average of 0.23 ± 0.09 mg CFZ/g tissue ($p < 0.05$, two-tailed Student's t-test); a reduction of nearly 66%. Similarly, the spleens of PBS-CFZ treated mice accumulated an average of 2.31 ± 0.40 mg CFZ/g tissue, compared to 0.70 ± 0.12 mg CFZ/g tissue in the clodronate-CFZ groups ($p < 0.01$, two-tailed Student's t-test); a reduction of 70%.

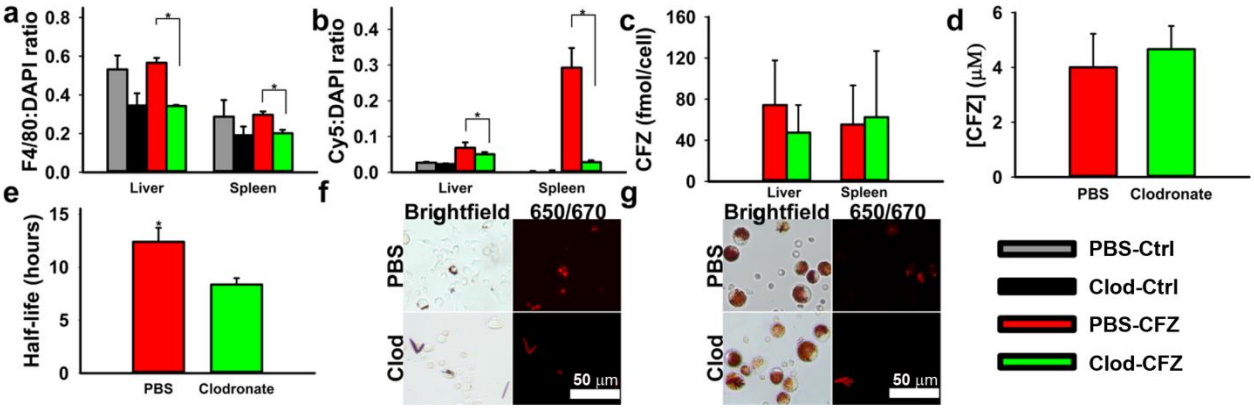

Figure 2.3 The role of macrophages on the intracellular accumulation of CFZ biocrystals *in vivo*.
a, Clodronate depletion significantly reduces both hepatic and splenic macrophages in Clodronate-CFZ treatment group. **b**, Depletion of macrophages results in concomitant reduction in CLDI loading within the livers and spleens of treated animals. **c**, Clodronate depletion does not significantly reduce the estimated clofazimine loading per macrophage in the livers and spleen. **d,** Clodronate depletion does not significantly impact the serum concentrations of clofazimine following four weeks of treatment. **e,** Depletion of peritoneal macrophages significantly increases the rate of degradation of CLDIs injected intraperitoneally, leading to a significantly faster half-life. **f,** Peritoneal exudate of PBS- and clodronate-liposome treated mice 48 hours following CLDI injection showing brightfield and Cy5 fluorescence (red fluorescence and red in brightfield images correspond to CLDIs) (* = $p < 0.05$, ANOVA or ANOVA, Tukey's HSD when applicable). **g,** Alveolar lavage from PBS- and clodronate-liposome treated mice. Clodronate treatment did not impact CLDI accumulation (red fluorescence and red in brightfield images correspond to CLDIs) within alveolar macrophages.

The individual drug loading within the macrophages of the liver and spleen was estimated based off of literature-reported values for macrophage populations in those two organs[26] and the total recovered drug within each organ, and there was no difference in total drug loading within either population of macrophage as a result of clodronate therapy (Fig. 2.3c). Furthermore, there was no significant difference in mean plasma concentrations of CFZ at the end of therapy (Fig. 2.3d). Taken together, this provides evidence that, while clodronate therapy was reducing the macrophage population and subsequent bioaccumulation within the liver and spleen, it was not impacting the general bioavailability and absorption of CFZ in the body. To determine how macrophages stabilized the self-assembled mechanopharmaceutical devices, isolated CLDIs were injected I.P. into clodronate and PBS liposome treated mice and collected at time points from 0 to 48 hours (n = 3 mice per group per time point). Without macrophages present in the peritoneal cavity to internalize the CLDI, there was a significant reduction in the estimated half-life of the biocrystal ($p < 0.05$, ANOVA) (Fig. 2.3e). This was confirmed via microscopic analysis of the peritoneal exudate 48 hours post-injection, with CLDIs becoming internalized by the macrophage and retaining their far-red fluorescence in the PBS-treatment group, while the clodronate-treated group showed reduced CLDI content within the exudate (Fig. 2.3f).

Additionally, in order to confirm that clodronate did not impact drug accumulation within other macrophage populations, alveolar macrophages were collected and analyzed. Within the alveolar macrophage population, there was no significant difference in total cell number collected between the PBS and clodronate-treated groups ($p = 0.48$, two-tailed Student's t-test), as well as in the ability of the cells to accumulate CFZ in the form of a CLDI; where each alveolar macrophage population contained approximately 20% CLDI-positive cells ($p = 0.36$,

two-tailed Student's t-test) (Fig. 2.3g). Thus, the specific effect of clodronate liposomes on liver and spleen CLDIs and CFZ content, as well as the increased rate of CLDI destabilization and solubilization in the absence of peritoneal macrophages provide evidence that these cells are directly responsible for the *in vivo* accumulation, self-assembly, and stabilization of CFZ-H^+Cl^-.

2.6.4. The intracellular accumulation, protonation, and self-assembly of the building block in cytoplasmic vesicles does not interfere with lysosomal pH.

Taking advantage of the aforementioned CFZ's unique fluorescence properties, we studied the accumulation of the un-protonated free base and protonated hydrochloride salt form of the drug in macrophages. Incubation of macrophages with CFZ *in vitro* revealed vesicular staining pattern consistent with free base CFZ (peak excitation: 540–560 nm, peak emission: 560–600 nm) as well as CFZ-H^+Cl^- (peak excitation: 560–600 nm, peak emission: 650–690 nm)[11]. Both fluorescent forms were visible in CFZ-treated cells and absent in untreated, control cells (Fig. 2.4a and see Appendix Fig. A.2). Based on the observed little overlap of their orthogonal fluorescence signals, CFZ-H^+Cl^- did not co-localize with free base CFZ (Pearson's Colocalization Coefficient - PCC between green and far-red fluorescence = 0.30 ± 0.29) (see Appendix Fig. A.3). In addition, when cells were co-incubated with both CFZ and Lysotracker Blue (LB), LB fluorescence signal (excitation: 373 nm, emission: 422 nm) was inhibited in the cytoplasm and displaced[38] to the nucleus (based on the observed nuclear staining), whereas the punctate green and far-red fluorescence of CFZ were clearly visible in the cytoplasm of these cells (Fig. 2.4c, see Appendix Figs. A.2 and A.3). As a control experiment, we measured the lysosomal pH of macrophages following phagocytosis of CLDIs in macrophage-derived RAW264.7 cells as well as in peritoneal macrophages of 8-week CFZ-fed mice (Fig. 2.4d). In

both cases, the lysosomal pH was not physiologically affected by the presence of the CFZ, as reflected by < 0.1 pH unit difference between the drug-free and drug-containing peritoneal macrophages and RAW264.7 cells. Thus, CFZ uptake in macrophage lysosomes does not perturb physiological lysosomal pH homeostasis, which is required for various lysosomal functions such as lysosomal trafficking and degradation of intrinsic and extrinsic materials within the lysosome by various pH-dependent hydrolytic lysosomal enzymes, which are essential for overall cellular homeostasis and viability[39]. Moreover, because the fluorescence signals of Lysotracker® probes are pH-independent[40], we interpret this to mean that intralysosomal CFZ accumulation interferes with Lysotracker probe accumulation through a mechanism that is independent of changes in lysosomal pH.

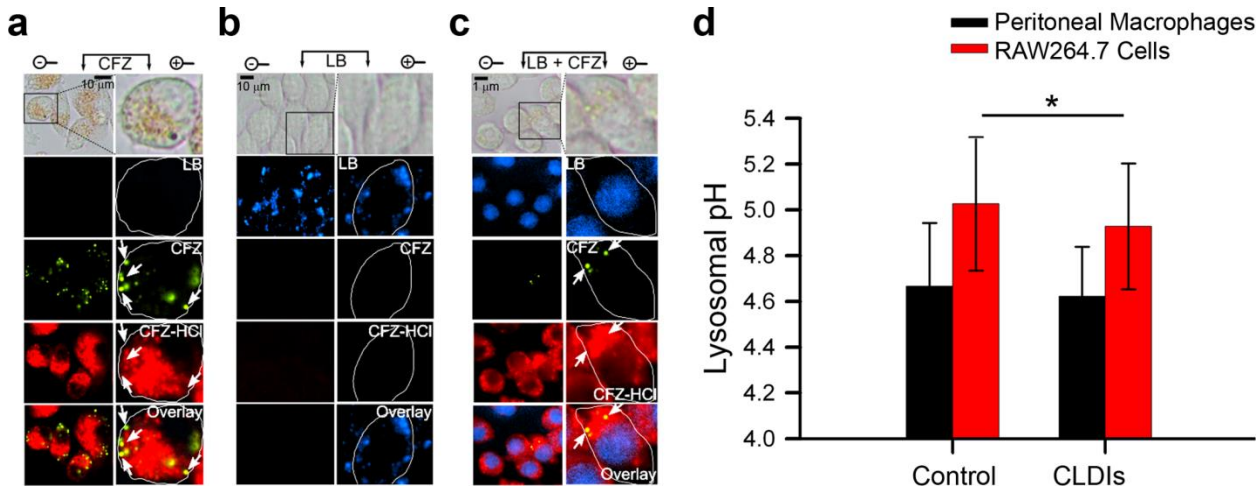

Figure 2.4. Evidence of lysosomal accumulation of CFZ via fluorescence staining patterns in RAW264.7 cells.
a, Epifluorescence microscopy of RAW264.7 cells (40X magnification) zoomed in (zoom factor of 2.5) when incubated with (**a**) CFZ (10 μM), (**b**) Lysotracker Blue (LB, 1 μM), and (**c**) CFZ (10 μM) and LB (1 μM) together at *t* = 24 hours. Green fluorescence spots indicative of CFZ are also further annotated using white arrows for cross-referencing with other images. Note the lack of any far-red fluorescence positive signal in the direction pointed by the arrows. Vesicular staining pattern of LB visible as blue punctate spots in (**b)** are absent in (**c**) while nuclear staining becomes visible due to LB displacement from the lysosome to the nucleus because of CFZ accumulation in the lysosome. Cell boundaries are shown in white in the digitally zoomed

panels. **d**, Lysosomal pH measurements of RAW26.7 cells in the presence and absence of CLDIs, and peritoneal macrophages of control versus 8-week CFZ fed mice. Data are mean ± S.D. of 29-181 measurements; * p = 0.026; analyzed by unpaired two-tailed Student *t*-test.

2.6.5. The building block's self-assembly mechanism is biocompatible with the lysosome.

To identify the candidate mechanism driving CFZ-H^+Cl^- accumulation and stabilization in lysosomes, we used a well-established systems-based mathematical model of lysosomal ion regulation. We first performed a simultaneous variation of the number of active V-ATPase and chloride channels per lysosome (resulting in 0 to 100% inhibition of both parameters from their respective baseline physiological input values of 300 and 5000) in the presence and absence of dose-dependent lysosomal CFZ-H^+Cl^- accumulation (0 to 0.01 picomoles/cell/day), as measured *in vitro*[4,29]. The simulation results indicated that CFZ-H^+Cl^- accumulates at the measured rate of 0.01 picomoles/cell/day exerting a negligible effect on lysosomal pH, Cl^-, and membrane potential from respective physiological baseline readout values (4.53 pH units, 224.6 mM, and 0.79 mV). Only a significant (≥ 97%) reduction in the total V-ATPase amount per lysosome led to changes in these values (Fig. 2.5a). Consistent with this, < 97% V-ATPase inhibition per lysosome was required for the physiological accommodation of lysosomal CFZ-H^+Cl^- accumulating at 0.01 picomoles/cell/day (Fig. 2.5b). However, unlike the number of V-ATPase, the number of chloride channel molecules per lysosome did not show any effect on the physiological CFZ-H^+Cl^- accumulation unless this chloride current was completely absent (Fig. 2.5b).

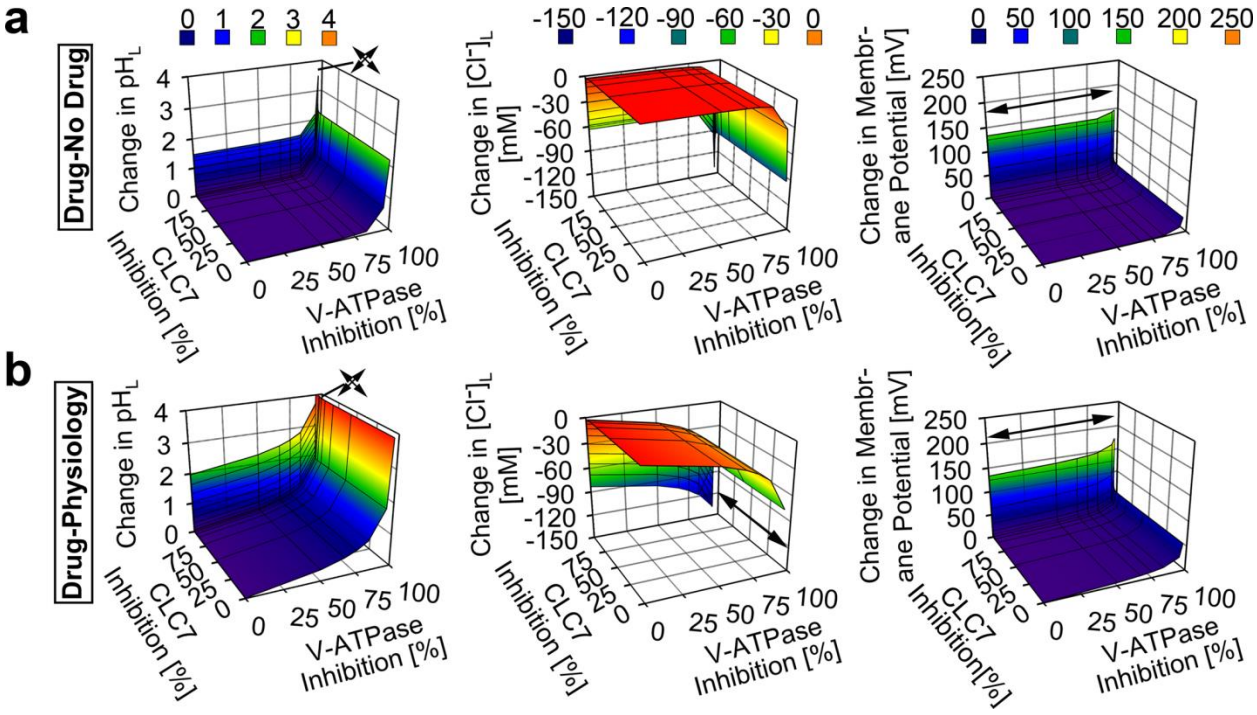

Figure 2.5. Model and simulation of the effects of V-ATPase and CLC7 on the lysosomal accumulation of CFZ-H^+Cl^-.
a, V-ATPase inhibition showed a more substantial effect than CLC7 inhibition on the accumulation of CFZ-H^+Cl^- at the rate of 0.01 picomol/cell/day, as reflected by the changes in the lysosomal pH, Cl^-, and membrane potential values of the CFZ-H^+Cl^- containing lysosome from that of the CFZ-H^+Cl^- free lysosome. **b**, V-ATPase inhibition showed a more substantial effect than CLC7 inhibition on the physiological accumulation of CFZ-H^+Cl^- at the rate of 0.01 picomol/cell/day, as reflected by the changes in the lysosomal pH, Cl^-, and membrane potential values of the CFZ-H^+Cl^- containing lysosome from respective baseline physiological values. Arrow signs represent values outside of the axes plot range.

In dose-dependent simulations, CFZ-H^+Cl^- accumulating at a ten-fold greater (non-physiological) rate of 0.1 picomoles/cell/day led to more pronounced changes in lysosomal pH, Cl^-, and membrane potential (Fig. 2.6a). At least < 68.3% V-ATPase inhibition per lysosome was required to sustain physiological ion concentrations in the presence of this 10-fold greater rate of CFZ-H^+Cl^- accumulation (Fig. 2.6b). In contrast, variations in the numbers of chloride channels did not affect the physiological lysosomal accumulation of CFZ-H^+Cl^- at a rate of 0.1 picomoles/cell/day, unless there was complete inhibition of the chloride current (Fig. 2.6b).

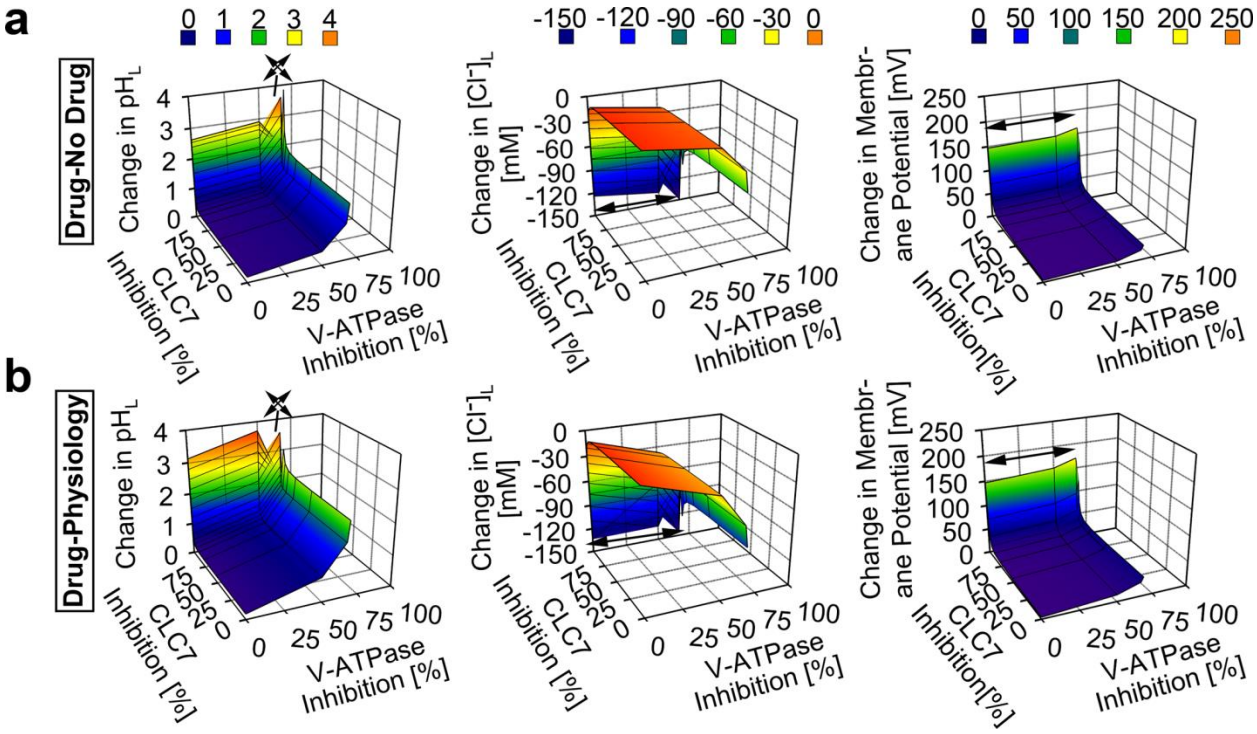

Figure 2.6. Model and simulation of the effects of V-ATPase and CLC7 on the lysosomal accumulation of CFZ-H^+Cl^- at a higher dose.
a, V-ATPase inhibition showed a more substantial effect than CLC7 inhibition on the accumulation of CFZ-H^+Cl^- at the rate of 0.1 picomol/cell/day, as reflected by the changes in the lysosomal pH, Cl^-, and membrane potential values of the CFZ-H^+Cl^- containing lysosome from that of the CFZ-H^+Cl^- free lysosome. **b**, V-ATPase inhibition showed a more substantial effect than CLC7 inhibition on the physiological accumulation of CFZ-H^+Cl^- at the rate of 0.1 picomol/cell/day, as reflected by the changes in the lysosomal pH, Cl^-, and membrane potential values of the CFZ-H^+Cl^- containing lysosome from respective baseline physiological values. Arrow signs represent values outside of the axes plot range.

2.6.6. V-ATPase is essential in the building block accumulation and self-assembly.

To verify our model and simulation findings, we performed experiments to detect the effects of V-ATPase and chloride channels on the intracellular accumulation of CFZ. All experiments regarding the incubation and accumulation of CFZ were performed under conditions in which cellular viability was maintained. In the absence of any inhibitor, 8 μM extracellular CFZ accumulated at a rate of 0.01 picomoles/cell/day, as previously reported[4,29]. However, inhibiting the V-ATPase with BafA1 reduced cellular CFZ accumulation by 80 ± 13% ($p < 0.01$)

in a 4h incubation, relative to control, uninhibited cells (Fig. 2.7a). This observation is consistent with our simulation results, where up to 50% V-ATPase inhibition resulted in a lysosomal pH increment (Fig. 2.5a), which associates with a reduction in cellular drug accumulation. In contrast, when cells were treated with the chloride channel inhibitor NPPB and exposed to CFZ, no significant change was measured in the accumulation of CFZ following a 4h incubation (Fig. 2.7b). This contrasts with the effect observed with BafA1 (Fig. 2.7a), and is consistent with our simulation results (Fig. 2.5a), thereby indicating that in the presence of CFZ uptake, lysosomal ion homeostasis is insensitive to chloride channel inhibition.

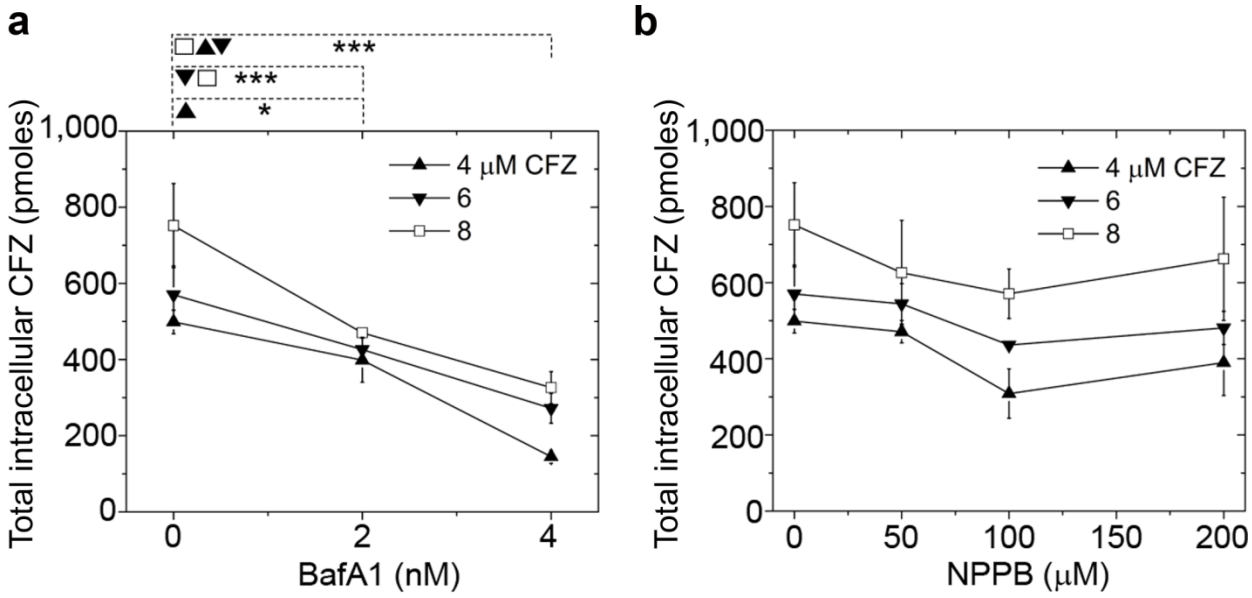

Figure 2.7. Intracellular CFZ accumulation.
Total intracellular CFZ accumulation in picomoles (pmoles) in RAW264.7 cells when pre-incubated with (**a**) BafA1 and (**b**) NPPB and initial concentration of CFZ = 4, 6, and 8 μM at *t* = 4 hours. Significant inhibition of CFZ accumulation was measured at *t* = 4 hours when cells were exposed to BafA1. To the contrary, no such inhibition was measured when cells were exposed to NPPB at *t* = 4 hours. Data are the mean ± S.D. of six experiments. * - $p < 0.05$, ** - $p < 0.01$, *** - $p < 0.001$. Each data point was compared in a pair-wise independent Student t-test.

2.7. Discussion

As a weakly basic, poorly soluble small-molecule chemical that is FDA-approved, orally

bioavailable, slowly cleared, and administered at high doses for prolonged periods of time, CFZ affords us the opportunity to reverse engineer the construction of a mechanopharmaceutical device that was found to form naturally inside cells. We report that, because of its physicochemical properties, CFZ is highly prone to precipitation in acidic endolysosomal compartments in macrophages, where it self-assembles into a highly ordered CFZ-H^+Cl^- biocrystalline, possessing many interesting optical and biomechanical features. Consistent with its accumulation in macrophage lysosomes, CFZ inhibited Lysotracker Blue fluorescence (Fig. 2.4). Furthermore, fluorescence imaging revealed that CFZ was present both as a free base and as a hydrochloride salt form within intracellular vesicles (Fig. 2.4). Thus, we performed computational simulations and experiments to probe the relationship between CFZ's pH dependent solubility properties, the formation of salt and free base crystals, and the molecular, ion transport mechanisms responsible for this mechanopharmaceutical phenomenon, which could be exploited for developing other weakly basic small molecule building blocks as cell-targeted, self-assembling mechanopharmaceutical devices[41,42].

Despite the complexities of lysosomal ion homeostasis, computational simulations and experimental results provide a straightforward explanation for the observed behavior of CFZ: the number of V-ATPase molecules that drive the lowering of macrophage lysosomal pH[43] plays a critical role in determining the intracellular bioaccumulation of CFZ in lysosomes without affecting lysosomal ion homeostasis. Our results show that very high levels of V-ATPase expression, that are typical of macrophages, are both necessary and sufficient to explain the accumulation and stabilization of CFZ-H^+Cl^- salt in these cells because they allow the cells to maintain physiological lysosomal pH and membrane potential in spite of the accumulation of the drug. In addition, the intrinsic solubility properties of CFZ are such that the protonated form of

the drug strongly interacts with chloride in a concentration range that is typically observed in lysosomes, which leads to the physiological accumulation of the drug in its hydrochloride salt form. Accordingly, V-ATPase expression establishes the ability of the cell to maintain physiological lysosomal pH[44], which, in relation to the drug's pH_{max} and K_{sp} (Fig. 2.1), can sustain the continuous accumulation of the hydrochloride salt form of the drug[19] in the lysosome.

More importantly, we found that experimental results[4,29] were highly consistent with model simulation results. First, the inhibition of V-ATPase activity resulted in the reduction of the total intracellular CFZ accumulation (Fig. 2.7a), which was consistent with the model simulation results (Figs. 2.5 and 2.6). In contrast, NPPB-mediated reduction of chloride channel activity did not affect the accumulation and stabilization of the salt form of the drug (Fig. 2.7b), which was also consistent with the model simulation results (Figs. 2.5 and 2.6, and see Appendix Figs. A.5 and A.6). Furthermore, the measured K_{sp} of CFZ-H^+Cl^- and our CLDIs/CFZ-H^+Cl^- stability results (Fig. 2.1) indicate that the physiological lysosomal chloride levels are sufficient to stabilize CFZ-H^+Cl^- salt formation through a common-ion "salting-out" mechanism[35]. Therefore, our findings collectively provide the first mechanistic framework that explains the accumulation of highly ordered, self-assembled CFZ-H^+Cl^- salt biocrystals in macrophages (Figs. 2.2 and 2.3); which depends on the high levels of V-ATPase expression that is unique to this cell type[16].

It is also noteworthy that macrophages have lysosomes which are an order of magnitude greater in size than that of other cell types[45]. This provides them with the capability to accommodate massive accumulation of weakly basic drugs[46]. Even in cases where the initial lysosomal size is small (< 1 μm, in radius), the macrophage lysosomes can undergo biogenesis[47,48]. A master regulator of lysosomal biogenesis and V-ATPase expression is

transcription factor EB (TFEB)[39,46,49]. Moreover, given the recent findings regarding the role of TFEB in upregulating lysosomal genes during inflammation[50], the role of TFEB in the bioaccumulation and stabilization of CFZ-H^+Cl^- salt in macrophage lysosomes, in relation to CFZ's anti-inflammatory activity[9,10], could be further investigated.

To conclude, we have discovered how lysosomal ion transport pathways play a major role in the self-assembly of a biocompatible, cell-targeted supramolecular structure formed by a weakly basic, small molecule building block. Together with the physicochemical properties of the freely soluble building blocks, these transport pathways can be exploited to develop novel types of drug depots and cell-directed drug delivery systems[51-53]. Indeed, interest has been raised in macrophages as drug delivery vehicles. As our studies have shown, macrophages may allow drugs to be locally stabilized and undergo a sustained release in a site-specific manner, offering a strategy for reducing off-target side effects[54,55]. Macrophages are also one of the few cell types, which are primarily involved in the phagocytosis of foreign particles of different sizes and shapes, including drugs[56,57], which offer yet another opportunity for loading these cells with massive amounts of chemotherapeutic agents. To this end, additional investigations into the manner in which these cells mechanically synergize with the self-assembled weakly basic small molecule building blocks in order to stabilize functional mechanopharmaceutical devices are warranted.

2.8. Acknowledgments and contributions

In the adapted portions of this chapter from Woldemichael, T. et al, (2017):

The authors acknowledge funding from M-Cubed and NIH grant R01GM078200 to GRR. We thank Dr. Nair Rodriguez-Hornedo (Department of Pharmaceutical Sciences, University of Michigan) for allowing the use of HPLC instrumentation in her lab.

T.W., R.K.K., P.R., K.A.S., and G.R.R. designed the research. T.W., R.K.K., P.R., M.D.M., B.G., and V.L. conducted the experiments. G.R.R. and J.A.S. contributed new reagents or analytic tools. T.W., R.K.K., P.R., B.G., and V.L. analyzed the data. T.W., R.K.K., P.R., M.D.M, V.L., K.A.S., B.G., J.A.S, and G.R.R wrote or contributed to the writing of the manuscript.

2.9. References

1 Zhang, Z. *et al.* Supersnowflakes: Stepwise Self-Assembly and Dynamic Exchange of Rhombus Star-Shaped Supramolecules. *J Am Chem Soc* **139**, 8174-8185, doi:10.1021/jacs.7b01326 (2017).

2 Deng, Y. *et al.* Multifunctional small molecule for controlled assembly of oligomeric nanoparticles and crosslinked polymers. *Org Biomol Chem* **9**, 6917-6919, doi:10.1039/c1ob06132a (2011).

3 Desikan, K. V., Ramanujam, K., Ramu, G. & Balakrishnan, S. Autopsy findings in a case of lepromatous leprosy treated with clofazimine. *Lepr Rev* **46**, 181-189 (1975).

4 Baik, J. & Rosania, G. R. Molecular imaging of intracellular drug-membrane aggregate formation. *Mol Pharm* **8**, 1742-1749, doi:10.1021/mp200101b (2011).

5 Baik, J., Stringer, K. A., Mane, G. & Rosania, G. R. Multiscale distribution and bioaccumulation analysis of clofazimine reveals a massive immune system-mediated xenobiotic sequestration response. *Antimicrob Agents Chemother* **57**, 1218-1230, doi:10.1128/AAC.01731-12 (2013).

6 O'Connor, R., O'Sullivan, J. F. & O'Kennedy, R. The pharmacology, metabolism, and chemistry of clofazimine. *Drug Metab Rev* **27**, 591-614, doi:10.3109/03602539508994208 (1995).

7 Horstman, E. M. *et al.* Elasticity in Macrophage-Synthesized Biocrystals. *Angew Chem Int Ed Engl* **56**, 1815-1819, doi:10.1002/anie.201611195 (2017).

8 Keswani, R. K. *et al.* Chemical Analysis of Drug Biocrystals: A Role for Counterion Transport Pathways in Intracellular Drug Disposition. *Mol Pharm* **12**, 2528-2536, doi:10.1021/acs.molpharmaceut.5b00032 (2015).

9 Yoon, G. S. *et al.* Clofazimine Biocrystal Accumulation in Macrophages Upregulates IL-1RA Production to Induce a Systemic Anti-Inflammatory State. *Antimicrob Agents Chemother*, doi:10.1128/AAC.00265-16 (2016).

10 Yoon, G. S. *et al.* Phagocytosed Clofazimine Biocrystals Can Modulate Innate Immune Signaling by Inhibiting TNFalpha and Boosting IL-1RA Secretion. *Mol Pharm* **12**, 2517-2527, doi:10.1021/acs.molpharmaceut.5b00035 (2015).

11 Keswani, R. K., Yoon, G. S., Sud, S., Stringer, K. A. & Rosania, G. R. A far-red fluorescent probe for flow cytometry and image-based functional studies of xenobiotic sequestering macrophages. *Cytometry A* **87**, 855-867, doi:10.1002/cyto.a.22706 (2015).

12 Wang, S. P., Krits, I., Bai, S. & Lee, B. S. Regulation of enhanced vacuolar H+-ATPase expression in macrophages. *J Biol Chem* **277**, 8827-8834, doi:10.1074/jbc.M111959200 (2002).

13 Hong, L. *et al.* Alteration of volume-regulated chloride channel during macrophage-derived foam cell formation in atherosclerosis. *Atherosclerosis* **216**, 59-66, doi:10.1016/j.atherosclerosis.2011.01.035 (2011).

14 Jiang, L. *et al.* Intracellular chloride channel protein CLIC1 regulates macrophage function through modulation of phagosomal acidification. *J Cell Sci* **125**, 5479-5488, doi:10.1242/jcs.110072 (2012).

15 Kazmi, F. *et al.* Lysosomal sequestration (trapping) of lipophilic amine (cationic amphiphilic) drugs in immortalized human hepatocytes (Fa2N-4 cells). *Drug Metab Dispos* **41**, 897-905, doi:10.1124/dmd.112.050054 (2013).

16 Ishida, Y., Nayak, S., Mindell, J. A. & Grabe, M. A model of lysosomal pH regulation. *J Gen Physiol* **141**, 705-720, doi:10.1085/jgp.201210930 (2013).

17 Yoshimori, T., Yamamoto, A., Moriyama, Y., Futai, M. & Tashiro, Y. Bafilomycin A1, a specific inhibitor of vacuolar-type H(+)-ATPase, inhibits acidification and protein degradation in lysosomes of cultured cells. *J Biol Chem* **266**, 17707-17712 (1991).

18 Wangemann, P. *et al.* Cl−-channel blockers in the thick ascending limb of the loop of Henle Structure activity relationship. *Pflügers Archiv* **407**, S128-S141, doi:10.1007/bf00584942 (1986).

19 Kramer, S. F. & Flynn, G. L. Solubility of organic hydrochlorides. *J Pharm Sci* **61**, 1896-1904 (1972).

20 van Rooijen, N. & Hendrikx, E. Liposomes for specific depletion of macrophages from organs and tissues. *Methods Mol Biol* **605**, 189-203, doi:10.1007/978-1-60327-360-2_13 (2010).

21 Baik, J. & Rosania, G. R. Macrophages sequester clofazimine in an intracellular liquid crystal-like supramolecular organization. *PLoS One* **7**, e47494, doi:10.1371/journal.pone.0047494 (2012).

22 Murashov, M. D. *et al.* The Physicochemical Basis of Clofazimine-Induced Skin Pigmentation. *J Invest Dermatol*, doi:10.1016/j.jid.2017.09.031 (2017).

23 Oldenbourg, R. Polarized light microscopy: principles and practice. *Cold Spring Harb Protoc* **2013**, doi:10.1101/pdb.top078600 (2013).

24 Rzeczycki, P. *et al.* Detecting ordered small molecule drug aggregates in live macrophages: a multi-parameter microscope image data acquisition and analysis strategy. *Biomed Opt Express* **8**, 860-872, doi:10.1364/BOE.8.000860 (2017).

25 van Rooijen, N. & Hendrikx, E. in *Liposomes* Vol. 605 *Methods in Molecular Biology* (ed Volkmar Weissig) Ch. 13, 189-203 (Humana Press, 2010).

26 Lee, S., Starkey, P. & Gordon, S. Quantitative analysis of total macrophage content in adult mouse tissues. Immunochemical studies with monoclonal antibody F4/80. *J Exp Med* **161**, 475-489 (1985).

27 Sakagami, H. *et al.* Cell death induced by nutritional starvation in mouse macrophage-like RAW264.7 cells. *Anticancer Res* **29**, 343-347 (2009).

28 Davis, M. J. & Swanson, J. A. Technical advance: Caspase-1 activation and IL-1beta release correlate with the degree of lysosome damage, as illustrated by a novel imaging method to quantify phagolysosome damage. *J Leukoc Biol* **88**, 813-822, doi:10.1189/jlb.0310159 (2010).

29 Min, K. A. *et al.* Massive Bioaccumulation and Self-Assembly of Phenazine Compounds in Live Cells. *Adv Sci (Weinh)* **2**, doi:10.1002/advs.201500025 (2015).

30 Heuser, J., Zhu, Q. & Clarke, M. Proton pumps populate the contractile vacuoles of Dictyostelium amoebae. *J Cell Biol* **121**, 1311-1327 (1993).

31 Van Dyke, R. W. Acidification of rat liver lysosomes: quantitation and comparison with endosomes. *Am J Physiol* **265**, C901-917 (1993).

32 Gambale, F., Kolb, H. A., Cantu, A. M. & Hedrich, R. The Voltage-Dependent H+-Atpase of the Sugar-Beet Vacuole Is Reversible. *Eur Biophys J Biophy* **22**, 399-403 (1994).

33 Sonawane, N. D., Thiagarajah, J. R. & Verkman, A. S. Chloride concentration in endosomes measured using a ratioable fluorescent Cl- indicator - Evidence for chloride accumulation during acidification. *Journal of Biological Chemistry* **277**, 5506-5513, doi:10.1074/jbc.M110818200 (2002).

34 Alberts, B. J., A.; Lewis, J.; Raff, M.; Roberts, K.; Walter, P. *Moelcular Biology of the Cell. Fifth edition*. (Garland Science, New York, 2008).

35 Serajuddin, A. T. Salt formation to improve drug solubility. *Adv Drug Deliv Rev* **59**, 603-616, doi:10.1016/j.addr.2007.05.010 (2007).

36 Keswani, R. K. *et al.* Repositioning Clofazimine as a Macrophage-Targeting Photoacoustic Contrast Agent. *Sci Rep* **6**, 23528, doi:10.1038/srep23528 (2016).

37 Keswani, R., Yoon, G., Sud, S., Stringer, K. & Rosania, G. A Far-Red Fluorescent Probe For Flow Cytometric Xenobiotic-Sequestering Cell Functional Studies. *Cytometry Part A* (2015).

38 Lemieux, B., Percival, M. D. & Falgueyret, J. P. Quantitation of the lysosomotropic character of cationic amphiphilic drugs using the fluorescent basic amine Red DND-99. *Anal Biochem* **327**, 247-251, doi:10.1016/j.ab.2004.01.010 (2004).

39 Samie, M. A. & Xu, H. Lysosomal exocytosis and lipid storage disorders. *J Lipid Res* **55**, 995-1009, doi:10.1194/jlr.R046896 (2014).

40 Life Technologies. *LysoTracker and LysoSensor Probes*, <https://tools.thermofisher.com/content/sfs/manuals/mp07525.pdf> (2013).

41 Huefner, A. *et al.* Gold nanoparticles explore cells: cellular uptake and their use as intracellular probes. *Methods* **68**, 354-363, doi:10.1016/j.ymeth.2014.02.006 (2014).

42 Rajendran, L., Knolker, H. J. & Simons, K. Subcellular targeting strategies for drug design and delivery. *Nat Rev Drug Discov* **9**, 29-42, doi:10.1038/nrd2897 (2010).

43 Beyenbach, K. W. & Wieczorek, H. The V-type H+ ATPase: molecular structure and function, physiological roles and regulation. *J Exp Biol* **209**, 577-589, doi:10.1242/jeb.02014 (2006).

44 Grabe, M., Wang, H. & Oster, G. The mechanochemistry of V-ATPase proton pumps. *Biophys J* **78**, 2798-2813, doi:10.1016/S0006-3495(00)76823-8 (2000).

45 Lüllmann-Rauch, R. in *Lysosomes* 1-16 (Springer US, 2005).

46 Logan, R., Kong, A. C. & Krise, J. P. Time-dependent effects of hydrophobic amine-containing drugs on lysosome structure and biogenesis in cultured human fibroblasts. *J Pharm Sci* **103**, 3287-3296, doi:10.1002/jps.24087 (2014).

47 Emanuel, R. *et al.* Induction of lysosomal biogenesis in atherosclerotic macrophages can rescue lipid-induced lysosomal dysfunction and downstream sequelae. *Arterioscler Thromb Vasc Biol* **34**, 1942-1952, doi:10.1161/ATVBAHA.114.303342 (2014).

48 Gao, Y. *et al.* Comprehensive proteome analysis of lysosomes reveals the diverse function of macrophages in immune responses. *Oncotarget* **8**, 7420-7440, doi:10.18632/oncotarget.14558 (2017).

49 Wang, W. *et al.* Up-regulation of lysosomal TRPML1 channels is essential for lysosomal adaptation to nutrient starvation. *Proc Natl Acad Sci U S A* **112**, E1373-1381, doi:10.1073/pnas.1419669112 (2015).

50 Pastore, N. *et al.* TFEB and TFE3 cooperate in the regulation of the innate immune response in activated macrophages. *Autophagy* **12**, 1240-1258, doi:10.1080/15548627.2016.1179405 (2016).

51 Brahler, M. *et al.* Magnetite-loaded carrier erythrocytes as contrast agents for magnetic resonance imaging. *Nano Lett* **6**, 2505-2509, doi:10.1021/nl0618501 (2006).

52 Wang, C. *et al.* Red Blood Cells for Glucose-Responsive Insulin Delivery. *Adv Mater*, doi:10.1002/adma.201606617 (2017).

53 Paukner, S. *et al.* Bacterial ghosts as a novel advanced targeting system for drug and DNA delivery. *Expert Opin Drug Deliv* **3**, 11-22, doi:10.1517/17425247.3.1.11 (2006).

54 Wang, C. *et al.* Multifunctional theranostic red blood cells for magnetic-field-enhanced in vivo combination therapy of cancer. *Adv Mater* **26**, 4794-4802, doi:10.1002/adma.201400158 (2014).

55 Gutierrez Millan, C., Bax, B. E., Castaneda, A. Z., Marinero, M. L. & Lanao, J. M. In vitro studies of amikacin-loaded human carrier erythrocytes. *Transl Res* **152**, 59-66, doi:10.1016/j.trsl.2008.05.008 (2008).

56 Rossi, L. *et al.* Effect of listeriolysin O-loaded erythrocytes on Mycobacterium avium replication within macrophages. *J Antimicrob Chemother* **53**, 863-866, doi:10.1093/jac/dkh164 (2004).

57 Mishra, P. R. & Jain, N. K. Surface modified methotrexate loaded erythrocytes for enhanced macrophage uptake. *J Drug Target* **8**, 217-224, doi:10.3109/10611860008997900 (2000).

Chapter 3: Elucidating the Key Lysosomal Parameters That Can Explain the Drug Accumulation Observed in Macrophages with Respect to Changes in Lysosomal Morphology

This chapter was adapted from the following publication:

Woldemichael, T. and Rosania, G.R. (2017) The physiological determinants of drug-induced lysosomal stress resistance. *PLoS One*, 12(11): e0187627. doi: 10.1371/journal.pone.0187627.

3.1. Relevance to Thesis

This chapter incorporates the effect of heterogeneous lysosomal morphology on lysosomal ion homeostasis. This is important to our understanding of the relationship between lysosomal physiology of cell-type dependent heterogeneous lysosomal morphology and physiological drug bioaccumulation. Given the dynamics of subcellular ion regulation and physiology, we utilized a computational approach to dissect out how combinations of different factors affecting lysosomal structure and function influence the ability of the organelle to recover from perturbations of physiological ion homeostasis. Our results emphasized the key biological determinants of sensitivity and resistance to lysosomal stress, which are critical in order to understand the cell-type specific toxicological effects of lysosomotropic drugs. Our findings lay the groundwork for the design of future wet lab experiments that investigate the physiological accumulation of weak base drugs in lysosomes, in a cell-type dependent manner. Moreover, because of the multi-faceted impact of our findings, experts from various fields, such as Biophysics, Pharmaceutics, Genetics, and Cell Biology could individually or collectively make

use of our work to study the biophysical features of lysosomal ion and cholesterol regulations, lysosomal morphology with respect to lysosomal membrane biophysics, the upregulation of lysosomal genes, and the implications on drug disposition, stabilization, and physiology in a cell-type dependent manner.

3.2. Personal Contribution

I used a computational model of lysosomal ion regulation to simulate the manner in which intrinsic and extrinsic factors affect the restoration of normal lysosomal physiology following perturbation in one or more physiological parameters affecting lysosomal ion homeostasis. I varied lysosomal membrane protein levels, lysosomal morphology, and ion content in the context of A) extrinsic factors, such as drug-induced changes in lysosomal morphology, drug-induced changes in lysosomal cholesterol and ion content, drug-induced changes in lysosomal membrane protein activity, and B) intrinsic cellular factors, such as cell-type dependent lysosomal gene regulation, cell-type dependent change in lysosomal morphology as may happen in endocytosis and exocytosis processes, and cell-type dependent ion and cholesterol regulation.

3.3. Abstract

Many weakly basic, lipophilic drugs accumulate in lysosomes and exert complex, pleiotropic effects on organelle structure and function. Thus, modeling how perturbations of lysosomal physiology affect the maintenance of lysosomal ion homeostasis is necessary to elucidate the key factors which determine the toxicological effects of lysosomotropic agents, in a cell-type dependent manner. Accordingly, a physiologically-based mathematical modeling and

simulation approach was used to explore the dynamic, multi-parameter phenomenon of lysosomal stress. With this approach, parameters that are either directly involved in lysosomal ion transportation or lysosomal morphology were transiently altered to investigate their downstream effects on lysosomal physiology reflected by the changes they induce in lysosomal pH, chloride, and membrane potential. In addition, combinations of parameters were simultaneously altered to assess which parameter was most critical for recovery of normal lysosomal physiology. Lastly, to explore the relationship between organelle morphology and induced stress, we investigated the effects of parameters controlling organelle geometry on the restoration of normal lysosomal physiology following a transient perturbation. Collectively, our results indicate a key, interdependent role of V-ATPase number and membrane proton permeability in lysosomal stress tolerance. This suggests that the cell-type dependent regulation of V-ATPase subunit expression and turnover, together with the proton permeability properties of the lysosomal membrane, is critical to understand the differential sensitivity or resistance of different cell types to the toxic effects of lysosomotropic drugs.

3.4. Introduction

Alterations in lysosomal structure and function can lead to complex, pathophysiological manifestations in living organisms[1,2]. For example, mutations which affect proteins mediating lysosomal membrane transport are associated with a variety of inherited diseases and developmental disorders which affect multiple organ systems[3-7]. Physiologically, lysosomal ion homeostasis is maintained by the action of different transmembrane channels and pumps, such as the proton-chloride antiporter known as CLC7[8], the non-selective cation transporter known as TRPML[9], and the lysosomal proton pump known as vacuolar ATPase (V-ATPase)[10]. *In vivo,*

mutations in CLC7 cause osteoporosis and neurodegeneration in mice, and are associated with similar phenotypic effects in humans[11-13]. Similarly, mutations in TRPML are associated with an autosomal-recessive lysosomal storage disease known as MLIV[14-16], whereas mutations in V-ATPase are associated with osteoporosis, renal tubular acidosis, and deafness in humans, and cause similar effects in mice[17-20]. Furthermore, perturbations in vesicular trafficking which affect ion transport functions can adversely affect cellular function which leads to muscle degeneration[21].

Like mutations in proteins affect the ion transport properties of lysosomal membranes, many drugs accumulate in lysosomes or interfere with lysosomal ion transport mechanisms, which lead to alterations in lysosomal structure and function. At the cellular level, the effects of drug accumulation often resemble that of genetic mutations which affect lysosomal ion homeostasis, such as lysosomal size expansion[22] and changes in organelle morphology[23]. Furthermore, *in vitro* experiments have revealed that the accumulation of lipophilic, weakly basic drugs in lysosomes can affect lysosomal pH[23], membrane potential[1], organelle morphology[23], and changes in transmembrane ion permeability[24-26]. Therefore, it is possible that drug-induced lysosomal stress may be manifested as idiosyncratic drug side effects, which include increased predisposition to microbial infections[27], osteoporosis[28,29], and neurodegenerative diseases; such as Alzheimer's disease, Huntington's disease, and Parkinson's diseases[11,30,31].

Interestingly, cells upregulate the expression of genes that allow lysosomes to recover normal physiological function following the disruption of physiological ion homeostasis[32]. At the transcriptional level, the transcription factor EB (TFEB) mediates lysosomal stress pathways[33] by upregulating the expression of lysosomal genes, such as V-ATPase[34] and TRPML[33]. In mice,

TFEB reverses expanded lysosomes by upregulating genes that directly or indirectly re-establish lysosomal ion homeostasis[33,35,36]. As a regulator of lysosomal biogenesis and stress tolerance, TFEB not only affects ion transport functions and membrane trafficking[37,38], but its activation has also been associated with cells' increased resistance to physiological perturbations induced by lysosomotropic drugs[39].

In order to further understand how lysosomotropic drugs may affect lysosomal ion homeostasis, a physiologically-based, mathematical modeling approach was utilized to shed light on key parameters which affect recovery from transient perturbations in lysosomal ion regulation. This approach was deemed necessary because pharmacological agents that accumulate in lysosomes can exert multiple effects on the molecular mechanisms that influence lysosomal pH, membrane potential, and chloride transport. These include inhibitors of the V-ATPase, such as Bafilomycin A, Concomycin, Salicylihalamide A, and Archazolid[40,41], chloride channel blockers, such as Cystic fibrosis transmembrane regulator (CFTR) inhibitors, which include Glibenclamide and Niflumic acid, and ClC channel inhibitor known as Lubiprostone[42], as well as other conditions that affect lysosomal morphology[43,44] and membrane permeability[45-49]. Upon simulating transient perturbations, parameter sensitivity analysis was used to reveal the most likely mechanistic determinants of the cell's ability to restore and maintain lysosomal ion homeostasis following exposure to one or more drug-induced lysosomal stresses, thereby providing important theoretical insights into the mechanistic determinants of drug-induced lysosomal stress and stress tolerance.

3.5. Methods

3.5.1. Model parameterization.

An established, systems-based mechanistic model of lysosomal ion transport, which is comprised of differential equations that capture the transmembrane transport properties of ions and water across the lysosomal membrane[8,50] was used to simulate the physiological consequences of drug-induced lysosomal stress (Fig. 3.1).

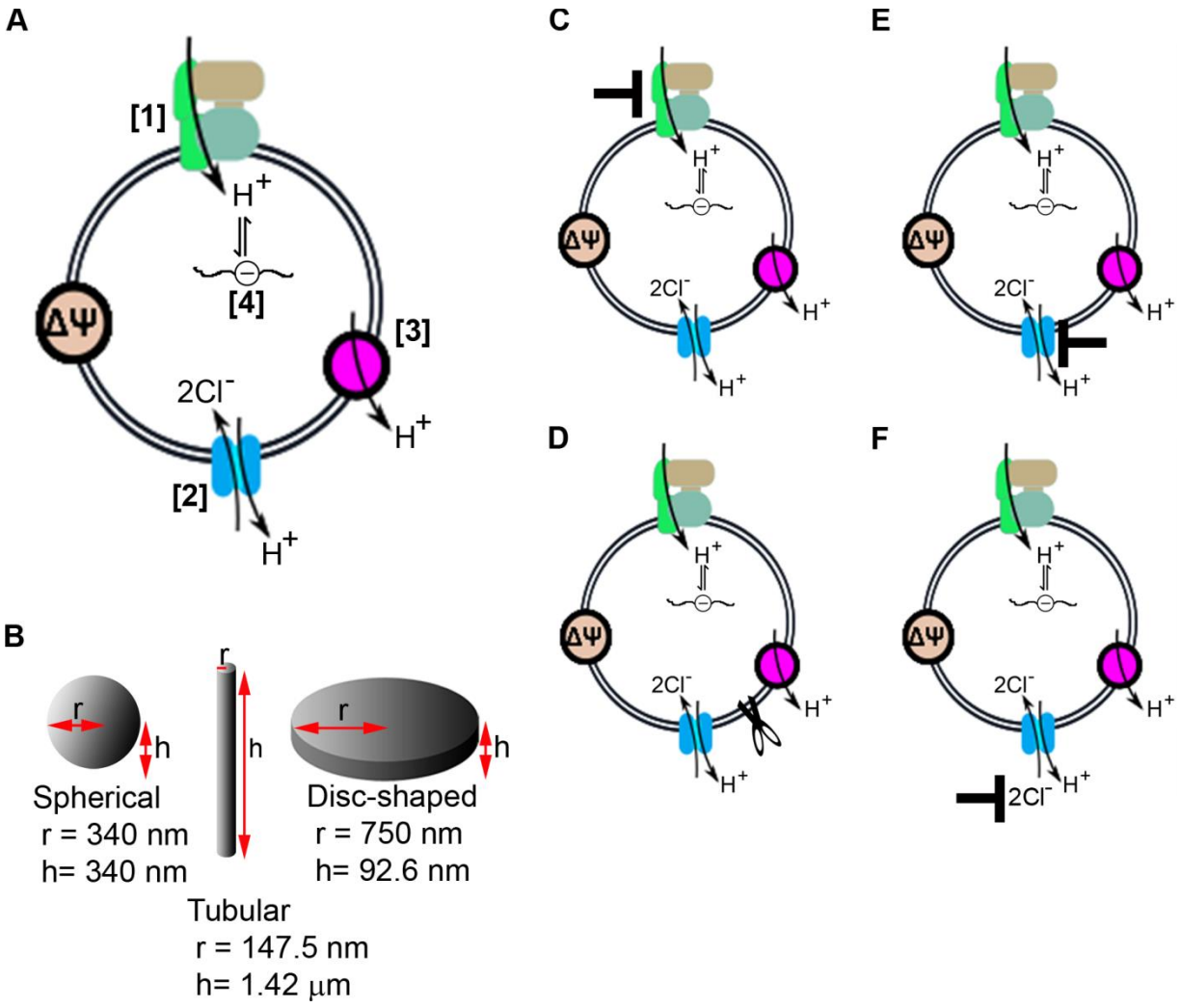

Figure 3.1. **Modeling the effects of drugs on lysosomal ion homeostasis.**
We utilized an established physiological framework to model lysosomal ion transport (**A**). Accordingly, the V-ATPase actively pumps protons into the lysosome (**1**) while the proton-chloride antiporter CLC7 dissipates the ensuing increase in membrane potential by coupling the efflux of protons with the influx of chloride (**2**). Protons escape the lysosomes through diffusion across the lysosomal membrane (**3**), and protons in the lysosome are sequestered through the buffering capacity of resident lysosomal components (**4**). Free protons that accumulate in the

lysosomal lumen contribute to the decrease in lysosomal pH. Based on this mechanism, the effect of drugs was captured by modeling different lysosomal shapes and volumes (**B**). Concomitantly, the drug-dependent inhibition of V-ATPase function was modeled by varying the proton pumping activity (**C**); the drug-dependent change in membrane proton permeability was modeled by varying the proton leak from the lysosome (**D**); and, the drug-dependent perturbation of membrane potential regulation was modeled by inhibiting CLC7 (**E**) or decreasing cytoplasmic chloride (**F**).

For the purpose of studying the lysosomal stress response, the model (see Appendix B.1) contained 22 parameters. Six out of the 22 parameters were varied to capture the effects of drugs on lysosomal structure and function, whereas the remaining sixteen were fixed (Table 3.1). Fixed parameters were set to published values, which give rise to physiological lysosomal function[50,51] and are referred to as "baseline input values". These parameters include lysosomal radius of 340 nm with volume and surface area corresponding to a spherical lysosomal vesicle, which was obtained from electron microscopy data[52], and the associated organellar ions and ion transporters, which include 300 V-ATPase molecules per lysosome, which was estimated from microscope data analysis and wet lab experimental data fitting[50,53,54], membrane proton permeability of $6x10^{-5}$ cm/s, which was estimated from wet lab experimental data fitting[50], cytoplasmic chloride concentration of 10 mM[55,56], and initial lysosomal ion concentrations estimated to equal that of extracellular ions[56]. A lysosome with the entire model parameters set to baseline input values is referred to as an "unperturbed lysosome".

Table 3.1. Model parameters.

Symbol	**Description**	**Baseline Input Value**	**Range of Input Value**	**Units**

pH_C	Cytosolic pH	7.2	Fixed	pH unit
pH_L	Luminal pH	7.4	Fixed	pH unit
$[Cl^-]_C$	Cytosolic chloride concentration	10	$1x10^{-5}$ - 10	mM
$[Cl^-]_L$	Luminal chloride concentration	110	Fixed	mM
$[Na^+]_L$	Luminal sodium concentration	145	Fixed	mM
$[K^+]_L$	Luminal potassium concentration	5	Fixed	mM
$[H^+]_L$	Luminal proton concentration	0	Fixed	mM
P_{H^+}	Membrane proton permeability	$6x10^{-5}$	$1.38x10^{-7}$ - 6	cm/s
V	Lysosomal volume	$1.65x10^{-16}$	$2.88x10^{-17}$ - $1.65x10^{-16}$	L
S	Lysosomal surface area	$1.45x10^{-8}$	$1.45x10^{-8}$ - $6.28x10^{-6}$	cm^2
C’	Specific bilayer capacitance	1	Fixed	μFarad/ cm^2
β	Buffering capacity	40	Fixed	mM/pH
N_{VATP}	V-ATPase number	300	$1x10^{-4}$ - $1.3x10^5$	
N_{ClC7}	CLC7 number	5000	$1x10^{-4}$ - 5000	
Ψ_{out} *	Outer surface potential	-50	Fixed	mV
Ψ_{in} *	Inner surface potential	0	Fixed	mV
CLC_Cl	CLC7 Cl^- stoichiometry	2	Fixed	
CLC_H	CLC7 H^+ stoichiometry	1	Fixed	
R	Gas constant	8.314	Fixed	$J.K^{-1}.mol^{-1}$

T	Absolute temperature	0	Fixed	Kelvin
F	Faraday's constant	96485	Fixed	J/volt
N_{av}	Avogadro's number	$6.02x10^{23}$	Fixed	molecules/ mol

Model parameters used to simulate various lysosomal stresses and stress tolerance mechanism. Baseline input values are literature values[52-56] representing physiological lysosomes and are in agreement with previously published models[50,51].
* estimated intrinsic surface potentials for inner, Ψ_{in}, and outer, Ψ_{out}, leaflets of the lysosomal membrane accounted for when modeling membrane transporter mediated dynamic lysosomal and cytoplasmic ion concentrations at the surface[51].

Adjustable parameters are those that were varied from their respective baseline input values in order to simulate the effects of lysosomal stressors. Accordingly, lysosomes that are modeled by changing one or multiple of these adjustable parameters are referred to as "perturbed lysosomes". Moreover, the lysosomal ion stressors reported here are associated with stressors inducing variations in lysosomal membrane proton permeability, cytoplasmic chloride concentration, and V-ATPase and CLC7 molecules per lysosome, whereas the lysosomal morphology stressors are associated with stressors inducing variations in lysosomal surface area and volume.

3.5.2 Simulating drug-induced changes in lysosomal morphology.

To study how drug-induced changes in lysosomal morphology affect ion homeostasis, simulations were performed in lysosomes of different surface areas and volumes. First, lysosomes were modeled as perfect spheres. Assuming there are approximately around 100 lysosomes in a cell, which occupy 1% of cellular volume, the volume of a single lysosome was

set to $1.65x10^{-16}$ L. For a spherical vesicle, this volume corresponds to a lysosomal radius of 0.34 μm and a surface area of $1.45x10^{-8}$ cm^2.

For comparison, tubular lysosomes (Fig. 3.1B) (radius = 40 nm - 270 nm, height = 585 nm - 5.73 μm) were modeled using a range of volumes ($2.88x10^{-17}$ L-$1.34x10^{-16}$ L). The dimensional relationship between the tubular radius and height, at constant lysosomal surface area of $1.45x10^{-8}$ cm^2 (equivalent to the surface area of a spherical lysosome (radius = 0.34 μm), as previously mentioned in our study of spherical lysosomes), was calculated using cylindrical equation ($V = \pi r^2 h$, where r is radius and h is height). These morphologies are consistent with measurements in other publications[44,57].

Next, to mimic disc-shaped lysosomes as have been reported in different cell types under other biologically relevant conditions[58-60], lysosomes (radius = 422 nm-10 μm, height = 0.5 nm-294.9 nm) were modeled using a rage of lysosomal surface area ($1.90x10^{-8}$ cm^2 -$6.28x10^{-6}$ cm^2). The dimensional relationship between the disc-shaped lysosomal radius and height, at constant lysosomal volume of $1.65x10^{-16}$ L (equivalent to the volume of a spherical lysosome, 0.34 μm in radius), was calculated using cylindrical equation ($S = 2\pi r^2 + 2\pi rh$, where r is radius and h is height).

3.5.3. Simulating stress tolerance following drug-induced changes in lysosomal morphology.

To understand how lysosomes possessing different structural and functional characteristics may respond differently to drugs, the number of V-ATPase and membrane proton permeability were individually varied. When studying the effects of these two particular lysosomal parameters on morphologically altered or otherwise stressed lysosome, we referred to

them as “stress tolerance inducers”. Thus, the number of V-ATPase molecules per lysosome was increased from physiological baseline input value of 300 to $1.3x10^5$ (resulting in 13 data generating points), while proton permeability was decreased from physiological baseline input value of $6x10^{-5}$ cm/s to $1.38x10^{-7}$ cm/s (resulting in 9 data generating points). These ranges of input values for both V-ATPase number and proton permeability allowed us to quantitatively compare and contrast the relationship of lysosomal surface area to the number of V-ATPase molecules and membrane proton permeability per lysosome. For example, we chose different fold increments in lysosomal surface area (say, 20- or 400-fold) and one simulation at a time set the corresponding lysosomal surface area as an input. So, in the case of a lysosome with a 20-fold lysosomal surface area expansion, we set the surface area to $2.9x10^{-7}$ cm^2. Then, to study the effect of the number of V-ATPase molecules on this expanded lysosome, we performed parametric simulation for the V-ATPase number ranging 0 to 6000, which corresponds to 0 to 20-fold increment in V-ATPase number per lysosome.

3.5.4. Simulating drug-induced lysosomal stress.

Parametric simulations were performed to study the effects of the following four drug-induced stresses on lysosomal physiology: V-ATPase inhibition, CLC7 inhibition, lysosomal membrane permeabilization, and decreased membrane potential dissipation based on lower cytoplasmic chloride concentration (Fig. 3.1). More specifically, membrane proton permeability was varied from physiological baseline input value of $6x10^{-5}$ cm/s to 6 cm/s (resulting in 8 data generating points), the number of V-ATPase molecules per lysosome was varied from 0 to physiological value of 300 (resulting in 10 data generating points), the number of CLC7 molecules per lysosome was varied from 0 to physiological value of 5000 (resulting in 25 data

generating points), and the cytoplasmic chloride concentration was varied from 0 to physiological value of 10 mM (resulting in 7-16 data generating points).

Using the aforementioned ranges of the adjustable lysosomal parameters, the corresponding lysosomal parameter inhibition range 0 to 100% was calculated for cytoplasmic chloride, V-ATPase and CLC7 number; where 0% represents no change from respective physiological baseline input value, and 100% represents the input value set to ~zero. The inhibition range was calculated as follows by comparing the corresponding input value (Adjusted Input Value) from the aforementioned given range with its respective physiological input value (Baseline Input Value):

$$\% \text{ Inhibition} = \frac{\text{Baseline Input Value} - \text{Adjusted Input Value}}{\text{Baseline Input Value}} \times 100\% \qquad (1)$$

3.5.5. Simulating individual lysosomal ion stressors.

The effects of the lysosomal ion stressors were individually studied in spherical and different sized tubular lysosomes by performing parametric simulation of the four parameters mentioned in the previous subsection (using the same ranges of input values with corresponding intervals) while setting the lysosomal volume and surface area input values to correspond to either a spherical or tubular lysosomal geometry, as indicated in the earlier subsection. For example, in the case of introducing CLC7 inhibitor to a spherical lysosome, lysosomal volume and surface area were set to 1.65×10^{-16} L and 1.45×10^{-8} cm^2, respectively. Then, the CLC7 number was varied from 0 to 5000, as previously indicated. Similar approach was applied when studying stressor effect in tubular lysosomes except the input value for lysosomal volume was

varied from 2.88×10^{-17} L to 1.65×10^{-16} L (resulting in 4 data generating points), while fixing lysosomal surface area at 1.45×10^{-8} cm^2.

3.5.6. Simulating combinations of lysosomal ion stressors.

The effects of the various combinations of the aforementioned lysosomal ion stressors were studied in spherical, tubular, and disc-shaped lysosomes. The stressor combinations included V-ATPase inhibition-CLC7 inhibition, V-ATPase inhibition-Cytoplasmic Cl^- depletion, V-ATPase inhibition-membrane proton permeabilization, CLC7 inhibition-Cytoplasmic Cl^- depletion, CLC7 inhibition-membrane proton permeabilization, Cytoplasmic Cl^- depletion-membrane proton permeabilization. The ranges of values, with the associated specific or arbitrarily chosen intervals for each parameter mentioned in the previous sections were applied here as well. For example, to simulate the administration of V-ATPase inhibition-CLC7 inhibition to a spherical lysosome, lysosomal volume and surface area input values were set to 1.65×10^{-16} L and 1.45×10^{-8} cm^2, respectively to adjust the lysosomal geometry as a sphere. Then, the CLC7 number was varied from 0 to 5000, whereas, the V-ATPase number was, one simulation at a time, manually set to a value within the range 0 to 300.

3.5.7. Calculating the effects of lysosomal stressors and tolerance on lysosomal physiology.

Time-plot simulations were performed to obtain physiological final lysosomal pH, Cl^-, and membrane potential readout values for an unperturbed lysosome, where all of the parameters are set to physiological baseline values. These readout values, which from hereon we refer to as "physiological baseline readout values", were specifically chosen as they are direct indicators of lysosomal ion homeostasis and physiology.

Similarly, when performing each of the aforementioned parametric lysosomal stress and stress tolerance simulations, final lysosomal pH, Cl^-, and membrane potential variables were chosen as readouts as a function of either a specific lysosomal stressor or stress tolerance inducer in order to generate two-dimensional data. Then, the 2D dataset was exported to Microsoft Excel for further analysis. The final lysosomal pH, Cl^-, and membrane potential values were subtracted from their respective physiological baseline readout values mentioned earlier in order to determine the net effect of the lysosomal stressor or the stress tolerance inducer on lysosomal physiology based on the changes in lysosomal pH, Cl^-, and membrane potential.

3.5.8. Confirmation of steady-state and mass balance.

For all of the aforementioned simulations, the final readout values were confirmed that they were steady-state values by performing the simulations for > 24 hours (simulation time). Furthermore, we confirmed that mass balance was attained for conditions where the thermodynamic limit of V-ATPase proton pump (up to 4.6 pH unit gradient)[61] was maintained across the lysosomal membrane.

3.5.9. 3D Data Visualization.

Multiple individual 2D datasets associated with the aforementioned parametric simulations performed to generate simultaneous inhibitions of various lysosomal parameters were obtained. The datasets associated with each simultaneous inhibitions of lysosomal parameters were exported from Berkeley Madonna and compiled into three separate matrices in an excel spreadsheet, such that the first rows and columns of the matrix correspond to the two parameters simultaneously varied in the model simulations to obtain the final lysosomal readout

values (lysosomal pH, Cl^-, and membrane potential), where each makes up the rest of the rows and columns of a single matrix. 3D surface plot of the matrix was generated using Sigmaplot®.

3.6. Results

Using a physiologically-based, mechanistic mathematical model of lysosomal ion transport regulation, we performed computational simulations to reveal how drug-induced variations in one or more ion transport mechanisms influenced lysosomal physiology, as captured by lysosomal pH, Cl^-, and membrane potential. To facilitate interpretation of these results, we separately considered lysosomal ion stressors and lysosomal morphology stressors. The earlier directly perturb lysosomal ion transportation, while the latter directly perturb lysosomal morphology. As elaborated in the following subsections, the effects of the aforementioned lysosomal stressors on lysosomal physiology were considered in the context of 1) biologically-determined variations in lysosomal morphology, 2) drug induced changes in lysosomal volume and surface area, 3) changes in lysosomal volume and surface area as may happen during endocytosis or exocytosis.

3.6.1. The effects of individual alteration of lysosomal proton and chloride transportation on lysosomal physiology

First, the effects of stress inducers that perturb lysosomal ion transporters (V-ATPase, CLC7, and membrane proton permeability) and ion content (cytoplasmic chloride) were studied in the context of a spherical lysosome (Fig. 3.2A). Among the stressors we modeled, maximum reduction in the number of V-ATPase molecule per lysosome induced significant physiological perturbation in a spherical lysosome, as evidenced by the changes in lysosomal pH and Cl^-

accumulation from their respective baseline values of 4.53 pH unit and 224.6 mM of an unperturbed lysosome (Fig. 3.2A). We observed a similar physiological perturbation following the modeling of the effect of increasing the lysosomal membrane proton permeability on lysosomal ion homeostasis (Fig. 3.2B). This indicates that lysosomal stressors that directly affect lysosomal proton level by perturbing either proton influx or efflux have similar effect not only on lysosomal pH, but also on lysosomal chloride homeostasis. To the contrary, CLC7 and cytoplasmic Cl^- stressors induced comparatively less perturbation to the overall lysosomal physiology (see Appendix Fig. B.1) as they only affected lysosomal pH and membrane potential when chloride transport or concentrations were completely abolished.

To understand how the same lysosomal ion stressors affect lysosomal ion homeostasis of different lysosomal morphologies, the lysosomal ion stressors were each varied along with lysosomal volume stressors that simultaneously reduced lysosomal radius and volume from an unperturbed lysosomal radius of 340 nm and a corresponding volume of 1.65×10^{-16} L, to 40 nm and 2.88×10^{-17} L, respectively. These dimensional changes capture the geometry of tubular lysosomes[57], which are narrower and more elongated than the typical, spherical lysosomes[44]. In spite of the lysosomal radius and volume differences, tubular lysosomes have the same surface area as spherical lysosomes. This assumption is reasonable because balance in cellular membrane material is maintained as a result of the regulation of membrane trafficking upon tubular lysosome mediated exocytosis of endocytosed material from the subcellular spherical lysosome to the plasma membrane. Notwithstanding, based on our results, the lysosomal ion stressors had similar effects on the physiology of tubular lysosome as they had on spherical lysosome, based on very similar changes in lysosomal pH, chloride, and membrane potential (Fig. 3.2).

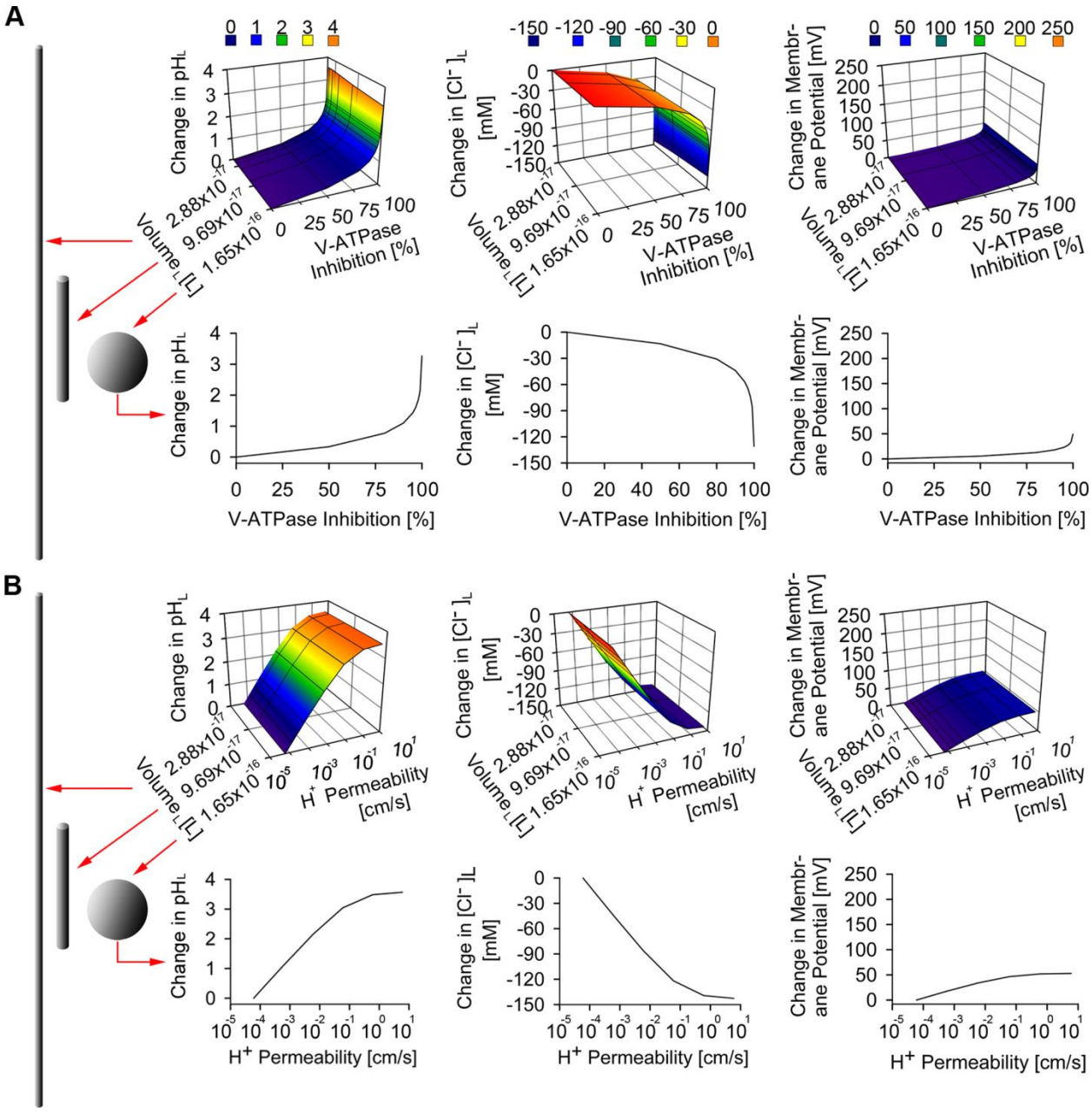

Figure 3.2 The effects of individual lysosomal ion stressors on spherical versus tubular lysosomal physiology.

(**A**) The effect of inhibiting the number of V-ATPase molecule per lysosome showed significant changes in lysosomal pH and Cl^-, with minimal change in membrane potential in both spherical and tubular lysosomes. (**B**) The effect of increasing proton-specific membrane permeability per lysosome showed significant changes in lysosomal pH and Cl^-, with minimal change in membrane potential in both spherical and tubular lysosomes. In both (**A**) and (**B**), only a slight difference is observed in the effect of the lysosomal ion stressors on spherical versus tubular lysosomal physiology.

3.6.2. The effects of lysosomal swelling on lysosomal ion homeostasis

Next, we modeled the effect of lysosomal swelling on lysosomal physiology by simultaneously increasing lysosomal radius and surface area while maintaining a fixed lysosomal volume of a spherical lysosomal morphology ($1.65x10^{-16}$ L in our model, baseline lysosome). Starting from a non-perturbed spherical lysosome (radius = 340 nm, surface area = $1.45x10^{-8}$ cm^2), the lysosomal radius and the corresponding surface area were expanded up to 10 μm and $6.28x10^{-6}$ cm^2 (433.3 fold change), respectively. Such lysosomal swelling led to changes in lysosomal pH, Cl^- accumulation, and membrane potential (Fig. 3.3A). Thus, lysosomal expansion compromised the maintenance of physiological lysosomal ion homeostasis, similar to that of V-ATPase inhibition and membrane proton permeabilization in tubular and spherical lysosomes (Fig. 3.2).

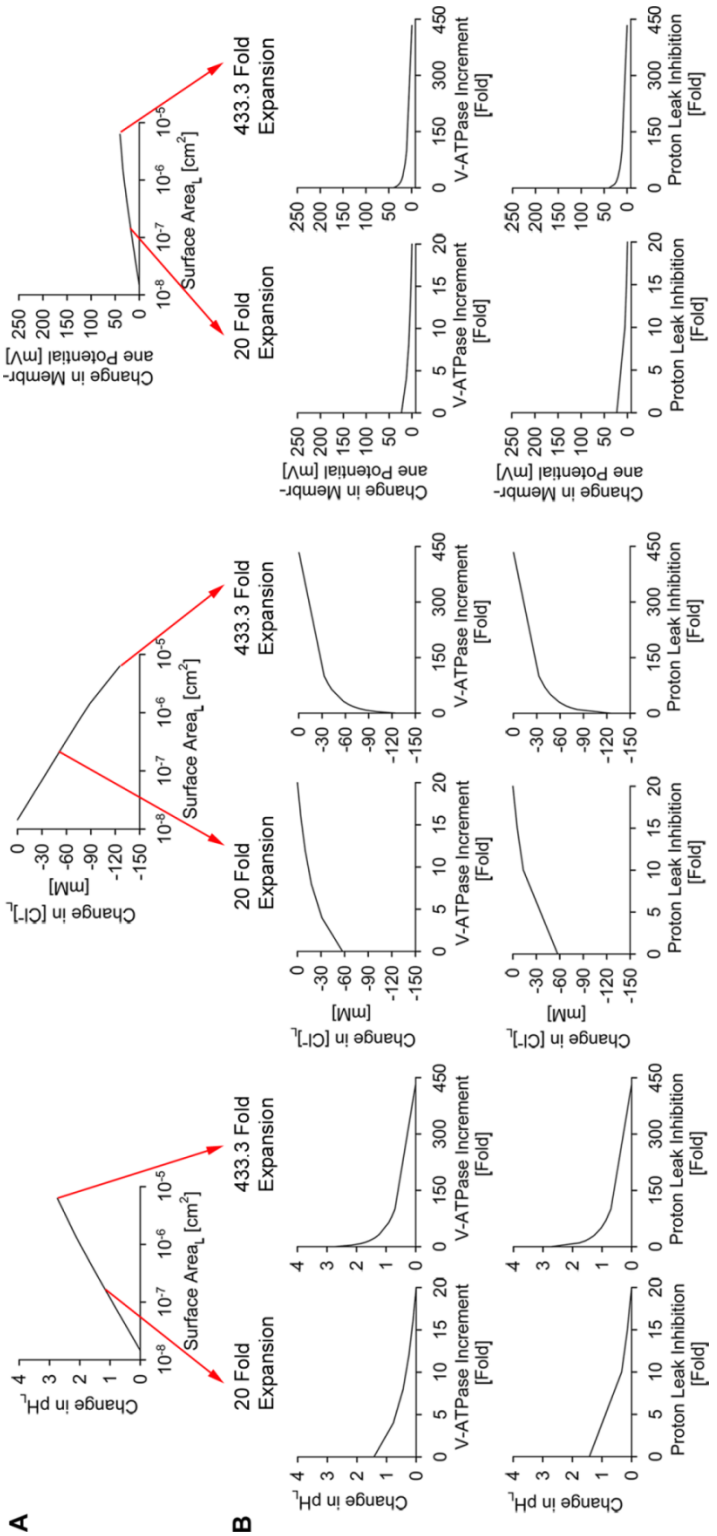

Figure 3.3 The effects of lysosomal surface expansion and associated stress tolerance on lysosomal physiology.

(**A**) Simultaneous increment in lysosomal radius and surface area, with a constant volume of $1.65x10^{-16}$ L induced progressive perturbation in lysosomal pH, Cl^-, and membrane potential. (**B**)

Individual effects of varying V-ATPase number and membrane proton permeability on the lysosomal physiology of surface area expansion-mediated lysosomal stress. Either increasing V-ATPase number or reducing membrane proton permeability reduces transient perturbations in lysosomal pH, Cl^-, and membrane potential following the simultaneous increment of lysosomal radius and surface area shown in (**A**).

3.6.3. The mechanisms of lysosomal stress tolerance in response to lysosomal swelling

To understand the mechanism by which cells can withstand stress generated from simultaneous lysosomal radius and surface area expansion, we identified V-ATPase numbers and membrane proton permeability as key parameters that mediate lysosomal stress tolerance; which we refer to as "lysosomal stress tolerance inducers". To illustrate this, V-ATPase number and membrane proton permeability were individually increased and decreased, respectively, 0 to 20 and 0 to 433.3 fold from their respective baseline input values. This was performed in order to maintain a constant number of proton influx and efflux mediated by V-ATPase and membrane proton permeability, respectively, for a given lysosomal surface area. We observed that physiological ion homeostasis was fully restored when either the number of V-ATPase molecules or the membrane proton permeability was kept proportional to the lysosomal surface area expansion at a fixed lysosomal volume of $1.65x10^{-16}$ L (Fig. 3.3B).

3.6.4. The effects of altering multiple lysosomal ion transport pathways on spherical, tubular, and disc-shaped lysosomal physiology

Next, we investigated the mechanism by which various combinations of lysosomal ion stressors exert their effects on the physiology of lysosomes with distinct morphology. Thus, we used different combinations of various ranges of lysosomal parameters to represent V-ATPase-CLC7 stressors, V-ATPase-cytoplasmic chloride stressors, V-ATPase -membrane proton permeability stressors, and CLC7-cytoplasmic chloride stressors. These stressor combinations

were simulated to study their effects on the physiology of spherical, tubular, and disc-shaped lysosomes. For all of the lysosomal morphologies, maximum alteration of either CLC7 or cytoplasmic chloride parameters in combination with alteration in either V-ATPase number or membrane proton permeability generally induced perturbation of lysosomal physiology due to the increment of membrane potential by up to > 250 mV (Figs. 3.4B, 3.5, and 3.6).

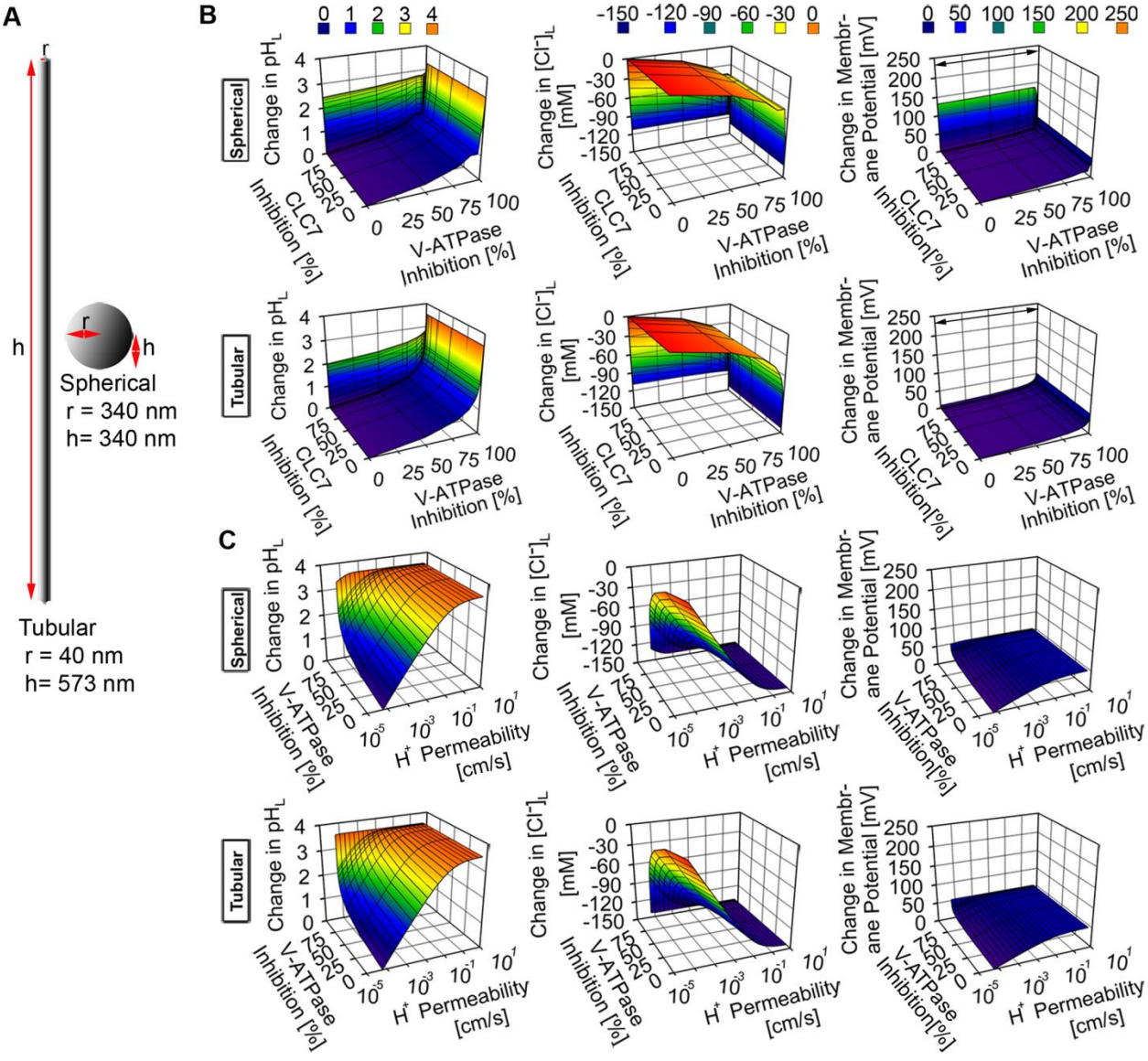

Figure 3.4. The effect of a combination of lysosomal ion stressors in spherical versus tubular lysosomes.

(**A**) Dimensions of tubular and spherical lysosomes. (**B**) The simultaneous inhibitions of V-ATPase and CLC7 numbers induced changes in both spherical and tubular lysosomes with minimal difference between the two lysosomal morphologies. The increment in V-ATPase inhibition induced the most significant change while only the complete depletion of CLC7 induced physiological perturbation which mainly arose from the significant change in membrane potential (> 250 mV, as indicated by the black arrow sign). (**C**) The simultaneous inhibition of V-ATPase and membrane proton permeabilization induced very similar and significant changes in the overall physiology of both spherical and tubular lysosomes.

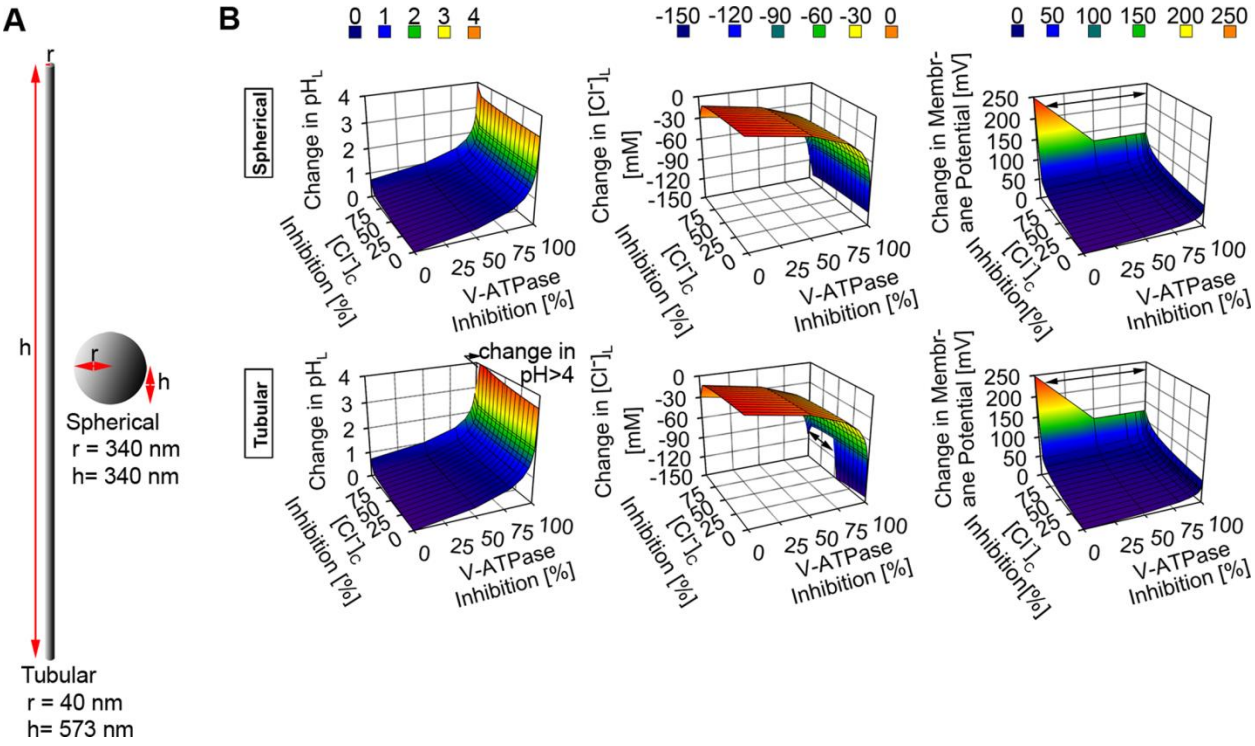

Figure 3.5 The effect of a simultaneous inhibition of the transport of chloride and proton ions in spherical versus tubular lysosomes.
(**A**) Dimensions of tubular and spherical lysosomes. (**B**) The simultaneous inhibitions of the cytoplasmic chloride and V-ATPase number per lysosome induced significant changes in lysosomal pH, Cl^-, and membrane potential. The effect was magnified in the tubular lysosome where the > 4 pH unit increment in lysosomal pH, > 150 mM reduction in lysosomal Cl^- accumulation, and > 250 mV increment in membrane potential were observed (as indicated by the black arrow signs).

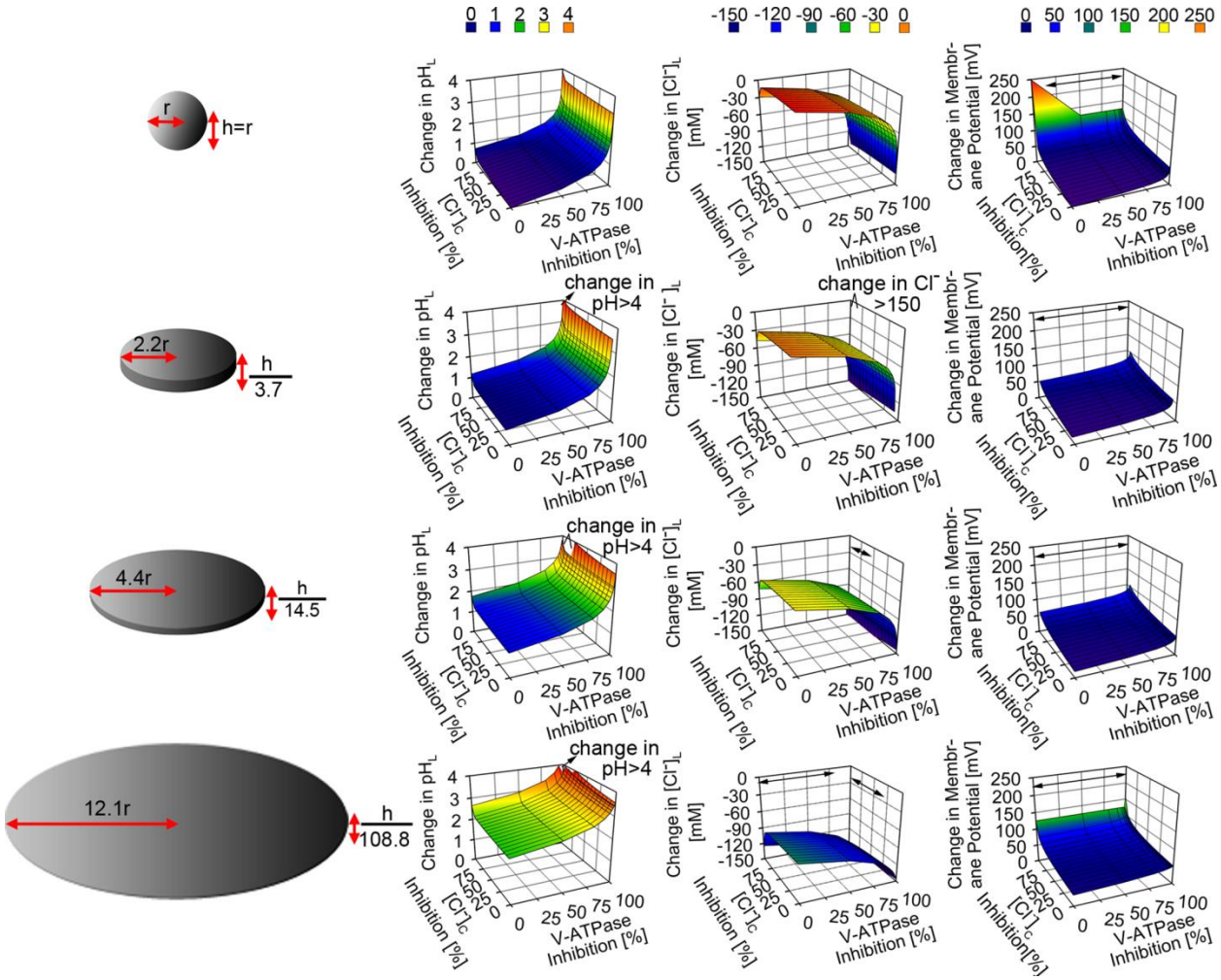

Figure 3.6 The effect of a simultaneous inhibition of proton and chloride transport in spherical versus various sized disc-shaped lysosomes.
The simultaneous inhibitions of the cytoplasmic chloride and V-ATPase number per lysosome induced significant changes in lysosomal pH, Cl^-, and membrane potential. The effect was more magnified in the disc-shaped lysosomes with lysosomal radius (> 2.2 fold) and height (< 3.7 fold) than in the spherical lysosome where the > 4 pH unit increment in lysosomal pH, > 150 mM reduction in lysosomal Cl^- accumulation, and > 250 mV increment in membrane potential were observed (as indicated by the black arrow signs).

Although such increment in membrane potential was associated with the increment in lysosomal pH and reduction in lysosomal chloride accumulation, greater perturbations in both variables were observed when at least either the V-ATPase number (Figs 3.4B, 3.4C, 3.5B, 3.6

and 3.7) or membrane proton permeability (Figs. 3.4C and 3.7), (see Appendix Figs. B.2 and B.3) were maximally altered from their respective baseline values.

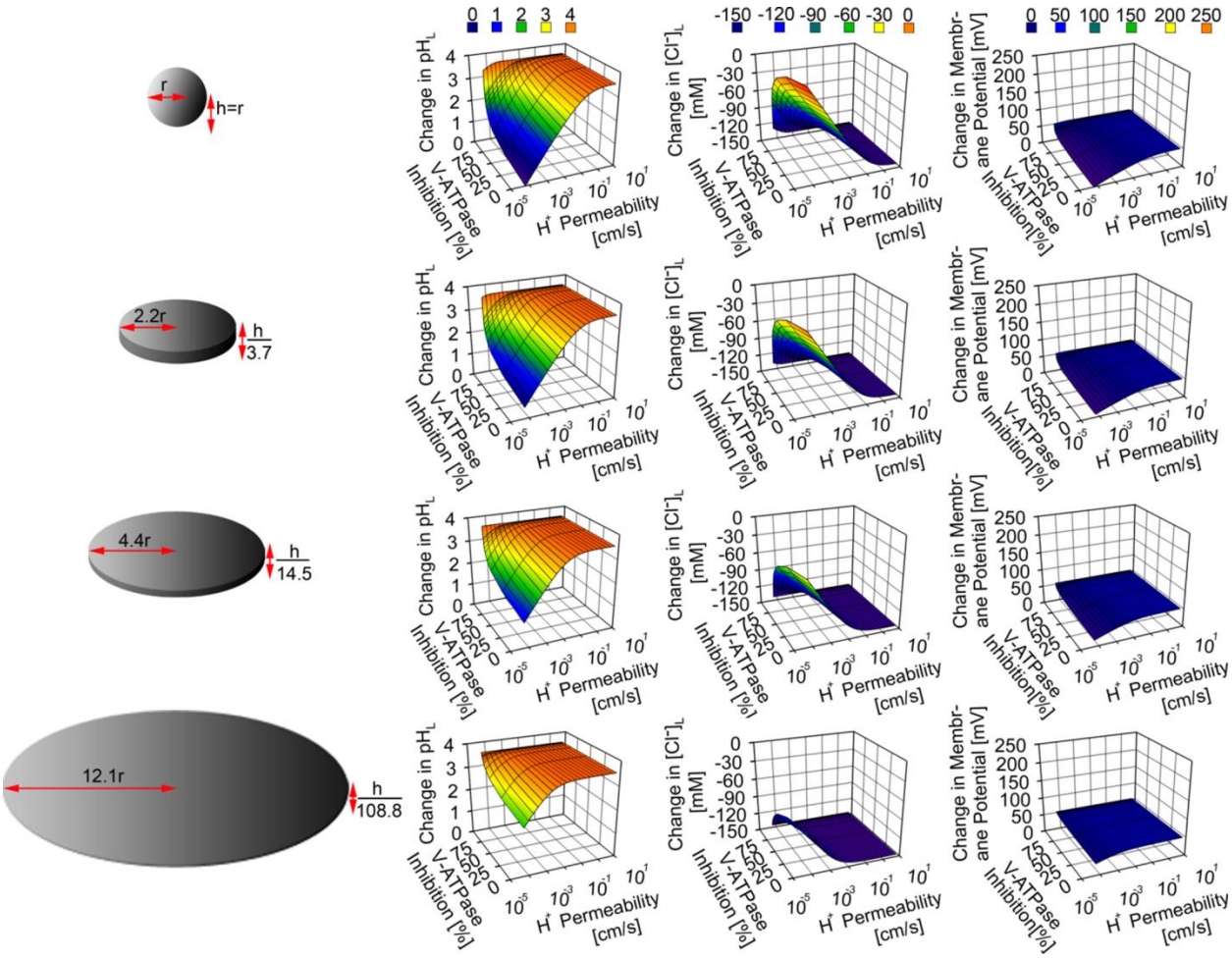

Figure 3.7 The effect of a simultaneous V-ATPase inhibition and membrane permeabilization in spherical versus various sized disc-shaped lysosomes.
The alterations of the V-ATPase number and membrane proton permeability per lysosome induced very similar changes to lysosomal pH, Cl^-, and membrane potential. For all of the disc-shaped lysosomes, as the lysosomal radius and height increased and decreased, respectively, more increment in the lysosomal pH, more reduction in the lysosomal Cl^- accumulation, and a slight increment in the lysosomal membrane potential were observed when there were no or very minimal alterations in both the V-ATPase number and membrane proton permeability, thus indicating the effect that the change in morphology alone has on lysosomal physiology.

Following the simultaneous reduction of both V-ATPase and CLC7 numbers, reduction of lysosomal chloride accumulation was observed to the extent of chloride efflux, in both spherical and tubular lysosomes (Fig. 3.4B). Beyond the perturbation of lysosomal chloride level, increment in lysosomal pH was also observed. Moreover, similar perturbation of lysosomal physiology was observed when the effect of the simultaneous alteration of membrane proton permeability and CLC7 number was simulated (see Appendix Fig. B.2). This indicates that the presence of lysosomal ion stressors, such as V-ATPase number and membrane proton permeability stressors which directly affect proton homeostasis, alone or in combination with lysosomal ion stressors, such as cytoplasmic Cl^- and CLC7 number stressors, which directly affect chloride homeostasis, perturb lysosomal physiology in a very similar manner.

Regardless of lysosomal morphology, perturbations of lysosomal pH, Cl^- and membrane potential were generally greatest when either V-ATPase number or membrane proton permeability was simultaneously lowered or increased, respectively, along with the lowering of cytoplasmic chloride concentration from baseline values (Figs. 3.5 and 3.6), and (see Appendix Fig. B.3). More specifically, the perturbations were greater in tubular (Fig. 3.5) and disc-shaped lysosomes with radial expansion > 2 fold (Fig. 3.6) than in spherical lysosome. When comparing whether V-ATPase number, membrane proton permeability, or cytoplasmic chloride level affected the aforementioned perturbation the most, it is evident that either the lowering of V-ATPase number or the increment of proton permeability similarly exerted more significant effect on lysosomal physiology (including the reduction in lysosomal chloride accumulation) than that of the lowering of cytoplasmic chloride concentration. This further corroborates the finding regarding the most significant role of net transmembrane proton flux on the regulation of lysosomal physiology.

3.7. Discussion

Here, a physiologically-based mathematical modeling approach was used to assess the toxicological effects of drugs on lysosomes. For this purpose, we simulated the effects of altering individual or multiple parameters controlling lysosomal morphology and ion regulation on the recovery of lysosomes from a transient perturbation. Related to this, different cell types are able to tolerate lysosomal stress to different extents. While lysosomes of different cell types are known to vary in size, shape, and the molecular transport phenomena responsible for maintaining lysosomal pH, membrane potential, and ion concentrations, computational modeling approach enables the probing of the effect of variations of specific parameters on lysosomal physiology in a manner that is difficult –if not impossible– to control with pharmacological experiments.

3.7.1. Simulation of cell-type dependent differences in lysosomal stress response

Variations in lysosomal morphology[62] and lysosomal protein expression[21] are manifested among different cell types. Our model simulations probed the mechanism by which such variations affected the cells' ability to maintain lysosomal physiology. In terms of lysosomal morphology, our findings indicate that cell types that either have tubular or spherical lysosomes have very similar physiological profile characterized by the observed similar changes in lysosomal pH, Cl^-, and membrane potential values following the introduction of various lysosomal ion stressors which induced the following lysosomal stresses: V-ATPase inhibition, CLC7 inhibition, cytoplasmic chloride inhibition, and membrane proton permeabilization. In spite of the difference in lysosomal volume between spherical and tubular lysosomal morphologies, as long as the lysosomal surface area is the same in both, their lysosomal physiology will only be dictated by the amount of active lysosomal V-ATPase and CLC7

proteins, and ion content, including cytoplasmic and lysosomal chloride and protons. Among the parameters that vary in a cell-type dependent manner, changes in the V-ATPase number and membrane proton permeability showed the most effect on lysosomal physiology as reflected by the significant changes in lysosomal pH, chloride, and membrane potential from their respective physiological baseline values. In contrast, alterations in CLC7 number and cytoplasmic chloride concentration had comparatively minimal effects on lysosomal physiology. This implies that the regulation of net proton transportation to and from the lysosome, for a given lysosomal surface area, plays a more significant role than that of net chloride transportation in the maintenance of lysosomal physiology.

Upon investigating the effect of simultaneously changing multiple, cell-type dependent lysosomal parameters, simulation results revealed that the degree of lysosomal physiology perturbation was mainly determined by changes in the V-ATPase number or membrane proton permeability. Moreover, varying either of these two parameters along with the level of cytoplasmic chloride resulted in distinct, lysosomal morphology-dependent perturbations of lysosomal pH, Cl^-, and membrane potential as the perturbation was heightened in tubular and disc shaped lysosomes. Tubular lysosomes are prevalent in cells with less lysosomal contents[44], whereas disc-shaped lysosomes are prevalent in cells with greater lysosomal content than that of spherical lysosomes[63-65]. Thus, our findings imply that cell types with tubular or disc-shaped lysosomes may be more prone to toxic effects of lysosomotropic agents, in comparison to cell types with spherical lysosomes.

3.7.2. Simulation of the effects of drugs on lysosomal physiology

Pharmacologically, various drugs can be used to disrupt lysosomal ion homeostasis, such as V-ATPase inhibitor, chloride channel inhibitor, membrane proton permeabilizer, and cytoplasmic chloride reducer[29,40,41,48,66,67]. Moreover, there are also drugs that induce changes to lysosomal morphology by either affecting lysosomal volume or surface area[39,43,44]. Thus, by modeling the effects of altering lysosomal parameters, we have obtained insights into the mechanism by which lysosomal stress inducing drugs affect the regulation of lysosomal pH, Cl^-, and membrane potential. Moreover, by altering various combinations of the lysosomal parameters, it is possible to obtain insights into the toxicological effects of drugs that exert pleiotropic effects on organelle ion homeostasis. Again, our results indicate that drugs that affect net proton flux across the lysosomal membrane, either by inhibiting the V-ATPase or by permeabilizing the lysosomal membrane to protons, exert the most significant perturbation to lysosomal physiology.

Of noteworthy significance, many lysosomotropic and cationic amphiphilic drugs[39] induce lysosomal volume expansion, which can profoundly alter lysosomal physiology in the absence of compensatory changes in either V-ATPase number or membrane proton permeability. In contrast to drugs that induce lysosomal vacuolation, drugs that reduce lysosomal volume do not exert significant physiological perturbations, as reflected by the minimum changes in lysosomal pH, Cl^-, and membrane potential. This emphasizes the necessity of regulation of net lysosomal proton flux dictated by the number of V-ATPase, membrane proton permeability, and lysosomal surface area.

In addition, our mathematical model predictions can be tailored to investigate the mechanism by which cell-death inducing lysosomal membrane permeabilizers (LMP) affect lysosomal physiology based on various factors, such as size of LMP agent, cell-type dependent

lysosomal size, and lysosomal ion content[68]. In the case where perturbed membrane proton permeability due to cholesterol imbalance is the causative agent for LMP-mediated cell death, the role of V-ATPase upregulation in lysosomal stress tolerance could be experimentally studied[69]. Alternatively, the role of cholesterol-mediated changes in the proton permeability of membranes could also be investigated in cells expressing varying V-ATPase levels.

3.7.3. Relationship between lysosomal morphology and stress response

In order to understand the mechanism by which lysosomal stress response is associated with lysosomal morphology[64], we altered various combinations of lysosomal ion parameters together with geometric parameters that determine lysosomal shape. Only under very specific conditions was there a distinctively different perturbation in the physiology of tubular lysosome versus spherical lysosome (Fig. 3.5). The perturbation of lysosomal physiology following the simultaneous presence of a membrane proton permeabilizer and a cytoplasmic chloride stressor can be associated with the cytotoxic phenomenon of LMP-mediated cytosolic acidification along with lysosomal alkalinization[68,70-72]. This mechanism may be relevant to the selective toxicity of lysosomotropic agents to cancer cells[73], because tubular lysosomes play a significant role in the shuttling of V-ATPase to the plasma membrane, which influences the survival and proliferation of cancer cells[40,66,74]. Moreover, this finding could shed light on the mechanism by which certain cationic amphiphilic drugs which destabilize lysosomal membrane induce anticancer effects[75].

3.7.4. Insights into how exocytosis, endocytosis, and cholesterol may affect lysosomal stress response

Based on our findings, even though exocytosis and endocytosis can affect changes in lysosomal volume and surface area, significant effects on lysosomal pH, membrane potential, and chloride regulation are only observed in the context of specific number of V-ATPases, membrane proton permeability, and cytoplasmic chloride level per lysosome. More specifically, the simultaneous inhibitions in V-ATPase number and cytoplasmic chloride resulted in high increment in lysosomal pH, reduction in lysosomal chloride accumulation, and increment in membrane potential (Figs. 3.5 and 3.6). Endocytosis or exocytosis affect lysosomal morphology through changes in membrane surface area, and hence could be linked to specific toxicological manifestations of lysosomotropic drugs (Fig. 3.6). The effect of endocytosis or exocytosis on lysosomal stress can be offset, either through V-ATPase upregulation or reduction in membrane proton permeability. Regulation of membrane proton permeability can be induced by cholesterol regulation. Because cholesterol transportation to and from the lysosomes is facilitated by Niemann-Pick type C1 (NPC1) proteins[76,77], these proteins themselves could also contribute to lysosomal stress response[78] during endocytosis or exocytosis.

3.7.5. Insights into the TFEB lysosomal stress response mechanism

Our finding suggests that V-ATPase expression plays a critical role in restoring lysosomal ion homeostasis following a transient perturbation. Transcription factor EB (TFEB) is a major transcriptional regulator of V-ATPase expression[79,80]. Thus, the upregulation of V-ATPase may be sufficient to explain how TFEB upregulation may confer resistance to perturbations of lysosomal physiology. Although previous findings have indicated that ions or channels involved in cation transport may explain how TFEB induces its role[79,80], appropriate interpretation of the experiments would depend on knowing any effects on the function of the V-

ATPase. This is especially important as there have been reports[43,81,82] showing TFEB mediated upregulation of lysosomal genes as a stress tolerance mechanism following the accumulation of weakly basic drugs. However, the induced stress tolerance may not necessarily be sufficient enough to restore full lysosomal function[81]. Thus, the extent of TFEB nuclear translocation and its transcriptional activity following lysosomal stress must be well understood in relation to the upregulation of V-ATPase expression. Indeed, additional cell growth regulators, such as mammalian target of rapamaycin (mTOR) complex 1 (mTORC1), which is associated with TFEB and V-ATPase regulation[34], could be investigated to quantify the relationship between TFEB nuclear translocation, V-ATPase expression, and amount and type of endocytosed or internalized lysosomal stress inducer.

3.8. Conclusion

To conclude, a mathematical model was used to probe the mechanistic determinants of drug induced lysosomal stress and stress resistance, in the presence of individual as well as combination of lysosomal stressors. By testing the effects of different parameters that determine organelle morphology and ion transport, the net proton flux with respect to lysosomal surface area emerged as the key parameter affecting lysosomal stress sensitivity and resistance. Accordingly, the expression levels of V-ATPase can act in concert with the regulation of membrane proton permeability to determine the differential sensitivity of different cell types to the toxic effects of lysosomotropic drugs.

3.7. Acknowledgment and contributions

In the adapted portions of this chapter from Woldemichael, T. and Rosania, G.R. (2017) *PLoS One*, 12(11): e0187627. doi: 10.1371/journal.pone.0187627:

This work was supported by National Institutes of Health grant R01GM078200 to GRR.
T.W.: Conceptualization, data curation, formal analysis, investigation, methodology, software, validation, visualization, writing- original draft, writing- review and editing.
G.R.R.: Conceptualization, funding acquisition, project administration, resources, supervision, validation, writing- original draft, writing- review and editing.

3.8. References

1 Padman, B. S., Bach, M., Lucarelli, G., Prescott, M. & Ramm, G. The protonophore CCCP interferes with lysosomal degradation of autophagic cargo in yeast and mammalian cells. *Autophagy* **9**, 1862-1875, doi:10.4161/auto.26557 (2013).

2 Shayman, J. A. & Abe, A. Drug induced phospholipidosis: an acquired lysosomal storage disorder. *Biochim Biophys Acta* **1831**, 602-611, doi:10.1016/j.bbalip.2012.08.013 (2013).

3 Nishino, I. *et al.* Primary LAMP-2 deficiency causes X-linked vacuolar cardiomyopathy and myopathy (Danon disease). *Nature* **406**, 906-910, doi:10.1038/35022604 (2000).

4 Berkovic, S. F. *et al.* Array-based gene discovery with three unrelated subjects shows SCARB2/LIMP-2 deficiency causes myoclonus epilepsy and glomerulosclerosis. *Am J Hum Genet* **82**, 673-684, doi:10.1016/j.ajhg.2007.12.019 (2008).

5 Siintola, E. *et al.* The novel neuronal ceroid lipofuscinosis gene MFSD8 encodes a putative lysosomal transporter. *Am J Hum Genet* **81**, 136-146, doi:10.1086/518902 (2007).

6 Carstea, E. D. *et al.* Niemann-Pick C1 disease gene: homology to mediators of cholesterol homeostasis. *Science* **277**, 228-231 (1997).

7 Rutsch, F. *et al.* Identification of a putative lysosomal cobalamin exporter altered in the cblF defect of vitamin B12 metabolism. *Nat Genet* **41**, 234-239, doi:10.1038/ng.294 (2009).

8 Graves, A. R., Curran, P. K., Smith, C. L. & Mindell, J. A. The Cl-/H+ antiporter ClC-7 is the primary chloride permeation pathway in lysosomes. *Nature* **453**, 788-792, doi:10.1038/nature06907 (2008).

9 Kiselyov, K. *et al.* TRPML: transporters of metals in lysosomes essential for cell survival? *Cell Calcium* **50**, 288-294, doi:10.1016/j.ceca.2011.04.009 (2011).

10 Orlowski, J. & Grinstein, S. Emerging roles of alkali cation/proton exchangers in organellar homeostasis. *Curr Opin Cell Biol* **19**, 483-492, doi:10.1016/j.ceb.2007.06.001 (2007).

11 Kasper, D. *et al.* Loss of the chloride channel ClC-7 leads to lysosomal storage disease and neurodegeneration. *EMBO J* **24**, 1079-1091, doi:10.1038/sj.emboj.7600576 (2005).

12 Quarello, P. *et al.* Severe malignant osteopetrosis caused by a GL gene mutation. *J Bone Miner Res* **19**, 1194-1199, doi:10.1359/JBMR.040407 (2004).

13 Pangrazio, A. *et al.* Mutations in OSTM1 (grey lethal) define a particularly severe form of autosomal recessive osteopetrosis with neural involvement. *J Bone Miner Res* **21**, 1098-1105, doi:10.1359/jbmr.060403 (2006).

14 Bach, G., Zeevi, D. A., Frumkin, A. & Kogot-Levin, A. Mucolipidosis type IV and the mucolipins. *Biochem Soc Trans* **38**, 1432-1435, doi:10.1042/BST0381432 (2010).

15 Slaugenhaupt, S. A. *et al.* Mapping of the mucolipidosis type IV gene to chromosome 19p and definition of founder haplotypes. *Am J Hum Genet* **65**, 773-778 (1999).

16 Bargal, R. *et al.* Identification of the gene causing mucolipidosis type IV. *Nat Genet* **26**, 118-123, doi:10.1038/79095 (2000).

17 Frattini, A. *et al.* Defects in TCIRG1 subunit of the vacuolar proton pump are responsible for a subset of human autosomal recessive osteopetrosis. *Nat Genet* **25**, 343-346, doi:10.1038/77131 (2000).

18 Kornak, U. *et al.* Mutations in the a3 subunit of the vacuolar H(+)-ATPase cause infantile malignant osteopetrosis. *Hum Mol Genet* **9**, 2059-2063 (2000).

19 Karet, F. E. *et al.* Mutations in the gene encoding B1 subunit of H+-ATPase cause renal tubular acidosis with sensorineural deafness. *Nat Genet* **21**, 84-90, doi:10.1038/5022 (1999).

20 Yang, Q., Li, G., Singh, S. K., Alexander, E. A. & Schwartz, J. H. Vacuolar H+ -ATPase B1 subunit mutations that cause inherited distal renal tubular acidosis affect proton pump assembly and trafficking in inner medullary collecting duct cells. *J Am Soc Nephrol* **17**, 1858-1866, doi:10.1681/ASN.2005121277 (2006).

21 Saftig, P. & Klumperman, J. Lysosome biogenesis and lysosomal membrane proteins: trafficking meets function. *Nat Rev Mol Cell Biol* **10**, 623-635, doi:10.1038/nrm2745 (2009).

22 Morissette, G., Lodge, R. & Marceau, F. Intense pseudotransport of a cationic drug mediated by vacuolar ATPase: procainamide-induced autophagic cell vacuolization. *Toxicol Appl Pharmacol* **228**, 364-377, doi:10.1016/j.taap.2007.12.031 (2008).

23 Logan, R., Funk, R. S., Axcell, E. & Krise, J. P. Drug-drug interactions involving lysosomes: mechanisms and potential clinical implications. *Expert Opin Drug Metab Toxicol* **8**, 943-958, doi:10.1517/17425255.2012.691165 (2012).

24 Tapper, H. & Sundler, R. Role of lysosomal and cytosolic pH in the regulation of macrophage lysosomal enzyme secretion. *Biochem J* **272**, 407-414 (1990).

25 Boya, P. *et al.* Lysosomal membrane permeabilization induces cell death in a mitochondrion-dependent fashion. *J Exp Med* **197**, 1323-1334, doi:10.1084/jem.20021952 (2003).

26 Zhao, H., Cai, Y., Santi, S., Lafrenie, R. & Lee, H. Chloroquine-mediated radiosensitization is due to the destabilization of the lysosomal membrane and subsequent induction of cell death by necrosis. *Radiat Res* **164**, 250-257 (2005).

27 Bruns, H. *et al.* Abelson tyrosine kinase controls phagosomal acidification required for killing of Mycobacterium tuberculosis in human macrophages. *J Immunol* **189**, 4069-4078, doi:10.4049/jimmunol.1201538 (2012).

28 Lange, P. F., Wartosch, L., Jentsch, T. J. & Fuhrmann, J. C. ClC-7 requires Ostm1 as a beta-subunit to support bone resorption and lysosomal function. *Nature* **440**, 220-223, doi:10.1038/nature04535 (2006).

29 Hara-Chikuma, M. *et al.* ClC-3 chloride channels facilitate endosomal acidification and chloride accumulation. *J Biol Chem* **280**, 1241-1247, doi:10.1074/jbc.M407030200 (2005).

30 Zhang, L., Sheng, R. & Qin, Z. The lysosome and neurodegenerative diseases. *Acta Biochim Biophys Sin (Shanghai)* **41**, 437-445 (2009).

31 Lee, J. H. *et al.* Lysosomal proteolysis and autophagy require presenilin 1 and are disrupted by Alzheimer-related PS1 mutations. *Cell* **141**, 1146-1158, doi:10.1016/j.cell.2010.05.008 (2010).

32 Ashoor, R., Yafawi, R., Jessen, B. & Lu, S. The contribution of lysosomotropism to autophagy perturbation. *PLoS One* **8**, e82481, doi:10.1371/journal.pone.0082481 (2013).

33 Settembre, C., Fraldi, A., Medina, D. L. & Ballabio, A. Signals from the lysosome: a control centre for cellular clearance and energy metabolism. *Nat Rev Mol Cell Biol* **14**, 283-296, doi:10.1038/nrm3565 (2013).

34 Pena-Llopis, S. *et al.* Regulation of TFEB and V-ATPases by mTORC1. *EMBO J* **30**, 3242-3258, doi:10.1038/emboj.2011.257 (2011).

35 Sardiello, M. *et al.* A gene network regulating lysosomal biogenesis and function. *Science* **325**, 473-477, doi:10.1126/science.1174447 (2009).

36 Sardiello, M. & Ballabio, A. Lysosomal enhancement: a CLEAR answer to cellular degradative needs. *Cell Cycle* **8**, 4021-4022 (2009).

37 Zeevi, D. A., Frumkin, A. & Bach, G. TRPML and lysosomal function. *Biochim Biophys Acta* **1772**, 851-858, doi:10.1016/j.bbadis.2007.01.004 (2007).

38 Li, X., Garrity, A. G. & Xu, H. Regulation of membrane trafficking by signalling on endosomal and lysosomal membranes. *J Physiol* **591**, 4389-4401, doi:10.1113/jphysiol.2013.258301 (2013).

39 Logan, R., Kong, A. C. & Krise, J. P. Time-dependent effects of hydrophobic amine-containing drugs on lysosome structure and biogenesis in cultured human fibroblasts. *J Pharm Sci* **103**, 3287-3296, doi:10.1002/jps.24087 (2014).

40 von Schwarzenberg, K. *et al.* Mode of cell death induction by pharmacological vacuolar H+-ATPase (V-ATPase) inhibition. *J Biol Chem* **288**, 1385-1396, doi:10.1074/jbc.M112.412007 (2013).

41 Xie, X. S. *et al.* Salicylihalamide A inhibits the V-0 sector of the V-ATPase through a mechanism distinct from bafilomycin A(1). *Journal of Biological Chemistry* **279**, 19755-19763, doi:10.1074/jbc.M313796200 (2004).

42 Verkman, A. S. & Galietta, L. J. Chloride channels as drug targets. *Nat Rev Drug Discov* **8**, 153-171, doi:10.1038/nrd2780 (2009).

43 Emanuel, R. *et al.* Induction of lysosomal biogenesis in atherosclerotic macrophages can rescue lipid-induced lysosomal dysfunction and downstream sequelae. *Arterioscler Thromb Vasc Biol* **34**, 1942-1952, doi:10.1161/ATVBAHA.114.303342 (2014).

44 Swanson, J., Burke, E. & Silverstein, S. C. Tubular lysosomes accompany stimulated pinocytosis in macrophages. *J Cell Biol* **104**, 1217-1222 (1987).

45 Dehay, B. *et al.* Pathogenic lysosomal depletion in Parkinson's disease. *J Neurosci* **30**, 12535-12544, doi:10.1523/JNEUROSCI.1920-10.2010 (2010).

46 Kirkegaard, T. *et al.* Hsp70 stabilizes lysosomes and reverts Niemann-Pick disease-associated lysosomal pathology. *Nature* **463**, 549-553, doi:10.1038/nature08710 (2010).

47 Repnik, U., Hafner Cesen, M. & Turk, B. Lysosomal membrane permeabilization in cell death: concepts and challenges. *Mitochondrion* **19 Pt A**, 49-57, doi:10.1016/j.mito.2014.06.006 (2014).

48 Zhang, G. J., Liu, H. W., Yang, L., Zhong, Y. G. & Zheng, Y. Z. Influence of membrane physical state on the lysosomal proton permeability. *J Membr Biol* **175**, 53-62 (2000).

49 Goldman, A. *et al.* The Na+/H+ exchanger controls deoxycholic acid-induced apoptosis by a H+-activated, Na+-dependent ionic shift in esophageal cells. *PLoS One* **6**, e23835, doi:10.1371/journal.pone.0023835 (2011).

50 Ishida, Y., Nayak, S., Mindell, J. A. & Grabe, M. A model of lysosomal pH regulation. *J Gen Physiol* **141**, 705-720, doi:10.1085/jgp.201210930 (2013).

51 Grabe, M. & Oster, G. Regulation of organelle acidity. *J Gen Physiol* **117**, 329-344 (2001).

52 Van Dyke, R. W. Acidification of rat liver lysosomes: quantitation and comparison with endosomes. *Am J Physiol* **265**, C901-917 (1993).

53 Gambale, F., Kolb, H. A., Cantu, A. M. & Hedrich, R. The Voltage-Dependent H+-Atpase of the Sugar-Beet Vacuole Is Reversible. *Eur Biophys J Biophy* **22**, 399-403 (1994).

54 Heuser, J., Zhu, Q. & Clarke, M. Proton pumps populate the contractile vacuoles of Dictyostelium amoebae. *J Cell Biol* **121**, 1311-1327 (1993).

55 Sonawane, N. D., Thiagarajah, J. R. & Verkman, A. S. Chloride concentration in endosomes measured using a ratioable fluorescent Cl- indicator - Evidence for chloride accumulation during acidification. *Journal of Biological Chemistry* **277**, 5506-5513, doi:10.1074/jbc.M110818200 (2002).

56 Boyle, J. Molecular biology of the cell, 5th edition by B. Alberts, A. Johnson, J. Lewis, M. Raff, K. Roberts, and P. Walter. *Biochemistry and Molecular Biology Education* **36**, 317-318, doi:10.1002/bmb.20192 (2008).

57 Knapp, P. E. & Swanson, J. A. Plasticity of the tubular lysosomal compartment in macrophages. *J Cell Sci* **95 (Pt 3)**, 433-439 (1990).

58 Agarwal, R. *et al.* Mammalian cells preferentially internalize hydrogel nanodiscs over nanorods and use shape-specific uptake mechanisms. *Proc Natl Acad Sci U S A* **110**, 17247-17252, doi:10.1073/pnas.1305000110 (2013).

59 Doshi, N., Zahr, A. S., Bhaskar, S., Lahann, J. & Mitragotri, S. Red blood cell-mimicking synthetic biomaterial particles. *Proc Natl Acad Sci U S A* **106**, 21495-21499, doi:10.1073/pnas.0907127106 (2009).

60 Mitragotri, S. & Lahann, J. Physical approaches to biomaterial design. *Nat Mater* **8**, 15-23, doi:10.1038/nmat2344 (2009).

61 Grabe, M., Wang, H. & Oster, G. The mechanochemistry of V-ATPase proton pumps. *Biophys J* **78**, 2798-2813, doi:10.1016/S0006-3495(00)76823-8 (2000).

62 Alberts B, J. A., Lewis J, Raff M, Roberts K, Walter P. Molecular Biology of the Cell. 4th edition. New York: Garland Science; 2002. Transport into the Cell from the Plasma Membrane: Endocytosis. Available from: https://www.ncbi.nlm.nih.gov/books/NBK26870/.

63 Strausbauch, P. & Sehgal, N. Three-dimensional reconstruction of anomalous beige mouse macrophage lysosomes. *J Leukoc Biol* **46**, 441-449 (1989).

64 Lüllmann-Rauch, R. in *Lysosomes* 1-16 (Springer US, 2005).

65 Ohkuma, S. & Poole, B. Cytoplasmic vacuolation of mouse peritoneal macrophages and the uptake into lysosomes of weakly basic substances. *J Cell Biol* **90**, 656-664 (1981).

66 Hosogi, S., Kusuzaki, K., Inui, T., Wang, X. & Marunaka, Y. Cytosolic chloride ion is a key factor in lysosomal acidification and function of autophagy in human gastric cancer cell. *J Cell Mol Med* **18**, 1124-1133, doi:10.1111/jcmm.12257 (2014).

67 Nyman, J. K. & Vaananen, H. K. A rationale for osteoclast selectivity of inhibiting the lysosomal V-ATPase a3 isoform. *Calcif Tissue Int* **87**, 273-283, doi:10.1007/s00223-010-9395-7 (2010).

68 Johansson, A. C. *et al.* Regulation of apoptosis-associated lysosomal membrane permeabilization. *Apoptosis* **15**, 527-540, doi:10.1007/s10495-009-0452-5 (2010).

69 Bourdenx, M. *et al.* Nanoparticles restore lysosomal acidification defects: Implications for Parkinson and other lysosomal-related diseases. *Autophagy* **12**, 472-483, doi:10.1080/15548627.2015.1136769 (2016).

70 Nilsson, C., Johansson, U., Johansson, A. C., Kagedal, K. & Ollinger, K. Cytosolic acidification and lysosomal alkalinization during TNF-alpha induced apoptosis in U937 cells. *Apoptosis* **11**, 1149-1159, doi:10.1007/s10495-006-7108-5 (2006).

71 Boya, P. & Kroemer, G. Lysosomal membrane permeabilization in cell death. *Oncogene* **27**, 6434-6451, doi:10.1038/onc.2008.310 (2008).

72 Deng, D., Jiang, N., Hao, S. J., Sun, H. & Zhang, G. J. Loss of membrane cholesterol influences lysosomal permeability to potassium ions and protons. *Biochim Biophys Acta* **1788**, 470-476, doi:10.1016/j.bbamem.2008.11.018 (2009).

73 Dielschneider, R. F. *et al.* Lysosomotropic agents selectively target chronic lymphocytic leukemia cells due to altered sphingolipid metabolism. *Leukemia* **30**, 1290-1300, doi:10.1038/leu.2016.4 (2016).

74 Graham, R. M., Thompson, J. W. & Webster, K. A. Inhibition of the vacuolar ATPase induces Bnip3-dependent death of cancer cells and a reduction in tumor burden and metastasis. *Oncotarget* **5**, 1162-1173, doi:10.18632/oncotarget.1699 (2014).

75 Petersen, N. H. *et al.* Transformation-associated changes in sphingolipid metabolism sensitize cells to lysosomal cell death induced by inhibitors of acid sphingomyelinase. *Cancer Cell* **24**, 379-393, doi:10.1016/j.ccr.2013.08.003 (2013).

76 Butler, J. D., Vanier, M. T. & Pentchev, P. G. Niemann-Pick C disease: cystine and lipids accumulate in the murine model of this lysosomal cholesterol lipidosis. *Biochem Biophys Res Commun* **196**, 154-159, doi:10.1006/bbrc.1993.2228 (1993).

77 te Vruchte, D. *et al.* Accumulation of glycosphingolipids in Niemann-Pick C disease disrupts endosomal transport. *J Biol Chem* **279**, 26167-26175, doi:10.1074/jbc.M311591200 (2004).

78 Parks, A. & Marceau, F. Lysosomotropic cationic drugs induce cytostatic and cytotoxic effects: Role of liposolubility and autophagic flux and antagonism by cholesterol ablation. *Toxicol Appl Pharmacol* **305**, 55-65, doi:10.1016/j.taap.2016.06.006 (2016).

79 Wang, W. *et al.* Up-regulation of lysosomal TRPML1 channels is essential for lysosomal adaptation to nutrient starvation. *Proc Natl Acad Sci U S A* **112**, E1373-1381, doi:10.1073/pnas.1419669112 (2015).

80 Samie, M. A. & Xu, H. Lysosomal exocytosis and lipid storage disorders. *J Lipid Res* **55**, 995-1009, doi:10.1194/jlr.R046896 (2014).

81 Lu, S., Sung, T., Lin, N., Abraham, R. T. & Jessen, B. A. Lysosomal adaptation: How cells respond to lysosomotropic compounds. *PLoS One* **12**, e0173771, doi:10.1371/journal.pone.0173771 (2017).

82 Moruno-Manchon, J. F. *et al.* TFEB ameliorates the impairment of the autophagy-lysosome pathway in neurons induced by doxorubicin. *Aging (Albany NY)* **8**, 3507-3519, doi:10.18632/aging.101144 (2016).

Chapter 4: Investigating How Phagosome Maturation Influences Phase-Transition-Dependent Biocrystal Biocompatibility

4.1. Introduction

Phase transition of drugs is one of the major factors that account for lack of well-defined pharmacokinetic properties of drugs in the drug development and discovery processes[1-3]. Given most drugs in development are weak base compounds[4], the phase-transition properties of such molecules must be well understood. It is well known that weak base compounds precipitate out of solution depending on the pH of the environment[5]. Indeed, the phase-transition properties of weak base compounds and their salt forms can be investigated using the well-established pH-dependent drug solubility studies[6]. Briefly, the total drug solubility is comprised of both the free base and the ionized form of the drug, and depending on the pH of the solution in relation to the pH_{max} (which is defined as the pH where both the free base and salt forms of the drug are in the solid phase), either the free base or the salt form precipitates out of solution. At high pH (relative to the pH_{max}), the free base precipitates out of solution, and the total drug solubility is primarily dictated by the solubility of the ionized drug in solution. To the contrary, at low pH (relative to the pH_{max}), the salt form precipitates out of solution and is further stabilized by the presence of counter-ions in the media through a common-ion effect[7].

Although most research focus in drug development and accumulation gravitate towards understanding the phase transition properties of one form of a drug, i.e. the precipitation of the free base or the salt form of a drug, the phase-transition properties of both forms must be well

understood. While the precipitation of free base drugs is well known to occur at high pH, such as the pH of the intestine[2,5], the stability and effects of the ionized drug once it is in a low pH environment, such as the lysosome, is not well known[8]. Thus, the phase-transition of weak base drugs with respect to cellular conditions must be well understood. Indeed, the dynamics of the cellular environment as well as the lack of experimental techniques that can detect and measure subcellular accumulation of different forms of a given drug makes this pursuit rather challenging. Thus, to overcome this barrier, various mathematical models have been devised over the years. However, these models treat cellular drug accumulation process as a separate phenomenon from the phase transition properties of the drug itself in relation to its cellular environment.

Thus, we adapt a mathematical model previously published from our lab[9] in order to investigate the cellular and subcellular accumulation of the free base and ionized forms of a model, weak base drug molecule known as clofazimine (CFZ). Moreover, using the steady-state concentration of both drug species in the non-membrane environments, we determine the accumulation of the drug species in cell membrane, mitochondrial membrane, and lysosomal membrane. In addition, using the physicochemical properties of the free base and hydrochloride salt forms of CFZ, which were obtained from mathematical fitting of wet lab pH-solubility studies (Chapter 2), we determine the degree of supersaturation, which is a prerequisite for the precipitation of drug species, in all of the cellular compartments.

4.2. Materials and Methods

4.2.1. Weak base drug species.

Following the laws of mass balance, the total activity of an ionizable weak base drug is the sum of the activities of both the neutral and ionized forms of the drug:

$$a_T = a_n + a_d \quad (1)$$

Where a is the activity of the weak base drug molecule, and the subscripts T, n, and d denote the total, neutral, and ionized weak base drug molecules, respectively.

The activities of the neutral and ionized weak base drug species are related to each other according to the pK_a of the drug molecule and the pH of its environment:

$$a_d = a_n \times 10^{pK_a - pH} \quad (2)$$

Moreover, the activity of the neutral drug molecule (a_n) can be related to the total drug concentration (C_T) according to the following relationship:

$$f_n = \frac{a_n}{C_T} = \frac{1}{\frac{W}{\gamma_n} + \frac{K_n}{\gamma_n} + \frac{W \times 10^{pK_a - pH}}{\gamma_d} + \frac{K_d \times 10^{pK_a - pH}}{\gamma_d}} \quad (3)$$

Where W is the volumetric water fraction, γ is the activity coefficient, and K is the sorption coefficient of the drug species.

Similarly, the activity of the ionized drug molecule (a_d) can be related to the total drug concentration (C_T) according to the following relationship:

$$f_d = \frac{a_d}{C_T} = f_n \times 10^{pK_a - pH} \quad (4)$$

For both the neutral and ionized drug species, the sorption coefficient of the drug species depends on both the lipid content of the subcellular compartment the drug partitions into, and the lipophilicity of the drug molecule itself:

$$K = L \times 1.22 \times K_{ow} \quad (5)$$

Where L is the lipid fraction of a given subcellular compartment, and K_{ow} is the octanol/water partition coefficient of the drug molecule.

4.2.2. Governing equations for cellular drug accumulation.

In order to calculate phase-transition-dependent drug concentration in different cellular compartments, we first adapted a mathematical model[9], which enables us to calculate the time-dependent subcellular drug concentration. The time-dependent subcellular accumulation of the unionized weak base drug concentration was modeled using Fick's First Law of Diffusion, assuming passive diffusion of the drug molecule across a given biological membrane:

$$J = P_n \times (a_{n,0} - a_{n,1}) \quad (6)$$

Where J is the flux of the drug molecule down its concentration gradient from compartment (0) to compartment (1) across a biological membrane and P_n is the membrane permeability of the neutral drug molecule.

We can rewrite equation (6) by accounting for the relationship of neutral drug activity and total drug concentration provided in equation (3) as follows:

$$J = P_n \times (f_{n,0} \times C_{T,0} - f_{n,1} \times C_{T,1}) \quad (7)$$

Moreover, the time-dependent cellular and subcellular accumulation of the ionized weak base drug was modeled using the Nernst-Planck equation[10], assuming a linear potential gradient across the membrane:

$$J = P_d \times Y \times Z \times \frac{a_{d,0} - a_{d,1} \times e^{Y \times Z}}{e^{Y \times Z} - 1} \quad (8)$$

Where P_d is the membrane permeability of the ionized drug molecule, Z is the valence of the ion (+1 for monoprotic weak base), $Y = \Psi F/RT$, where F is Faraday's constant, T is absolute temperature, R is universal gas constant, Ψ is membrane potential and the following sign convention is used: Ψ is more positive or negative if there is more cation or anion, respectively, in the external compartment than in the internal compartment.

Thus, by combining equations (7 and 8), the total drug molecule flux can be written as follows:

$$J = P_n \times \left(f_{n,0} \times C_{T,0} - f_{n,1} \times C_{T,1}\right) + P_d \times Y \times Z \times \frac{f_{d,0} \times C_{T,0} - f_{d,1} \times C_{T,1} \times e^{Y \times Z}}{e^{Y \times Z} - 1} \quad (9)$$

More specifically, the total drug molecule flux from i) the extracellular to the cytoplasm (equation 10), ii) the cytoplasm to subcellular organelles, such as mitochondria (equation 11) and lysosome (equation 12) can be represented as follows:

$$J_{E,C} = P_n \times \left(f_{n,E} \times C_{T,E} - f_{n,C} \times C_{T,C}\right) + P_d \times Y \times Z \times \frac{f_{d,E} \times C_{T,E} - f_{d,C} \times C_{T,C} \times e^{Y \times Z}}{e^{Y \times Z} - 1} \quad (10)$$

$$J_{C,M} = P_n \times \left(f_{n,C} \times C_{T,C} - f_{n,M} \times C_{T,M}\right) + P_d \times Y \times Z \times \frac{f_{d,C} \times C_{T,C} - f_{d,M} \times C_{T,M} \times e^{Y \times Z}}{e^{Y \times Z} - 1} \quad (11)$$

$$J_{C,L} = P_n \times \left(f_{n,C} \times C_{T,C} - f_{n,L} \times C_{T,L}\right) + P_d \times Y \times Z \times \frac{f_{d,C} \times C_{T,C} - f_{d,L} \times C_{T,L} \times e^{Y \times Z}}{e^{Y \times Z} - 1} \quad (12)$$

Where subscripts e, c, m, and l represent the extracellular, cytoplasm, mitochondria, and lysosome.

Using the above specific flux descriptions, the time-dependent changes of total drug concentrations in the different compartments can be modeled using the following equations:

$$\frac{dC_C}{dt} = \frac{S_C \times J_{E,C}}{V_C} - \frac{S_M \times J_{C,M}}{V_C} - \frac{S_L \times J_{C,L}}{V_C} \quad (13)$$

$$\frac{dC_M}{dt} = \frac{S_M \times J_{C,M}}{V_M} \quad (14)$$

$$\frac{dC_L}{dt} = \frac{S_L \times J_{C,L}}{V_L} \quad (15)$$

Where each flux term is multiplied by S, membrane surface area, in order to obtain the total amount of drug transported across the total area of a given membrane (i.e. cell membrane, mitochondria membrane or lysosomal membrane), V is the volume of a given compartment used to convert the units of drug molecule from mol/s to Molar/second.

4.2.3. Defining membrane partition coefficient of a drug.

Membrane permeability of a drug molecule is given by the following relationship:

$$P = \frac{D \times K}{l} \quad (16)$$

Where D is the diffusion coefficient of the drug molecule, K is the partition coefficient of the drug molecule, and for our purpose, we specifically focused on biological membrane partition coefficient of the drug molecule as described below, and l is the thickness of the biological membrane.

In order to estimate the biological membrane partition coefficient of the neutral drug, we used the following equation[11]:

$$\log K_{m,n} = 0.33 \times \log K_{ow,n} + 2.2 \quad (17)$$

Where $K_{m,n}$ is the biological membrane partition coefficient of the neutral drug molecule, and $K_{ow,n}$ is the octanol/water partition coefficient of the neutral drug molecule.

Similarly, we have the following relationship for the biological membrane partition coefficient of the ionized weak base drug[11]:

$$\log K_{m,d} = 0.37 \times \log K_{ow,d} + 2 \quad (18)$$

Where $K_{m,d}$ is the biological membrane partition coefficient of the ionized drug molecule, and $K_{ow,d}$ is the octanol/water partition coefficient of the ionized drug molecule, which can be determined from the octanol/water partition coefficient of the neutral drug molecule based on the following equation[10]:

$$\log K_{ow,d} = \log K_{ow,n} - 3.7 \quad (19)$$

4.2.4. Numerical analysis.

Equations (13-15) were solved by numerical integration in Virtual Cell® using combined stiff solver as a numerical integrator.

4.2.5. Determining concentration of weak base drug species.

The total drug concentration obtained from model simulation is comprised of the concentration of the neutral and ionized forms of the drug:

$$C_T = [B] + [BH^+] \quad (20)$$

Where C_T is the total drug concentration, [B] is the concentration of the neutral drug, and $[BH^+]$ is the concentration of the ionized drug.

Thus, using equation (20) and the Henderson-Hasselbach equation (equation 21), we calculated the concentrations of the neutral and ionized forms of the weak base drug from the total drug concentration in the extracellular, cytoplasm, mitochondria, and lysosome:

$$\mathrm{pH} - \mathrm{p}K_a = \log \frac{[B]}{[BH^+]} \quad (21)$$

Moreover, the steady-state drug concentrations in the non-membrane environments, such as the extracellular, cytoplasm, mitochondria, and lysosome were used to calculate the steady-state drug concentration in the biological membranes, such as the cell membrane, mitochondrial membrane, and lysosomal membrane, assuming that each biological membrane can serve as a micellar surfactant[12]:

$$K_{m,n} = \frac{[B]_{m,ss}}{[B]_{nm,ss}} \quad (22)$$

Where $K_{m,n}$ is the biological membrane partition coefficient of the neutral drug, $[B]_{m,ss}$ is the steady-state concentration of the neutral drug in a membrane, and $[B]_{nm,ss}$ is the steady-state concentration of the neutral drug in a non-membrane environment.

Thus, we can derive the following equations from equation (22) to calculate the steady-state concentration of the neutral drug in the cell membrane, mitochondrial membrane, and lysosomal membrane:

$$[B]_{cm,ss} = \left(K_{cm,n\_e} \times [B]_{E,ss}\right) + \left(K_{cm,n\_i} \times [B]_{C,ss}\right) \quad (23)$$

$$[B]_{mm,ss} = \left(K_{mm,n\_e} \times [B]_{C,ss}\right) + \left(K_{mm,n\_i} \times [B]_{M,ss}\right) \quad (24)$$

$$[B]_{lm,ss} = \left(K_{lm,n\_e} \times [B]_{C,ss}\right) + \left(K_{lm,n\_i} \times [B]_{L,ss}\right) \quad (25)$$

Where subscripts cm, mm, and lm refer to cell membrane, mitochondrial membrane, and lysosomal membrane, respectively; subscript ss refers to the drug concentration at steady state; subscripts e and i refer to external and internal leaflets of each membrane, which account for the effect of asymmetric membrane lipid distribution[13-15] on membrane drug concentration.

Similarly, we can derive the following equations to calculate the steady-state concentration of the ionized drug in the cell membrane, mitochondrial membrane, and lysosomal membrane:

$$[BH^+]_{cm,ss} = \left(K_{cm,d\_e} \times [BH^+]_{E,ss}\right) + \left(K_{cm,d\_i} \times [BH^+]_{C,ss}\right) \quad (26)$$

$$[BH^+]_{mm,ss} = \left(K_{mm,d\_e} \times [BH^+]_{C,ss}\right) + \left(K_{mm,d\_i} \times [BH^+]_{M,ss}\right) \quad (27)$$

$$[BH^+]_{lm,ss} = \left(K_{lm,d\_e} \times [BH^+]_{C,ss}\right) + \left(K_{lm,d\_i} \times [BH^+]_{L,ss}\right) \quad (28)$$

4.2.6. Determining the phase transition of drug species.

Drug concentration above thermodynamic drug solubility leads to supersaturation[5]. Thus, using experimentally determined thermodynamic solubility value of the free base drug, we can calculate the degree of supersaturation (DS) of the free base as follows[5]:

$$DS = \frac{[B]}{[B]_s} \quad (29)$$

Where [B] is the free base drug concentration, and $[B]_s$ is the thermodynamic solubility of the free base drug, also known as intrinsic free base solubility.

Similarly, we have the following relationship to calculate the degree of supersaturation for the salt form of the drug:

$$DS = \frac{[BH^+] \times [Cl^-]}{K_{sp}} \quad (30)$$

Where K_{sp} is the solubility product of the salt form of the drug, $[BH^+]$ is the dissolved concentration of the ionized drug, and $[Cl^-]$ is the chloride concertation that interacts with the ionized drug through ion-ion interaction, producing the salt form of the drug.

Table 4.1. Cellular drug accumulation model parameters

Symbol	Description	Value	Units
init $C_{T,E}$	Initial total extracellular drug concentration	10	μM
init $C_{T,C}$	Initial total cytoplasmic drug concentration	0	μM
init $C_{T,M}$	Initial total mitochondrial drug concentration	0	μM
init $C_{T,L}$	Initial total lysosomal drug concentration	0	μM
init $C_{T,CM}$	Initial total cell membrane drug concentration	0	μM
init $C_{T,MM}$	Initial total mitochondrial membrane drug concentration	0	μM
init $C_{T,LM}$	Initial total lysosomal membrane drug concentration	0	μM
$pK_{a'}$	Apparent pK_a	6.08	
$[B]_S$	Intrinsic free base solubility	0.48	μM
K_{sp}	Salt solubility product	332.3	μM^2
$[Cl^-]_L$	Lysosomal chloride concentration	110	mM
pH_E	Extracellular pH	7.4	
pH_C	Cytoplasmic pH	7.2	
pH_M	Mitochondrial pH	8	
pH_L	Lysosomal pH	4.5	
$\log K_{ow,n}$	Octanol/water partition coefficient of unionized weak base	7.66	
L_E	Extracellular lipid fraction	0	
L_C	Cytoplasmic lipid fraction	0.05	
L_M	Mitochondrial lipid fraction	0.05	
L_L	Lysosomal lipid fraction	0.05	
W_E	Extracellular water fraction	1	
W_C	Cytoplasmic water fraction	0.95	

W_M	Mitochondrial water fraction	0.95	
W_L	Lysosomal water fraction	0.95	
γ_n*	Activity coefficient of unionized drug	1	
γ_d*	Activity coefficient of ionized drug	0.74	
Ψ_{CM}	Cell membrane potential	-70	mV
Ψ_{MM}	Mitochondrial membrane potential	-160	mV
Ψ_{LM}	Lysosomal membrane potential	10	mV
V_E	Extracellular volume	1.00E-04	L
D_C	Cytoplasmic diameter	12.4	μm
D_M	Mitochondrial diameter	5.76	μm
D_L	Lysosomal diameter	5.76	μm

* activity coefficients of unionized and ionized molecules were obtained from the literature[16]. The physicochemical properties were obtained from experimental data fitting elaborated in Chapter 2 for CFZ free base and CFZ-H^+Cl^- salt. The diameters of the cellular compartments were used to calculate volume and surface area, assuming spherical geometry. The effect of asymmetric membrane lipid distribution[13-15] on drug membrane partition coefficient was accounted for based on literature values[17,18].

4.3. Results

4.3.1. Intracellular accumulation of drug species

We used clofazimine (CFZ) as a model drug to predict its subcellular phase-transition dependent accumulation. CFZ is a poorly soluble, weak base drug molecule with two predicted ionizable groups (p$K_{a,1}$ = 2.31 and p$K_{a,2}$ = 9.29). It is known to form crystal like drug inclusions (CLDIs), which are composed of hydrochloride salts of the weak base (CFZ-H^+Cl^-), in mice and humans. Thus, using predetermined physicochemical properties of the free base as well as the salt form of the drug (Table 4.1), we calculated the time-dependent subcellular distribution of both drug species as a function of an extracellular total drug concentration of 10 μm, which is within the range of a typical drug concentration introduced in *in vitro* systems. We set the extracellular volume to a high value (Table 4.1), so that the extracellular drug concentration (Fig. 4.1a) would not be a rate-limiting step in the subcellular drug distribution process.

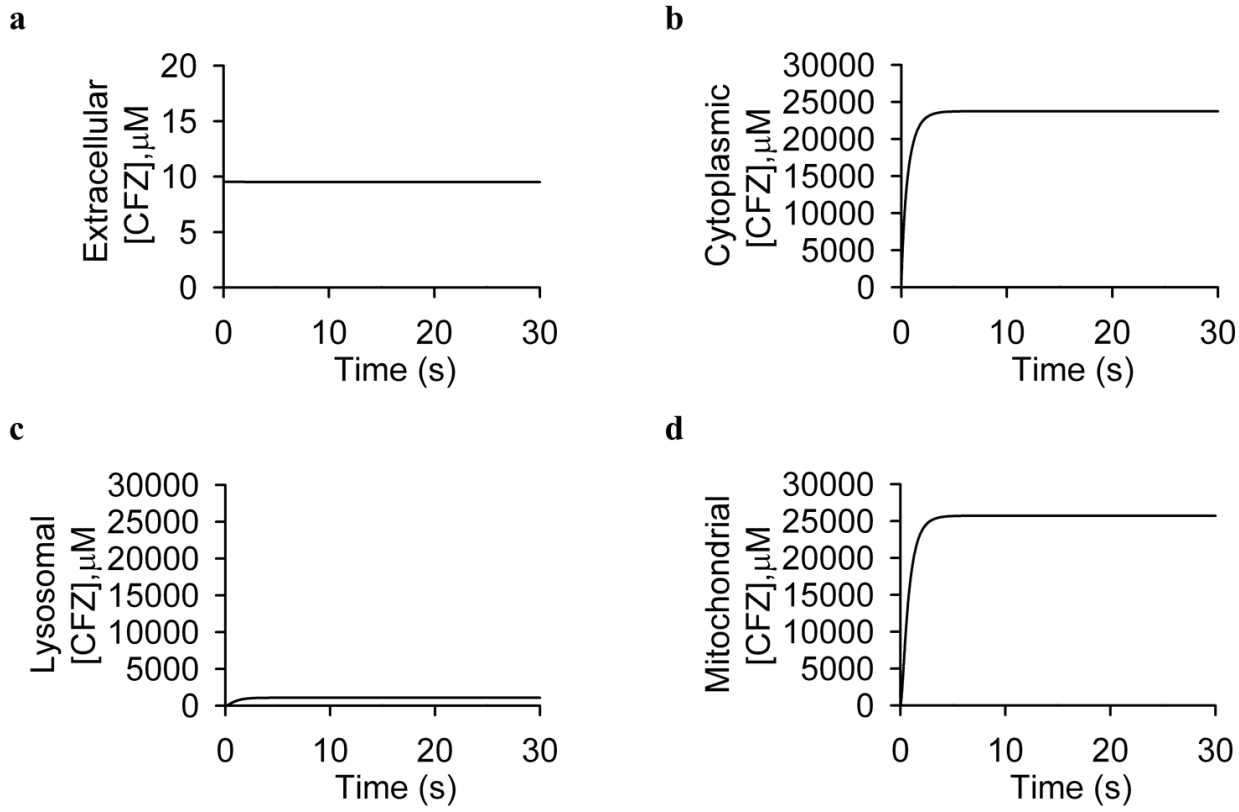

Figure 4.1 Time-plot simulations of extracellular and intracellular free base drug accumulation.

a, Extracellular drug accumulation of CFZ free base remains constant while most of the free base drug is distributed to the cytoplasm (**b**). **c,** The lysosomal compartment does not have high free base drug concentration due to its low pH. **d,** The mitochondrial compartment has the highest free base drug concentration, consistent with the fact that it has the highest pH.

As expected, the free base concentration was higher in the cytoplasm and mitochondria, than in the lysosome (Fig. 4.1b, c, d). Consistent with this, the ionized drug concentration is lower in the cytoplasm (Fig. 4.2b) than in the lysosome (Fig. 4.2c), which is explained by the lysosomotropic effect of the low lysosomal pH[19]. In fact, it is indeed in the lysosome that the highest drug concentration was observed (Fig. 4.2c). Moreover, even though the mitochondrial membrane potential was set to a physiological value of -160 mV, which is lower than the cell membrane potential (-70 mV), the higher ionized drug accumulation in the cytoplasm (Fig. 4.2b) than in the mitochondria (Fig. 4.2d) indicates that the relatively lower pH in the cytoplasm (pH =

7.2) than in the mitochondria (pH = 8.0) plays more substantial role than higher negative membrane potential in the amount of ionized drug accumulation within the compartments. Moreover, we expect both the free base and ionized drug concentrations in all of the compartments would proportionally decrease when the total initial extracellular CFZ concentration is reduced (sub-micromolar to picomolar) in a large extracellular volume.

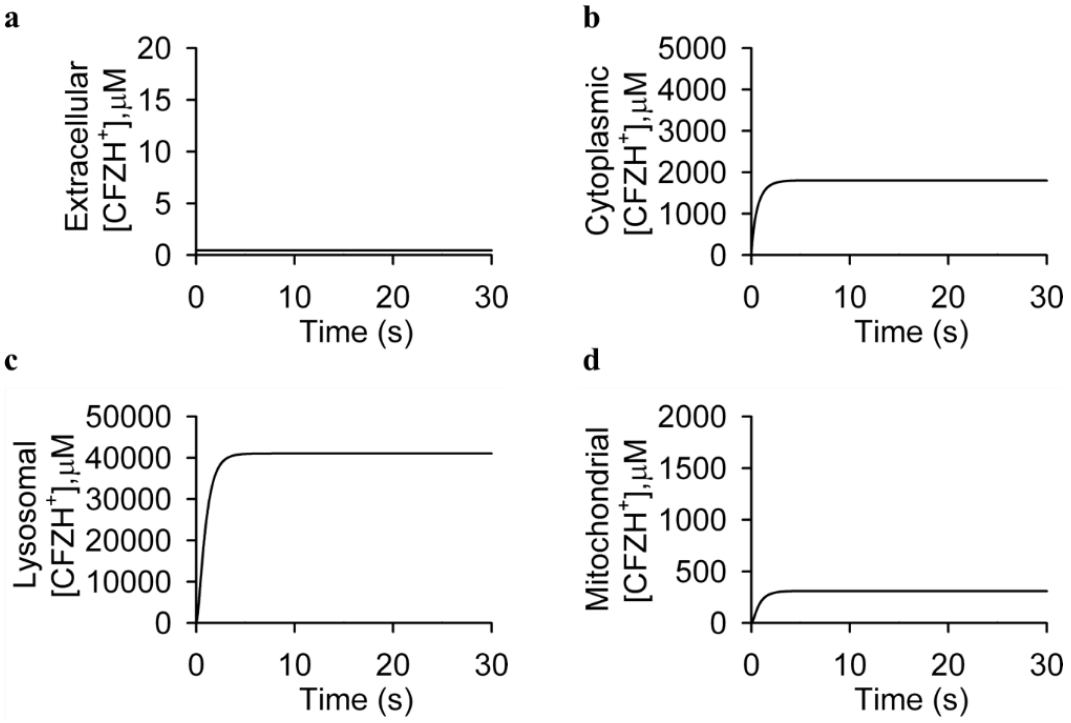

Figure 4.2 Time-plot simulations of extracellular and intracellular ionized drug accumulation.
a, Extracellular drug accumulation of ionized CFZ ($CFZH^+$) remains constant. **b,** The cytoplasmic compartment, due to its high pH, doesn't protonate most of the free base drug. **c,** The lysosomal compartment has the highest ionized drug concentration due to its low pH. **d,** The mitochondrial compartment, due to its high pH, doesn't protonate most of the free base drug.

Using the steady-state concentrations in the non-membrane environments, we calculated the concentrations of both the free base and ionized forms of the drug in the cell membrane, mitochondrial membrane, and lysosomal membrane. The free base drug concentrations in all of

the membranes were higher than the ionized drug concentrations (Table 4.2), which attribute to the fact that the partitioning coefficient of the neutral drug is greater than that of the ionized drug[20,21]. Consistent with the highest free base drug concentration in the mitochondria (Fig. 4.1), we observed the highest free base drug concentration in the mitochondrial membrane (Table 4.2). Surprisingly, the free base drug concentration was greater in the lysosomal membrane than in the cell membrane (Table 4.2), which indicates that beyond drug concentration in the non-membrane environment – from which the drug partitions into its immediate membrane environment – the lipid amount on the membrane leaflets plays a substantial role in the amount of drug partitioning into the membrane[20].

Table 4.2. Drug concentration in membrane

Membrane	[CFZ] (μM)	[CFZ-H^+Cl^-] (μM)
Cell membrane	$5.18x10^7$	$2.11x10^5$
Mitochondrial membrane	$5.04x10^8$	$1.29x10^6$
Lysosomal membrane	$1.39x10^8$	$3.65x10^7$

4.3.2. Phase transition of drug species in cell

In order to determine the propensity of the free base and ionized forms of the drug to precipitate out in the different cellular compartments, we calculated the degree of supersaturation of both forms of the drug using their solubility properties obtained from experimental measurements and experimental-data fitting (Table 4.1). Consistent with the high free base drug concentration observed in the cytoplasm and mitochondria (Fig. 4.1b, d), high degree of supersaturation of the free base was also observed in both compartments (Fig. 4.3b, d), (Table 4.3). However, the highest degree of supersaturation in the non-membrane environment was

observed for the ionized from of the drug in the lysosomal compartment (Fig. 4.4). Indeed, the supersaturation of the CFZ-H^+Cl^- salt occurs only within the lysosome (Table 4.3) because of the drug's pH_{max} in relation to the physiological lysosomal pH. Moreover, the degree of supersaturation of CFZ-H^+Cl^- salt in the lysosome exceeds (3-6 orders of magnitude) that of CFZ free base in the non-membrane as well as membrane environments (Table 4.3); which suggests that the salt form of the drug has greater thermodynamic tendency for precipitation than the free base drug even when introducing a low total initial extracellular CFZ concentration (sub-micromolar to picomolar) in a large extracellular volume.

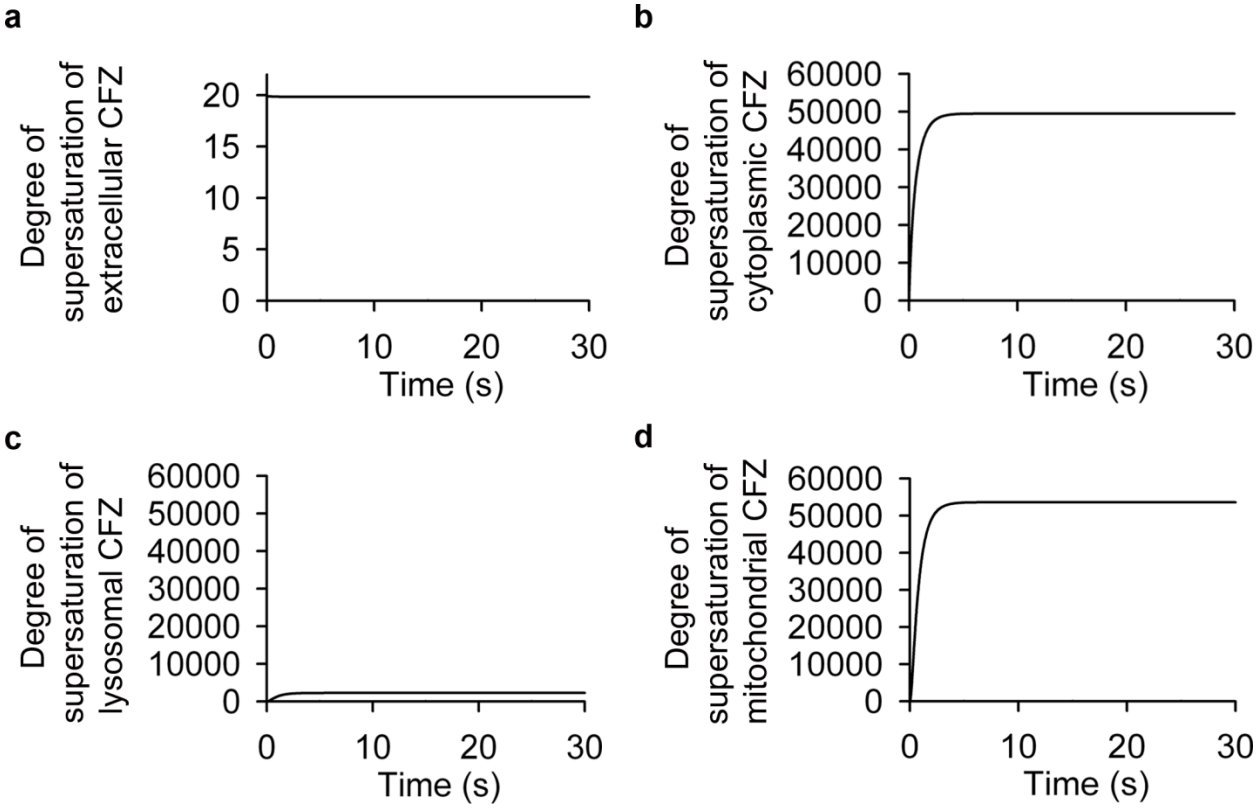

Figure 4.3 Degree of supersaturation of extracellular and intracellular free base drug. **a**, The degree of supersaturation of the free base drug in the extracellular compartment is relatively low due to low free base drug concentration. **b**, The degree of supersaturation of the free base drug in the cytoplasmic compartment is consistent with the high free base drug concentration in the compartment. **c,** The relatively low degree of supersaturation of the free base drug in the lysosomal compartment is consistent with the low free base drug concentration in the compartment. **d,** The degree of supersaturation of the free base drug in the mitochondrial compartment is consistent with the high free base drug concentration in the compartment.

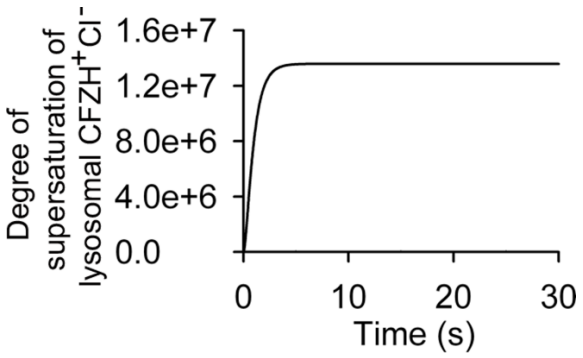

Figure 4.4 Degree of supersaturation of ionized drug in the lysosome.
High degree of supersaturation of the ionized drug species occurs in the lysosome

Table 4.3. Steady-state degree of supersaturation of free base CFZ and CFZ-H^+Cl^-

Compartments	Steady-state degree of supersaturation of free base CFZ	Steady-state degree of supersaturation of CFZ-H^+Cl^-
Extracellular	$1.98x10^1$	
Cell membrane	$5.21x10^3$	
Cytoplasm	$4.95x10^4$	
Mitochondrial membrane	$5.07x10^4$	
Mitochondria	$5.36x10^4$	
Lysosomal membrane	$1.40x10^4$	
Lysosome	$2.25x10^3$	$1.36x10^7$

4.4. Discussion

CFZ is a weak base compound which is known to accumulate and supersaturate as CFZ-H^+Cl^- biocrystalline in macrophages of mice and humans[22-24]. Although the exact mechanism by which such crystal formation and stabilization occurs in macrophages is not known, possible mechanisms that explain the accumulation and precipitation of the CFZ-H^+Cl^- salt gravitate towards the interdependence of cellular properties and the physicochemical properties of the

drug. In this report, by performing model simulation of the phase-transition-dependent distribution and accumulation of both the free base CFZ and CFZ-H^+Cl^- salt in the different cellular compartments, we observed that the free base CFZ accumulation was high in compartments with high pH (> 7), such as mitochondria and cytoplasm (Fig. 4.1b, d). However, the ionized drug concentration was greater than that of the free base in the lysosomal compartment due to the lysosomotropic effect (Fig. 4.2c). Moreover, the extent of the ionized drug accumulation in the lysosome is within the same order of magnitude to what has been previously reported for other weakly basic compounds[25]. However, in this report, we show the effect of lysosomal chloride and the K_{sp} of CFZ-H^+Cl^- salt, in relation to the drug's pH_{max}, on the precipitation of the ionized drug as a hydrochloride salt, through a common-ion effect.

Although lysosomotropic effect is common to weak base compounds, the extent of weak base drug accumulation in lysosomes varies significantly even for weak base drug molecules with similar properties, such as pK_a, logP, and intrinsic free base solubility, which are commonly used physicochemical properties in drug classification[26]. In fact, the lysosomal accumulation of some weak base drugs is associated with toxic effects, such as perturbation of lysosomal ion homeostasis and function by increasing lysosomal pH, increasing the lysosomal size, and permeabilizing the lysosomal membrane[27-29]. Moreover, it is suggested that the lysosomal accumulation of the ionized form of cationic drugs is associated with lysosomal membrane permeabilization[28,29]. Indeed, based on our findings, the ionized drug concentration in lysosomes can be very high even at low extracellular drug concentration unless the ionized drug precipitates out of solution in its salt form. Therefore, in addition to determining the logP and pK_a of a given weak base drug molecule, the physicochemical properties of its salt form can be insightful in

predicting the extent and stability of the drug accumulation in lysosomes, and the associated effects on lysosomal physiology.

In fact, the degree of supersaturation of the free base and salt forms of various weak base drugs, including amiodarone, carvedilol, and desipramine could be estimated using their reported solubility properties[30-32], assuming that the extent of accumulation of these drugs in the various cellular compartments is within the same order of magnitude to that of CFZ. For weak base drugs with pK_a values 6.2 – 10.1[30-32], the estimated degree of supersaturation of the salt form of the weak base drugs in a lysosomal environment would be 1 to 12 orders of magnitude fold less than that of CFZ-H^+Cl^-. This suggests that the propensity of salt precipitation for some, if not most, weak base drugs[30-32] is primarily dictated by their solubility properties than by their logP and pK_a values. Indeed, hydrochloride salt forms of weak base drugs with high K_{sp} values (> 8 orders of magnitude μM^2) have low tendency to precipitate out even when administered at high dose, which does not perturb cellular physiology.

To the contrary, the estimated degree of supersaturation of the free base drugs would be 1-5 orders of magnitude fold greater than that of free base CFZ, with the exception of amiodarone, which has a low intrinsic free base solubility[32]. This suggests that the weak base drugs are more stabilized in their free base forms than in their salt forms, which could have implications regarding their physiological cellular disposition and accumulation that in turn affects their overall PK profile. Therefore, further studies which incorporate mathematical model predictions as well as model-prediction guided wet-lab experiments of the phase-transition dependent cellular distribution and accumulation of weak base drugs and their salt forms are warranted.

4.4.1. Insights into weak base drug-induced phospholipidosis

Phospholipidosis, also known as acquired lysosomal storage disorder, is the accumulation of lipids in lysosomes, and is caused by weak base drugs such as amiodarone, azithromycin, and chloroquine, which are classified as cationic amphiphilic drugs (CADs)[33,34]. One of the suggested mechanisms by which weak base drug-induced phospholipidosis occurs is through the accumulation of a weak base drug molecule in the lysosomal membrane, which thereby displaces lysosomal phospholipase A2 (LPLA2) enzyme that is responsible for the degradation of membrane phospholipids, such as phosphatidylcholine and phosphatidylethanolamine[33,35]. Thus, it could be useful to predict the dose-dependent relationship of the ionized weak base drug accumulation in the lysosomal membrane and LPLA2 inhibition to better understand the effect of weak base drug-induced phospholipidosis[34]. Alternatively, the physicochemical properties of the hydrochloride salts of such weak base drugs, such as K_{sp}, intrinsic salt solubility, and pH_{max}, could be investigated in order to stabilize the salt form of the weak base drugs within the lysosome as a mechanistic way to reduce the amount of the ionized weak base drug that inhibits LPLA2. This would especially be important in the case where most weak base drugs that are in development or already in the market, which are known to induce phospholipidosis could be repurposed in order to retain their notable efficacies.

4.4.2. Cell-type dependent phagocytosis of biocrystal

Our findings are also helpful in understanding the biocompatibility of phagocytosis of crystal drugs[22,36-38]. In the case where salt forms of weak base drugs are directly administered to cells, the stability and amount of drug distributed across cells can be determined using modeling prediction. For our model drug, CFZ, we have observed that although the ionized drug

accumulates in all of the cellular compartments, CFZ-H^+Cl^- salt is only stabilized in a lysosomal environment. Thus, future studies that further investigate the effect of cell-type dependent lysosomal lipid content[13-15,39-41] on the phase-transition-dependent weak base drug accumulation and stabilization could elucidate the previously reported heterogeneous phagocytosed drug bioaccumulation and stabilization processes[38] with respect to the maintenance of cell physiology.

4.5. Acknowledgment and contributions

This work was supported by National Institutes of Health grant R01GM078200 to GRR and Rackham Merit Fellowship to TW.
T.W. designed, performed, and analyzed computational experiments. T.W. and G.R.R. designed the project and G.R.R. directed the research.

4.6. References

1 Augustijns, P. & Brewster, M. E. Supersaturating drug delivery systems: fast is not necessarily good enough. *J Pharm Sci* **101**, 7-9, doi:10.1002/jps.22750 (2012).

2 Miller, D. A., DiNunzio, J. C., Yang, W., McGinity, J. W. & Williams, R. O., 3rd. Enhanced in vivo absorption of itraconazole via stabilization of supersaturation following acidic-to-neutral pH transition. *Drug Dev Ind Pharm* **34**, 890-902, doi:10.1080/03639040801929273 (2008).

3 Yalkowsky, S. H., Valvani, S. C. & Johnson, B. W. In vitro method for detecting precipitation of parenteral formulations after injection. *J Pharm Sci* **72**, 1014-1017 (1983).

4 Charifson, P. S. & Walters, W. P. Acidic and basic drugs in medicinal chemistry: a perspective. *J Med Chem* **57**, 9701-9717, doi:10.1021/jm501000a (2014).

5 Hens, B., Brouwers, J., Corsetti, M. & Augustijns, P. Supersaturation and Precipitation of Posaconazole Upon Entry in the Upper Small Intestine in Humans. *J Pharm Sci* **105**, 2677-2684, doi:10.1002/jps.24690 (2016).

6 Kramer, S. F. & Flynn, G. L. Solubility of organic hydrochlorides. *J Pharm Sci* **61**, 1896-1904 (1972).

7 Serajuddin, A. T. Salt formation to improve drug solubility. *Adv Drug Deliv Rev* **59**, 603-616, doi:10.1016/j.addr.2007.05.010 (2007).

8 Duvvuri, M. & Krise, J. P. A novel assay reveals that weakly basic model compounds concentrate in lysosomes to an extent greater than pH-partitioning theory would predict. *Mol Pharm* **2**, 440-448, doi:10.1021/mp050043s (2005).

9 Baik, J. & Rosania, G. R. Modeling and Simulation of Intracellular Drug Transport and Disposition Pathways with Virtual Cell. *J Pharm Pharmacol (Los Angel)* **1**, doi:10.13188/2327-204X.1000004 (2013).

10 Trapp, S. & Horobin, R. W. A predictive model for the selective accumulation of chemicals in tumor cells. *Eur Biophys J* **34**, 959-966, doi:10.1007/s00249-005-0472-1 (2005).

11 Balon, K., Riebesehl, B. U. & Muller, B. W. Drug liposome partitioning as a tool for the prediction of human passive intestinal absorption. *Pharm Res* **16**, 882-888 (1999).

12 Kadam, Y., Yerramilli, U. & Bahadur, A. Solubilization of poorly water-soluble drug carbamezapine in pluronic micelles: effect of molecular characteristics, temperature and added salt on the solubilizing capacity. *Colloids Surf B Biointerfaces* **72**, 141-147, doi:10.1016/j.colsurfb.2009.03.027 (2009).

13 van Meer, G., Voelker, D. R. & Feigenson, G. W. Membrane lipids: where they are and how they behave. *Nat Rev Mol Cell Biol* **9**, 112-124, doi:10.1038/nrm2330 (2008).

14 van Meer, G. Transport and sorting of membrane lipids. *Curr Opin Cell Biol* **5**, 661-673 (1993).

15 Bohdanowicz, M. & Grinstein, S. Role of phospholipids in endocytosis, phagocytosis, and macropinocytosis. *Physiol Rev* **93**, 69-106, doi:10.1152/physrev.00002.2012 (2013).

16 Zhang, X., Shedden, K. & Rosania, G. R. A cell-based molecular transport simulator for pharmacokinetic prediction and cheminformatic exploration. *Mol Pharm* **3**, 704-716, doi:10.1021/mp060046k (2006).

17 Calderon, R. O. & DeVries, G. H. Lipid composition and phospholipid asymmetry of membranes from a Schwann cell line. *J Neurosci Res* **49**, 372-380 (1997).

18 Horvath, S. E. & Daum, G. Lipids of mitochondria. *Prog Lipid Res* **52**, 590-614, doi:10.1016/j.plipres.2013.07.002 (2013).

19 de Duve, C. *et al.* Commentary. Lysosomotropic agents. *Biochem Pharmacol* **23**, 2495-2531 (1974).

20 Williams, H. D. *et al.* Strategies to address low drug solubility in discovery and development. *Pharmacol Rev* **65**, 315-499 (2013).

21 Jain, N., Yang, G., Tabibi, S. E. & Yalkowsky, S. H. Solubilization of NSC-639829. *Int J Pharm* **225**, 41-47 (2001).

22 Baik, J., Stringer, K. A., Mane, G. & Rosania, G. R. Multiscale distribution and bioaccumulation analysis of clofazimine reveals a massive immune system-mediated xenobiotic sequestration response. *Antimicrob Agents Chemother* **57**, 1218-1230, doi:10.1128/AAC.01731-12 (2013).

23 Desikan, K. V., Ramanujam, K., Ramu, G. & Balakrishnan, S. Autopsy findings in a case of lepromatous leprosy treated with clofazimine. *Lepr Rev* **46**, 181-189 (1975).

24 Lewis, J. T., Candelora, J. N., Hogan, R. B., Briggs, F. R. & Abraham, S. C. Crystal-storing histiocytosis due to massive accumulation of charcot-leyden crystals: a unique association producing colonic polyposis in a 78-year-old woman with eosinophilic colitis. *Am J Surg Pathol* **31**, 481-485, doi:10.1097/01.pas.0000213420.46127.9c (2007).

25 Fu, D. *et al.* Imaging the intracellular distribution of tyrosine kinase inhibitors in living cells with quantitative hyperspectral stimulated Raman scattering. *Nat Chem* **6**, 614-622, doi:10.1038/nchem.1961 (2014).

26 Ohkuma, S. & Poole, B. Cytoplasmic vacuolation of mouse peritoneal macrophages and the uptake into lysosomes of weakly basic substances. *J Cell Biol* **90**, 656-664 (1981).

27 Moruno-Manchon, J. F. *et al.* TFEB ameliorates the impairment of the autophagy-lysosome pathway in neurons induced by doxorubicin. *Aging (Albany NY)* **8**, 3507-3519, doi:10.18632/aging.101144 (2016).

28 Boya, P. & Kroemer, G. Lysosomal membrane permeabilization in cell death. *Oncogene* **27**, 6434-6451, doi:10.1038/onc.2008.310 (2008).

29 Boya, P. *et al.* Lysosomal membrane permeabilization induces cell death in a mitochondrion-dependent fashion. *J Exp Med* **197**, 1323-1334, doi:10.1084/jem.20021952 (2003).

30 Avdeef, A. *et al. Equilibrium solubility measurement of ionizable drugs - Consensus recommendations for improving data quality*. Vol. 4 (2016).

31 Avdeef, A. Solubility of sparingly-soluble ionizable drugs. *Adv Drug Deliv Rev* **59**, 568-590, doi:10.1016/j.addr.2007.05.008 (2007).

32 Bergstrom, C. A., Luthman, K. & Artursson, P. Accuracy of calculated pH-dependent aqueous drug solubility. *Eur J Pharm Sci* **22**, 387-398, doi:10.1016/j.ejps.2004.04.006 (2004).

33 Shayman, J. A. & Abe, A. Drug induced phospholipidosis: an acquired lysosomal storage disorder. *Biochim Biophys Acta* **1831**, 602-611, doi:10.1016/j.bbalip.2012.08.013 (2013).

34 Bauch, C., Bevan, S., Woodhouse, H., Dilworth, C. & Walker, P. Predicting in vivo phospholipidosis-inducing potential of drugs by a combined high content screening and in silico modelling approach. *Toxicol In Vitro* **29**, 621-630, doi:10.1016/j.tiv.2015.01.014 (2015).

35 Abe, A. *et al.* Lysosomal phospholipase A2 is selectively expressed in alveolar macrophages. *J Biol Chem* **279**, 42605-42611, doi:10.1074/jbc.M407834200 (2004).

36 Baik, J. & Rosania, G. R. Macrophages sequester clofazimine in an intracellular liquid crystal-like supramolecular organization. *PLoS One* **7**, e47494, doi:10.1371/journal.pone.0047494 (2012).

37 Baik, J. & Rosania, G. R. Molecular imaging of intracellular drug-membrane aggregate formation. *Mol Pharm* **8**, 1742-1749, doi:10.1021/mp200101b (2011).

38 Yoon, G. S. *et al.* Phagocytosed Clofazimine Biocrystals Can Modulate Innate Immune Signaling by Inhibiting TNFalpha and Boosting IL-1RA Secretion. *Mol Pharm* **12**, 2517-2527, doi:10.1021/acs.molpharmaceut.5b00035 (2015).

39 Andreyev, A. Y. *et al.* Subcellular organelle lipidomics in TLR-4-activated macrophages. *J Lipid Res* **51**, 2785-2797, doi:10.1194/jlr.M008748 (2010).

40 Murakami, T. & Yumoto, R. Role of phosphatidylserine binding in tissue distribution of amine-containing basic compounds. *Expert Opin Drug Metab Toxicol* **7**, 353-364, doi:10.1517/17425255.2011.548805 (2011).

41 Spector, A. A. & Yorek, M. A. Membrane lipid composition and cellular function. *J Lipid Res* **26**, 1015-1035 (1985).

Chapter 5: The Adaptive Cargo Carrying Capacity of Macrophages Expands the Drug Volume of Distribution

The content of this chapter will be included in the following reference:

Rzeczycki, P., Baik, J., Woldemichael, T., Keswani, R.K., Yoon, G.S., Stringer, K.A., Rosania, G.R. The Adaptive Cargo Carrying Capacity of Macrophages Expands the Drug Volume of Drug Distribution. (2017), *In Preparation.*

5.1. Relevance to Thesis

This chapter incorporates computational pharmacokinetic analysis of *in vivo* clofazimine accumulation and efflux experiments, which have allowed us to determine the steady-state clofazimine accumulation in different macrophage population. Our findings have elucidated the mechanistic role of macrophages in accommodating and stabilizing massive drug bioaccumulation in a physiological manner.

In addition, our findings and conclusions would enable us to design future experiments to better understand the difference in the accommodation and stabilization processes of drug bioaccumulation within different macrophage population. Moreover, our model predictions would allow us to design experiments that can better capture the biochemical and biophysical features of the different macrophage types, especially in relation to the macrophage lysosomes, that can explain the stabilization of the prolonged internalization of the drug by the cells.

5.2. Personal Contribution

Using experimentally determined CFZ uptake (assumed to be zero order) and release rates (assumed to be 1st order exponential decay) by peritoneal and alveolar macrophages, I modeled and performed simulations of the time-dependent drug accumulation in both peritoneal and alveolar macrophages using ordinary differential equations in Berkeley Madonna® software.

5.3. Abstract

Through phagocytosis or fluid phase pinocytosis, cultured macrophages are capable of internalizing massive amounts of solids and solutes from the extracellular medium ('massive' defined as surpassing every other cellular component, except water). Nevertheless, the cargo carrying capacity of macrophages has never been measured *in vivo*. Here, we used an orally bioavailable drug -clofazimine- as a molecular reporter of the extent of macrophage loading. Upon increasing the whole-body drug cargo load, macrophages adjusted their size, number and membrane organization to accommodate an increasing cargo volume. Ultimately, the total volume of intracellular cargo exceeded 5% of the total cell volume across the entire macrophage population. Most interestingly, macrophages adaptively maximized their cargo capacity, not only by stabilizing and reshaping the intracellular cargo space, but also by remodeling their intracellular membrane architecture to minimize the surface area of the cargo space while maximizing the cargo volume. By stabilizing a solute-to-solid phase transition, the apparent volume of distribution of the reporter probe continuously increased through treatment, and exceeded the cell volume by more than ten thousand-fold. As expected from an active sequestration mechanism, experimentally depleting macrophages in liver and spleen reduced the total amount of drug cargo accumulated in those organs, without affecting the loading of the remaining cells. Altogether, the results indicate a coordinated, immunological response

mechanism across the entire macrophage population, which expands their endolysosomal cargo carrying capacity to accommodate an increasingly massive load of drug cargo.

5.4. Introduction

Throughout the body, macrophages are especially equipped to internalize extracellular solutes and particles through pinocytosis and phagocytosis, respectively. This allows them to carry out a number of critical cellular immune functions ranging from destruction of pathogens to removal and recycling of dead cells and aged tissue components[1-3]. In addition to being highly phagocytic, the endolysosomal system of the macrophage is especially capable of accommodating and degrading foreign material due to higher expression levels of lysosomal acidification mechanisms[4], particularly the vacuolar-type proton ATP-ase (V-ATPase)[5]. Little is known about the *in vivo* phagocytic capacity of macrophages, with the majority of work having been performed *in vitro* using fluorescent tracer molecules[6] or inert beads of varying sizes[7]. For example, Cannon et al performed a study to determine the extent to which murine bone marrow macrophages were able to phagocytose polystyrene beads of various sizes, revealing that the phagocytic capacity of these cells is limited by the amount of membrane that is available to spread out and engulf the particle, rather than the volume of the cell[8].

Even though the macrophage is a major immune regulator, its role as a determinant of drug distribution is underappreciated. Due to their high rates of endocytosis, pinocytosis and phagocytosis, and because of their ubiquitous presence throughout the body, they are poised to impact the performance and efficacy of many therapeutic agents. For example, liposomal formulations must be optimized to avoid phagocytosis of particles and removal of drug from the systemic circulation, increasing therapeutic efficiency[9,10]. The action of macrophages may also

impact small molecule drugs, such as antibiotics[11-13]. Many antibiotics will display large volumes of distribution and long elimination half-lives[14], causing them to linger within the body for extended periods of time. The accumulation of weakly basic, hydrophobic drug molecules within acidic subcellular compartments is a well-documented phenomenon, referred to as ion-trapping [15]. Cationic, amphiphilic molecules, particularly weakly basic molecules, tend to become trapped within lysosomes following protonation within the acidic lysosomal microenvironment[15-17]. Because macrophages have very active endolysosomal systems and express high levels of biomolecular ion transporters, they could significantly impact the volumes of distribution of many weakly basic drugs.

Here, in order to study both how macrophages impact the volume of distribution of a therapeutic agent, and to determine the *in vivo* cargo carrying capacity of the macrophage, the FDA-approved and biocompatible antibiotic clofazimine was chosen as a reporter probe. Clofazimine is an anti-mycobacterial agent clinically used to treat leprosy and multi-drug resistant tuberculosis[18-20]. It exhibits extensive accumulation throughout the body following oral administration, in both humans and in animal models[21-23]. Because clofazimine is both highly lipophilic (LogP > 7) and contains a weakly basic, ionizable amine group, it is expected to accumulate in adipose tissue, intracellular membranes and in acidic organelles, such as lysosomes. In both human and animal models, it has been shown that following prolonged oral dosing, CFZ accumulates extensively within macrophages[24].

Previously, we have shown that the accumulation of clofazimine within macrophages leads to the formation of large, insoluble crystal-like drug inclusions (CLDIs) within these cells comprised of highly organized domains of clofazimine hydrochloride[25,26]. In this manner, CLDIs can provide a solid, stable volume marker to assess the macrophage's cargo carrying capacity

and its contribution to the drug's volume of distribution. Because of the crystallinity and low solubility, CLDIs are easily isolated and are readily detectable through a variety of analytical techniques[24,26]. Thus, we proceeded to study the cargo loading capacity of different macrophage populations to probe the patterns of macrophage loading in different organs, and to determine how the macrophages impact the volume of distribution. Additionally, the effects of macrophage depletion on cargo loading was probed, and the theoretical macrophage loading capacity within different tissues was calculated and related to the measured, tissue-specific variations in macrophage loading and its contribution to the volume of distribution.

5.5. Materials and Methods

5.5.1. Clofazimine administration to mice.

Animal care was provided by the University of Michigan's Unit for Laboratory Animal Medicine (ULAM), and the experimental protocol was approved by the Committee on Use and Care of Animals (Protocol PRO00005542). Mice (4 week old, male C57Bl6) were purchased from the Jackson Laboratory (Bar Harbor, ME) and acclimatized for 1 week in a specific-pathogen-free animal facility. Clofazimine (C8895; Sigma, St. Louis, MO) was dissolved in sesame oil (Shirakiku, Japan) to achieve a concentration of 3 mg/ml, which was mixed with Powdered Lab Diet 5001 (PMI International, Inc., St. Louis, MO) to produce a 0.03% drug to powdered feed mix, and orally administered ad libitum for up to eight weeks. A corresponding amount of sesame oil was mixed with chow for vehicle treatment (control). For washout experiments, mice were fed the vehicle-containing diet for eight weeks, after an eight-week loading period with the CFZ-containing diet. Mice were euthanized via carbon dioxide asphyxiation and exsanguination.

5.5.2. Alveolar macrophage isolation.

Following euthanasia, the trachea was surgically exposed and cannulated with an 20G needle and the lungs were lavaged by instilling DPBS (Life Technologies) containing 0.5 mM EDTA (Sigma) in 1 ml aliquots for a total of 6 ml. Approximately 90% of the bronchoalveolar lavage (BAL) was retrieved. The BAL was then centrifuged for 10 min at 400 x g, 4 °C, resuspended in RPMI 1640 media (Life Technologies) with 5% FBS (Life Technologies) and Penicillin/Streptomycin (Thermofisher), macrophages were counted, and an aliquot of cells were then plated onto 4 or 8 chamber coverglass (#1.5, Lab-Tek II, Nunc, Rochester, NY) for imaging studies. The cells were allowed to attach overnight and then washed with media. The remaining cells were analyzed for drug content.

5.5.3. Peritoneal macrophage isolation.

Following euthanasia, a small incision was made in the lower abdomen. The peritoneal cavity was then flushed 10 mL of ice cold DPBS containing 5% FBS (Sigma) and collected. The peritoneal lavage was centrifuged for 10 min at 400 x g, 4 °C, and then resuspended in DMEM media (Life Technologies) with 5% FBS and Penicillin /Streptomycin, macrophages were counted, and an aliquot of cells were then plated onto 4 or 8 chamber coverglass (#1.5, Lab-Tek II, Nunc, Rochester, NY) for imaging. The cells were allowed to attach overnight and then washed with media. The remaining cells were analyzed for drug content.

5.5.4. Bone marrow monocyte isolation.

Following euthanasia, an incision was made above the hip bone and the skin was removed down the entire leg. The femur was then cut from the knee joint and the hip, the muscle

was removed, and the bone was placed in ice cold DPBS. The tips of the femur were then cut, and the bone was flushed with 5 mL of ice cold PBS to collect the bone marrow monocytes. The suspension was centrifuged for 10 min at 400 x g, 4 °C, and resuspended in RPMI 1640 media with 5% FBS and Penicillin/Streptomycin, counted with a hemocytometer, and an aliquot of cells were plated onto 4 or 8 chamber coverglass (#1.5, Lab-Tek II, Nunc, Rochester, NY) for imaging. The cells were allowed to attach overnight and then washed with media. The remaining cells were analyzed for drug content.

5.5.5. Kupffer cell isolation.

Following euthanasia, the portal vein was injected with 10 mL of 1 mg/mL Collagenase D (Worthington Biochemical Corporation, Lakewood, NJ) in DMEM-low glucose (Life Technologies) with 15 mM HEPES (Life Technologies). The tissue was then removed, placed in a sterile petri dish, and minced into small (2-4 mm) pieces using a sterile scalpel blade. 15 mL of the Collagenase solution was added, and the tissue was incubated for 40 minutes at 37 °C, with occasional pipetting to dissociate tissue. The suspension was then filtered through a 100 µm cell strainer (Fisher Scientific, Waltham, MA) and centrifuged at 200 x g for 5 minutes. The supernatant was discarded, and the cells were resuspended in 15 mL DMEM-low glucose with 15 mM HEPES, and centrifuged at 200 x g for 5 minutes. This was repeated for two additional washes. After the final wash, the cells were suspended in DMEM: F/12 (1:1) (Life Technologies) with 10% FBS and Penicillin/Streptomycin, macrophages were counted, and an aliquot was plated onto 4 or 8 chamber coverglass(#1.5, Lab-Tek II, Nunc, Rochester, NY) coated with Collagen 1 (Corning, Corning, New York) for imaging. The cells were allowed to attach overnight and then washed with media.

5.5.6. Multi-parameter microscope imaging and analysis of xenobiotic sequestering macrophage populations.

Multi-parameter polarization, brightfield, and fluorescence imaging and analysis were performed using the imaging method previously described by Rzeczycki et al[26]. Briefly, cells were plated on chamber slides and allowed to attach overnight. Following attachment, cells were imaged with brightfield, fluorescence, and polarization imaging modalities. Images were then analyzed using ImageJ software[27,28]. Values for dichroism and optical density are reported as an average signal per cell, from 0-1. At least 150 cells of each type were analyzed at each time point. Following loading with 7 and 14 mg of cargo, macrophages were classified as xenobiotic sequestering based on whether or not they contained a detectable Cy5 signal from clofazimine hydrochloride[24] using a K-means clustering analysis, with the clusters set to 2 based off of the Log_{10}(Intracellular Cy5 fluorescence).

5.5.7. Biochemical analysis of clofazimine in cells.

The concentration of clofazimine in cells was determined after measuring clofazimine content in isolated macrophage populations and organ homogenates using established methods [22,24,25,29]. For isolated macrophage populations, cells were counted within each cell sample using a hemocytometer to determine the total recovered macrophage population. The cells were then centrifuged and the media was removed. The cell pellet was suspended in 1 mL of DI water, and the drug was extracted with three passes of 1 mL of xylenes. The drug was then extracted from the xylene with three 1 mL passes of 9 M sulfuric acid. The concentration of clofazimine present in the cell sample was then determined using a plate reader (Biotek Synergy 2, Winooksi, VT) at wavelength 450 nm, and background corrected at wavelength 750 nm, with the concentration

determined using a standard curve made of standards with known concentrations of clofazimine, and is reported as fmol clofazimine/xenobiotic sequestering cell.

5.5.8. Sample preparation for microscopy.

Cryosectioning was carried out using a Leica 3050S Cryostat (Leica Biosystems Inc., Buffalo Grove, IL). Samples were sectioned to 5 µm. In preparation for cryosectioning, portions of the organ were removed, immediately submerged in OCT (Tissue-Tek catalog no. 4583; Sakura), and frozen (-80 °C). For transmission electron microscopy, organs were submerged in fixative and cut into small (< 1 mm) sized pieces. The organs were preserved in a glass vial with fixative and stored at 4 °C. After three rinses with Sorensen's buffer (0.1 M), tissues were stained with 1% osmium tetroxide in Sorensen's buffer and washed three times in Sorensen's buffer. Dehydration was carried out with a graded ethanol-water series (50, 70, and 90% and two changes of 100%) for 15 min each. After washing with three changes of propylene oxide, the tissues were treated with Epon resin (Electron Microscopy Sciences) and polymerized at 60 °C for 24 hours. The blocks were then sectioned to 70 nm using an ultramicrotome and mounted on a copper EM grid (Electron Microscopy Sciences), which was then stained with uranyl acetate and lead citrate before imaging. Immunohistochemistry of F4/80 (Abcam, 1:500 dilution) was performed using Alexa-Fluor 488 (Abcam, 1:500 dilution).

5.5.9. Clofazimine volume occupancy.

The volume that clofazimine occupies within the macrophage was determined using the reported crystal-packing density of 1.36 g/mL[25] for CFZ-H^+Cl^-, which was then converted to a

molar volume of 0.377 μm^3/ fmol. Cellular volume occupancy was then estimated using the measured drug loading per cell and this calculated molar volume.

5.5.10. Determination of vesicle size and shape.

Vesicle loading per cell was performed using the Cy5 fluorescence of the alveolar macrophage. Using ImageJ[27,28], the radius of each vesicle was determined. Vesicles which showed Cy5 fluorescence were counted as clofazimine sequestering. Volume of the vesicle for 3.5 and 7 mg treated cells was estimated assuming spherical shape, while CLDI volume was estimated assuming a cylindrical shape.

5.5.11. Macrophage expansion analysis.

To determine the expansion in macrophage population in lung, liver, and spleen from animals treated with clofazimine, cryosections were obtained of the same thickness. The relative number of macrophages in a volume of tissue was determined by dividing the total F4/80 signal staining intensity between 8 week clofazimine-treated sample by the total F4/80 signal staining intensity of a vehicle-treated sample (the area and thickness of the sections analyzed were kept the same). The expanded macrophage population was then determined by multiplying literature reported (baseline) macrophage population values for each organ[30] by the relative expansion factor. To determine the percentage of xenobiotic sequestering cells, the total number of cells which showed Cy5 fluorescence and F4/80 staining were determined using a mask of the F4/80 staining. 5 images per organ per animal were analyzed for each measurement.

5.5.12. Measurement of CLDI mass within tissues.

The CLDI mass present in lung, liver, and spleen tissues at eight weeks of treatment was determined using established protocols[29]. Tissues (n = 3) were removed, weighed, and placed in a sterile petri dish, where they were manually minced and homogenized using a scalpel and syringe plunger. The tissue homogenate was filtered through a 40 µm cell strainer to remove larger cellular debris. The filtrate was then centrifuged for 10 min at 300 *x* g to pellet the CLDIs. The supernatant was removed and the pellet was resuspended in 10% sucrose in DPBS (Life Technologies, Carlsbad, CA) without calcium chloride or magnesium chloride, pH=7.4. CLDIs were further purified using a 3-layer sucrose gradient (50%, 30%, and 10% sucrose in DPBS) centrifugation method (3200 *x* g for 60 minutes). The pelleted CLDIs were then dissolved in 9 M H_2SO_4 and the mass of drug was determined using a plate reader (Biotek Synergy 2, Winooksi, VT) at wavelength 450 nm, and background corrected at wavelength 750 nm, with the aid of a standard curve made with solutions of known concentration.

5.5.13. CLDI loading within individual macrophages.

Using the total recovered mass of CLDIs within the liver, lung, and spleen, the CLDI loading within individual xenobiotic-sequestering macrophages was estimated using the total expanded macrophage population, which was corrected for the percentage of CLDI containing cells. The percentage of cellular volume that is occupied by the CLDI was estimated using literature reported values for the cellular volume of macrophages[31].

5.5.14. Macrophage depletion.

To deplete tissue macrophages, mice were treated with liposomes containing either 7 mg/mL of clodronate or phosphate-buffered saline (PBS) (FormuMax Scientific Inc., Sunnyvale,

CA). Liposomes were injected intraperitoneally, as previously described[32]. Mice were initially treated with 200 µL of liposomes followed by 100 µL injections twice per week to ensure continual macrophage depletion. Mice were fed clofazimine or control diet continuously for a four-week period. Following two weeks of feeding, liposome administration began for two weeks. After completing four weeks of feeding and two weeks of liposome treatment, mice were sacrificed and tissues were collected.

5.5.15. Biochemical analysis of clofazimine in tissues.

After loading with clofazimine, mice were euthanized via CO_2 asphyxiation, and organs were removed and weighed. Tissue (20-30 mg) was homogenized in 500 µL of radioimmunoprecipitation assay buffer (Sigma) with added protease inhibitors (Halt protease and phosphatase inhibitor cocktail and 0.5 M EDTA; Thermo Pierce, Rockford, IL), and 350 µL of homogenate was removed. The drug was then extracted from the xylene with three 1 mL passes of 9 M sulfuric acid. The recovery yield was determined by spiking samples with a known concentration of clofazimine. The concentration of clofazimine present in the tissue was then determined using the plate reader assay (Biotek Synergy 2, Winooksi, VT) at wavelength 450 nm, and background corrected at wavelength 750 nm, with the aid of a standard curve made with solutions of known concentration.

5.5.16. Biochemical analysis of clofazimine in plasma.

Blood was collected and centrifuged (7,000 × g for 5 minutes). The resulting supernatant serum was extracted with acetonitrile (90% extraction efficiency) for 10 min at 4 °C with vortexing. After centrifugation (15,000 rpm, 4 °C), the supernatant was injected into a Waters

Acquity UPLC H-Class (Waters, Milford, MA) equipped with an Acquity UPLC BEH C18 column (1.7 μm, 2.1 mm [inner diameter] by 100 mm; Waters, Milford, MA). Mobile phase A was 5 mM ammonium acetate, adjusted to pH 9.9 with ammonium hydroxide, and mobile phase B was acetonitrile. The flow rate was 0.35 ml/min, with a linear gradient from 50 to 100% phase B over 1.5 min, followed by holding at 100% for 1.5 min, a return to 50% phase B, and then re-equilibration for 2.5 min. Standards were prepared by spiking untreated plasma samples with known amounts of clofazimine, ranging from 0 to 30 μM. Peak area was determined using Empower 3 Software (Waters, Milford, MA).

5.5.17. Determination of the volume of distribution of clofazimine at various stages of drug loading.

Following treatment with 5.25 or 14 mg of clofazimine, mice (n = 3 per time point) were euthanized and the liver, spleen, small intestine, fat, kidney, and lung were removed, weighed, and the mass of clofazimine within each tissue and concentration within plasma was determined using the previously described protocols. The volume of distribution of the drug within macrophages, tissue, and the whole body at the different loading amounts was determined using the ratio between the total drug within tissues or individual cells and the measured plasma concentration, and is reported as L/kg tissue or L/kg body weight, assuming a 25 gram mouse.

5.5.18. CLDI injection and stabilization assay.

To determine how macrophages stabilize CLDIs, mice were treated with either liposomal PBS or liposomal clodronate, as previously described[32]. 48 hours after liposome administration, mice were injected I.P. with 200 μg of CLDIs suspended in 1 mL of PBS (n = 3 mice per group

per time point). At time points ranging from 0 to 48 hours, the mice were euthanized, the peritoneal lavage was collected and pelleted, and the drug content within the pellet was analyzed using the previously described spectrophotometric analysis method. Using a simple exponential regression with recovered drug content, the half-life was estimated.

5.5.19. Statistical analysis.

All data are expressed as means ± the standard deviations (SD). For multiple comparisons, statistical analysis was performed with one-way analysis of variance (ANOVA) and Tukey's post hoc comparisons. The half-life of injected CLDIs was determined using a simple, first order exponential regression of the recovered drug mass. All statistical analyses were performed using IBM SPSS Statistics version 24.0 (IBM Software, Armonk, New York). P values less than 0.05 were considered statistically significant.

5.6. Results

5.6.1 Macrophages adjusted internal membrane arrangement to maximize cargo loading.

Experimentally, a moderate, whole-body cargo load (3.5 mg, Fig. 5.1) mostly led to accumulation in alveolar macrophages (Fig. 5.1a). This cargo was associated with red, optically dense cytoplasmic vesicles which exhibited little dichroism signal, corresponding to a disordered, amorphous supramolecular organization[33,34] (Fig. 5.1b). A larger cargo load resulted in a modest increase in accumulation in the alveolar macrophages (Fig. 5.1c), plus a fraction of peritoneal and liver macrophages were also loaded. However, the structure of the intracellular cargo became more organized (Fig. 5.1b) as reflected in the elevated optical density and dichroism of peritoneal and liver macrophages (Fig. 5.1b-d). Doubling the whole-body cargo

load caused all macrophages to redistribute their internal cargo loads into large, highly ordered CLDIs exhibiting strong dichroism signals (Fig. 5.1b). Under all loading conditions, the less mature bone marrow monocytes were free of cargo. At a population level, these trends were confirmed by multi-parameter image-based cytometric analyses (Fig. 5.1c, d).

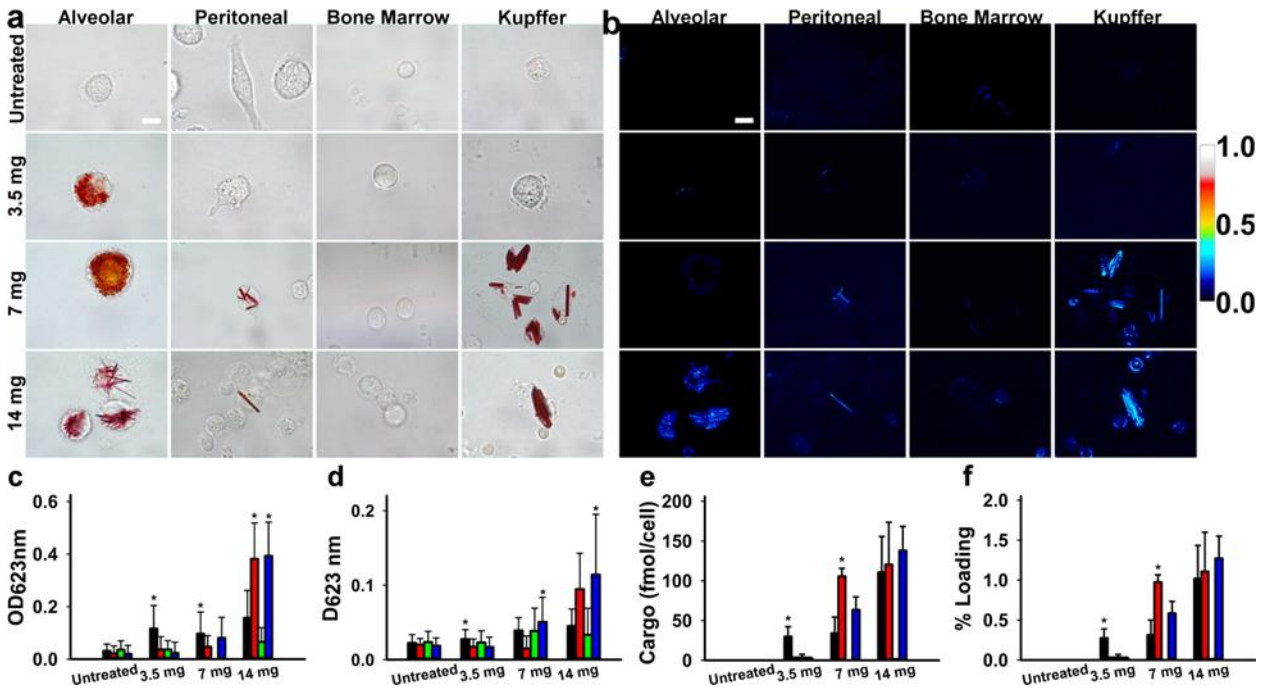

Figure 5.1 Microscopic imaging cytometry reveals variations in cargo loading of macrophage and monocyte populations.
a, Brightfield images of isolated macrophage and monocytes following increasing whole-body cargo loading. **b,** Linear diattenuation images of isolated macrophage and monocytes following increasing whole-body cargo loading. **c,** Mean optical density of alveolar macrophage (black), peritoneal macrophage (red), bone marrow monocyte (green), and Kupffer cell (blue) at increasing cargo loading. **d,** Mean linear diattenuation of alveolar macrophage (black), peritoneal macrophage (red), bone marrow monocyte (green), and Kupffer cell at increasing cargo loading. **e,** Mean cargo loading per xenobiotic-sequestering cell at increasing cargo loading. **f,** Percentage of maximal cargo loading within each cell type at increasing cargo loading. Error bars represent standard deviation. (n = 150 cells per time point for imaging studies, n = 3 mice per cargo treatment for drug accumulation, * = $p < 0.05$, ANOVA, Tukey's HSD). Scale bar is 10 µm.

The results of chemical analyses confirmed the observed, uneven distribution of cargo amongst the different macrophage populations. At low (3.5 mg) cargo loading, alveolar

macrophages sequestered 29.9 ± 12.4 fmol of cargo/cell, with the other populations showing minimal loading (Fig. 5.1e). Within the alveolar macrophages, after a whole-body load of 3.5 mg, less than 0.3% of the maximal phagocytic capacity of the cells was reached (Fig. 5.1f). At a larger (7 mgs) whole-body cargo load, alveolar macrophages accumulated 34.0 ± 20.3 fmol cargo/cell, which primarily remained in disordered form as reflected in the low dichroism signal (Fig. 5.1b, d). Peritoneal and liver macrophage populations, due to their differential accumulation pattern (Fig. 5.1b), increased their cargo loading per cell to 105.7 ± 10.0 and 63.5 ± 16.2 fmol/cell, respectively. At the highest loads of cargo (14 mgs), alveolar, peritoneal, and liver macrophage populations showed similar levels of cargo loading (Fig. 5.1e). By accumulating cargo as CLDIs, the macrophages maximized intracellular cargo loading. The highest cargo volume corresponded to ~ 1% of the reported, maximal phagocytic capacity of macrophages (Fig. 5.1f)[8]. Thus, with CLDI formation, only a small fraction of the potential, intracellular cargo space was occupied at the highest loading capacity measured *in vivo*.

In order to efficiently accommodate this massive cargo load, macrophages also adjusted their intracellular membrane organization. At low levels of loading (3.5 mgs), the alveolar macrophage population accumulated an average of 21.6 ± 5.0 vesicles per cell, with each vesicle occupying a mean volume of 0.43 ± 0.29 μm^3 (Table 5.1). Transmission electron micrographs of alveolar macrophages revealed numerous dark, lipid bound inclusions within the cytoplasm (Fig. 5.2a). An even larger (7 mgs) whole-body cargo load resulted in the cytoplasmic vesicles increasing to 32.6 ± 6.8 per cell ($n = 30$ cells, $p < 0.05$, ANOVA, Tukey's HSD), with the vesicular volume slightly increasing to 0.97 ± 0.96 μm^3 (Table 5.1). Nevertheless, at 14 mg of cargo loading, the AMΦ's membrane bound cargo compartment was visibly expanded (Fig. 5.2b). At this point, the number of loaded vesicles per cell dropped to 18.4 ± 11.1 and their

volume increased to 13.8 ± 10.4 μm^3. The larger, solid, membrane bound compartments were stable and remained within the macrophage even after an eight-week cargo washout period (Fig. 5.2c).

Table 5.1 Changes in vesicle number, size, and volume occupancy in cargo-treated alveolar macrophages.

Cargo Loading	Mean number of vesicles per cell (n=30 cells)	Mean vesicle volume (n=50 vesicles)	Mean total volume occupied by vesicles (n=50 vesicles)
3.5 mg	21.6 ± 5.0	0.43 ± 0.29 μm^3	9.2 ± 6.7 μm^3
7 mg	32.6 ± 6.8*	0.97 ± 0.96 μm^3	31.7 ± 32.1 μm^3
14 mg	18.4 ± 11.1	13.8 ± 10.4 μm^3*	253.8 ± 244.5 μm^3

(* = $p < 0.05$, ANOVA, Tukey's HSD).

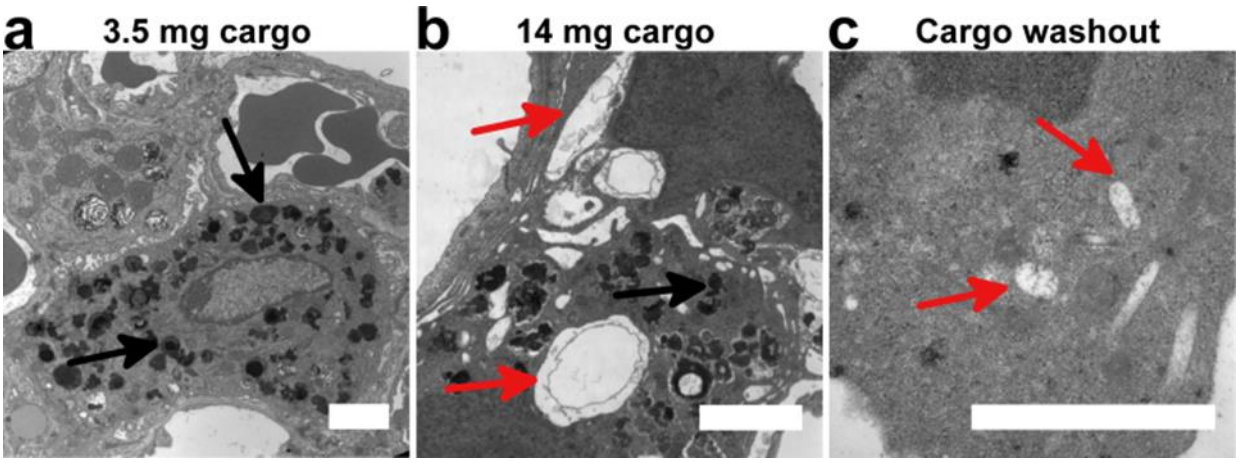

Figure 5.2 Cargo accumulation induces reorganization in the internal membrane architecture of macrophages.
a, Following whole-body loading of 3.5 mg of the cargo volume marker, macrophages of the lung are loaded with small vesicles that fill the cytoplasm. **b,** Increasing doses of the marker results in the accumulation of crystal-like drug inclusions (CLDIs) throughout the cytoplasm. **c,** These larger aggregates remain stable intracellularly even following an eight-week washout period. Black arrows denote cargo-laden vesicles and red arrows denote cavities left from CLDIs removed during sample preparation. Scale bars are 2000 nm.

5.6.2 Insoluble cargo accounts for majority of intracellular loading, and leads to increased volume of distribution.

Of noteworthy significance, the amount of cargo in the isolated macrophage populations effectively accounted for most of the total cargo load measured in whole organ homogenates (Table 5.2). Based on the amount of cargo within each organ, the volume of blood that was cleared by the macrophages in the different organs was estimated (the organ-specific Volume of Distribution, Vo_D; Table 5.3). In pharmacokinetic terms, the whole body V_D of a molecule is the ratio between the amount of drug in the organism and the plasma concentration of the drug[35]. V_D represents the extent of tissue distribution[36] as reflected in the theoretical volume required to contain an administered amount of drug, at the same concentration as found in the plasma. With an increasing cargo load, each macrophage population significantly contributed to the increase in V_{OD} and hence, to V_D (Table 5.3). Given that the volume of a single macrophage is ~ 1 pL, the macrophages' contribution to V_D was mostly due to the solute-to-solid phase transition that accompanied CLDI formation. At the whole organ level, there was a nearly 100-fold increase in the V_{OD} within the liver and small intestine, a 60-fold increase within the spleen, and a 10-fold increase within the lung upon increasing the whole-body cargo loading from 5.25 to 14 mg (Table 5.4). Within the fat and kidney, which do not contain the large populations of tissue macrophages typical of the previously mentioned organs, there were modest increases in the V_{OD}, but nowhere near the increases in V_{OD} observed in liver, spleen, lung and intestine (Table 5.4).

Table 5.2 Estimated cargo loading within liver, spleen, and lung macrophages following 14 mg of cargo loading.

Macrophage Population	Cargo mass (mg)	Percent Xenobiotic Sequestering	Total Xenobiotic Sequestering Population	Fmol Cargo/Xenobiotic Sequestering Cell	% Cell Volume Occupied by Cargo
Liver	4.57 ± 0.78	88.5 ± 3.3%	$8.0 \times 10^7 \pm 1.9 \times 10^7$	120.9 ± 35.3	2.11 ± 0.62%
Spleen	3.23 ± 0.27	83.9 ± 12.5%	$2.2 \times 10^7 \pm 5.9 \times 10^6$	310.5 ± 86.9	5.42 ± 1.52%
Lung	0.32 ± 0.06	81.1 ± 3.2%	$3.7 \times 10^6 \pm 1.7 \times$	183.2 ± 91.5	3.20 ± 1.60%

			10^6		

Table 5.3 Volume of distribution of cargo marker in liver, lung, and spleen macrophage, at 5.25 and 14 mg of whole-body loading

Macrophage Population	5.25 mg cargo V_{OD} (nL/macrophage)	14 mg cargo V_{OD} (nL/macrophage)
Liver	$0.66 \pm 9.8x10^{-5}$	33.51 ± 0.01*
Lung	$5.51 \pm 9.5x10^{-5}$	42.73 ± 0.01*
Spleen	$0.49 \pm 2.5x10^{-4}$	64.25 ± 0.01*

(* = $p < 0.05$, Two-Tailed Student's T-Test)

Table 5.4 Volume of distribution of cargo marker in various organs, at 5.25 and 14 mg of whole-body loading

Tissue (n=3 per treatment)	5.25 mg cargo V_{OD} (L/kg tissue)	14 mg cargo V_{OD} (L/kg tissue)
Liver	33.9 ± 13.1	2232.5 ± 958.2*
Spleen	118.8 ± 85.4	6139.3 ± 2637.0*
Fat	91.8 ± 15.2	129.1 ± 61.1
Jejunum and Ileum	11.1 ± 6.3	1085.2 ± 606.2*
Lung	91.2 ± 12.0	902.3 ± 524.1
Kidney	31.1 ± 7.3	125.6 ± 55.5

(* = $p < 0.05$, Two-Tailed Student's T-Test)

5.6.3 Macrophages are necessary to acquire and stabilize intracellular cargo

Interestingly, the number of macrophages in various organs increased following loading with the maximum cargo treatment (Fig. 5.3a). Thus, to test whether macrophages played an active role in determining cargo accumulation and distribution, liposomal clodronate injections were used to deplete hepatic and splenic macrophages[32]. Following clodronate treatment, the cargo carrying capacity of liver and spleen was significantly reduced. However, within the kidney, which did not undergo depletion, there was no significant reduction in cargo load (Fig. 5.3b). Quantitatively, due to the reduction in macrophage numbers (Fig. 5.3c), there was a concomitant reduction in CLDI accumulation within the liver and spleen (Fig. 5.3d). Most interestingly, cargo loading within liver and spleen macrophages was similar between the two treatment groups (Fig. 5.3e). Furthermore, the serum concentration of clofazimine was similar between the groups (Fig. 5.3f), indicating that the effects of clodronate on cargo accumulation

were specifically due to macrophage depletion, and not to a decrease in circulating drug concentrations or an associated decrease in drug bioavailability, absorption or macrophage loading, which would have been apparent as a decrease in drug accumulation in the remaining macrophages. Finally, injecting CLDIs directly into the peritoneal cavity of macrophage-depleted mice led to a significant reduction in half-life compared to their control, PBS-treated counterparts (Fig. 5.3g). The peritoneal macrophages imparted stability to the injected CLDI by internalizing them via phagocytosis, while extracellular CLDIs degraded more rapidly (Fig. 5.3h). These results indicate that the macrophages are actively involved in the sequestration and stabilization of cargo as insoluble, highly organized, and biocompatible supramolecular complexes.

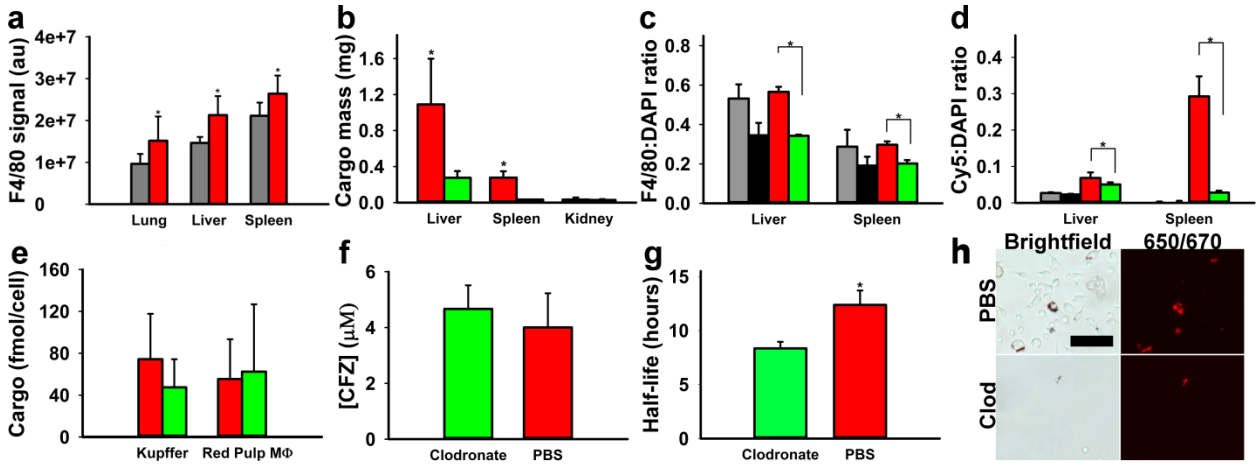

Figure 5.3 Macrophages increase in number and actively sequester cargo (primarily by stabilizing it in an insoluble form).
a, Comparison of total F4/80 macrophage signal in untreated (grey) and 14 mg cargo loading (red) tissue sections. **b,** Total cargo loading in PBS- (red) and clodronate-liposome (green) tissues. **c,** Quantification of tissue macrophage population in PBS-vehicle diet (grey), clodronate-vehicle diet (black), PBS-cargo diet (red), and clodronate-cargo diet (green) using F4/80 signal. **d,** Quantification of insoluble cargo accumulation in PBS-vehicle diet (grey), clodronate-vehicle diet (black), PBS-cargo diet (red), and clodronate-cargo diet (green) using Cy5 fluorescence. **e,** Individual macrophage cargo loading in PBS-cargo diet (red) and clodronate-cargo diet (green). **f,** Serum concentration of clofazimine in clodronate- and PBS-cargo diet treatment groups. **g,** Estimated half-life of injected CLDIs within peritoneal cavity of clodronate and PBS liposome

treated mice. **h,** Peritoneal lavage of PBS and clodronate treated liposome groups 48 hours post injection. Scale bar is 50 μm. Error bars represent standard deviation (* = $p < 0.05$, Student's Two-tailed T-test or ANOVA, Tukey's HSD).

5.7. Discussion

While the volume of distribution of most hydrophobic drugs is typically ascribed to drug partitioning into adipose tissue, the experimental results presented in this study indicate how macrophages can account for most of the accumulation and distribution of the reporter probe *in vivo*, with macrophage cargo carrying capacity increasing in parallel to the increase in whole body load. In the experiments reported in this study, the mass and volume of cargo per cell was nowhere near the maximal cargo capacity of macrophages, as determined *in vitro* following phagocytosis of spherical beads of increasing size[8]. When macrophages of the liver and spleen were depleted, there was a reduction in the whole-organ cargo carrying capacity in proportion to the decrease in the macrophage population, but the cargo carrying capacity of the remaining macrophages was unaffected. There has been extensive research in the past on how therapeutic agents can impact the immune system[37]. However, few, if any, small molecule drugs have been shown to have their ADME properties dependent on the action of macrophages or other specific populations of immune cells. Using clofazimine as a weakly basic reporter molecule[38], we found that the extent of tissue distribution was actively impacted by the action of tissue macrophages. Lung and liver macrophages are often where bacteria reside during persistent bacterial infections (particularly with infections of *Mycobacterium tuberculosis*[39] and *Mycobacterium leprae*[40]). By extension, the efficacy of many of the antibiotics used to treat these infections may be dependent on a synergistic interaction between the macrophages, which harbor these intracellular

pathogens, and the antibiotic, which is sequestered by these cells and ultimately destroys these pathogens.

Most interestingly, our results indicate that macrophage-mediated small molecule drug sequestration can have a profound impact on pharmacokinetics. While it is often assumed that the volume of distribution of a therapeutic is a constant, and is only significantly impacted by disease states affecting organ function[41,42], our measurements indicate that this is not necessarily the case. Rather, in the case of drugs that show significant levels of bioaccumulation, undergo phase transitions (solute-solid or solute-amorphous), or are able to become concentrated within particular cellular populations, it is possible that the volume that the drug distributes can change significantly as treatment progresses. With clofazimine, this remarkable phenomenon was first evident as a significant reduction in the plasma concentration of the drug from weeks 3 to 8 in treatment[22]. Concurrently, in this study we found a ~100-fold increase in the organ-specific volume of distribution (V_{OD}) within the liver and spleen, and a ~10-fold increase of V_{OD} within the lung. The blood volume cleared by different organs corresponded to the extent of loading of the macrophages in those organs, with the spleen showing the highest loading per unit tissue weight, followed by liver and lung[22]. The preferential accumulation of the cargo in spleen was primarily associated with the accumulation of drug molecules as an insoluble, ordered supramolecular aggregates[43]. By depleting the macrophages of the liver and spleen with clodronate, we deduce that this phenomenon is largely due to the action of macrophages. Beyond clofazimine, it is known that the intracellular sequestration of other hydrophobic, cationic drugs such as amiodarone[44] or quinacrine[45] is highly dependent on the proton pump V-ATPase, which is expressed at higher levels within macrophages[5]. Thus, beyond clofazimine, this mechanism is likely to impact the pharmacokinetics of other therapeutic agents.

In terms of the biological mechanisms that underpin their ability to sequester an increasingly massive load of cargo, the macrophage endolysosomal system is particularly adept at accommodating an increasing cargo load due to the low pH and high chloride environment of their lysosome (Chapter 2)[43]. The high levels of V-ATPase expressed in macrophage lysosomes are a likely explanation for the active solute to solid transition that seems to occur selectively within these cells. Due to the active concentrative proton and chloride pumping[46] within the endolysosomal system, massive amounts of solid cargo can be sequestered and accommodated within membrane bound intracellular compartments. In addition to the activity of lysosomal proton and chloride transporters present in macrophage lysosomes, these cells can also alter their internal membrane architecture to maximize the volume of cargo within a minimal amount of membrane surface area. As our results indicate, at low levels of cargo treatment, macrophages acquired soluble cargo in the form of small, spherical vesicles. Continued accumulation of cargo led to the formation of larger volume vesicles and to the disappearance of the smaller vesicles. We infer that, by expanding the volume of intracellular vesicles, macrophages maximized the available cargo space while minimizing the overall membrane surface area delimiting the cargo compartments[47,48], allowing for increased cargo accumulation within the cell, and consequently, an increase in V_{OD}.

In addition to the adaptive changes that were observed to occur at the level of the individual macrophages, measurements of the entire cell population of liver, lung, and spleen indicated an increase in the number of macrophages occurring in parallel to the increase in cargo loading. Pathologically, an expansion in the macrophage population is typically associated with a pro-inflammatory response[49,50]. However, the accumulation of insoluble intracellular drug cargo in macrophages of clofazimine-treated animals was accompanied by the activation of anti-

inflammatory signaling pathways and was not associated with obvious toxicological manifestations[29,51]. As a candidate anti-inflammatory signaling mechanism, it is possible that the lysosomal accumulation of weakly basic molecules may induce activation of transcription factor EB (TFEB)[52,53]. Increased cargo loading can therefore lead to TFEB becoming chronically activated, resulting in increased lysosomal biogenesis, which would reduce lysosomal stress and actively allow for increased intracellular cargo sequestration. Nevertheless, because this macrophage-mediated drug sequestration phenomenon is also linked to concomitant changes in organ mass (e.g. splenomegaly[22]) and histological organization (e.g. granuloma formation[22,54]), these results warrant additional studies into the functional sequelae of the pro- and anti-inflammatory signaling mechanisms that are activated in response to a massive intracellular cargo load.

5.8. Conclusion

To conclude, the results presented in this study point to a stimulus-dependent, macrophage-mediated biological response mechanism that is activated by the extent of cargo accumulation in these cells. In this process, macrophages actively stabilize intracellular drug as insoluble complexes that are trapped within membrane-bound compartments. To accommodate increasingly massive loads of cargo, macrophages increase in numbers and adapt their intracellular membrane organization so as to maximize the intracellular cargo space. While resident macrophages of different organs demonstrated significant variations in their response to increasing loads of cargo, all differentiated macrophage populations were capable of sequestering large loads of cargo. The adaptive cargo carrying capacity of macrophages ultimately accounted for the observed increment in the drug volume of distribution, which was

directly measured based on the amount of drug cargo sequestered within each organ. Of noteworthy significance, to our knowledge, this is the first time that the volume of distribution of a small molecule drug has been directly measured and associated with an adaptive, immune system-mediated biological response.

5.9. Acknowledgements

The authors acknowledge funding from the University of Michigan M-Cubed program and NIH grant RO1GM078200.

5.10. References

1 Epelman, S., Lavine, K. J. & Randolph, G. J. Origin and Functions of Tissue Macrophages. *Immunity* **41**, 21-33 (2014).

2 Murray, P. J. & Wynn, T. A. Protective and pathogenic functions of macrophage subsets. *Nature Reviews Immunology* **11**, 723-737 (2011).

3 Davies, L. C., Jenkins, S. J., Allen, J. E. & Taylor, P. R. Tissue-resident macrophages. *Nat Immunol* **14**, 986-995, doi:10.1038/ni.2705 (2013).

4 Mindell, J. A. Lysosomal Acidification Mechanisms. *Annual Review of Physiology* **74**, 69-86, doi:doi:10.1146/annurev-physiol-012110-142317 (2012).

5 Wang, S.-P., Krits, I., Bai, S. & Lee, B. S. Regulation of Enhanced Vacuolar H+-ATPase Expression in Macrophages. *Journal of Biological Chemistry* **277**, 8827-8834, doi:10.1074/jbc.M111959200 (2002).

6 Hamczyk, M. R., Villa-Bellosta, R. & Andrés, V. in *Methods in Mouse Atherosclerosis* (eds Vicente Andrés & Beatriz Dorado) 235-246 (Springer New York, 2015).

7 Steinberg, B. E. & Grinstein, S. Analysis of macrophage phagocytosis: quantitative assays of phagosome formation and maturation using high-throughput fluorescence microscopy. *Methods in molecular biology (Clifton, N.J.)* **531**, 45-56, doi:10.1007/978-1-59745-396-7_4 (2009).

8 Cannon, G. J. & Swanson, J. A. The macrophage capacity for phagocytosis. *Journal of Cell Science* **101**, 907-913 (1992).

9 Broz, P. *et al.* Inhibition of macrophage phagocytotic activity by a receptor-targeted polymer vesicle-based drug delivery formulation of pravastatin. *Journal of cardiovascular pharmacology* **51**, 246-252, doi:10.1097/FJC.0b013e3181624aed (2008).

10 Hirota, K. & Terada, H. in *Molecular Regulation of Endocytosis* (ed Brian Ceresa) Ch. 16 (InTech, 2012).

11 Lemaire, S., Tulkens, P. M. & Van Bambeke, F. Cellular Pharmacokinetics of the Novel Biaryloxazolidinone Radezolid in Phagocytic Cells: Studies with Macrophages and Polymorphonuclear Neutrophils. *Antimicrobial Agents and Chemotherapy* **54**, 2540-2548, doi:10.1128/aac.01723-09 (2010).

12 Carryn, S. *et al.* Intracellular pharmacodynamics of antibiotics. *Infectious disease clinics of North America* **17**, 615-634 (2003).

13 Stamler, D. A., Edelstein, M. A. & Edelstein, P. H. Azithromycin pharmacokinetics and intracellular concentrations in Legionella pneumophila-infected and uninfected guinea pigs and their alveolar macrophages. *Antimicrob Agents Chemother* **38**, 217-222 (1994).

14 Foulds, G., Shepard, R. M. & Johnson, R. B. The pharmacokinetics of azithromycin in human serum and tissues. *Journal of Antimicrobial Chemotherapy* **25**, 73-82, doi:10.1093/jac/25.suppl_A.73 (1990).

15 Logan, R., Kong, A. C., Axcell, E. & Krise, J. P. Amine-Containing Molecules and the Induction of an Expanded Lysosomal Volume Phenotype: A Structure–Activity Relationship Study. *Journal of Pharmaceutical Sciences* **103**, 1572-1580, doi:http://dx.doi.org/10.1002/jps.23949 (2014).

16 Funk, R. & Krise, J. Cationic amphiphillic drugs cause a marked expansion of apparent lysosomal volume: implications for an intracellular distribution-based drug interaction. *Mol. Pharmaceutics* **9**, 1384-1395, doi:10.1021/mp200641e (2012).

17 Kaufmann, A. & Krise, J. Lysosomal Sequestration of Amine-Containing Drugs: Analysis and Therapeutic Implications. *Journal of Pharmaceutical Sciences* **96**, 729-746, doi:DOI 10.1002/jps (2006).

18 Arbiser, J. & Moschella, S. Clofazimine: A review of its medical uses and mechanisms of action. *Journal of the American Academy of Dermatology* **32**, 241-247, doi:doi:10.1016/0190-9622(95)90134-5 (1995).

19 Cholo, M., Steel, H., Fourie, P., Germishuizen, W. & Anderson, R. Clofazimine: current status and future prospects. *Journal of Antimicrobial Chemotherapy*, doi:10.1093/jac/dkr444 (2011).

20 DrugBank. (drugbank.ca, 2013).

21 Baik, J. & Rosania, G. R. Macrophages Sequester Clofazimine in an Intracellular Liquid Crystal-Like Supramolecular Organization. *PLoS ONE* **7**, e47494, doi:10.1371/journal.pone.0047494 (2012).

22 Baik, J., Stringer, K. A., Mane, G. & Rosania, G. R. Multiscale Distribution and Bioaccumulation Analysis of Clofazimine Reveals a Massive Immune System-Mediated Xenobiotic Sequestration Response. *Antimicrob. Agents. Chemother.* **57**, 1218-1230 (2013).

23 Sukpanichnant, S. *et al.* Clofazimine-induced crystal-storing histiocytosis producing chronic abdominal pain in a leprosy patient. *Am J Surg Pathol* **24**, 129-135 (2000).

24 Keswani, R., Yoon, G., Sud, S., Stringer, K. & Rosania, G. A Far-Red Fluorescent Probe For Flow Cytometric Xenobiotic-Sequestering Cell Functional Studies. *Cytometry Part A* (2015).

25 Keswani, R. *et al.* Chemical Analysis of Drug Biocrystals: A Role for Counterion Transport Pathways in Intracellular Drug Disposition. *Molecular Pharmaceutics*, doi:10.1021/acs.molpharmaceut.5b00032 (2015).

26 Rzeczycki, P. *et al.* Detecting ordered small molecule drug aggregates in live macrophages: a multi-parameter microscope image data acquisition and analysis strategy. *Biomed. Opt. Express* **8**, 860-872, doi:10.1364/BOE.8.000860 (2017).

27 Schneider, C. A., Rasband, W. S. & Eliceiri, K. W. NIH Image to ImageJ: 25 years of image analysis. *Nat Meth* **9**, 671-675 (2012).

28 Abramoff, M. D., Magalhaes, P. J. & Ram, S. J. Image Processing With ImageJ. *Biophotonics International* **11**, 36-42 (2004).

29 Yoon, G. *et al.* Phagocytosed Clofazimine Biocrystals can Modulate Innate Immune Signaling by Inhibiting TNF Alpha and Boosting IL-1RA Secretion. *Mol. Pharmaceutics*, doi:10.1021/acs.molpharmaceut.5b00035 (2015).

30 Lee, S., Starkey, P. & Gordon, S. Quantitative analysis of total macrophage content in adult mouse tissues. Immunochemical studies with monoclonal antibody F4/80. *J Exp Med* **161**, 475-489 (1985).

31 Champion, J. A. & Mitragotri, S. Role of target geometry in phagocytosis. *Proceedings of the National Academy of Sciences of the United States of America* **103**, 4930-4934, doi:10.1073/pnas.0600997103 (2006).

32 van Rooijen, N. & Hendrikx, E. in *Liposomes* Vol. 605 *Methods in Molecular Biology* (ed Volkmar Weissig) Ch. 13, 189-203 (Humana Press, 2010).

33 Mehta, S. B., Shribak, M. & Oldenbourg, R. Polarized light imaging of birefringence and diattenuation at high resolution and high sensitivity. *Journal of Optics* **15**, 094007 (2013).

34 Oldenbourg, R. Polarized light microscopy: principles and practice. *Cold Spring Harb Protoc* **2013**, doi:10.1101/pdb.top078600 (2013).

35 Toutain, P. L. & Bousquet-MÉLou, A. Volumes of distribution. *Journal of Veterinary Pharmacology and Therapeutics* **27**, 441-453, doi:10.1111/j.1365-2885.2004.00602.x (2004).

36 Smith, D. A., Beaumont, K., Maurer, T. S. & Di, L. Volume of Distribution in Drug Design. *Journal of Medicinal Chemistry* **58**, 5691-5698, doi:10.1021/acs.jmedchem.5b00201 (2015).

37 Kidd, B. A. *et al.* Mapping the effects of drugs on the immune system. *Nat Biotech* **34**, 47-54, doi:10.1038/nbt.3367 http://www.nature.com/nbt/journal/v34/n1/abs/nbt.3367.html#supplementary-information (2016).

38 Logan, R., Funk, R. S., Axcell, E. & Krise, J. P. Drug-drug interactions involving lysosomes: mechanisms and potential clinical implications. *Expert Opin Drug Metab Toxicol* **8**, 943-958, doi:10.1517/17425255.2012.691165 (2012).

39 Flynn, J. L. & Chan, J. Immunology of tuberculosis. *Annual review of immunology* **19**, 93-129, doi:10.1146/annurev.immunol.19.1.93 (2001).

40 Organization, W. H. *Leprosy*, <http://www.who.int/mediacentre/factsheets/fs101/en/> (2015).

41 Blot, S. I., Pea, F. & Lipman, J. The effect of pathophysiology on pharmacokinetics in the critically ill patient — Concepts appraised by the example of antimicrobial agents. *Advanced Drug Delivery Reviews* **77**, 3-11, doi:http://dx.doi.org/10.1016/j.addr.2014.07.006 (2014).

42 Shammas, F. V. & Dickstein, K. Clinical pharmacokinetics in heart failure. An updated review. *Clinical pharmacokinetics* **15**, 94-113, doi:10.2165/00003088-198815020-00002 (1988).

43 Woldemichael, T. *et al.* Reverse Engineering the Intracellular Self-Assembly of a Functional Mechanopharmaceutical Device. *Submitted manuscript* (2017).

44 Morissette, G. *et al.* Intracellular sequestration of amiodarone: role of vacuolar ATPase and macroautophagic transition of the resulting vacuolar cytopathology. *Br J Pharmacol* **157**, 1531-1540, doi:10.1111/j.1476-5381.2009.00320.x (2009).

45 Marceau, F., Bawolak, M. T., Bouthillier, J. & Morissette, G. Vacuolar ATPase-mediated cellular concentration and retention of quinacrine: a model for the distribution of lipophilic cationic drugs to autophagic vacuoles. *Drug metabolism and disposition: the biological fate of chemicals* **37**, 2271-2274, doi:10.1124/dmd.109.028480 (2009).

46 Leisle, L., Ludwig, C. F., Wagner, F. A., Jentsch, T. J. & Stauber, T. ClC-7 is a slowly voltage-gated 2Cl(−)/1H(+)-exchanger and requires Ostm1 for transport activity. *The EMBO Journal* **30**, 2140-2152, doi:10.1038/emboj.2011.137 (2011).

47 Stachowiak, J. C., Brodsky, F. M. & Miller, E. A. A cost-benefit analysis of the physical mechanisms of membrane curvature. *Nat Cell Biol* **15**, 1019-1027, doi:10.1038/ncb2832 (2013).

48 Vigant, F., Santos, N. C. & Lee, B. Broad-spectrum antivirals against viral fusion. *Nat Rev Micro* **13**, 426-437, doi:10.1038/nrmicro3475 (2015).

49 Movita, D. *et al.* Inflammatory Monocytes Recruited to the Liver within 24 Hours after Virus-Induced Inflammation Resemble Kupffer Cells but Are Functionally Distinct. *Journal of Virology* **89**, 4809-4817, doi:10.1128/jvi.03733-14 (2015).

50 Shi, C. & Pamer, E. G. Monocyte recruitment during infection and inflammation. *Nature Reviews Immunology* **11**, 762-774 (2011).

51 Yoon, G. S. *et al.* Clofazimine Biocrystal Accumulation in Macrophages Upregulates Interleukin 1 Receptor Antagonist Production To Induce a Systemic Anti-Inflammatory State. *Antimicrob Agents Chemother* **60**, 3470-3479, doi:10.1128/aac.00265-16 (2016).

52 Napolitano, G. & Ballabio, A. TFEB at a glance. *Journal of Cell Science*, doi:10.1242/jcs.146365 (2016).

53 Zhitomirsky, B. & Assaraf, Y. G. Lysosomal sequestration of hydrophobic weak base chemotherapeutics triggers lysosomal biogenesis and lysosome-dependent cancer multidrug resistance. *Oncotarget* **6**, 1143-1156 (2015).

54 Trexel, J. *et al.* Macrophage-Mediated Clofazimine Sequestration Is Accompanied by a Shift in Host Energy Metabolism. *J Pharm Sci* **106**, 1162-1174, doi:10.1016/j.xphs.2016.12.009 (2017).

Chapter 6: Conclusions and Future Outlook

6.1 General Conclusions

In this dissertation, we have investigated two of the key features of pharmacokinetic properties of drugs: the phase-transition-dependent subcellular accumulation and stabilization processes. We specifically focused on weak base compounds as they are the most developed and marketed drugs. Moreover, we chose clofazimine (CFZ), an FDA-approved, weakly basic and poorly soluble antibiotic used as part of the standard treatment of leprosy[1], as our model drug. Upon prolonged oral administration, CFZ accumulates in macrophages of mice as well as humans in the form of insoluble complexes known as Crystal-Like Drug Inclusions (CLDIs)[2-4]. These insoluble complexes have been chemically characterized to contain hydrochloride salts of CFZ (CFZ-H^+Cl^-) crystals[5]. However, little is known regarding the biomolecular mechanisms that determine the intracellular formation and stabilization of drug salt crystals in a physiological manner[2].

Thus, based on the well-established lysosomotropic[6] phenomenon of weak base drugs, which elaborates that weak base drug accumulation occurs in cells, more specifically in lysosomes based on the low lysosomal pH environment that ionizes the weak based drug and sequesters it within the lysosomes, we hypothesized that the physiological cellular drug bioaccumulation and stabilization of CFZ is highly interconnected with endolysosomal ion homeostasis and function. Accordingly, we confirmed the physiological lysosomal accumulation of CFZ-H^+Cl^- in relation to the drug's physicochemical properties, such as pH_{max}, K_{sp}, intrinsic

free base solubility, intrinsic salt solubility, and apparent pK_a. Furthermore, we investigated the roles of lysosomal proton and chloride transporters, which regulate cellular ion homeostasis, and their potential involvement in the formation and stabilization of CFZ-H^+Cl^- crystal in macrophage lysosomes (Chapter 2).

Using a mathematical modeling and simulation approach, the experimentally measured[7,8] rate of intracellular CFZ-H^+Cl^- salt formation in macrophages (0.01 – 1 picomol/cell/day) was investigated in relation to the maintenance of physiological conditions with respect to different numbers of V-ATPase molecules/lysosome (0 - 300), chloride channels/lysosome (0 - 5000), lysosomal membrane proton permeability ($6x10^{-5}$ to 6 cm/s), and cytoplasmic chloride concentration (0 - 10 mM). The simulation results were further confirmed in wet lab experiments where pharmacological inhibitors of proton and chloride channels were used to observe their individual effects on CFZ-H^+Cl^- accumulation. Moreover, drug accumulation and formation of CFZ-H^+Cl^- was confirmed using CFZ's bathochromic shift in fluorescence upon protonation and epifluorescence microscopy.

Collectively, our modeling and simulation results, as well as wet lab experimental findings point to a critical role of the number of lysosomal V-ATPases in the formation of a hydrochloride salt form of a weak base drug in macrophage lysosomes, as has been reported with clofazimine. While the V-ATPase proton-pump is needed to maintain lysosomal physiology in the presence of CFZ-H^+Cl^- crystal formation, pharmacological experiments reveal that agents inhibiting its function influence the rate of intracellular CFZ-H^+Cl^- crystal formation to a much greater extent than agents inhibiting chloride transport mechanisms. Thus, the variations in the number of V-ATPases present on lysosomal membranes suffice to explain the differences in the

phase-transition-dependent accumulation and stabilization of CFZ-H^+Cl^- crystals in macrophages vs. other cell types in a manner that is consistent with the drug's physicochemical properties.

Moreover, given the heterogeneous size and shape of lysosomal morphologies[6,9,10], and the pleiotropic effects of weak base drugs on lysosomal structure and function[11,12], we investigated the relationship between the different lysosomal morphologies and lysosomal physiology, and how perturbations of lysosomal physiology[12-14] affect the maintenance of lysosomal ion homeostasis to elucidate the key factors which determine the toxicological effects of lysosomotropic agents, in a cell-type dependent manner (Chapter 3). Accordingly, we used a computational approach to explore the mechanisms of drug-induced lysosomal stress and stress tolerance. For this purpose, we utilized a well-established physiological model of lysosomal ion regulation, and transiently altered the model parameters, both individually and in combination. We assessed the effects of these perturbations on lysosomal physiology by monitoring the downstream dynamics of lysosomal pH, chloride, and membrane electrical potential. The results point to variations in proton transport properties as the main mechanistic determinant of lysosomal stress sensitivity and resistance. Furthermore, we discuss the effects of drugs that are known to inhibit lysosomal membrane channels and accumulate in the lysosomes, such as lysosomotropic and cationic amphiphilic drugs in relation to cell-type specific variations in the mechanisms of stress tolerance.

In Chapter 4, we broaden our studies regarding phase-transition-dependent drug accumulation and stabilization by using a cellular model with various subcellular compartments, comprised of key cellular features, such as pH, membrane potential, and lipid content, all of which impact drug accumulation and stability within cells. Using our model drug, CFZ, we investigated the subcellular distribution and stability of the different species of the drug as a

function of a total extracellular drug concentration. The distribution of the soluble drug species in the non-membrane environments were primarily dependent on pH and non-membrane lipid; whereas the phase transitions of free base CFZ and CFZ-H^+Cl^- salt were dictated by the physicochemical properties of the drug in relation to the cellular environment. Indeed, the degree of supersaturation of free base CFZ was observed in the membrane as well as non-membrane environments, whereas that of the CFZ-H^+Cl^- salt was substantial and specific to the lysosomal environment, suggesting that the precipitation of CFZ-H^+Cl^- salt is likely to occur in the lysosomes even at low (sub-micromolar to picomolar) initial total extracellular drug concentration.

6.2 Future Outlook

Characterization of pharmacokinetic properties of weak base drugs remains to be the most challenging and costly process in drug development and discovery. In this dissertation, we have highlighted the importance of mathematical modeling approach to monitor and investigate the dynamic changes in cells and subcellular compartments, which are essential to our understanding of the behavior of weak base drugs in regards to their extent of accumulation, disposition, and stabilization in concert with the different cellular environments. Indeed, such approach can be done in conjunction with wet lab experiments to strengthen findings and conclusions. Moreover, results and conclusions from modeling and simulation experiments would aid the design of wet lab experiments, which are essential for understanding and characterizing PK properties of drugs in a cell-type dependent manner.

As we have observed from our findings (Chapter 2), cell-type specific protein levels, such as the Vacuolar ATPase (V-ATPase) do play significant role in the accumulation of weak

base drugs within subcellular organelles, such as the lysosome. Thus, designing wet-lab experiments that monitor key lysosomal protein levels in the presence of weak base drug accumulation in various cell types could help elucidate the physiological accommodation of drugs within cells. Indeed, this would be beneficial in classifying weak base drugs based on their physicochemical properties and their extent of cell-type dependent cellular accumulation. Furthermore, the study of cellular morphological rearrangement upon drug accumulation could be conducted to better characterize the relationship between drug-dose and cellular morphological changes that will be important in determining effective drug-dose regimen in a cell-type specific manner. Key cellular features, such as the translocation of Transcription Factor EB (TFEB) and the downstream lysosomal genes it regulates[15,16], could be monitored to understand their roles in drug-dose dependent cellular accumulation[17,18]. This is especially necessary to avoid the toxic effect of unregulated cellular expansion, which is implicated in various lysosomal storage diseases[19,20].

Furthermore, our findings emphasize the importance of understanding the phase-transition-dependent cellular accumulation and stabilization of weak base drugs. Given the various cellular properties such as pH, ion and lipid content within subcellular environments, including organelles and membranes, it is essential to understand the individual as well as combinatorial effects of these properties on the disposition and phase transition of drugs within cells. Our mathematical model (Chapter 4) could be used to perform further studies on phase-transition-dependent drug accumulation and stabilization in a cell-type dependent manner by varying certain model parameters. Indeed, this would establish the importance of cell-type dependent membrane and non-membrane lipids on drug disposition and stabilization in subcellular environments, which is a very novel and necessary arena that must be investigated.

Moreover, it would help not only experts in Pharmaceutical Sciences, but also in Biophysics, Cell Biology, and Genetics, to understand the relationship between membrane and non-membrane lipid and protein regulations, and their individual as well as combined effects on phase-transition-dependent drug accumulation and stabilization. Such understandings would be applicable to the mechanistic elucidation of drug-induced phospholipidosis and its impact on overall cell physiology and drug PK properties.

However, it is important to note the wet-lab experimental challenges associated with determining and simulating biological membranes with their corresponding lipid content (including lipid type). Thus, various combinations of lipid type as well as lipid amount must be considered when studying their impacts on drug accumulation and stabilization. Indeed, this is beneficial in understanding the stability and extent of cellular and subcellular drug accumulation in the pursuit of improved drug-targeting and efficacy. In addition, it would enable further investigation of drugs that have rather been neglected due to lack of full understanding of their physicochemical properties in relation to the physiology of their cellular environment. Thus, the interdisciplinary approach of phase-transition-dependent cellular drug accumulation and stabilization studies is warranted in current and future drug discovery and development fields.

6.3. References

1 Yawalkar, S. J. & Vischer, W. Lamprene (clofazimine) in leprosy. Basic information. *Lepr Rev* **50**, 135-144 (1979).

2 Baik, J., Stringer, K. A., Mane, G. & Rosania, G. R. Multiscale distribution and bioaccumulation analysis of clofazimine reveals a massive immune system-mediated xenobiotic sequestration response. *Antimicrob Agents Chemother* **57**, 1218-1230, doi:10.1128/AAC.01731-12 (2013).

3 Desikan, K. V., Ramanujam, K., Ramu, G. & Balakrishnan, S. Autopsy findings in a case of lepromatous leprosy treated with clofazimine. *Lepr Rev* **46**, 181-189 (1975).

4 Lewis, J. T., Candelora, J. N., Hogan, R. B., Briggs, F. R. & Abraham, S. C. Crystal-storing histiocytosis due to massive accumulation of charcot-leyden crystals: a unique association producing colonic polyposis in a 78-year-old woman with eosinophilic colitis. *Am J Surg Pathol* **31**, 481-485, doi:10.1097/01.pas.0000213420.46127.9c (2007).

5 Keswani, R. K. *et al.* Chemical Analysis of Drug Biocrystals: A Role for Counterion Transport Pathways in Intracellular Drug Disposition. *Mol Pharm* **12**, 2528-2536, doi:10.1021/acs.molpharmaceut.5b00032 (2015).

6 de Duve, C. *et al.* Commentary. Lysosomotropic agents. *Biochem Pharmacol* **23**, 2495-2531 (1974).

7 Min, K. A. *et al.* Massive Bioaccumulation and Self-Assembly of Phenazine Compounds in Live Cells. *Adv Sci (Weinh)* **2**, doi:10.1002/advs.201500025 (2015).

8 Baik, J. & Rosania, G. R. Molecular imaging of intracellular drug-membrane aggregate formation. *Mol Pharm* **8**, 1742-1749, doi:10.1021/mp200101b (2011).

9 Knapp, P. E. & Swanson, J. A. Plasticity of the tubular lysosomal compartment in macrophages. *J Cell Sci* **95 (Pt 3)**, 433-439 (1990).

10 Swanson, J., Burke, E. & Silverstein, S. C. Tubular lysosomes accompany stimulated pinocytosis in macrophages. *J Cell Biol* **104**, 1217-1222 (1987).

11 Morissette, G., Lodge, R. & Marceau, F. Intense pseudotransport of a cationic drug mediated by vacuolar ATPase: procainamide-induced autophagic cell vacuolization. *Toxicol Appl Pharmacol* **228**, 364-377, doi:10.1016/j.taap.2007.12.031 (2008).

12 Logan, R., Funk, R. S., Axcell, E. & Krise, J. P. Drug-drug interactions involving lysosomes: mechanisms and potential clinical implications. *Expert Opin Drug Metab Toxicol* **8**, 943-958, doi:10.1517/17425255.2012.691165 (2012).

13 Tapper, H. & Sundler, R. Role of lysosomal and cytosolic pH in the regulation of macrophage lysosomal enzyme secretion. *Biochem J* **272**, 407-414 (1990).

14 Zhao, H., Cai, Y., Santi, S., Lafrenie, R. & Lee, H. Chloroquine-mediated radiosensitization is due to the destabilization of the lysosomal membrane and subsequent induction of cell death by necrosis. *Radiat Res* **164**, 250-257 (2005).

15 Samie, M. A. & Xu, H. Lysosomal exocytosis and lipid storage disorders. *J Lipid Res* **55**, 995-1009, doi:10.1194/jlr.R046896 (2014).

16 Wang, W. *et al.* Up-regulation of lysosomal TRPML1 channels is essential for lysosomal adaptation to nutrient starvation. *Proc Natl Acad Sci U S A* **112**, E1373-1381, doi:10.1073/pnas.1419669112 (2015).

17 Lu, S., Sung, T., Lin, N., Abraham, R. T. & Jessen, B. A. Lysosomal adaptation: How cells respond to lysosomotropic compounds. *PLoS One* **12**, e0173771, doi:10.1371/journal.pone.0173771 (2017).

18 Moruno-Manchon, J. F. *et al.* TFEB ameliorates the impairment of the autophagy-lysosome pathway in neurons induced by doxorubicin. *Aging (Albany NY)* **8**, 3507-3519, doi:10.18632/aging.101144 (2016).

19 te Vruchte, D. *et al.* Accumulation of glycosphingolipids in Niemann-Pick C disease disrupts endosomal transport. *J Biol Chem* **279**, 26167-26175, doi:10.1074/jbc.M311591200 (2004).

20 Butler, J. D., Vanier, M. T. & Pentchev, P. G. Niemann-Pick C disease: cystine and lipids accumulate in the murine model of this lysosomal cholesterol lipidosis. *Biochem Biophys Res Commun* **196**, 154-159, doi:10.1006/bbrc.1993.2228 (1993).

APPENDICES

Appendix A

Supporting Information for Chapter 2

A.1. Additional Experimental Methods:

A.1.1. HPLC analysis.

For the HPLC assay, the mobile phase was methanol: water (80:20) with 0.1% trifluoroacetic acid (1 ml/min flow rate). The stationary phase (column) was a C18 (unbonded silica particles) column (Atlantis® T3, 5 µm, 100Å), and the HPLC was equipped with a UV detector (Waters, Photodiode Array Detector 2996) @ 285 nm detection for CFZ. The retention time for CFZ was determined to be 4.75 min.

A.1.2. Determination of solubility parameters.

We used a mathematical proof approach to determine $[CFZH^+]_S$ as detailed below: First, we calculated $[CFZH^+]$ using the total solubility (S_T) at each pH value and the constant intrinsic free base solubility, $[CFZ]_S$, using the following equation, which was obtained by rearranging the terms in equation (14) (see Chapter 2):

$$[CFZH^+] = S_T - [CFZ]_S \qquad \text{(Supplementary Equation 1)}$$

Then, we chose a value, say "y", from the list of the computed $[CFZH^+]$ values, and let "y" equal $[CFZH^+]_S$. By substituting "y' in place of $[CFZH^+]_S$, we calculated for total solubility at the different pH values using equation (15) (see main article). Then, we compared this total

solubility-pH dataset to that obtained using equation (13) (see Chapter 2). Then, we checked if there was the same total solubility value at a given pH in both datasets, which would represent the intersection point of the two solubility-pH curves mentioned previously. This can be represented by the following equation:

$$S_T' = [CFZ]_S + [CFZH^+]_S \qquad \text{(Supplementary Equation 2)}$$

Where S_T' is the total solubility value at the intersection of the two solubility-pH curves, and both forms of the drug, CFZ and $CFZH^+$, are present in equilibrium with their respective solid forms in the solid phase denoted by the subscript *s*.

Moreover, to prove if our earlier assumption ("y" is equal to $[CFZH^+]_S$) was valid, we calculated the total solubility by plugging "y" in place of $[CFZH^+]_S$, supplementary equation (2), and checked if it was equal to S_T'. Furthermore, by definition, the pH where both the intrinsic free base and salt forms of the drug are in the solid phase is known as pH_{max}. Thus, the pH associated with S_T' was deduced to be pH_{max}.

A.1.3. Modeling proton influx.

V-ATPase is an electrogenic proton-pump, which inserts protons from the cytoplasm into the lysosome against an electrochemical gradient upon ATP hydrolysis[1,2]. The rate at which a proton molecule is inserted per second (J_{HVATP}) was obtained from published experimental studies[1] as a function of transmembrane pH gradient (Δ pH) in units of pH unit and membrane potential difference, which is also interchangeably known as membrane potential (ΔΨ), in units of mV. This rate was multiplied by the total number of active V-ATPase molecules per lysosome

(N_{VATP}) to obtain the total amount of proton molecules inserted into the lysosome in units of molecules per second, as follows:

$$H_{pump} = N_{VATP} \times J_{H_{VATP}}(\Delta pH, \Delta \Psi) \qquad \text{(Supplementary Equation 3)}$$

Where lysosomal $\Delta\Psi$ is dictated by the total net change in lysosomal ion content and is represented by the following relationship[3]:

$$\Delta \Psi = \frac{F \times V_L}{C' \times S} \times [(\sum_i Z_i[\text{cations}]_i + \sum_i Z_i[\text{anions}]_i) - B] \qquad \text{(Supplementary Equation 4)}$$

Where V_L is the lysosomal volume in units of L; Faraday's constant (F) which equals 96485 Coulomb/mol and is used to convert the lysosomal ion content in units of moles to units of Coulomb; C' is the specific membrane capacitance per unit area of a biological membrane[4], which is experimentally approximated to be 1μF/cm^2 and is multiplied by the lysosomal surface area S represented in units of cm^2 to obtain the total lysosomal membrane capacitance; Z_i is valence for ion i; [cation] the concentration of cation i at a given time *t* in units of Molar; [anion] is the concentration of anion i at a given time *t* in units of Molar; B is the Donnan particles in units of Molar, which are impermeable lysosomal contents defined by initial lysosomal ion concentrations and net change in the intrinsic surface potentials, supplementary equation (5). In the model and simulations communicated herein, the initial lysosomal ions consist of proton, potassium, sodium, and chloride with their respective charge (+ or -1) represented as a coefficient of their respective concentration, which is denoted by the square brackets, supplementary equation (5).

$$B = [H^+]_{L,initial} + [K^+]_{L,initial} + [Na^+]_{L,initial} - [Cl^-]_{L,initial} - \frac{C \times S}{F \times V_L} \times \{(\Psi_{in} - \Psi_{out}) + \Psi_{initial}\} \qquad \text{(Supplementary Equation 5)}$$

Where Ψ_{in} and Ψ_{out} are the intrinsic inner and outer surface potentials, respectively, in units of mV, which contribute to the change in ion concentration at membrane surface as described later, $\Psi_{initial}$ is the initial lysosomal membrane potential which is set to zero mV in order to maintain initial lysosomal membrane electroneutrality.

A.1.4. Modeling chloride influx.

V-ATPase mediated proton influx into the lysosome is followed by lysosomal membrane potential increase which consequentially arrests further proton influx. Thus, to lower the membrane potential for the continuation of V-ATPase proton-pumping activity, which is essential to lower lysosomal pH to physiological pH, the removal of lysosomal cation or the insertion of lysosomal anion is required. Accordingly, CLC7 is considered as the primary membrane potential dissipating protein which transports two chloride ions from the cytoplasm to the lysosome for every proton it transports from the lysosome to the cytoplasm[5]. The rate ($J_{Cl,\ HClC7}$) at which the ion transportations occur was empirically derived from a current-voltage experimental data[3] as a function of chemical (ΔpH, ΔCl) and electric potential gradients, ($\Delta\Psi$), as detailed in supplementary equations (6) and (7). This rate was multiplied by the total number of CLC7 molecules per lysosome (N_{ClC7}) in order to obtain the total amount of proton and chloride molecules transported across the lysosomal membrane through CLC7, as follows:

$$H_{CLC7} = N_{CLC7} \times J_{Cl,H_{CLC7}}(\Delta pH, \Delta Cl, \Delta \Psi) \qquad \text{(Supplementary Equation 6)}$$

$$Cl_{CLC7} = 2 \times N_{CLC7} \times J_{Cl,H_{CLC7}}(\Delta pH, \Delta Cl, \Delta \Psi) \qquad \text{(Supplementary Equation 7)}$$

Where ΔCl is the chloride gradient comprised of the luminal chloride (Cl_L) and the cytoplasmic chloride (Cl_C). Moreover, the coefficient 2 in supplementary equation (7) defines the 2:1

stoichiometric relationship between the chloride and proton ions transported by CLC7 across the lysosomal membrane.

A.1.5. Modeling proton efflux.

In addition to CLC7, the passive diffusion of protons across the lysosomal membrane can also contribute to the dissipation of membrane potential in order to facilitate the proton pumping activity of V-ATPase. This passive proton leak is modeled by supplementary equation (8), which is derived from the Goldman-Hodgkin-Katz (GHK) ion flux equation[6] that is commonly used to describe the passive diffusion of a given ion across a biological membrane, assuming a linear potential gradient across a lipid membrane[3].

$$H_{leak} = \left(S \times P_{H^+} \times Y \times Z \times \frac{10^{-pH_L} - \left(10^{-pH_C} \times e^{-Z \times Y}\right)}{1 - e^{-Z \times Y}}\right) \times N_{av}$$

(Supplementary Equation 8)

Where S is the total lysosomal surface area in units of cm^2 used to obtain the total amount of proton which passively diffuses across the lysosomal membrane; P_{H^+} is the lysosomal membrane proton permeability in units of cm/s; Z is the valence of the ion (i.e. +1 for proton); pH_L is the luminal pH used to calculate the total free lysosomal proton based on the logarithmic relationship of pH and free proton ($pH_L = -\log[H^+]$); pH_c is the cytoplasmic pH used to calculate the total free cytoplasmic proton based on the logarithmic relationship of pH and free proton ($pH_C = -\log[H^+]$); N_{av} is Avogadro's number used to convert the amount of transported protons in unit of moles to unit of molecules; Y is used to convert proton transportation in unit of charge per second to moles per second and is defined as: $Y = \frac{\Delta \Psi \times F}{R \times T}$, where R is universal gas constant, F is Faraday's constant, and T is absolute temperature. Moreover, for cells at room temperature (25 °C), RT/F

equals 25.69 mV^4, and is used for normalizing the lysosomal membrane potential communicated in this report.

A.1.6. Modeling the effect of membrane leaflet potentials on ions.

In order to account for the effects of intrinsic external ($\Psi_{i,out}$) and internal ($\Psi_{i,in}$) leaflet potentials of the lysosomal membrane on cytoplasmic and lysosomal ion *i* concentrations, respectively, the individual cytoplasmic and lysosomal ion concentrations are computed using the following relationships, supplementary equations (9 and 10), derived from the GHK equation for a single ion concentration gradient, by setting net current flow equal to zero.

$$\Delta\ \Psi_{i,in} = \frac{-Z\times R\times T}{F} \ln \frac{C_{i,in}}{C_{i,L}} \qquad \text{(Supplementary Equation 9)}$$

$$\Delta\ \Psi_{i,out} = \frac{-Z\times R\times T}{F} \ln \frac{C_{i,out}}{C_{i,C}} \qquad \text{(Supplementary Equation 10)}$$

Where $C_{i,in}$ is the internal concentration of a given ion (i) at the membrane surface facing the lysosomal compartment, $C_{i,L}$ is the concentration of the ion (i) inside the lysosome, $C_{i,out}$ is the external concentration of the ion (i) at the membrane surface facing the cytoplasmic compartment, $C_{i,C}$ is the concentration of the ion (i) inside the cytoplasm. All units are molar.

A.1.7. Governing equations.

Supplementary equations (3-10) were used in supplementary equations (11-13) to further define the ion movements as a function of time, in units of molecules per second.

$$\frac{dH^+}{dt} = H_{pump} - H_{CLC7} - H_{leak} - H_{sequestered} \qquad \text{(Supplementary Equation 11)}$$

$$\frac{dCl^-}{dt} = 2 \times N_{CLC7} \times J_{Cl,H_{CLC7}} (\Delta pH, \Delta Cl, \Delta \Psi) - Cl_{sequestered}$$

(Supplementary Equation 12)

Moreover, extending supplementary equation (11), we can denote the change in lysosomal pH with respect to time by following the relationship between the lysosomal lumen buffering capacity (β) of the Donnan particles, which sequester non-free lysosomal protons, and free lysosomal protons which give rise to lysosomal pH as follows:

$$\frac{dpH}{dt} = \frac{(-H_{pump} + H_{CLC7} + H_{leak} + H_{sequestered})}{V \times N_{av} \times \beta}$$ (Supplementary Equation 13)

Where V is the lysosomal volume and is multiplied by N_{av} to convert the unit of molecules per second to molar per second, where the inverse of β is in units of pH units per molar.

A.1.8. Numerical analysis.

Supplementary equations (11-13) were solved by numerical integration in Berkeley Madonna® using Rosenbrock stiff solver as a numerical integrator.

A.1.9. Data visualization.

Multiple individual 2D datasets associated with the parametric simulations performed to generate simultaneous inhibitions of various lysosomal parameters were obtained. The datasets associated with each simultaneous inhibitions of lysosomal parameters were exported from Berkeley Madonna and compiled into three separate matrices in a MS-Excel spreadsheet, such that the first rows and columns of the matrix correspond to the two parameters simultaneously varied in the model simulations to obtain the final lysosomal readout values (lysosomal pH, Cl^-,

and membrane potential), where each makes up the rest of the rows and columns of a single matrix.

A.1.10. Model script.

```
METHOD STIFF
STARTTIME = 0
STOPTIME =86400
DT = 0.02
DTMAX = 100
TOLERANCE = 1e-6

{Baseline Input Parameter List----------}
{Baseline Lysosomal Dimensions Assuming Spherical Geometry}
R = 0.34                    {Radius [microns]}
V = 1.65e-16                {Volume [liters]}
SA = 1.45e-8                {Surface area [cm^2]}

{Baseline Cytosolic Volume}
Vc = 1.65e10                {Volume [liters]-arbitrarily chosen to result
in almost constant cytoplasmic ion concentration}

{Intrinsic Surface Potentials-- used for calculating surface charges of each ion}
```

psi_out = -50 {Outer surface potential- used as outer resting membrane potential [mV]}

psi_in = 0 {Inner surface potential - used as inner resting membrane potential [mV]}

{Fixed Standard Constants}

mole = 6.02e23 {Avogadro's Number [1/mol]}

RTF = 25.69 {RT/F membrane potential for cells at room temperature[mV]}

F = 96485 {Faraday's Constant that converts unit of membrane potential [Coulomb/mol]}

cap_0 = 1e-6 {Capacitance per unit area of the lysosomal membrane [Farad/cm^2]}

cap = cap_0*SA/1000 {Total capacitance per lysosome [Farad]}

{Baseline Cytosolic Concentrations}

initpHbulk = 7.2 {pH [pH units]}

Kbulk = 0.145 {K+ [M]}

initclbulk = 0.01 {Cl- [M]}

Nabulk = 0.01 {Na+ [M]}

initHbulk = 0 {Total H+ [M]}

{Baseline Luminal Concentrations}

initpH = 7.4 {pH [pH units]}

initk = 0.005 {K+ [M]}

initcl = 0.11 {Cl- [M]}

initna = 0.145 {Na+ [M]}

initH = 0.00 {Total H+ [M]}

{Donnan Particles [M]: constitute the initial impermeant luminal ions that give rise to Donnan potential to balance the negatively charged proteins in the luminal matrix}

B = initk+initna+initH-initcl - cap/F/V*(psi_in - psi_out) - initpsi_total*cap/F/V {[M]}

{Set Initial Total Membrane Potential [mV]}

initpsi_total = 0

beta = 0.04 {Buffering capacity [M/pH unit] of the luminal matrix that sequesters protons from solution}

beta_bulk = 0.04 {Buffering capacity [M/pH unit] of the cytoplasm that sequesters protons from solution}

{Baseline Input Kinetic Parameters----------}

P = 6e-5 {Membrane H+ permeability. Experimentally determined- Ishida et al 2013}

N_VATP = 300 {Number of V-ATPases per lysosome. Experimentally estimated- Ishida et al 2013}

N_CLC7 = 5000 {Number of ClC7 antiporters per lysosome. Estimated- Ishida et al 2013}

CLC_Cl = 2 {CLC7 Cl- Stoichiometry. Experimentally determined- Graves et al 2008}

CLC_H = 1 {CLC7 H+ Stoichiometry. Experimentally determined- Graves et al 2008}

{ODE- Time Dependent Ion Flows----------}

d/dt (pH) = ((NH_entrapment-Hpump - Hleak - (CLC_H*CLC7))/V/mole)/beta

INIT pH = initpH {Lysosomal pH as a function of time [pH unit/sec]}

d/dt (NCl) = -CLC_Cl*CLC7-NCl_entrapment

INIT NCl = initcl*V*mole {Lysosomal Cl as a function of time [Cl-/sec]}

d/dt (NH) = -NH_entrapment+Hpump + Hleak + (CLC_H*CLC7)

INIT NH = initH*V*mole {Total lysosomal H+ as a function of time [H+/sec]}

d/dt (pHbulk) = ((-NH_entrapment+Hpump + Hleak + (CLC_H*CLC7))/Vc/mole)/beta_bulk

INIT pHbulk = initpHbulk {Cytoplasmic pH as a function of time [pH unit/sec]}

d/dt (NHbulk) = NH_entrapment- Hpump- Hleak - (CLC_H*CLC7)

INIT NHbulk = initHbulk*Vc*mole {Cytoplasmic H+ as a function of time [H+/sec]}

d/dt (NClbulk) = +CLC_Cl*CLC7 + NCl_entrapment

INIT NClbulk = initclbulk*Vc*mole {Cytoplasmic Cl as a function of time [Cl-/sec]}

{Ion Flows Through Lysosomal Membrane Channels and Pumps----------}

{Proton Pump}

JH_VATP = #protonpump2 (pH,psi) {Proton pump [H+/sec] by a single V-ATPase molecule as a function of luminal pH gradient and membrane potential. Surface dataset ("protonpump2") imported from Matlab as a call-in function}

Hpump = N_VATP*JH_VATP {Total proton pump flow [H+/sec] by a total number of VATPases per lysosome}

{ClC7 Antiporter: Membrane Potential Dissipation}

clc7f = (CLC_Cl+CLC_H)*psi + RTF*(2.3*(pHe - pHi) + CLC_Cl*LOGN(Cle/Cli)) {Transmembrane H+ and Cl- motive force across lysosomal membrane that drives CLC7 antiporter's function- Ishida et al 2013}

G1 = -0.3*clc7f {0.3 was determined by experimental fitting- Ishida et al 2013. Linear function for positive "psi"}

G3 = -1.5E-5*clc7f^3 {1.5 was determined by experimental fitting- Ishida et al 2013. Cubic function for negative "psi"}

S = 0.5+0.5*TANH((clc7f+250)/75) {Switching function that ranges 0 to 1 depending on the sign of "psi"}

JCLC7 = S*G1+ (1-S)*G3 {Single CLC7 antiporter turnover. Function switches from linear to a 3-degree polynomial function depending on "S" to empirically fit experimental data- Ishida et al 2013}

CLC7 = N_CLC7*JCLC7 {Total ClC7 antiporter turnover [1/sec]}

{Define Terms for Goldman-Hodgkin-Katz Flux (GHK) Equation}

gg = IF abs(psi) > .01 THEN psi/(1-exp(-psi/RTF))/RTF ELSE

1/(1 - (psi/RTF)/2 + (psi/RTF)^2/6 - (psi/RTF)^3/24 +(psi/RTF)^4/120) {IF THEN statement to avoid computational error when psi = 0. Taylor series expansion about a point = (psi/RTF) when psi is less than RTF}

{Passive Flows Across Lysosomal Membrane Modeled According to GHK Flux Equation}

Hleak = P*SA*(10^(-pHe)*exp(-psi/RTF)-10^(-pHi))*gg*mole/1000

{[H+/sec]}

NCl_entrapment = (a)*mole

a = (1e-16)/86400 {Rate of CLDI formation = 0.01 picomol/day in the cell = 0.0001 picomol/day in the lysosome}

NH_entrapment = NCl_entrapment

{Functions/Conversions----------}

{Membrane Potentials}

psi = F*(V*(H+initk+initna- Cl - B))/cap {Membrane potential [mV] dictated by the net change in lysosomal ions, lysosomal membrane capacitance, buffering capacity, and Donnan Particles, characteristics of the luminal matrix. Valence of each ion (plus or minus 1) is implicitly considered}

psi_total = psi + psi_out-psi_in {Total membrane potential [mV]}

{Luminal Concentrations}

Cl = NCl/V/mole {[M]}

H = NH/V/mole {Total H+ [M]}

{Luminal Content [mol]}

Cl_mol = Cl*V {Cl [mol]}

H_mol = H*V {Total H+ [mol]}

{Cytosolic Concentrations}

Clbulk = NClbulk/Vc/mole {Cl [M]}

Hbulk = NHbulk/Vc/mole {Total H+ [M]}

{Cytosolic Content [mol]}

Clbulk_mol = Clbulk*Vc {Cl [mol]}

Hbulk_mol = Hbulk*Vc {Total H+ [mol]}

{Modified Cytoplasmic Surface Concentrations Dictated by Surface Potential- Derived from GHK for a single ion in the case of zero net current flow; also known as Nernst equation}

Cle = Clbulk*exp(psi_out/RTF) {[M]}

Ke = Kbulk*exp(-psi_out/RTF) {[M]}

Nae = Nabulk*exp(-psi_out/RTF) {[M]}

pHe = (pHbulk+psi_out/(RTF*2.3)) {[pH units]}

{Modified Luminal Surface Concentrations Dictated by Surface Potential - Derived from GHK for a single ion in the case of zero net current flow; also known as Nernst equation}

Cli = Cl*exp(psi_in/RTF) {[M]}

Ki = initK*exp(-psi_in/RTF) {[M]}

Nai = initNa*exp(-psi_in/RTF) {[M]}

pHi = (pH+psi_in/(RTF*2.3)) {[pH units]}

A.2. Supplementary Figures

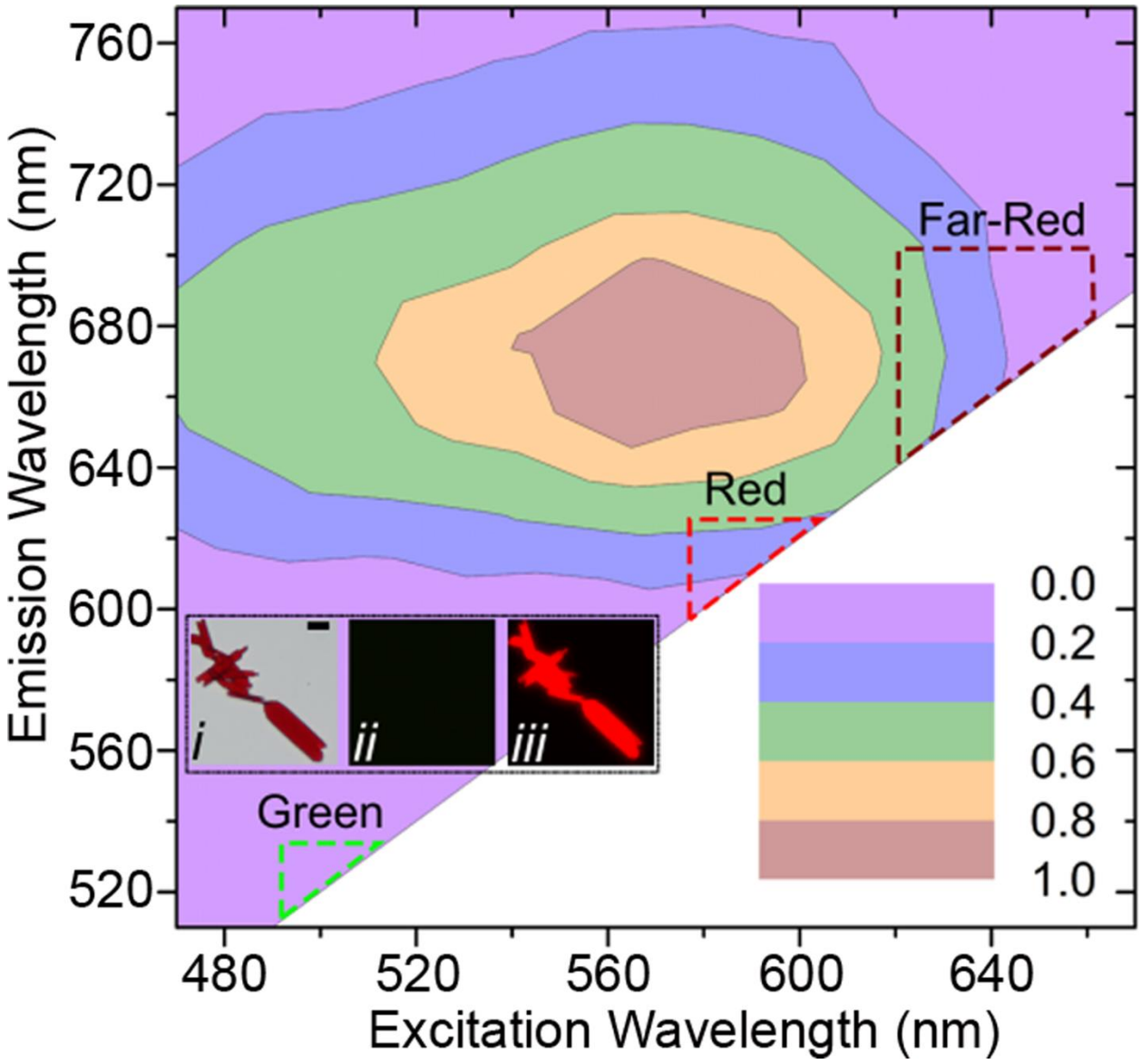

Figure A.1 Fluorescence Microspectroscopy and (inset, *i* = brightfield, *ii* = green fluorescence, *iii* = far-red fluorescence) Epifluorescence Microscopy of CFZ-H^+Cl^- crystals indicating the lack of green fluorescence while being fluorescent in the far-red fluorescence range. The excitation wavelength (nm, Ex) and emission wavelength (nm, Em) are shown on the X-axis and Y-axis, respectively. The normalized fluorescence yield is shown by a contour plot that was normalized using a control slide first and then to the maximum measured fluorescence yield. The colors as shown represent contour levels from 0-1 in steps of 0.2. The green, red, and far-red fluorescence bandwidths are overlaid on top of the normalized fluorescence spectra.

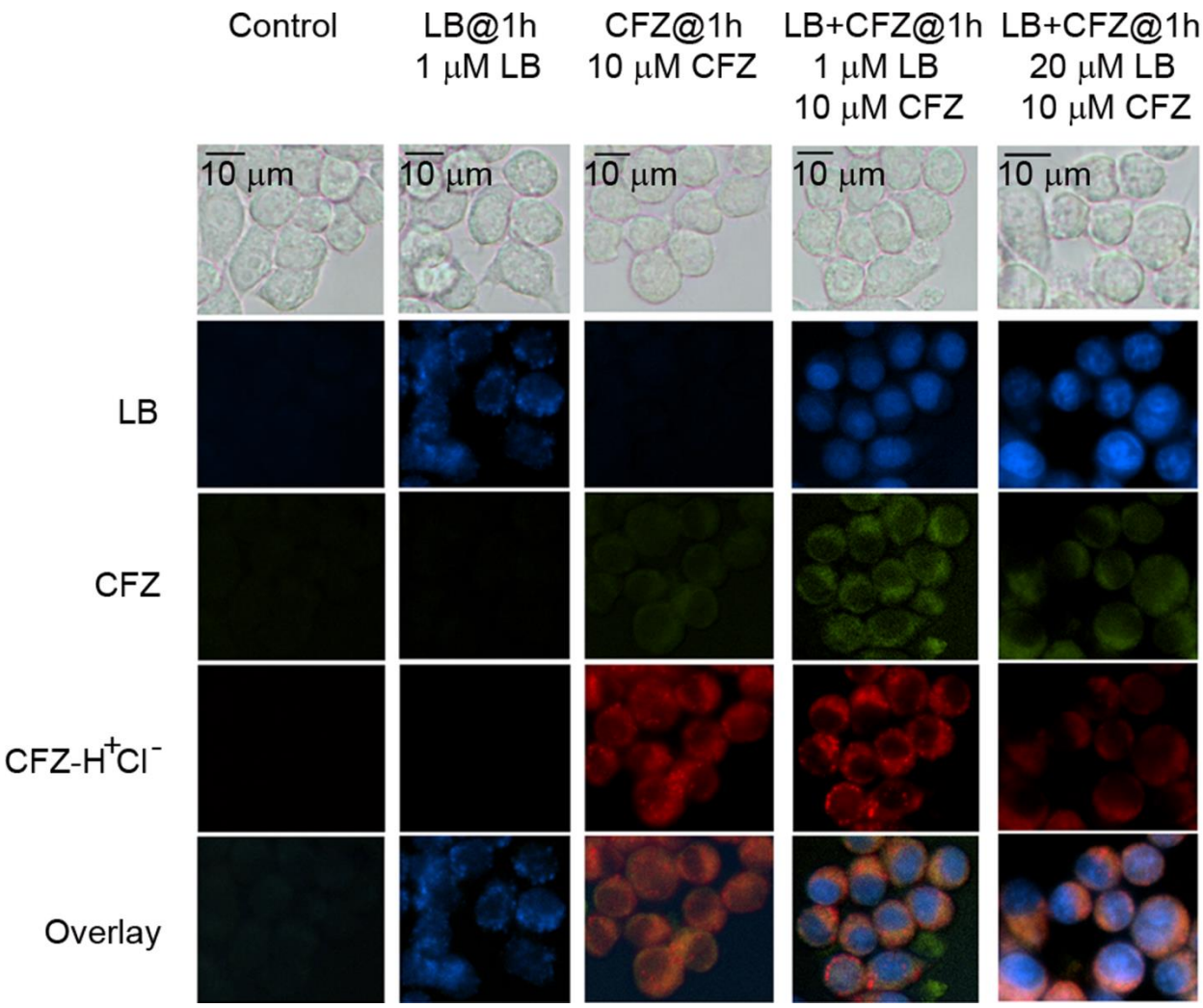

Figure A.2 Epifluorescence microscopy of RAW264.7 cells when incubated with CFZ (10 μM), Lysotracker® Blue (LB, 1 and 20 μM) at *t* = 1 hour. Scale bar, 10 μm. At 1 hour, green fluorescence spots indicative of CFZ are visible as mild diffuse staining rather than punctate staining observed at *t* = 24 hours. Vesicular staining pattern of LB, visible as blue punctate spots when incubated on its own, are absent when co-incubated with CFZ at both LB = 1 and 20 μM. The control images were taken at *t* = 24 hours post initiation of experiments.

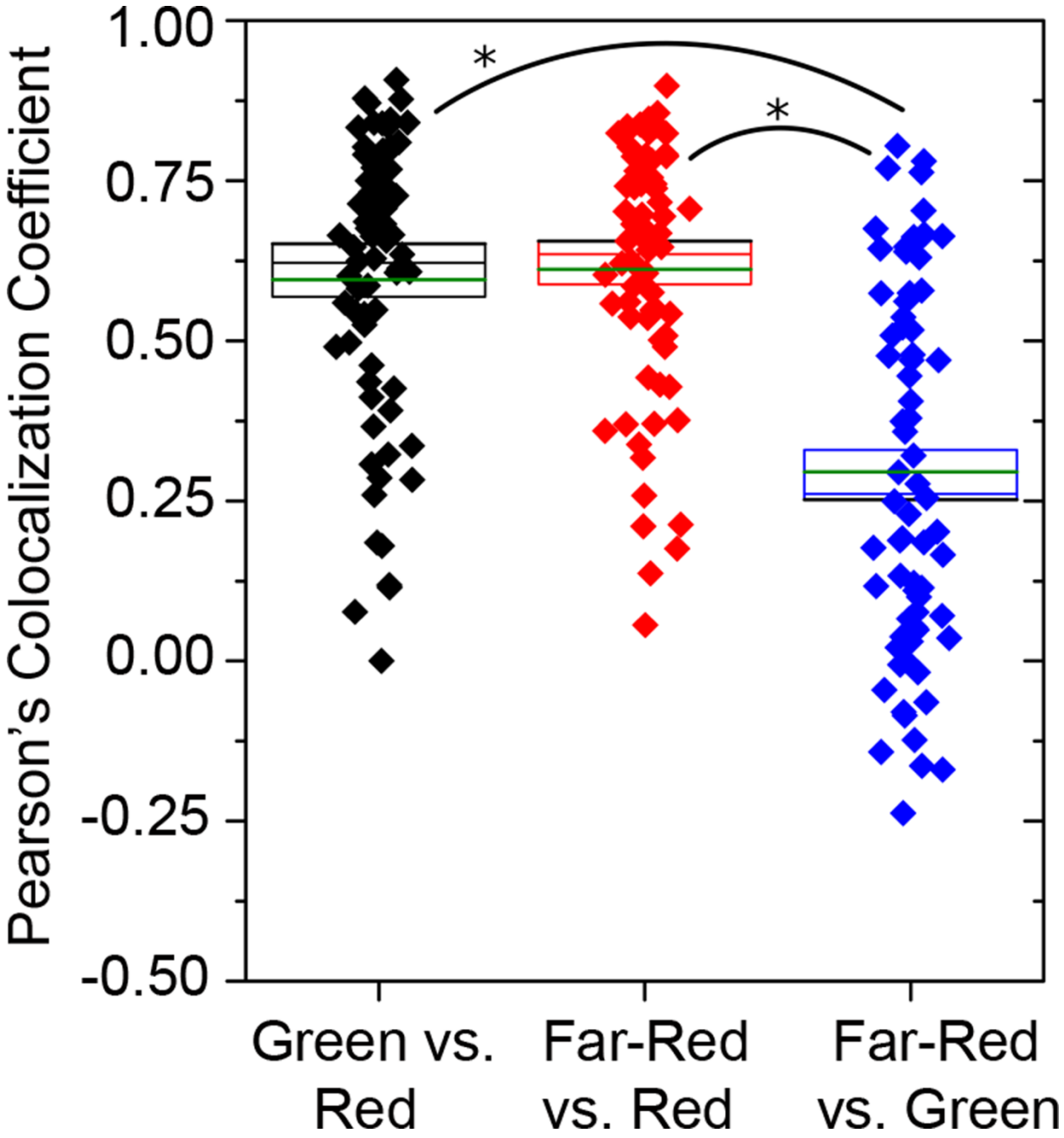

Figure A.3 Pearson's Colocalization Coefficient for multiple cell ROIs (n = 70) as obtained post epifluorescence microscopy of RAW264.7 cells incubated with CFZ (10 μM) at *t* = 24-72 hours. Fluorescence channel description is provided in Table A.2. The scatter distribution is further annotated with four horizontal lines denoting the Mean ± S.E. (same color lines as the distribution), Mean (green line) and the Median (black line) of the distribution. * -$p < 0.005$.

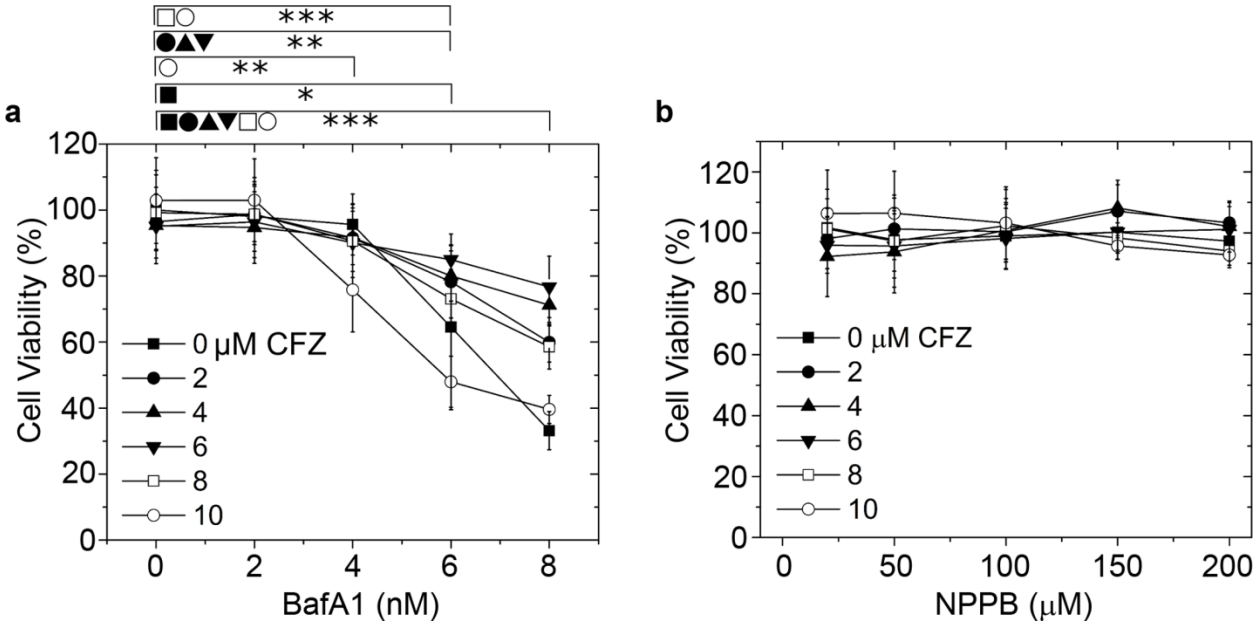

Figure A.4 Viability of RAW264.7 cells treated with a) BafA1 and b) NPPB in the presence of CFZ (0-10 μM). Data was collected at n = 6 with * - $p < 0.05$, ** - $p < 0.01$, *** - $p < 0.001$. Each point is compared in a pair-wise independent Student *t*-test.

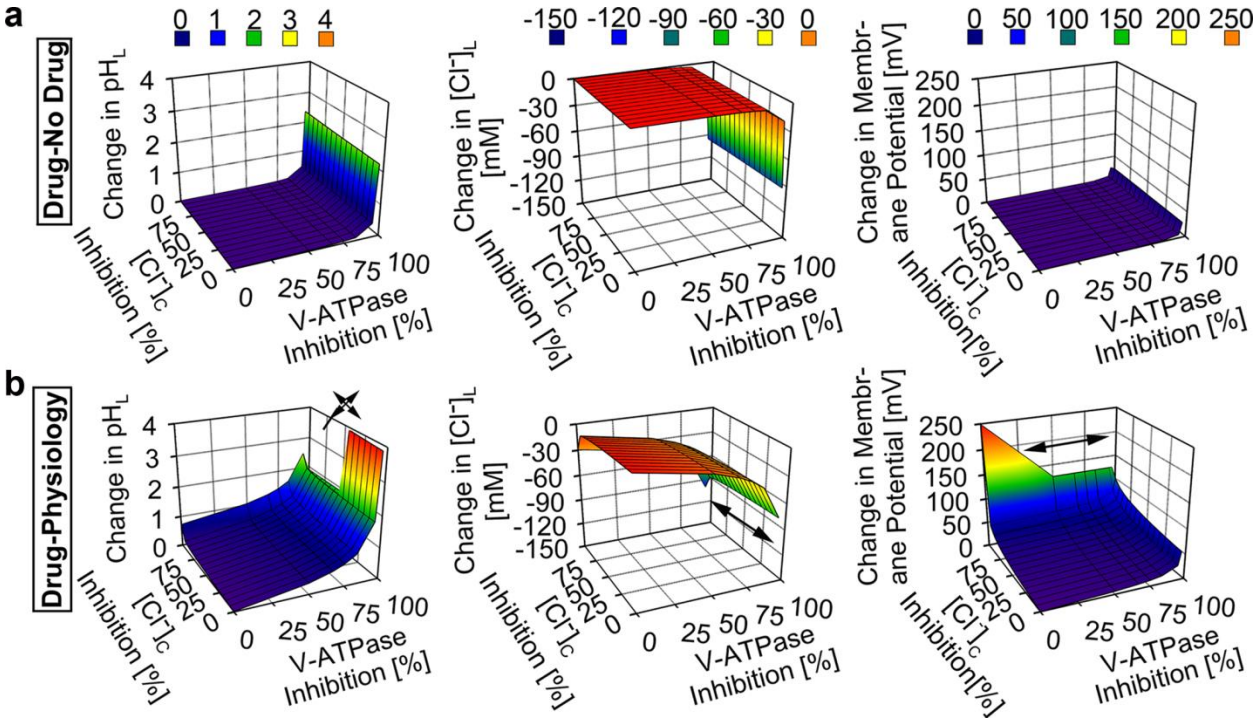

Figure A.5 Model and simulation of the effects of V-ATPase and cytoplasmic chloride on the lysosomal accumulation of CFZ-H$^+$Cl$^-$.

a, V-ATPase inhibition showed a more substantial effect than cytoplasmic chloride inhibition on the accumulation of CFZ-H^+Cl^- at the rate of 0.01 picomol/cell/day, as reflected by the changes in the lysosomal pH, Cl^-, and membrane potential values of the CFZ-H^+Cl^- containing lysosome from that of the CFZ-H^+Cl^- free lysosome. **b**, V-ATPase inhibition generally showed a more substantial effect than cytoplasmic chloride inhibition although the simultaneous inhibition of both parameters showed even more pronounced effect on the physiological accumulation of CFZ-H^+Cl^- at the rate of 0.01 picomol/cell/day, as reflected by the changes in the lysosomal pH, Cl^-, and membrane potential values of the CFZ-H^+Cl^- containing lysosome from respective baseline physiological values. Arrow signs represent values outside of the axes plot range.

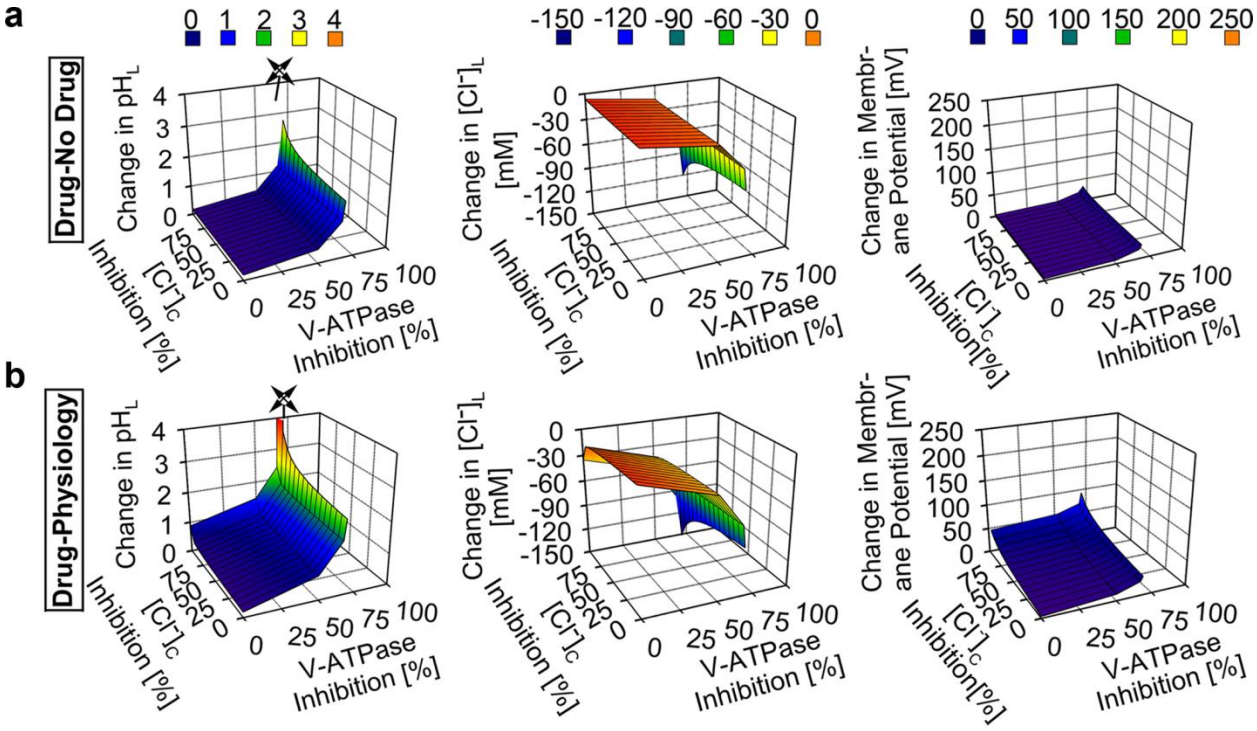

Figure A.6 Model and simulation of the effects of V-ATPase and cytoplasmic chloride on the lysosomal accumulation of CFZ-H^+Cl^- at a higher dose.
a, V-ATPase inhibition showed a more substantial effect than cytoplasmic chloride inhibition on the accumulation of CFZ-H^+Cl^- at the rate of 0.1 picomol/cell/day, as reflected by the changes in the lysosomal pH, Cl^-, and membrane potential values of the CFZ-H^+Cl^- containing lysosome from that of the CFZ-H^+Cl^- free lysosome. **b**, V-ATPase inhibition generally showed a more substantial effect than cytoplasmic chloride inhibition although the simultaneous inhibition of both parameters showed even more pronounced effect on the physiological accumulation of CFZ-H^+Cl^- at the rate of 0.1 picomol/cell/day, as reflected by the changes in the lysosomal pH, Cl^-, and membrane potential values of the CFZ-H^+Cl^- containing lysosome from respective baseline physiological values. Arrow signs represent values outside of the axes plot range.

A.3. Supplementary Tables

Table A.1 Model Parameters

Symbol	Description	Baseline Input Value	Range of Input Value	Units
pH_C	Cytosolic pH	7.2	Fixed	pH Unit
pH_L	Luminal pH	7.4	Fixed	pH Unit
$[Cl^-]_C$	Cytosolic chloride concentration	10	$1x10^{-5}$ - 10	mM
$[Cl^-]_L$	Luminal chloride concentration	110	Fixed	mM
$[Na^+]_L$	Luminal sodium concentration	145	Fixed	mM
$[K^+]_L$	Luminal potassium concentration	5	Fixed	mM
$[H^+]_L$	Luminal proton concentration	0	Fixed	mM
P_{H^+}	Membrane proton permeability	$6x10^{-5}$	Fixed	cm/s
V	Lysosomal volume	$1.65x10^{-16}$	Fixed	L
S	Lysosomal surface area	$1.45x10^{-8}$	Fixed	cm^2
C'	Specific bilayer capacitance	1	Fixed	$\mu Farad/cm^2$
β	Buffering capacity	40	Fixed	mM/pH unit
N_{VATP}	V-ATPase number	300	$1x10^{-4}$ - 300	
N_{CLC7}	CLC7 number	5000	$1x10^{-4}$ - 5000	
Ψ_{out}	Outer surface potential	-50[b]	Fixed	mV
Ψ_{in}	Inner surface potential	0[b]	Fixed	mV
CLC_Cl	CLC7 Cl^- stoichiometry	2	Fixed	
CLC_H	CLC7 H^+ stoichiometry	1	Fixed	
R	Gas constant	8.314	Fixed	$J.K^{-1}.mol^{-1}$
T	Absolute temperature	0	Fixed	Kelvin
F	Faraday's constant	96485	Fixed	J/Volt
N_{av}	Avogardro's number	$6.02x10^{23}$	Fixed	molecules/mol
a	Rate of proton and chloride sequestration by CFZ to form CFZ-H^+Cl^-	0	$1.16x10^{-21}$ - $1.16x10^{-20}$	Moles/day

[a] Baseline input values are literature values[7-11] representing physiological lysosomes and are in agreement with previously published model[2,3].

[b] Estimated intrinsic surface potentials for inner (Ψ_{in}) and outer (Ψ_{out}) leaflets of the lysosomal membrane accounted for when modeling membrane transporter mediated dynamic lysosomal and cytoplasmic ion concentrations at the membrane surface[2].

Table A.2 Fluorescence in RAW264.7 cells.

(Channels (Ex/Em)) – Blue (350/405 nm), Green (490/510 nm), Red (590/610 nm), and Far-Red (640/670 nm).

	Blue	Green	Red	Far-Red
CFZ	-	+	+	-
CFZ-H^+Cl^-	-	-	+	+
Lysotracker® Blue	+	-	-	-

A.4. References

1 Grabe, M., Wang, H. & Oster, G. The mechanochemistry of V-ATPase proton pumps. *Biophys J* **78**, 2798-2813, doi:10.1016/S0006-3495(00)76823-8 (2000).

2 Grabe, M. & Oster, G. Regulation of organelle acidity. *J Gen Physiol* **117**, 329-344 (2001).

3 Ishida, Y., Nayak, S., Mindell, J. A. & Grabe, M. A model of lysosomal pH regulation. *J Gen Physiol* **141**, 705-720, doi:10.1085/jgp.201210930 (2013).

4 Hille, B. *Ionic Channels of Excitable Membranes. 2nd Edition*. 607 (Sinauer Associates, Inc. , 1992).

5 Graves, A. R., Curran, P. K., Smith, C. L. & Mindell, J. A. The Cl-/H+ antiporter ClC-7 is the primary chloride permeation pathway in lysosomes. *Nature* **453**, 788-792, doi:10.1038/nature06907 (2008).

6 Weiss, T. F. *Cellular Biophysics: Transport*. (MIT Press, 1996).

7 Van Dyke, R. W. Acidification of rat liver lysosomes: quantitation and comparison with endosomes. *Am J Physiol* **265**, C901-917 (1993).

8 Gambale, F., Kolb, H. A., Cantu, A. M. & Hedrich, R. The Voltage-Dependent H+-Atpase of the Sugar-Beet Vacuole Is Reversible. *Eur Biophys J Biophy* **22**, 399-403 (1994).

9 Heuser, J., Zhu, Q. & Clarke, M. Proton pumps populate the contractile vacuoles of Dictyostelium amoebae. *J Cell Biol* **121**, 1311-1327 (1993).

10 Sonawane, N. D., Thiagarajah, J. R. & Verkman, A. S. Chloride concentration in endosomes measured using a ratioable fluorescent Cl- indicator - Evidence for chloride accumulation during acidification. *Journal of Biological Chemistry* **277**, 5506-5513, doi:10.1074/jbc.M110818200 (2002).

11 Alberts, B. J., A.; Lewis, J.; Raff, M.; Roberts, K.; Walter, P. *Moelcular Biology of the Cell. Fifth edition*. (Garland Science, New York, 2008).

Appendix B

Supporting Information for Chapter 3

B.1. Additional Experimental Methods:

B.1.1. Lysosomal ion transport model description.

The transportation of ions to and from the lysosome induces charge, ΔQ, and membrane potential difference, ΔΨ, between the lysosome and the cytoplasm. By definition, membrane potential difference, which simply is referred hereon as membrane potential, across a given membrane is the difference between the potential of one side of the membrane and that of the other side of the membrane (i.e. the lysosome and the cytoplasm in our case). It can be calculated using the following relationship between the charge of a given ion(s) and capacitance, assuming that the lipid bilayer of lysosomal membrane can serve as a parallel plate capacitor:

$$\Delta\Psi = \frac{\Delta Q}{C'} \quad (1)$$

Where C' is the specific bilayer capacitance of the lysosomal membrane per unit area of the lysosomal surface area, which represents the measure of the net charge transported, ΔQ, in units of Coulomb, from one side of the membrane to the other resulting in membrane potential, ΔΨ, across the membrane, in units of mV. For biological membranes, C' has been experimentally approximated to $1\mu F/cm^2$ [1,2].

Charge on a mole of a monovalent ion is represented by Faraday's constant, F, which equals 96485 Coulomb/mol. Moreover, depending on the charge and valence, Z_i, of the monovalent ion "i", F will be + or -; where the earlier is for a cation and the latter for an anion.

Thus, using F we can obtain the charge of the ions in the cytoplasm and the lysosome from the cytoplasmic and lysosomal ion concentration, respectively, in units of Coulomb.

$$\Delta Q = F \times (\sum_i Z_i \times [i]_C \times V_C - \sum_i Z_i \times [i]_L \times V_L) \quad (2)$$

With $[i_C]$ and $[i_L]$ being the net concentration in the cytoplasm and lysosome in units of Molar, respectively. Both terms are multiplied by their respective compartmental volume to convert the units of Molar to mol. In both compartments, the net concentration comprises of permeable and impermeable ions.

Furthermore, we utilize a physiological sign convention that the membrane potential is more positive or negative if there is more cation or anion, respectively, in the internal compartment (i.e. lysosome, in our case), than in the external compartment (i.e. cytoplasm, in our case). Thus, equation 2 is re-written as:

$$\Delta Q = F \times (\sum_i Z_i \times [i]_L \times V_L - \sum_i Z_i \times [i]_C \times V_C) \quad (3)$$

More specifically, the following relationship is obtained to define the ion content in the cytoplasmic compartment:

$$\sum_i [i]_C \times V_C = \sum_i ([i]_C \times V_C)_f - \sum_i ([i]_C \times V_C)_o \quad (4)$$

Where the subscript f denotes the final value of the permeable ions in units of mole, and the subscript o denotes the initial value of the impermeable ions in units of mole. However, because the cytoplasmic volume is comparatively big, we assume that the concentration of cytoplasmic ions remains more or less constant. Thus, we set: $\sum_i ([i]_C \times V_C)_o = 0$

Similar to equation 4, we have the following relationship for the case of lysosomal ion content:

$$\sum_i [i]_L \times V_L = \sum_i ([i]_L \times V_L)_f - \sum_i ([i]_L \times V_L)_o \quad (5)$$

Thus, by substituting the terms in equation 3 with those in equations 4 and 5, we obtain;

$$\Delta Q = F \times (\sum_i Z_i \times ([i]_L \times V_L)_f - \sum_i Z_i \times ([i]_L \times V_L)_o) \quad (6)$$

In addition, because we treat the lysosomal volume as a parameter, equation 6 can be re-written as:

$$\Delta Q = F \times V_L \times ((\sum_i Z_i \times [i]_L)_f - \sum_i Z_i \times ([i]_L)_o) \quad (7)$$

Moreover, for the purpose of distinguishing notations, $\sum_i Z_i \times ([i]_L)_o)$ is replaced by "B". This term is known as Donnan particles, which is represented in units of Molar. Thus, equation 7 is re-written as:

$$\Delta Q = F \times V_L \times ((\sum_i Z_i \times [i]_L)_f - B) \quad (8)$$

Thus, by plugging equation 8 into equation 1, membrane potential is equated as;

$$\Delta \Psi = \frac{F \times V_L}{C'} \times ((\sum_i Z_i \times [i]_L)_f - B) \quad (9)$$

As previously mentioned, because the capacitance is a measurement per unit area of the lysosomal surface, equation 9 must be multiplied by the total lysosomal surface area (S), in units of cm^2, to obtain total capacitance per lysosome, hence the total membrane potential.

$$\Delta \Psi = \frac{F \times V_L}{C' \times S} * ((\sum_i Z_i \times [i]_L)_f - B) \quad (10)$$

Furthermore, the final luminal ion concentrations $[i_L]_f$ can be classified into cations and anions:

$$\Delta \Psi = \frac{F \times V_L}{C' \times S} * [(\sum_i Z_i \times [cations]_i + \sum_i Z_i \times [anions]_i) - B] \quad (11)$$

In addition, the Donnan particles (B), in units of Molar, are explicitly defined using the initial lysosomal contents, including the net change in the intrinsic surface potential:

$$B = [H^+]_{L,initial} + [K^+]_{L,initial} + [Na^+]_{L,initial} - [Cl^-]_{L,initial} - \frac{C' \times S}{F \times V_L} \times \{(\Psi_{in} - \Psi_{out}) + \Psi_{initial}\} \quad (12)$$

With the subscript (initial) denoting the fixed initial luminal content, (Ψ_{in}) and (Ψ_{out}) being the intrinsic surface potentials for inner and outer leaflets in units of mV, respectively, of the

lysosomal membrane, as estimated in the literature[3], ($\Psi_{initial}$) being the initial membrane potential, which is set to 0 mV for the purpose of maintaining initial electroneutrality. Substituting equation 12 into equation 11 will give:

$$\Delta\Psi = \frac{F\times V_L}{C'S} \times \{[H^+]_{L,final} - [Cl^-]_{L,final} - [H^+]_{L,initial} + [Cl^-]_{L,initial}\} + \Psi_{in} - \Psi_{out}\} \quad (13)$$

With the subscript (final) denoting the luminal contents at a given time "t".

B.1.2. Modeling ion transportation.

Briefly, in this model, V-ATPase is an electrogenic proton pump which lowers the lysosomal pH by working against a proton motive force build-up that arises from membrane potential and proton concentration gradient. To capture this phenomenon, the rate of proton influx, J_{HVATP}, by a single V-ATPase molecule per lysosome per second was incorporated to the model based on the instantaneous transmembrane pH gradient, ΔpH, and membrane potential, ΔΨ, (equation 14). This rate was multiplied by the total number of active V-ATPase molecules in a lysosome, N_{VATP} [3,4] to obtain the total number of protons inserted into the lysosome in units of molecules per second (H_{pump}), (equation 14).

$$H_{pump} = N_{VATP} \times J_{H_{VATP}}(\Delta pH, \Delta\Psi) \quad (14)$$

Following proton pump by the V-ATPase, membrane potential would increase in the absence of some other mechanism that dissipates the increment. Physiologically, membrane potential is dissipated by the efflux of cations from the lysosomes, or the influx of anions. In this regard, CLC7 plays a dominant role [4]. Accordingly, the model represents the rate of proton removal per second, J_{Cl,H_CLC7}, as well-elaborated in a previously published model [3], by a single CLC7 molecule per lysosome as a function of chloride concentration gradient dictated by

cytoplasmic and lysosomal chloride concentrations, Cl_C and Cl_L, respectively, and electrical gradient dictated by $\Delta\Psi$, (equation 15). This rate was multiplied by the total number of CLC7 molecules per lysosome, N_{ClC7}, [3] in order to obtain the total amount of protons removed in units of molecules per second by CLC7, H_{ClC7},(equation 15).

$$H_{ClC7} = N_{ClC7} \times J_{Cl,H_{ClC7}}(\Delta pH, Cl_L, Cl_C, \Delta\Psi) \quad (15)$$

In addition to CLC7, membrane potential dissipation is also facilitated by the process of proton transportation from the lysosome to the cytoplasm. In order to capture the passive diffusion of protons across the semi-permeable lysosomal membrane, the Goldman-Hodgkin-Katz (GHK) flux equation [5] was used. GHK flux equation was derived to model the flux of an ion "i", j_i, dictated by chemical, dC/dX, and electrical potential, dΨ/dX, gradients across a biological membrane:

$$j_i = -Z_i \times u_i \times R \times T \times \left(\frac{dC}{dX} + Z_i \times C \times \frac{F}{R \times T} \times \frac{d\Psi}{dX}\right) \quad (16)$$

Where Z is charge and valence of the ion, "i", C is the ion concentration, R is gas constant, T is absolute temperature, i.e. 0 Kelvin, and u_i is the electro-kinetic ion mobility and is further related to the diffusion coefficient, D_i, of the ion by the following Einstein relation:

$$u_i = D_i \times \frac{Z_i \times F}{R \times T} \quad (17)$$

Assuming a constant electric field across a homogenous membrane with thickness of l, the above equation is integrated at steady state to give the flux of ion "i" across the membrane using boundary conditions where at x = 0, the ion concentration = C_0 (i.e. ion concentration before transportation at one side of the membrane) and at x = l, the ion concentration = C_1 (i.e. ion concentration following transportation to the other side of the membrane):

$$j_i = \frac{u_i}{l} \times \Delta\Psi \times \frac{C_o - (C_1 \times e^{-Z \times Y})}{1 - e^{-Z \times Y}} \quad (18)$$

Where Y is ΔΨ normalized by RT/F (equation 19) for cells at room temperature, 25°C, which equals 25.69 mV [6]:

$$Y = \frac{\Delta\Psi \times F}{R \times T} \tag{19}$$

Thus, substituting terms in equation 18 by the ones in equations 17, we obtain:

$$j_i = \frac{D_i \times Z_i \times F}{R \times T \times l} \times \Delta\Psi \times \frac{C_o - (C_1 \times e^{-Z \times Y})}{1 - e^{-Z \times Y}} \tag{20}$$

Moreover, equation 20 can be further simplified using the relationship in equation 19:

$$j_i = \frac{D_i \times Z_i \times Y}{l} \times \frac{C_o - (C_1 \times e^{-Z \times Y})}{1 - e^{-Z \times Y}} \tag{21}$$

Furthermore, the diffusion coefficient can be written in terms of the permeability of the ion across the membrane using the following equation:

$$P_i = \frac{K_i \times D_i}{l} \tag{22}$$

Where K_i is the water-membrane partition coefficient of the ion “i" and measures the solubility of the ion in lipids. This term is set to 1 for either a co-ion or a counterion since the pore size of an ion membrane transporter is generally large and the partition coefficient of an ion in a pore approaches 1 as the pore size increases [7].

Thus, by substituting equation 22 into equation 21, we obtain:

$$j_i = P_i \times Y \times Z \times \frac{C_o - (C_1 \times e^{-Z \times Y})}{1 - e^{-Z \times Y}} \tag{23}$$

Because equation 23 gives the ion flux over a single area in units of Molar per second, the rate is multiplied by the total lysosomal surface area, S, to determine the total ion flux, as follows:

$$j_i = S \times P_i \times Y \times Z \times \frac{C_o - (C_1 \times e^{-Z \times Y})}{1 - e^{-Z \times Y}} \tag{24}$$

Accordingly, the total amount of free proton that can be transported from the lysosome to the cytoplasm, H_{leak}, in units of Molar per second (which is further converted into molecules per

second by multiplying it by Avogardo's number, N_{av}) follows the derivation of equation 24 and thus, can be written as:

$$H_{leak} = \left(S \times P_{H^+} \times Y \times Z \times \frac{10^{-pH_L} - \left(10^{-pH_C} \times e^{-Z\times Y}\right)}{1 - e^{-Z\times Y}}\right) \times N_{av} \quad (25)$$

With pH^+ being the proton permeability in units of cm/s, pH_L is the lysosomal luminal pH in units of pH units used to calculate the free lysosomal proton, 10^{-pH_L}, in units of Molar, pH_c is the cytoplasmic pH in units of pH units used to calculate the free cytoplasmic proton, 10^{-pH_C}, in units of Molar, Z, S, and Y are the same terms as previously described.

B.1.3. Modeling the effect of membrane leaflet potentials on ions.

Using an equation derived from the previously defined GHK flux equation, the concentrations of the transported ions are further modified based on the surface membrane potential exposed to either the cytoplasm or the lysosomal compartment [6]. In the case where net current flow is zero, the GHK equation that defines the membrane potential, which in this case is also defined as Nernst potential, $\Delta\Psi_i$, of a given ion "i", is presented as:

$$\Delta\Psi = \Delta\Psi_i = \frac{-Z\times R\times T}{F} \times \ln\frac{C_{i,0}}{C_{i,1}} \quad (26)$$

With C_i being the concentration of the ion "i" in units of Molar and the position of the ion are denoted by the subscripts 0 and 1.

Thus, by inserting the intrinsic internal leaflet potential, Ψ_{in}, in units of mV into equation 26, the concentration of a given ion at the membrane surface facing the lysosomal compartment is calculated according to the following relationship:

$$\Delta\Psi_{i,in} = \frac{-Z\times R\times T}{F} \times \ln\frac{C_{i,in}}{C_{i,L}} \quad (27)$$

With $C_{i,in}$ being the internal concentration of a given ion at the membrane surface facing the lysosomal compartment in units of Molar, and $C_{i,L}$ is the concentration of the same ion in the non-membrane region of the lysosomal compartment in units of Molar.

Similarly, by inserting intrinsic external or outer leaflet potential, Ψ_{out}, in units of mV into equation 26, the concentration of a given ion at the membrane surface facing the cytoplasmic compartment is calculated according to the following relationship:

$$\Delta\Psi_{i,out} = \frac{-Z\times R\times T}{F} \times \ln\frac{C_{i,out}}{C_{i,C}} \quad (28)$$

With $C_{i,out}$ being the external concentration of a given ion at the membrane surface facing the cytoplasmic compartment in units of Molar, and $C_{i,c}$ is the concentration of the same ion in the non-membrane region of the cytoplasmic compartment in units of Molar.

B.1.4. Governing equations.

The aforementioned ion flux equations are used to generate a kinetic model to monitor the time-dependent changes in lysosomal proton and chloride molecules per second as described by equations 29 and 30:

$$\frac{dH^+}{dt} = H_{pump} - H_{ClC7} - H_{leak} \quad (29)$$

$$\frac{dCl^-}{dt} = 2 \times N_{ClC} \times J_{Cl,H_{ClC7}}(\Delta pH, Cl_L, Cl_C, \Delta\Psi) \quad (30)$$

The coefficient "2" in equation 30 indicates that CLC7 transports chloride and proton across the lysosomal membrane in 2:1 stoichiometric ratio, which was used in published model [3] based on analysis of experimental studies[4].

We can further define the time-dependent change in pH by converting the total amount of lysosomal proton in units of molecules per second (equation 29) into units of Molar per second by dividing the terms in equation 29 by lysosomal volume and Avogadro's number. Moreover,

the Molar per second unit is converted into units of pH unit per second by dividing the entire term by the buffering capacity, β, which is represented in units of Molar per pH unit:

$$\frac{dpH}{dt} = \frac{(-H_{pump} + H_{ClC7} + H_{leak})}{V \times N_{av} \times \beta} \quad (31)$$

The lysosomal lumen buffering capacity of the Donnan particles entraps protons and thus, dictates lysosomal pH. It is experimentally measured by introducing a strong acid or base (in units of Molar) that can induce change of 1 pH unit. Thus, the physiological accumulation of weakly basic compounds, such as cationic amphiphilic and lysosomotropic drugs, will have insignificant effect on the buffering capacity, at least in theory, as the amount of proton they sequester from the lysosome will be fully released upon the hydration of the protonated drug, thereby maintaining mass-balance mediated physiological lysosomal pH. Although the buffering capacity varies with pH, for simplicity purpose, it was set to a constant according to literature values[3,8].

B.1.5. Numerical analysis.

The set of differential equations 29-31 was solved by numerical integration in Berkeley Madonna® using Rosenbrock stiff solver as a numerical integrator.

B.1.6. Model script

METHOD STIFF

STARTTIME = 0

STOPTIME =86400

DT = 0.02

DTMAX = 100

TOLERANCE = 1e-6

{Baseline Input Parameter List----------}

{Baseline Lysosomal Dimensions Assuming Spherical Geometry}

R = 0.34 {Radius [microns]}

V = 1.65e-16 {Volume [liters]}

SA = 1.45e-8 {Surface area [cm^2]}

{Baseline Cytosolic Volume}

Vc = 1.65e10 {Volume [liters]-arbitrarily chosen to result in almost constant cytoplasmic ion concentration}

{Intrinsic Surface Potentials-- used for calculating surface charges of each ion}

psi_out = -50 {Outer surface potential- used as outer resting membrane potential [mV]}

psi_in = 0 {Inner surface potential - used as inner resting membrane potential [mV]}

{Fixed Standard Constants}

mole = 6.02e23 {Avogadro's Number [1/mol]}

RTF = 25.69 {RT/F membrane potential for cells at room temperature [mV]}

F = 96485 {Faraday's Constant that converts unit of membrane potential [Coulomb/mol]}

cap_0 = 1e-6 {Capacitance per unit area of the lysosomal membrane [Farad/cm^2]}

cap = cap_0*SA/1000 {Total capacitance per lysosome [Farad]}

{Baseline Cytosolic Concentrations}

initpHbulk = 7.2 {pH [pH units]}

Kbulk = 0.145 {K+ [M]}

initclbulk = 0.01 {Cl- [M]}

Nabulk = 0.01 {Na+ [M]}

initHbulk = 0 {Total H+ [M]}

{Baseline Luminal Concentrations}

initpH = 7.4 {pH [pH units]}

initk = 0.005 {K+ [M]}

initcl = 0.11 {Cl- [M]}

initna = 0.145 {Na+ [M]}

initH = 0.00 {Total H+ [M]}

{Donnan Particles [M]: constitute the initial impermeant luminal ions that give rise to Donnan potential to balance the negatively charged proteins in the luminal matrix}

B = initk+initna+initH-initcl - cap/F/V*(psi_in - psi_out) - initpsi_total*cap/F/V {[M]}

{Set Initial Total Membrane Potential [mV]}

initpsi_total = 0

beta = 0.04 {Buffering capacity [M/pH unit] of the luminal matrix that sequesters protons from solution}

beta_bulk = 0.04 {Buffering capacity [M/pH unit] of the cytoplasm that sequesters protons from solution}

{Baseline Input Kinetic Parameters----------}

P = 6e-5 {Membrane H+ permeability. Experimentally determined- Ishida et al 2013}

N_VATP = 300 {Number of V-ATPases per lysosome. Experimentally estimated- Ishida et al 2013}

N_CLC7 = 5000 {Number of ClC7 antiporters per lysosome. Estimated- Ishida et al 2013}

CLC_Cl = 2 {CLC7 Cl- Stoichiometry. Experimentally determined- Graves et al 2008}

CLC_H = 1 {CLC7 H+ Stoichiometry. Experimentally determined- Graves et al 2008}

{ODE- Time Dependent Ion Flows----------}

d/dt (pH) = ((-Hpump - Hleak - (CLC_H*CLC7))/V/mole)/beta

INIT pH = initpH {Lysosomal pH as a function of time [pH unit/sec]}

d/dt (NCl) = -CLC_Cl*CLC7

INIT NCl = initcl*V*mole {Lysosomal Cl- as a function of time [Cl-/sec]}

d/dt (NH) = +Hpump + Hleak + (CLC_H*CLC7)

INIT NH = initH*V*mole {Total lysosomal H+ as a function of time [H+/sec]}

d/dt (pHbulk) = ((+Hpump + Hleak + (CLC_H*CLC7))/Vc/mole)/beta_bulk

INIT pHbulk = initpHbulk {Cytoplasmic pH as a function of time [pH unit/sec]}

d/dt (NHbulk) = -Hpump- Hleak - (CLC_H*CLC7)

INIT NHbulk = initHbulk*Vc*mole {Cytoplasmic H+ as a function of time [H+/sec]}

d/dt (NClbulk) = +CLC_Cl*CLC7

INIT NClbulk = initclbulk*Vc*mole {Cytoplasmic Cl^- as a function of time [Cl-/sec]}

{Ion Flows Through Lysosomal Membrane Channels and Pumps----------}

{Proton Pump}

JH_VATP = #protonpump2 (pH, psi) {Proton pump [H^+/sec] by a single V-ATPase molecule as a function of luminal pH gradient and membrane potential. Surface dataset ("protonpump2") imported from Matlab as a call-in function}

Hpump = N_VATP*JH_VATP {Total proton pump flow [H+/sec] by a total number of VATPases per lysosome}

{ClC7 Antiporter: Membrane Potential Dissipation}

clc7f = (CLC_Cl+CLC_H)*psi + RTF*(2.3*(pHe - pHi) + CLC_Cl*LOGN(Cle/Cli))

{Transmembrane H+ and Cl- motive force across lysosomal membrane that drives CLC7 antiporter's function- Ishida et al 2013}

G1 = -0.3*clc7f {0.3 was determined by experimental fitting- Ishida et al 2013. Linear function for positive "psi"}

G3 = -1.5E-5*clc7f^3 {1.5 was determined by experimental fitting- Ishida et al 2013. Cubic function for negative "psi"}

S = 0.5+0.5*TANH((clc7f+250)/75) {Switching function that ranges 0 to 1 depending on the sign of "psi"}

JCLC7 = S*G1+ (1-S)*G3 {Single CLC7 antiporter turnover. Function switches from linear to a 3-degree polynomial function depending on "S" to empirically fit experimental data- Ishida et al 2013}

CLC7 = N_CLC7*JCLC7 {Total ClC7 antiporter turnover [1/sec]}

{Define Terms for Goldman-Hodgkin-Katz Flux (GHK) Equation}

gg = IF abs(psi) > .01 THEN psi/(1-exp(-psi/RTF))/RTF ELSE

1/(1 - (psi/RTF)/2 + (psi/RTF)^2/6 - (psi/RTF)^3/24 +(psi/RTF)^4/120) {IF THEN statement to avoid computational error when psi = 0. Taylor series expansion about a point = (psi/RTF) when psi is less than RTF}

{Passive Flows Across Lysosomal Membrane Modeled According to GHK Flux Equation}

Hleak = P*SA*(10^(-pHe)*exp(-psi/RTF)-10^(-pHi))*gg*mole/1000

{[H^+/sec]}

{Functions/Conversions----------}

{Membrane Potentials}

psi = F*(V*(H+initk+initna- Cl - B))/cap {Membrane potential [mV] dictated by the net change in lysosomal ions, lysosomal membrane capacitance, buffering capacity, and Donnan Particles, characteristics of the luminal matrix. Valence of each ion (plus or minus 1) is implicitly considered}

psi_total = psi + psi_out-psi_in {Total membrane potential [mV]}

{Luminal Concentrations}

Cl = NCl/V/mole {[M]}

H = NH/V/mole {Total H+ [M]}

{Luminal Content}

Cl_mol = Cl*V {Cl-}

H_mol = H*V {Total H+}

{Cytosolic Concentrations}

Clbulk = NClbulk/Vc/mole {Cl [M]}

Hbulk = NHbulk/Vc/mole {Total H+ [M]}

{Cytosolic Content}

Clbulk_mol = Clbulk*Vc {Cl-}

Hbulk_mol = Hbulk*Vc {Total H+}

{Modified Cytoplasmic Surface Concentrations Dictated by Surface Potential- Derived from GHK for a single ion in the case of zero net current flow; also known as Nernst equation}

Cle = Clbulk*exp(psi_out/RTF) {[M]}

Ke = Kbulk*exp(-psi_out/RTF) {[M]}

Nae = Nabulk*exp(-psi_out/RTF) {[M]}

pHe = (pHbulk+psi_out/(RTF*2.3)) {[pH units]}

{Modified Luminal Surface Concentrations Dictated by Surface Potential - Derived from GHK for a single ion in the case of zero net current flow; also known as Nernst equation}

Cli = Cl*exp(psi_in/RTF) {[M]}

Ki = initK*exp(-psi_in/RTF) {[M]}

Nai = initNa*exp(-psi_in/RTF) {[M]}

pHi = (pH+psi_in/(RTF*2.3)) {[pH units]}

B.2. Supplementary Figures

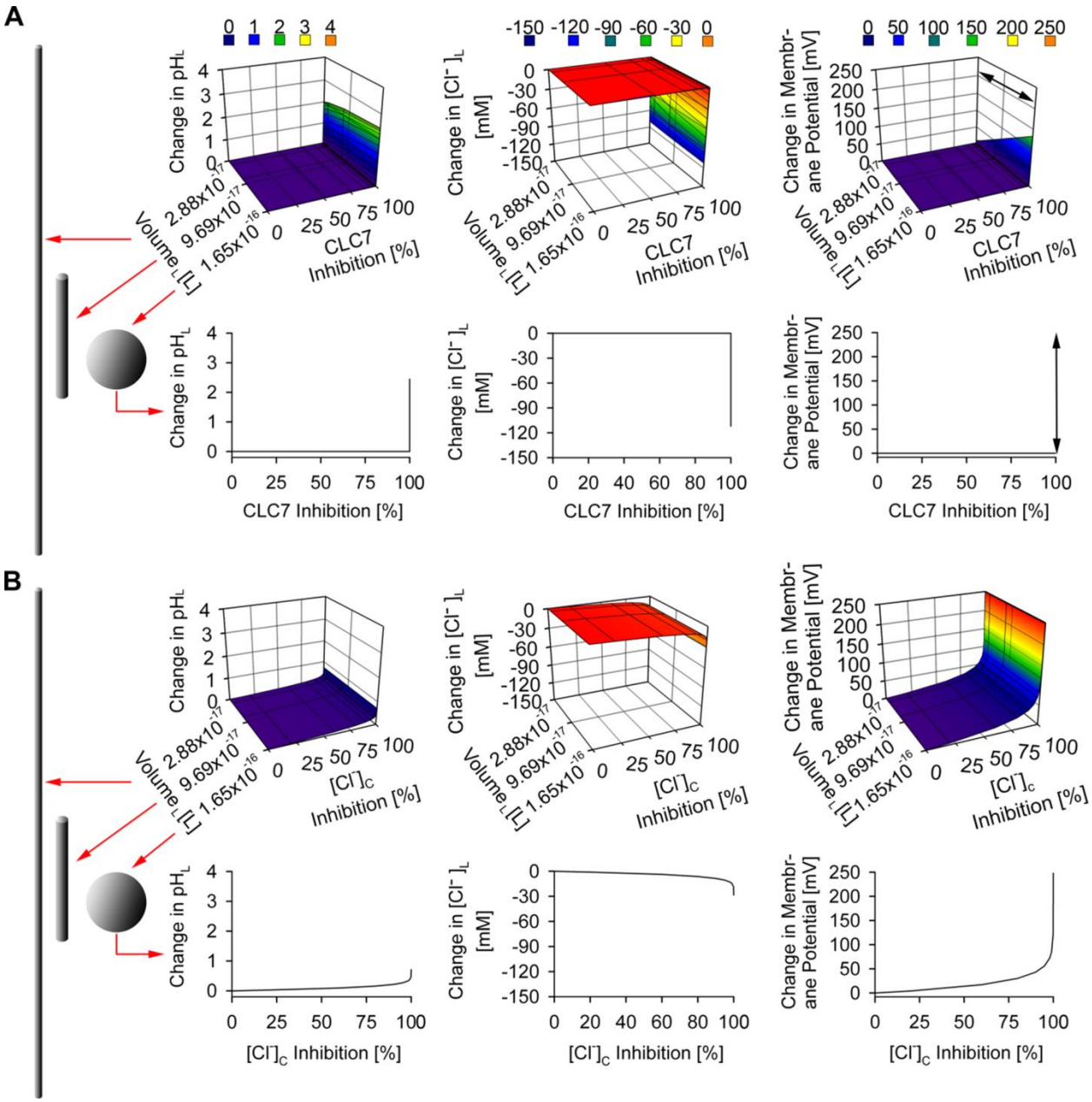

Figure B.1 The effects of individual lysosomal chloride transportation stressors on the physiology of spherical versus tubular lysosomes.
(**A**) Modeling the effect of varying CLC7 number on lysosomal pH, Cl^-, and membrane potential with respect to different lysosomal morphology. Maximum depletion of CLC7 has a slightly more pronounced effect on spherical lysosomal physiology than on tubular lysosomal physiology, as reflected by the maximum increment in membrane potential (> 250 mV, represented by the black arrow). (**B**) Modeling the effect of varying cytoplasmic chloride concentration on lysosomal pH, Cl^-, and membrane potential with respect to different lysosomal morphology. Maximum depletion of cytoplasmic chloride induced maximum increment in membrane potential (up to 248.3 mV), with minimal changes in lysosomal pH and Cl^- accumulation.

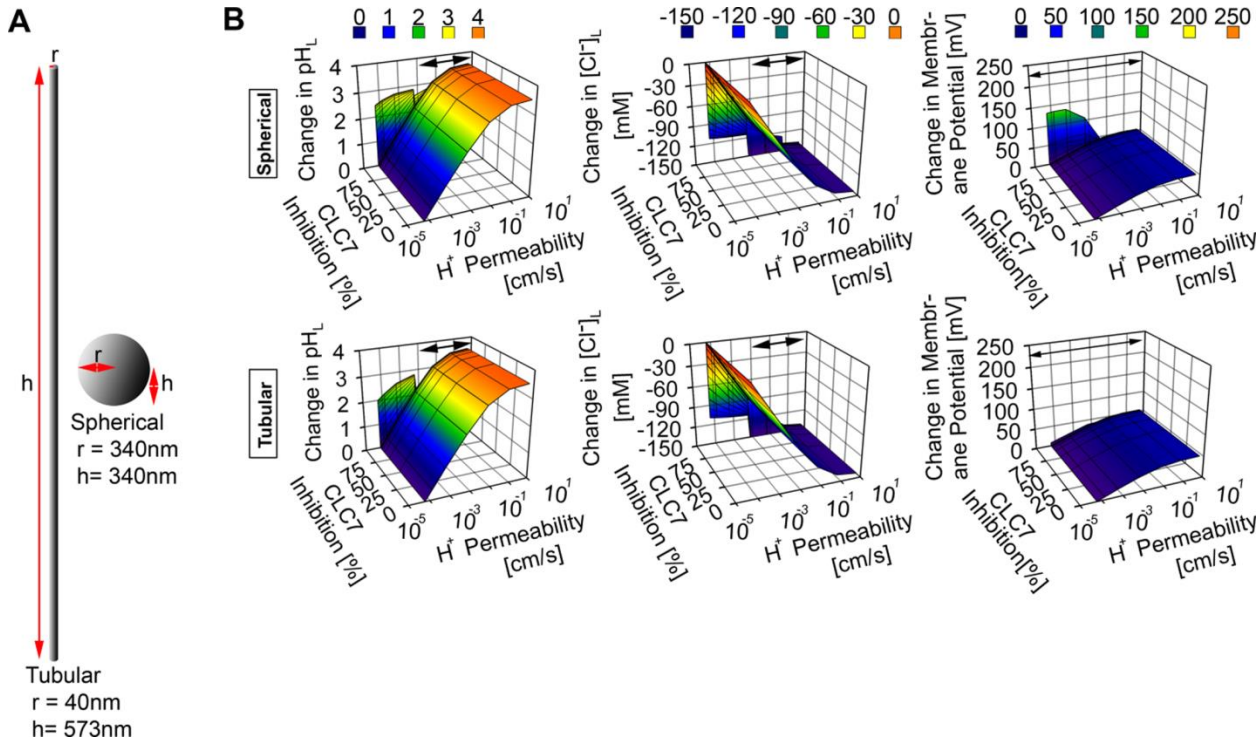

Figure B.2 The effect of a simultaneous CLC7 inhibition and membrane proton permeabilization on the physiology of spherical versus tubular lysosomes.
(**A**) Lysosomal dimensions used to generate spherical and tubular lysosomes. (**B**) Modeling the effect of simultaneous variations of CLC7 number and membrane proton permeability on lysosomal pH, Cl^-, and membrane potential**.** The simultaneous maximum depletion of CLC7 number and increment in membrane proton permeability (> $6x10^{-3}$ cm/s in the case of the effect on lysosomal pH and Cl^-, and > $6 x10^{-5}$ cm/s in the case of the effect on lysosomal membrane potential) induces > 4 pH unit increment in lysosomal pH, > 150 mM reduction in lysosomal Cl^- accumulation, and > 250 mV increment in membrane potential, as indicated by the black arrows. Although the overall effect of these stressors is very similar in both spherical and tubular lysosomal physiology, the effect is slightly more pronounced on spherical lysosomal physiology.

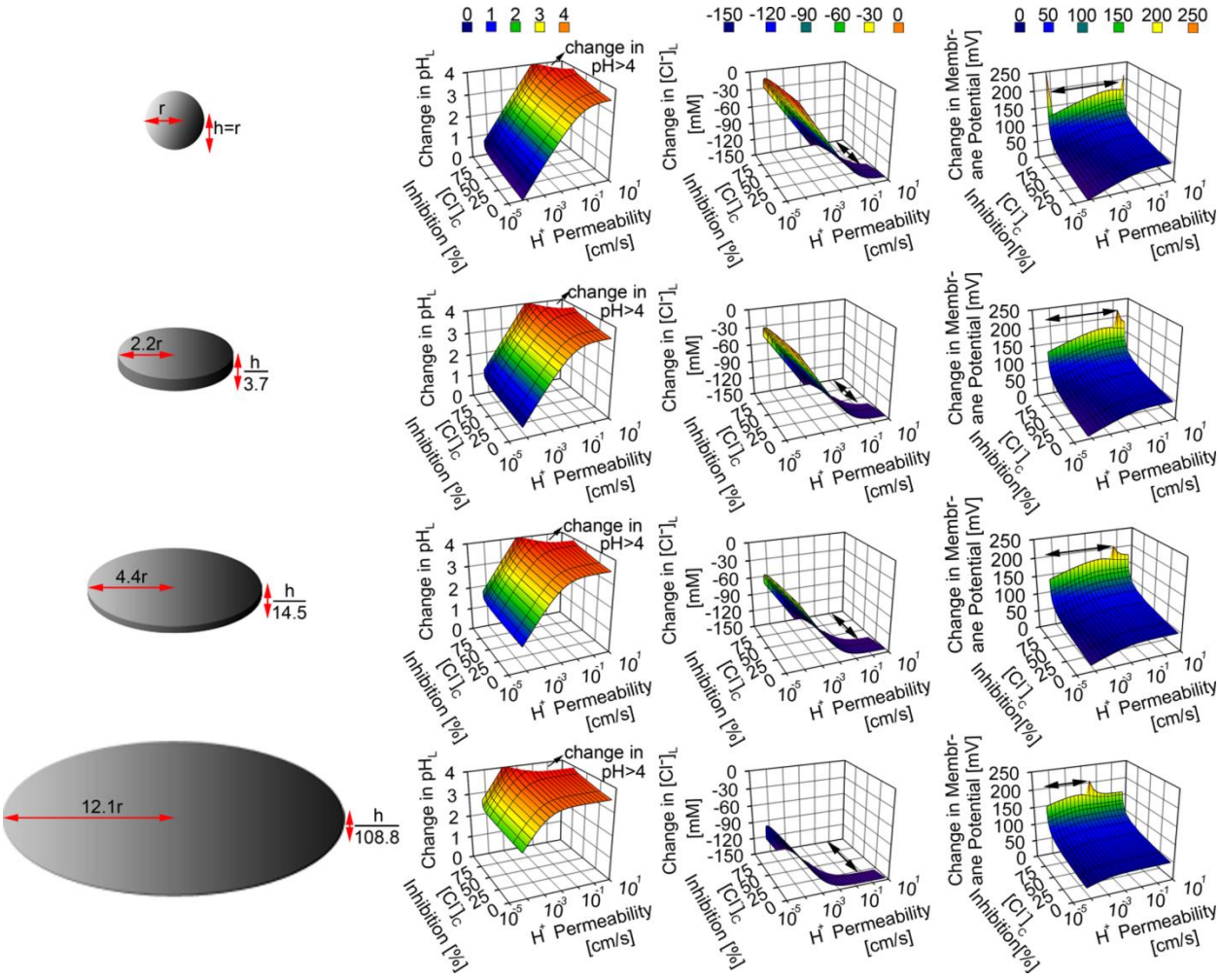

Figure B.3 The effect of a simultaneous cytoplasmic chloride inhibition and membrane proton permeabilization on spherical versus disc-shaped lysosomal physiology. Cytoplasmic chloride concentration and membrane proton permeability were simultaneously varied in spherical and different sized disc-shaped lysosomes to observe their combined effects on lysosomal pH, Cl^-, and membrane potential. Simultaneously increasing the cytoplasmic chloride inhibition (> 80%) and membrane proton permeability (> 0.06 cm/s) induced > 4 pH unit increment in lysosomal pH and > 150 mM reduction in lysosomal Cl^- accumulation, represented by the black arrows. For all lysosomal morphologies, maximum increment in membrane potential (> 250 mV, represented by the black arrows) is observed at maximum cytoplasmic chloride inhibition. However, the perturbation in lysosomal physiology was generally pronounced as the lysosomal radius and surface area expansions were increased.

B.3. References

1 Fricke, H. The Electric Capacity of Suspensions with Special Reference to Blood. *J Gen Physiol* **9**, 137-152 (1925).

2 Fenwick, E. M., Marty, A. & Neher, E. Sodium and calcium channels in bovine chromaffin cells. *J Physiol* **331**, 599-635 (1982).

3 Ishida, Y., Nayak, S., Mindell, J. A. & Grabe, M. A model of lysosomal pH regulation. *J Gen Physiol* **141**, 705-720, doi:10.1085/jgp.201210930 (2013).

4 Graves, A. R., Curran, P. K., Smith, C. L. & Mindell, J. A. The Cl-/H+ antiporter ClC-7 is the primary chloride permeation pathway in lysosomes. *Nature* **453**, 788-792, doi:10.1038/nature06907 (2008).

5 Weiss, T. F. *Cellular Biophysics: Transport*. (MIT Press, 1996).

6 Hille, B. *Ionic Channels of Excitable Membranes. 2nd Edition*. 607 (Sinauer Associates, Inc. , 1992).

7 Buyukdagli, S., Manghi, M. & Palmeri, J. Variational approach for electrolyte solutions: from dielectric interfaces to charged nanopores. *Phys Rev E Stat Nonlin Soft Matter Phys* **81**, 041601, doi:10.1103/PhysRevE.81.041601 (2010).

8 Gekle, M. & Silbernagl, S. Comparison of the buffer capacity of endocytotic vesicles, lysosomes and cytoplasm in cells derived from the proximal tubule of the kidney (opossum kidney cells). *Pflugers Arch* **429**, 452-454 (1995).

9 Alberts B, J. A., Lewis J, Raff M, Roberts K, Walter P. Molecular Biology of the Cell. 4th edition. New York: Garland Science; 2002. Transport into the Cell from the Plasma Membrane: Endocytosis. Available from: https://www.ncbi.nlm.nih.gov/books/NBK26870/.